UCLouvain
Institute of Mechanics,
Materials and Civil Engineering

Residual stresses, Geometrical Defects and Surface Hardening: Impacts on Lifetime of Biomedical Implants

Maïté Croonenborghs

Thesis submitted in partial fulfillment
of the requirements for the degree of
Docteur en sciences de l'ingénieur

Dissertation committee:

Prof. Pascal Jacques (UCLouvain, Belgium) - **advisor**
Prof. Thomas Pardoen (UCLouvain, Belgium) - **advisor**
Prof. Sandra Soares Frazao (UCLouvain, Belgium) - **chair**
Prof. Xavier Banse (UCLouvain, Belgium)
Prof. Laurent Delannay (UCLouvain, Belgium)
Dr. Pascale Kanouté (ONERA, France)
Prof. Clément Keller (Ecole Nationale d'Ingénieurs de Tarbes, France)
Prof. Greet Kerckhofs (UCLouvain, Belgium)

Version of February 12, 2024.

Remerciements

Une thèse, c'est un peu comme un tour du monde à la voile, où l'on prend la barre d'un bateau en ne connaissant que le chemin global à suivre et dont le voyage est parsemé de nombreuses surprises.

Avant de se lancer dans un tel voyage, il y a d'autres grands navigateurs qui nous ont inspirés et qui nous ont demandé "et pourquoi pas toi?". Je voudrais donc remercier Charles et Muriel pour m'avoir fait découvrir la vie de chercheur au sein du laboratoire SIMAP, mais également Karim pour son encadrement inspirant durant mon mémoire.

Et puis un jour le projet prend forme et nous voilà lancés sur l'océan de la recherche, avec une multitude de routes possibles. Tout au long de ce voyage, j'ai pu être guidée par mes deux promoteurs, Thomas Pardoen et Pascal J. Jacques. Merci à tous les deux d'avoir partagé avec passion vos plus précieux conseils. Une thèse est un voyage plein de rebondissements : vous avez su me guider avec sagesse, ajustant le cap pour éviter le naufrage, me remotiver lors des quelques avaries, mais aussi vous émerveiller avec moi devant de beaux paysages (plus communément appelés slides) lors de nos réunions régulières. Merci pour votre confiance durant toutes ces années.

Merci également aux membres de mon jury, présents à l'arrivée de cette incroyable expérience. Les discussions que nous avons eues ont été très enrichissantes et m'ont permis de réaliser le chemin parcouru. Merci d'avoir pris le temps de participer à ce jury et d'avoir installé une atmosphère accueillante durant la défense privée.

Un voilier ne pourrait pas réaliser un tel périple sans une équipe technique des plus ingénieuses et disponibles et une équipe administrative réactive

et à l'écoute. C'est pourquoi je voudrais remercier toutes les équipes techniques des différents laboratoires, sans qui nous n'avancerions pas beaucoup dans nos recherches. De l'usinage, aux analyses, en passant par le fonctionnement au jour le jour des plateformes, leur travail nous est précieux ! Alors merci à Marc, Alban, Bruno, Jonathan, Nadine, Ronny, Fred, Maxence, Armand, Laurence, Catherine, Quentin et Alex. Nous sommes entourés également d'une équipe administrative en or capable de répondre à nos nombreuses demandes, souvent un peu en dernière minute. Alors merci beaucoup à Catherine, Isabelle et Rania!

Une expédition scientifique donne également l'occasion de collaborer avec des personnes riches de nombreuses compétences. A special thanks to Alexander M. Korsunsky and Joris Everaerts from the Department of Engineering Science (University of Oxford) for the FIB-DIC measurements and for their contribution to the associated article. Merci également à Laurent et à Colin, qui m'ont aidé à développer les modèles numériques de ma recherche (... moi qui pensais ne plus jamais faire d'éléments finis après mon mémoire). Merci à Xavier qui a su redoubler d'imagination pour concevoir et élaborer le setup de flexion en fatigue. Merci à Olivier m'avoir fait découvrir l'interférométrie à la platerforme du Welcome. Toute la partie de ma recherche sur les tiges de croissance n'aurait pas pu exister sans l'intervention de Maryline Mousny qui a questionné ses pratiques chirurgicales dans le but d'améliorer les soins de ses patients. Je la remercie pour sa curiosité et son regard externe qui nous ont permis de faire un pas de plus dans la compréhension de la rupture de ces implants. Je me souviendrai toujours de ton soutien bienveillant durant nos rencontres.

Et puis il y a tous ces autres marins, à côté de qui on navigue et avec qui on se crée des souvenirs à chaque escale. Alors merci à tous les doctorants que j'ai rencontrés sur la route. Merci à Karim et Aude de m'avoir conseillée durant mes premières années, merci à la team pâtisserie pour tous ces délicieux gâteaux partagés en très bonne compagnie, merci à la team Poulet qui danse pour ces moments de détente, bien nécessaires, pendant la période Covid, merci à toute la brochette de mariées pour les pauses conseils et bons plans à la kfet, un énorme merci à la team des fous du 2ème pour tous ces beaux moments partagés autour de projets communs, comme les cloches de Pâques, les 24h vélo, ou simplement autour d'une tasse de thé mais merci également pour vos nombreux conseils en anglais ces derniers mois ;-) Merci à Laurine et Marion d'avoir toujours été disponibles pour discuter de science quand j'en avais besoin, merci pour

vos précieux conseils mais aussi pour vos compliments qui m'ont fait gagner en confiance en moi. Plus généralement, mais tout aussi important à mes yeux, je voudrais remercier tous les membres du pôle IMAP pour leur participation à ce climat si familial et bienveillant que l'on y trouve. Enfin, un grand merci aux deux très belles personnes que sont Charles et Anne-Sophie pour ces moments de complicité loin de la science passés ensemble.

Entre deux traversées dans les mers expérimentales ou numériques, j'ai eu la chance d'encadrer les séances d'exercices, projets et laboratoires de nombreux étudiants. Je voudrais les remercier de s'être prêté au jeu quand je cherchais à augmenter l'interaction des séances, remercier les collègues que j'ai embarqués dans ces séances pour leur entrain malgré la nouveauté, mais également remercier les professeurs qui m'ont fait confiance et qui m'ont donné l'opportunité de me découvrir une vraie passion. J'ai donc aussi pris du temps durant ce voyage pour faire un petit détour et me former davantage en pédagogie. Merci encore à mes promoteurs de m'avoir laissé du temps pour mener ce projet à terme, merci particulièrement à Pascal pour s'être prêté au jeu en me laissant créer et donner deux séances d'exercices qui sortent de l'ordinaire. Merci M-C pour toutes les chouettes discussions que l'on a pu avoir durant cette formation et pour tes feedbacks! J'ai adoré partager nos idéaux de formation chez les ingénieurs pendant ces deux années.

Merci également à Pierre-Yves Gousenbourger pour le partage de son template LaTeXqui m'a fait gagner un temps fou au moment de la rédaction et grâce à toi: "oh mon bateau, c'est le plus beau des bateaux" [♫ Eric Morena, 1989]

Aux personnes qui ont suivi mon voyage d'un peu plus loin: merci à tous mes amis proches et à ma famille qui m'ont régulièrement questionnée sur l'avancement de ma thèse et son contenu, mais qui m'ont aussi encouragée. Vous avez entre vos mains ma *petite rédaction* comme certains aimaient l'appeler. Un merci particulier pour ma petite mascotte: Mr blocus! Toujours au taquet pour aller travailler! Ta présence pendant la rédaction m'a souvent remotivée.

Pour finir, merci infiniment à mon super-prince charmant (ou plus communément, mon mari) Adrien, pour tout son soutien apporté durant ces années, et plus particulièrement durant cette fin de thèse qui a été intense à gérer en parallèle de tous nos merveilleux projets. Merci d'avoir été à l'écoute quand j'en avais besoin, de m'avoir encouragée encore et encore,

d'avoir assuré de nombreuses tâches quand je n'avais plus le temps ou l'énergie, ... Ainsi j'ai pu trouver à la maison, un mouillage paradisiaque à l'abri de toutes les tempêtes. C'est maintenant ensemble qu'on largue les amarres pour une aventure en duo :-)

To children and families awaiting scientific breakthroughs. May this research, contribute to the collective pursuit of medical advancements for all,

To Esther and Sarah,

Contents

Abstract . . . . . **xi**

Résumé . . . . . **xiii**

I Context and fundamentals

1 Introduction **3**

2 State of the art on biomedical implants **9**

2.1 Context about the human body 10

2.1.1 Implants 10

2.1.2 Materials 11

2.1.3 Impact of surface finish 14

2.2 Mechanical properties of metallic alloys 15

2.2.1 Strain hardening 15

2.2.2 Necking 18

2.2.3 Fatigue 21

2.3 From origins to impact: understanding residual stresses 24

2.3.1 Origins and types of RS 25

2.3.2 Elevating material performance: The role of shot-peening . . 28

2.3.3 From residual stress to kinematic hardening 30

2.4 Conclusions and open questions 32

II Failure analysis of growing rods

3 Context of growing rods: surgical practices and failure problems 37

3.1 Planes, directions and deformities . . . 38
3.2 Scoliosis . . . 39
3.2.1 Causes . . . 40
3.2.2 Treatments . . . 41
3.3 Growing rod implants . . . 42
3.3.1 Lifetime of growing rods . . . 44
3.4 State of the art on growing rod failure . . . 49
3.4.1 Identification of failure mechanism . . . 50
3.4.2 Fatigue resistance and plasticity . . . 51
3.4.3 Fatigue resistance and indents . . . 53
3.5 Research questions . . . 54

4 Residual Stresses in Surgical Growing Rods . . . 61
4.1 Context . . . 62
4.2 Materials and methods . . . 65
4.2.1 Materials . . . 65
4.2.2 Methods . . . 67
4.3 Experimental results . . . 68
4.4 Modelling and simulation . . . 70
4.4.1 Finite element model . . . 71
4.4.2 Results . . . 73
4.5 Discussion . . . 80
4.5.1 Prediction of the residual stress profile . . . 81
4.5.2 Towards favoring compressive residual stresses . . . 81
4.5.3 Limitations of the model and perspectives . . . 86
4.6 Conclusions . . . 87

5 Fatigue testing of curved rods . . . 89
5.1 Introduction . . . 90
5.2 Design process . . . 91
5.3 FE Model of a curved rod under loading . . . 94
5.3.1 Numerical model . . . 94
5.3.2 Strain life or stress life approach . . . 96
5.4 Validation and experimental results . . . 97
5.4.1 Materials . . . 97
5.4.2 Methods . . . 98
5.4.3 Validation for monotonic loading . . . 100
5.4.4 Validation for cyclic loading . . . 102
5.4.5 Fatigue test campaign on bent Ti rods . . . 104

5.5 Discussion . . . 105
5.6 Conclusion . . . 109

6 On the mitigation of fatigue failure in growing rods through plastic deformation . . . 111
6.1 Context . . . 112
6.2 Materials and methods . . . 118
6.2.1 Materials . . . 118
6.2.2 Characterization Methods . . . 120
6.2.3 Experimental and numerical methods . . . 122
6.3 Results . . . 125
6.3.1 Fatigue lifetime . . . 125
6.3.2 Fractographies . . . 131
6.4 Discussion . . . 132
6.5 Conclusion . . . 136

III Failure analysis of stents

7 Context of stents: characteristic sizes and expansion process . 141
7.1 Arteriosclerosis . . . 142
7.1.1 Treatments . . . 142
7.2 Stent implants . . . 143
7.2.1 Surface state . . . 145
7.2.2 Mechanical answer of a stent . . . 148
7.3 Research questions . . . 152

8 Plastic localization in inhomogeneous rods . . . 155
8.1 Introduction . . . 156
8.1.1 Localization length definitions . . . 156
8.1.2 Effect of geometrical imperfections on necking . . . 161
8.2 Experimental and numerical procedures . . . 167
8.2.1 Material characterization . . . 167
8.2.2 Imperfection characterization . . . 169
8.2.3 Mechanical testing . . . 170
8.2.4 Finite element model . . . 171
8.3 Results . . . 172
8.3.1 Deformation along the surface . . . 173
8.3.2 Comparison of neck length based on imperfection characteristic dimensions . . . 184

8.3.3 Total elongation criteria 186
8.3.4 Discussion 189
8.4 Conclusions and perspectives 190

9 Conclusions and perspectives **193**
9.1 Increasing the fatigue resistance of growing rods 193
9.2 Geometrical imperfections in long metallic components 198

Bibliography **199**

A Fracture mechanisms in Ti and Co–Cr growing rods and impact on clinical practice **219**

B Appendix of Chapter 6 - Hardening laws **247**

C Supplementary of Chapter 6 - Fractographies **249**

D Appendix of Chapter 8 - Samples Dimensions **253**

E Appendix of Chapter 8 - Mesh convergence analysis **257**

Abstract

The imperative of reliability of biomedical implants is crucial to ensure their long-term functionality, thereby reducing the need for additional, sometimes invasive, surgical interventions. In this context, growing rods used to correct scoliosis in growing children face challenges related to a high fatigue failure rate. Similarly, future generations of stents designed to restore blood flow in arteries must overcome potentially rough surface conditions while ensuring effective deployment without failure.

The primary aim of this thesis is to investigate the relative impact of shot-peening and bending within growing rods on the generation of residual stresses, employing mechanical tests and numerical methods. While shot-peening proves to be beneficial by enhancing compressive stresses, bending has been found detrimental, even if the magnitude of the imposed bending angle itself is not crucial. The multiple surface hardening steps guide towards the selection of metals with significant kinematic hardening capacity. Comparing these numerical results with experimental findings reveals an unexpected fatigue resistance of untreated rods under certain conditions, raising concerns about the shaping processes used by the suppliers.

The second part of the work explored the impact of surface quality. The roughness resulting from shaping processes appears to be the cause of the fatigue resistance reduction in growing rods. Furthermore, geometric irregularities can limit the elongation capacity of structures like in stent struts due to the decrease resistance to plastic localization. This finding, established since the 1960s through closed form models, has been verified using a finite element numerical model and experimental measurements relying on digital image correlation. Additionally, the length of the inhomogeneity has been shown to influence the length of the neck.

Résumé

L'impératif de fiabilité des implants biomédicaux revêt une importance cruciale afin d'assurer leur fonctionnalité à long terme, limitant ainsi la nécessité d'interventions chirurgicales supplémentaires, parfois invasives. Dans ce contexte, les tiges de croissance, utilisées pour corriger les scolioses chez les enfants en pleine croissance, se heurtent à des défis liés à un haut taux de rupture par fatigue. De même, les futures générations de stents, conçus pour restaurer le flux sanguin dans les artères, devront surmonter des états de surface potentiellement rugueux tout en garantissant leur déploiement efficace sans rupture.

L'objectif principal de cette thèse est d'étudier l'impact relatif du grenaillage et du pliage au sein des tiges de croissance sur la génération des contraintes résiduelles, à l'aide d'essais mécaniques et de méthodes numériques. Alors que le grenaillage s'avère bénéfique en augmentant les contraintes de compression, il a été démontré que le pliage est néfaste, même si l'amplitude de l'angle n'est pas déterminant. Les multiples étapes de durcissement superficiel guident vers une sélection des métaux présentant un écrouissage cinématique important. La comparaison des résultats numériques avec les résultats expérimentaux révèle une résistance à la fatigue inattendue des tiges non grenaillées dans certaines conditions, remettant en question les procédés de mise en forme utilisés par les fournisseurs.

La seconde partie a exploré l'impact de la qualité de surface. La rugosité issue du grenaillage semble être responsable de la diminution de la résistance en fatigue des tiges de croissance. De plus, des irrégularités géométriques peuvent restreindre la capacité d'allongement de structures telles que les stents, du à la réduction de la résistance à la localisation plastique. Cette constatation, établie dès les années 60 à l'aide de modèles semi-analytiques, a été vérifiée par un modèle numérique (éléments finis) et des mesures expérimentales (corrélation d'images numériques). En outre, il a été observé que la longueur de l'inhomogénéité influe sur celle du col de striction.

PART I
Context and fundamentals

1

Introduction

WHEN a new device is designed, it has to fulfill precise specifications. This includes on one hand objectives and on the other hand constraints. Those constraints can have different origins: mechanical, thermal, electrical,... depending on the environment of the objects. Engineers in charge of their conception must anticipate any source of imperfections that could undermine their assumed performances to size it properly. Indeed, if imperfections are not well predicted in the conception step, devices may fail prematurely (see Figure 1.1). To this end, it is important to identify the potential origins of imperfections but also to predict if their size may lead to functional issues. Defects can be present at the surface as well as inside the pieces. In this thesis, we will focus on the first ones.

(a) (b) (c)

Figure 1.1 Broken devices: (a) Failure of a stent's strut [1]; (b) Crack in a steel I-beam [2]; (c) Blown turbine disc [3].

Any object surfaces present a certain level of roughness. Roughness quantifies the average variation of surface irregularities over a long distance. The roughness amplitude of a device is generally managed during the last shaping process. However, during production, surface irregularities larger than the specification instructions may appear (see Figure 1.2). Some are unexpected, due to clumsy handling, and others are foreseeable, resulting from a planned handling in its manufacturing process. The unexpected one should be detected and measured before the quality department states if the piece can continue to its useful life, or if it should be set aside. In other cases, devices will undergo planned handling with tools, that leave marks at pieces surfaces. As these handling are scheduled, the process should be adapted to ensure that the specifications are met despite the presence of an imperfection.

(a) (b) (c)

Figure 1.2 Surface irregularities: (a) Surface state of an over-peened aluminum [4]; (b) Imprint on a metallic sheet resulting from the presence of dirt on the die during stamping [5]; (c) Shrinkage cavities appearing during casting [6].

Systems reliability will therefore depend on imperfections presence and roughness (see Figure 1.3a and b). In addition to this geometrical aspect, internal stress variations close to the imperfection may superimpose with the pre-existing stresses of the part (see Figure 1.3c). The combination of those two effects will lead to mechanical resistance alteration, or even in some cases, to anticipated fracture of the system. Failure mode will depend on mechanical loading (see Figure 1.3d). Some systems must resist to static and continuous load, and therefore resist to creep. Other systems are loaded only once in their lifetime, during their installation or during their use. They must keep sufficient mechanical resistance. In other cases, systems should withstand multiple loading processes, thus they need good fatigue resistance. All these different loading conditions will not interact in the same way with the presence of a surface imperfection. In addition to the solicitation type, system dimensions also bring variability (see Figure

1.3e). By reducing the size of a system, the number of grains across the thickness of the part will decrease. All these parameters lead to changes in mechanical responses, but also, to the sensitivity to the presence of an unexpected imperfection. The tolerance on imperfections dimensions will thus not be the same depending on the application of the pieces.

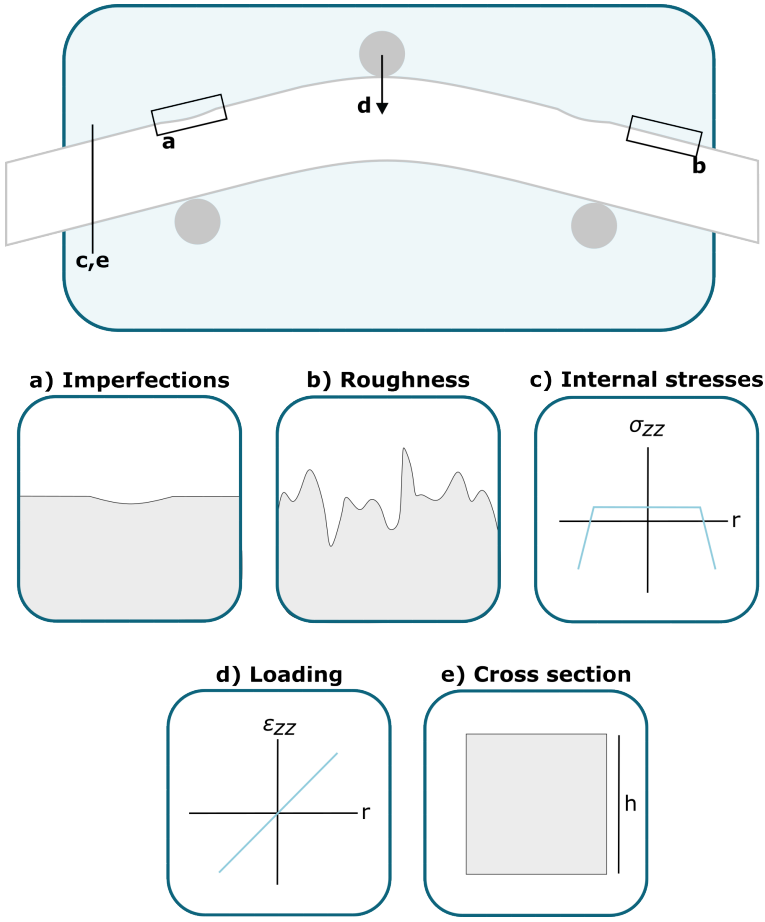

Figure 1.3 Multiple origins of a change in mechanical response in a structure: (a) geometric imperfections such as indents; (b) surface roughness; (c) internal stress field from processing; (d) type of loading; (e) characteristics of the section such as its dimensions, shape, or internal microstructure.

In this work, various imperfection geometries and loading conditions are evaluated. To go further, two applications were considered. The biomedical field presents really interesting systems. Implant failure is a major issue in the biomedical field. Therefore, the presence of imperfections should be well controlled. From materials selection to processing, many parameters should be controlled to produce devices that reach the expected performances without failure. Each category of implants has to support specific loading conditions during lifetime, (i) surgeon manipulations, (ii) plastic deformation, (iii) cyclic loadings, (iv) assembly process, ... The first system considered are metallic rods placed along scoliotic spine of children. These implants are called *growing rods*. During the surgery, the surgeon bends the rod to fit the natural shape of the patient spine. This bending process as well as the marking of the material due to contact during bending are believed to affect the fatigue resistance of the rod. The second implant analyzed, called *stent*, consists in a metallic mesh in tubular form which is placed in blood vessel to restore sufficient blood flow. Stents are expanded by large plastic deformations and then periodically stressed due to pulse beats. Their small size makes them more sensitive to the possible presence of geometric imperfections.

This thesis is composed of nine chapters divided into three main parts. **Part I** presents the context of this work. After this introduction, *Chapter 2* describes the topic of implants in an intentionally general way. The emphasis is on mechanical properties in metallic implants with a review of the associated general theories. **Part II** and **Part III** deal respectively with the problematic of growing rods and stents failure. While *Chapter 3* and *Chapter 7* review the state of the art on their respective implant, *Chapter 4* to *6* and *Chapter 8* present the progress made on these challenges during this thesis. The structure of these two parts will be presented at the end of their respective introductory chapters.

Reading map

Dear Reader,

Throughout your journey in this manuscript, you'll encounter panels like this, distinguished by three distinct symbols. Each symbol carries a specific type of information.

The ℹ boxes, such as this one, deliver insights into the structure and content of the thesis. Look out for these as they unravel the organization and essence of the research.

Boxes along with the 🗏 symbol, located at the beginning of chapters, specify the progression of the chapter's publication process.

Lastly, the 💬 boxes weave intriguing anecdotes related to the current section, adding a touch of curiosity to your reading.

Happy exploration!

2

State of the art on biomedical implants

THIS chapter outlines the issues associated with biomedical implants from a materials science perspective, with particular reference to geometric surface imperfections and stress fields. It begins with a brief description of implants, emphasizing on their mechanical properties as well as the importance of their surface finish. This is followed by a review of the general theories associated with the main mechanical properties of metallic implants, addressing in particular the effects of geometrical imperfections as well as surface residual stresses.

Thesis structure
This state of the art chapter is concise, highlighting general messages about biomedical implants and material properties of metallic alloys. In the following, each key chapter is structured as a self contained publication and provides in-depth coverage of the specific literature in its dedicated section, optimizing clarity and readability for each contribution.

2.1 Context about the human body

2.1.1 Implants

One might think that biomedical implants are mature technologies developed decades ago and that the current technological development focuses on more fashionable subjects. If the implants appeared in the literature for the first time around the 1970s, as illustrated in Figure 2.1, the number of publications per year is still significantly increasing. Newer hot topics such as **global warming** and **3D printing** are still less covered in the current scientific literature. However, in contrast, **machine learning** takes an huge part of the modern scientific interest.

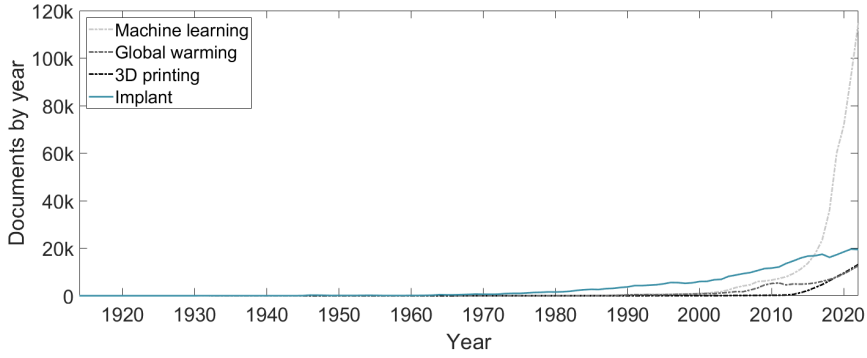

Figure 2.1 Frequency of appearance of four scientific buzzword in titles, abstracts and keywords of scientific articles over the last century - Source: Scopus.

The current challenges are multiple: from the development of new materials, to the customization of implants for patients, via the miniaturization of electronics or the use of new manufacturing methods, the field still has many areas of ongoing development.

Implants are used to *replace or improve the function of diseased or missing tissues and organs* [7]. Implantation may be necessary for accident victims, people with illnesses or for the natural aging of the body when the natural regenerative capacity of the human body is not sufficient. These interventions can therefore take place throughout life, depending on individual circumstances. The areas of the human body that can benefit from implant surgery are many and varied as illustrated in Figure 2.2 [8]. Among these

implants, some help to heal or correct deformities, others, called prostheses restore a lost function, while others monitor body functions [9].

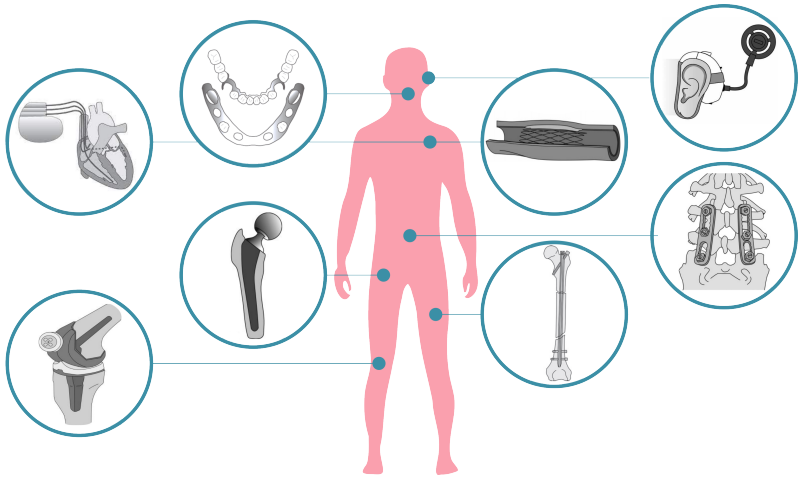

Figure 2.2 Various biomedical implants - Adapted from [10], [11] and [12].

Design of biomedical implant is a complex and multifactorial challenge. Indeed, many requirements need to be met before it can be used on a commercial scale [7] :

1. Acceptance of the implant as a foreign body
2. Chemical stability over time
3. Sufficient mechanical strength
4. Adequate fatigue life
5. Suitable physical properties (such as density)
6. Scalable to an industrial production

The present thesis seeks to improve our understanding of the origins of implant fracture as directly linked to item *3* and *4* above. In this respect, the following section provides a coverage of the mechanical properties found in typical implant specifications.

2.1.2 Materials

Each implant comes with its specific set of requirements based on the application. Here are the principal properties and their relative importance in the biomedical context.

- ***Stiffness:*** the stiffness of the material, denoted by Young's modulus (E) and shown in Figure 2.3, determines the rigidity of the assembly for a given cross-section. This parameter is key especially in orthopedics. A too large stiffness mismatch between an implant and the bone potentially leads to recurrent implant failures [13].
- ***Yield strength:*** when implants need to be plastically deformed to give the definitive geometry, its initial yield strength, denoted σ_0 and represented in Figure 2.3, must be included in a specific range. While it is too high, the surgeon will not be able to confer the required shape, while a too low yield strength gives a too large sensitivity to the implant which may be deformed plastically during the life of the patient.
- ***Ultimate tensile strength:*** denoted σ_{UTS} and highlighted in Figure 2.3, the ultimate tensile strength represents the highest bearing capacity of an assembly. Under uniaxial tension conditions, while the equivalent stress reaches this limit, the mechanical integrity is no more guaranteed.
- ***Strain hardening capacity:*** the capacity of a material to harden by a plastic deformation is linked to the intricate mechanisms of dislocation storage and annihilation combined or not with twinning. The strain hardening capacity is given by $\frac{\delta\sigma_y}{\delta\epsilon^p_{acc}}\frac{\epsilon^p_{acc}}{\sigma_y}$ where σ_y is the current yield strength and ϵ^p_{acc} the accumulated plastic strain. The hardening capacity of a biomedical implant helps to regulate irreversible deformation. Indeed, materials with a low yield strength but a high strain hardening capacity will be easily deformed by the surgeon but, once deformed, the patient will feel more resistance to extra plastic deformation.
- ***Ductility:*** if a material is able to deform irreversibly without breaking, it belongs to the ductile family of materials in contrast with brittle materials. There is no metrics attributed to this qualifier. However, if the implant needs to be plastically deformed, the deformation reached at σ_{UTS} can give insights into the material capacity to deform. All parts in implants do not need to have this capacity, but if they do, metals are good candidates regarding this property.
- ***Fracture toughness:*** In the case the implant presents defects as cracks, its fracture toughness, denoted K_c, needs to be high. Indeed a tough

material is able to withstand crack propagation. A typical example of crack propagation is breast implant failure, where the silicone outer shell tears itself, releasing the filler in the human body.

- ***Fatigue resistance:*** Contrarily to the ultimate tensile strength, where the load overcomes at once the material limit, fatigue occurs when the load stays in a range that would be safe for a monotonic condition. While this loading is repeated over and over, the material may not be able to withstand it, as it accumulates plastic strain progressively. In the human body, repetitive motions are unavoidable. Breathing, heartbeat, chewing, walking, ... If the associated load is below the endurance limit, σ_e, the implant is not affected by it. Otherwise, a premature fracture can happen.

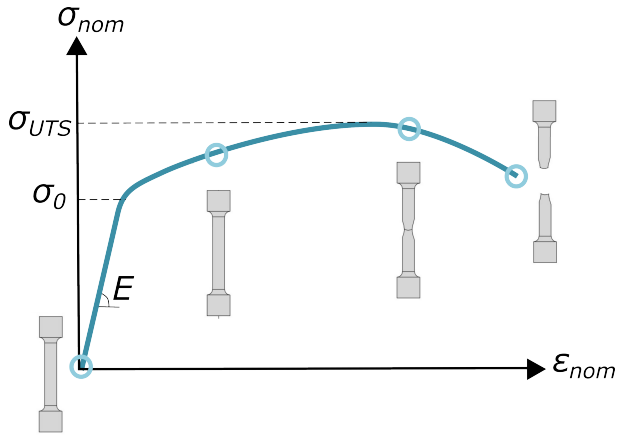

Figure 2.3 Typical tensile curve of a metallic sample in traction - Adapted from [14].

Of the three main categories of materials, metals account for 70% of the components of implants [15]. Among the most commonly used metals are titanium (and its alloys), cobalt-chromium alloys, gold, silver or stainless steels [7]. This selection is based on their good corrosion resistance, biocompatibility, but also on their high mechanical properties as detailed hereafter [7, 10, 15].

Old is gold
Historically, in dentistry, the most basic solution was simply to pull out the problematic teeth, leaving a gap in the dentition and causing the opposite tooth to fall out over time. Then dental restorations were progressively attempted. By 2500 BC, there were already attempts of restoration, where worn teeth were connected to neighboring healthy teeth using gold wire [16]. Our ancestors already understood that gold was a good candidate for biocompatibility.

2.1.3 Impact of surface finish

Surface modifications in biomedical implants constitute a major part of the implant design. Indeed, the implant's surface interacts with the biological medium after implantation and the surface finish can modify its properties [17]. Depending on the location and the role of the implant, the functional requirements can be different. While some implants need osteointegration to strengthen the anchors, other implants, like stents, need to prevent blood cell proliferation to avoid restenosis [18]. Therefore, the surface finish of an implant needs to be tailored to its environment to promote functional requirements while hindering undesired interactions [17].

Surface modification includes adjustments on features such as topography, hardness, chemical functionalities or even electronic characteristics [18]. All theses changes can influence biocompatibility, longevity or functional properties of the implant. As this work focuses on geometrical defects and on surface hardening, the next paragraphs will explore in more details the effects of topography and hardness variations in the context of biomedical implants.

Topographic modifications are frequently addressed in biomedical research. While a rough surface promotes blood coagulation [7], it seems to play also an important role in endothelialisation process on stents [19]. Therefore, it is important to understand how the roughness amplitude and the roughness pattern could adapt to each context. In advanced roughness tuning, the patterning can take place at various scales. For endosseous implant, some surface features at the sub-micron, micron and coarse micron scales are introduced to address different biological mechanisms [20]. However, topology is not only changing the biological response of the implant as

larger roughness goes with more stress concentrators, which can decrease the fatigue lifespan of implants [10].

Increasing the surface hardness is a well known solution to avoid or postpone fatigue failure or wear resistance enhancement. In orthopaedics, as well as in other specialties as neurosurgery, spinal implants are known to suffer from fatigue. The approach to increase their fatigue lifetime is to introduce compressive residual stresses below the surface. Methods like shot-peening or cavitation peening aim at hardening the surface through plastic deformation, which is associated to work hardening [21]. However, peening can come with roughening of the surface which can reduce fatigue resistance. In applications such as for hip replacement, the head surface should be smooth to limit the generation of fragments from the polymeric cup, and hard to be wear resistant. In such cases, other solutions such as physical vapor deposition and diffusion hardening methods can be used to increase the surface hardness while having a smooth surface state [22].

2.2 Mechanical properties of metallic alloys

As mentioned in Section 2.1.1, this research focuses on the mechanical strength and the fatigue life of metallic biomedical implants. As some implants are meant to be plastically deformed during implantation surgeries, strain hardening is developed in Section 2.2.1 while necking localization is then introduced in Section 2.2.2. The fatigue origins and the fatigue strength are discussed in Section 2.2.3. Finally, Section 2.3 presents the origins of residual stresses and discusses how they play an major role in durability problems.

2.2.1 Strain hardening

During the deformation of a material, two regimes can be distinguished: the elastic and the elastoplastic regime. The transition is called the yield stress, denoted σ_y. While a material has not been plastically deformed yet, its *initial* yield stress is specifically denoted by σ_0. Beyond this limit, permanent deformations are induced. In the stress space, as represented in Figure 2.4, this limit is represented by a yield surface. For a general loading, the material enters plasticity when the equivalent stress exceeds the current yield stress $\sigma_{eq} > \sigma_y$. One definition for the equivalent stress valid for plastically isotropic materials is the von Mises equivalent stress:

$$\sigma_{eq} = \sqrt{\frac{1}{2}[(\sigma_1 - \sigma_2)^2 + (\sigma_2 - \sigma_3)^2 + (\sigma_3 - \sigma_1)^2] - 3\tau_1^2 + 3\tau_2^2 + 3\tau_3^2}. \quad (2.1)$$

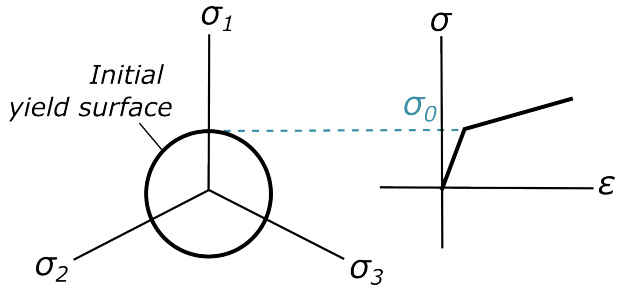

Figure 2.4 Yield surface - adapted from [23].

The stress to overcome the yield stress is linked to the motion of dislocations in the crystals which constitute the structure of metals. It is the dislocation glide that allows metals to plastically deform. The yield stress, σ_y is linked to the critical resolved shear stress, τ_c, which is the shear stress needed to initiate dislocation motion. It results from the addition of different resistive stresses as:

$$\tau_c = \tau_p + \tau_{SS} + \tau_m + \tau_d + \tau_{pr}. \quad (2.2)$$

The first term, σ_p also called Peierls stress, originates from lattice friction forces. All the others are the results of interactions of dislocations with solid solution atoms (σ_{SS}), other dislocations (σ_m), grain boundaries (σ_d) and precipitates (σ_{pr}). As the material is plastically deformed, the arrangement and density of dislocations in the crystal evolves and these barriers vary. Essentially, as the material is deformed, the critical resolved shear stress increases, making the material harder to deform. This phenomenon is called strain-hardening as already defined in the previous section.

As a metal strain hardens, the yield stress increases. Two distinct/major variations can occur to accommodate this change of strength: (i) the enlargement of the yield surface, (ii) the translation of its center. The former, called **isotropic hardening**, is illustrated in Figure 2.5a, while the latter is called **kinematic hardening** and is shown in Figure 2.5b.

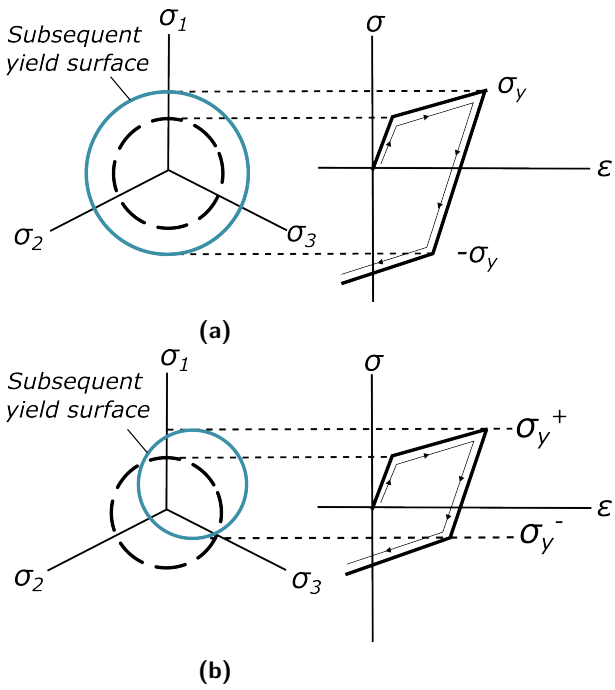

Figure 2.5 Evolution of the yield surface during loading for (a) isotropic hardening and (b) kinematic hardening - adapted from [23].

In the case of an hypothetical perfect isotropic hardening behavior, the yield surface expands uniformly as plastic deformation increases, which results in an increase of the yield stress σ_y in all directions. Therefore, the yield point in compression is the same as the yield point in tension [23]. This kind of strain hardening behavior can be expressed as

$$\sigma_y = F(\sigma_0, \epsilon^p_{acc}, \text{other parameters}), \tag{2.3}$$

where σ_0 is the initial yield stress and ϵ^p_{acc} is the accumulated plastic strain. One example is the Ludwik equation:

$$\sigma_y = \sigma_0 + K(\epsilon^p)^n, \tag{2.4}$$

where K is a hardening parameter and n is the strain-hardening exponent.

Many alternative phenomenological isotropic strain hardening laws have been proposed.

In the case of hypothetical perfect kinematic hardening, as the yield surface shifts without expansion, it creates an asymmetry in the yield stress. As the material yields in tension, its yield stress, σ_y^+ increases due to hardening, while its yield point in compression σ_y^- decreases. This is called the Bauschinger effect. This translation is characterized by a tensor called backstress $\mathbf{X}$. Its evolution can also be related to plastic deformation as

$$\dot{\mathbf{X}} = A\dot{\boldsymbol{\epsilon}}^{\boldsymbol{p}} - B\mathbf{X}\dot{p}, \tag{2.5}$$

where A and B are two scalar parameters, $\dot{\boldsymbol{\epsilon}}^{\boldsymbol{p}}$ is the plastic strain rate and $\dot{p}$ is the rate of increase of the accumulated plastic strain. The physical origin of kinematic hardening is explained in Section 2.3.3.

2.2.2 Necking

At the start of a tensile test, each increment of deformation uniformly elongates the specimen. This is because as a section of the specimen lengthens, and therefore becomes thinner, it hardens. Even if this section is thinner, the force required to deform it may be larger than a neighboring section that has not yet undergone (by a very small amount) the same level of deformation. Then this zone gets more prone to deformation than the neighboring zone and the mechanism self stabilize any localization. The deformation remains uniform even though the material is never perfectly uniform. In Equation 2.6, it means that the first (positive) term, linked to hardening effect ($\delta\sigma A$) is larger than the second (negative) term reflecting the section reduction ($\sigma\delta A$); i.e. the force level is increasing.

$$\delta F = \delta\sigma A + \sigma\delta A \tag{2.6}$$

At some point, a maximum force (δF=0) is reached, representing the self-compensation of the hardening and the thinning effects. Beyond this limit, the magnitude of the second term is larger than the first one and necking begins. Necking is a localization phenomenon: the deformation is no more uniform through the specimen and the region with the lowest cross-sectional area undergoes the largest rate of contraction. While strain is localized in a portion of the sample, the rest of the sample unloads elas-

tically. The strain level reached in the outer zone is called the *strain limit* and is denoted as ϵ^*. In a perfect specimen, subjected to uniaxial tension and independent of strain rate, the strain limit is equal to the hardening exponent, n.

In cylindrical specimens, the necking starts to develop in a diffuse way as illustrated in Figure 2.6. At a final stage of localization, a localized neck, which is much thinner and oriented with an angle with respect to the main axis can appear. This localized neck is difficult to observe in cylindrical specimens. As the diffuse neck appears, the stress state in no longer uniaxial in the sample. The neighboring section of the smallest thickness tends to resist the further contraction of it. This adds lateral stresses which complicate the stress state and thus increases the local triaxiality [24].

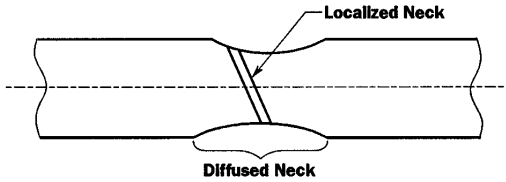

Figure 2.6 Illustration of diffuse and localized neck - [25].

If theory usually assumes homogeneity through the specimen, real materials present variations in grain size, texture, or solute concentration as well as in their geometry. In 1967, Marciniak and Kurzynski suggested an approach to consider the effect of inhomogeneity under biaxial stretching [26]. The basis of their approach can be applied to uniaxial tension on a tensile specimen with a dimensional inhomogeneity as illustrated in Figure 2.7a. The cross-sectional difference between the two regions, a and b, is characterized by the inhomogeneity factor, f, as:

$$f = \frac{A_{a0}}{A_{b0}}, \tag{2.7}$$

with A_{i0} the initial cross-section at section i.

The approach starts with the principle that each zone supports the same force

$$F_a = F_b, \tag{2.8}$$

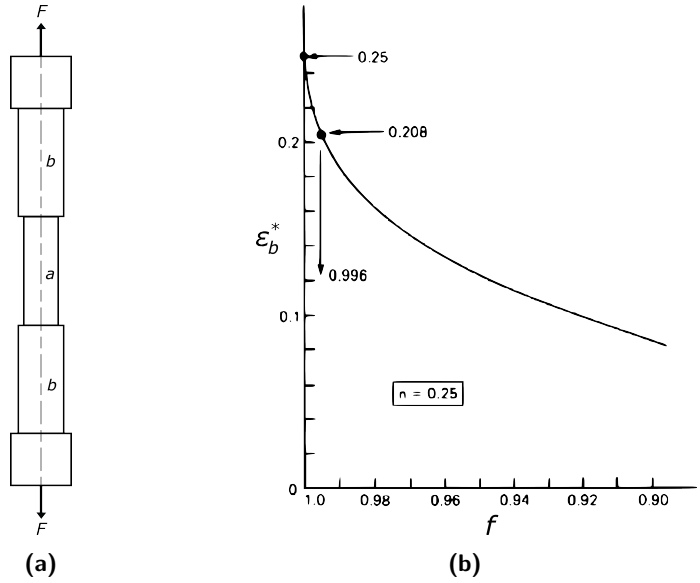

Figure 2.7 Effect of inhomogeneity during uniaxial tension: (a) inhomogeneous tensile specimen; (b) strain limit in zone b as a function of inhomogeneity factor for n=0.25 - adapted from [24].

which can be rewritten as

$$A_a\sigma_a = A_b\sigma_b, \tag{2.9}$$

where A_i and σ_i are the current cross-section and stress in section i.

Considering a hardening law of Hollomon type ($\sigma = K\epsilon^p$), and expressing the current cross-section with respect to its initial dimension by mean of the strain parameter ($A_i = A_{i0}e^{-\epsilon_i}$), the Equation 2.9 becomes

$$A_{a0}e^{-\epsilon_a}K\epsilon_a^n = A_{b0}e^{-\epsilon_b}K\epsilon_b^n. \tag{2.10}$$

Finally, injecting Equation 2.7 in Equation 2.10 gives

$$f\epsilon_a^n e^{-\epsilon_a} = \epsilon_b^n e^{-\epsilon_b}. \tag{2.11}$$

From Equation 2.11, the strain in zone b can be found numerically for given values of ϵ_a, n and f. Figure 2.7b represents the strain limit, ϵ_b^*, as a function

of the inhomogeneity factor, assuming n=0.25. As indicated in the graph, small levels of inhomogeneity are already responsible for a large decrease in strain limit.

2.2.3 Fatigue

Fatigue failure *occurs under a cyclic or alternating stress of an amplitude that would not cause failure if applied only once* [27]. Among all service failure mechanisms in metallic part, fatigue is by far the most common one. It can be easily recognized by a careful observation of the fracture surface which indicates how the crack propagates in the structure. The origin of fatigue failure as well as the methods used to characterize fatigue resistance are presented below.

Breaking bad
Bone fractures are common injuries. However, these are usually caused by strong forces hitting the body. A lesser known origin is *stress fracture*, which occurs when the bone undergoes a repetitive force over a long period of time [28]. Most affected people are athletes at the beginning of a new sporting season and soldiers during initial military training [29, 30]. An unfamiliar category in stress fractures are the musicians who most commonly break their fourth and fifth metacarpals as a result of repetitive hand movements [31].

a. Origins

Fatigue failure consists in three stages: initiation, propagation and rupture. As the name suggests, the first step consists in the initiation of a crack. While some cracks can appear in the sub-surface region, most of them initiate from the surface. As the structure is periodically loaded, small quantities of plastic deformation occur inside the metal. Close to the surface, the material is less constrained than in the bulk, and the slip resulting from plastic deformation create new fresh surfaces. As shown in Figure 2.8, as plastic deformations are generated at each cycle, multiple slips accumulate close to each other, generating extrusions and intrusions at the surface. With cyclic repetitions, the intrusions become preferential sites for crack initiation and the crack initiates at approximately 45°, following the slip

bands [4, 32]. After this stage, the fatigue failure enters propagation step. At each cycle, some plasticity occur at crack tip. The propagation direction changes to become perpendicular to the principal stress. The crack progresses by small steps giving to the fracture surface its typical striated pattern. As the crack propagates, the effective section of the structure decreases. The last stage is a single-step process which leads to the total fracture of the specimen. As the effective section decreases, its loading capacity also does so, until an overload finishes breaking the part. This last stage produces a characteristic shear lip zone on the fracture surface.

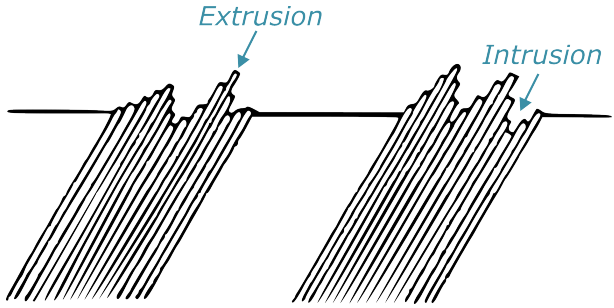

Figure 2.8 Crack initiation site formed by accumulated slip bands - adapted from [33].

b. Fatigue resistance

Fatigue can occur only if three elements are simultaneously gathered. First, the loading should produce significant tensile stresses in the part. Secondly, the loading should vary in intensity overtime (i.e. cyclic). Finally, a sufficiently large number of cycles should be accomplished. It is only under these three conditions that fatigue failure can occur [4].

In experimental fatigue assessment, a well controlled loading is usually used. As illustrated in Figure 2.9, this loading is characterized by several components:

- σ_{max}, the maximum stress;
- σ_m, the mean stress;
- σ_{min}, the minimum stress;
- $\Delta\sigma$, the stress range;

as well as some ratios:

- R, the stress ratio, defined as $\sigma_{min}/\sigma_{max}$;
- A, the amplitude ratio, defined as σ_a/σ_m.

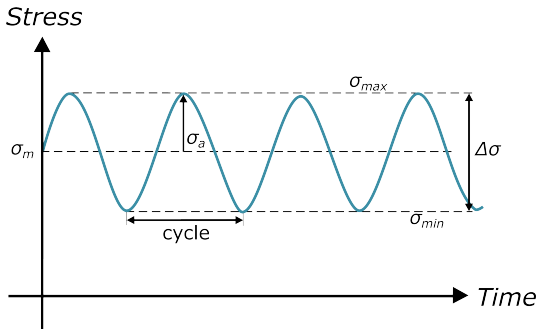

Figure 2.9 Characterization of stress signal - adapted from [32].

For each broken sample tested at a certain stress level, a number of cycles to failure (N) is obtained. As shown in Figure 2.10, results are presented in S-N curves which represent the number of cycles on a logarithmic scale as a function of the stress ($\sigma_{max}, \sigma_{min}$ or σ_a). By replicating the test, some scatter will be found in the results. As the stress level is decreased, the number of cycles to failure increases, until the endurance limit, σ_e, is attained. Indeed, if the stress is below this level, the samples can undergo a large number of cycles without failure, which is called a run-out. The test is then stopped at a arbitrary number of cycles, and the points are indicated on S-N curves with an right pointing arrow.

The fatigue resistance of a material can be characterized by two ways. The first is defined as the finite life area. The larger the number of cycles achieved before failure, the larger the so-called **fatigue life**. On the other hand, when the endurance limit, σ_e is larger, it is said that the material has a higher **fatigue strength**. This fatigue strength is usually linked to another material property: the ultimate tensile strength, σ_{UTS}. In steels, the endurance limit is usually in the range of $\frac{\sigma_{UTS}}{3}$ [4, 33].

Increasing fatigue resistance is not only a matter of material selection. As a matter of fact, surface conditions (residual stresses, roughness, presence of inclusions,...) as well as test conditions (cycle frequency, amplitude ratio, environmental conditions,...) can strongly influence the fatigue results.

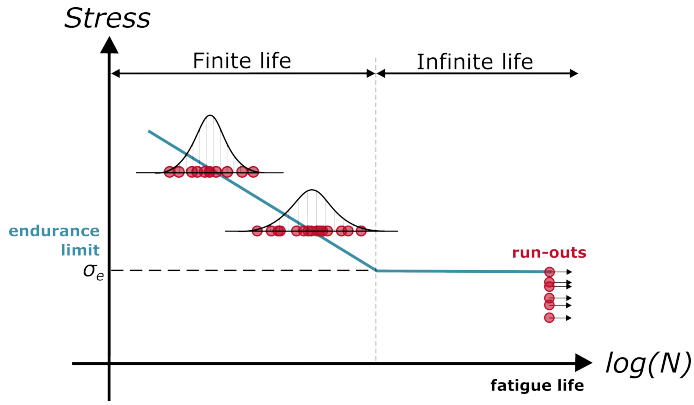

Figure 2.10 Illustration of a typical S-N graph superposed with the statistical spread in results.

Depending on the loading conditions, the number of cycles to failure will vary. Indeed, if the stress is below the elastic limit, we can expect a large number of cycles. It is frequent to reach more than 10^5 cycles in such conditions. This kind of regime is called *high cycle fatigue* (HCF). On the contrary, when the loading amplitude is higher and results in plastic deformation, the fatigue life is reduced. This other kind of regime corresponds to the so-called *low cycle fatigue* (LCF) [33]. It is common to switch to strain-life curve (ϵ-N) which takes into account elastic *and* plastic strains.

2.3 From origins to impact: understanding residual stresses [1]

Residual stresses (RS) are mechanical loadings present *in* materials, components and structures, when these one are not yet exposed to any external force or moment. With the addition of an external loading, the final internal stress distribution results from the contributions of both mechanical loadings. Residual stresses can contribute in a positive or in an negative way and therefore it is essential for a vast number of engineering applications to know how to introduce or to reduce them as much as possible.

[1] This section is mainly based on the chapter 18 of the book "Mechanical behaviour of Materials" of Hosford, William F [27], the article "Introduction to residual stress" of Macherauch, Eckard [34], the book " Handbook of residual stress and deformation of steel" of Totten, George E [35], Chapter 3 on Residual stresses from the unpublished syllabus "LMAPR2483 Durability of materials" of Pardoen, Thomas [36] and "A teaching essay on residual stresses and eigenstrains" of Korsunsky, Alexander [37].

2.3.1 Origins and types of RS

Residual stress are necessarily originating from the presence of elastic strains in the solid. One simple way to illustrate the logic behind the origin of RS is depicted by Figure 2.11. A segment from the sample, initially stress-free, is fictitiously extracted (Fig. 2.11a and b). A transformation is applied to this segment by the mean of a solicitation (apart from elastic deformation) as illustrated in Figure 2.11c. The transformation can originate from plastic deformation, thermal variation, phase transformation,... Keeping the solicitation on the segment, a stress (denoted σ) is applied to recover its initial dimension (Fig. 2.11d) and the segment is reintroduced in the original sample (Fig. 2.11e). When the mechanical load, σ, is finally removed (Fig. 2.11f), the segment wants to recover its shape from step c. By doing so, the matrix and the segment will find an equilibrium where both portions are elastically deformed, resulting in residual stresses in both portions.

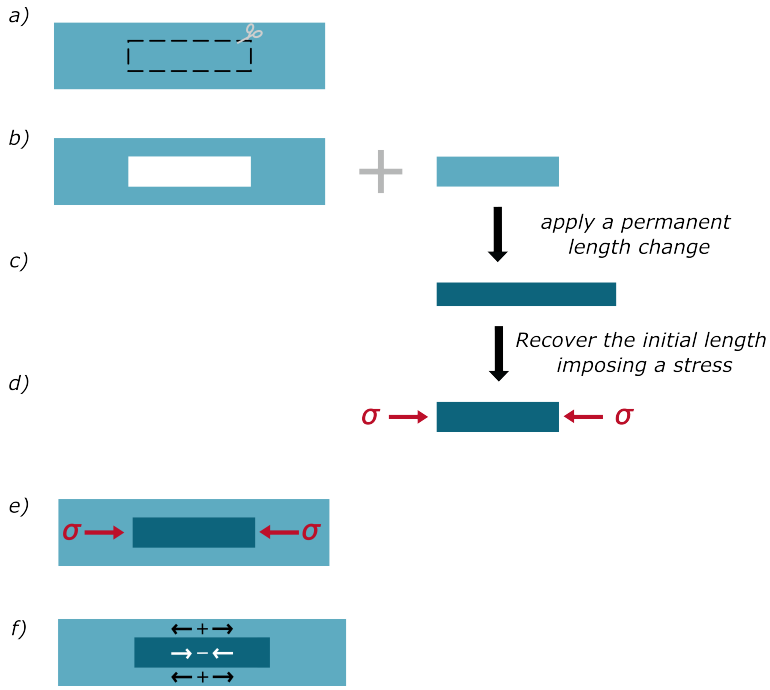

Figure 2.11 Thinking experiment to visualize the generation of internal stresses in a 1D structure - adapted from [36].

From a realistic point of view, solids presenting residual stresses were rarely cut and reassembled as illustrated in Figure 2.11. The link with some specific processes known as introducing RS (i.e. shot-peening, bending, welding,...) are presented in Figure 2.12.

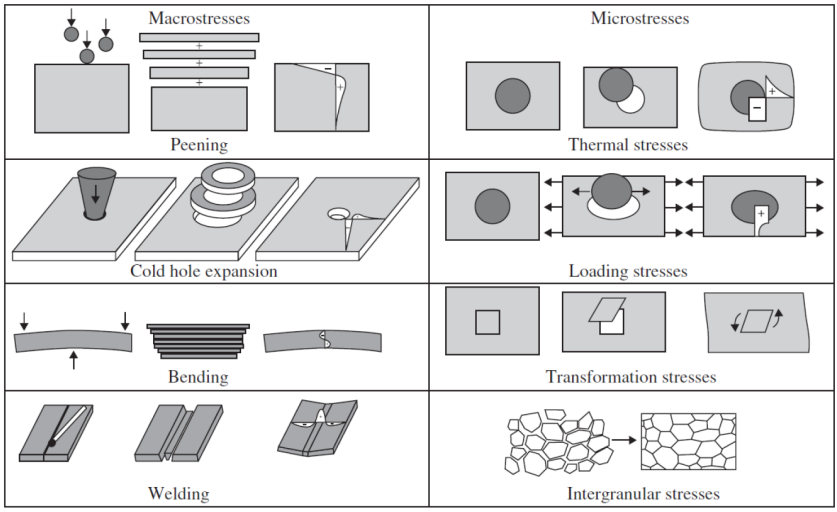

Figure 2.12 Illustrations of various residual stresses origins - [38].

In case of de-stress, break the glass

Residual stresses are at the origin of tempered glass working principle. These glassy sheets have high resistance to fracture under bending thanks to a compressive stress state on both surfaces. However, if a crack manages to initiate at the surface, the properties of the internal layer will come into play to ensure a safe fracture pattern. Indeed, as the central layer is under residual tensile stresses, the crack will preferably spread in this layer and generate a large number of small pieces [27].

Depending on the type of misfits, residual stresses can develop at various scales. Figure 2.13 summarizes the three types of residual stresses alongside with their respective length scale. This classification has been introduced by E. Macherauch.

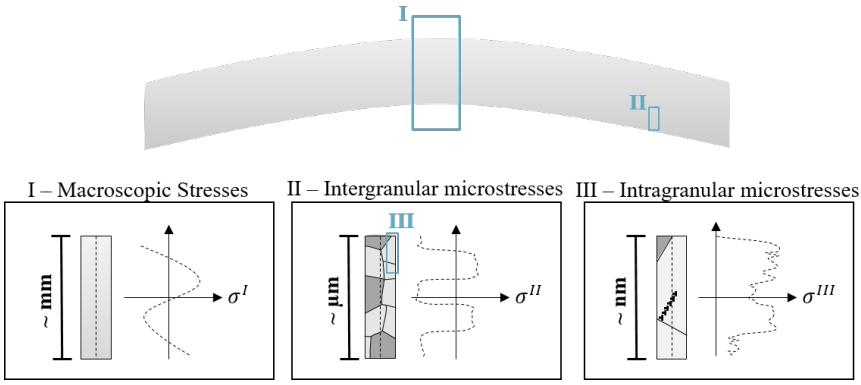

Figure 2.13 Illustration of the three scales of residual stresses.

A simple loading mode, like permanent bending, illustrates the first scale of residual stresses. On Figure 2.13, a bent rod after elastic recovery is represented. At the macroscopic level, an oscillating residual stress profile can be observed across the whole structure. Residual stresses developing on a macroscopic point of view belongs to residual stress of type I, referred to as σ^I.

Residual stresses can also develop at the intergranular scale. By zooming in on Figure 2.13, a subset of few neighboring grains can be observed. Differences in terms of slip systems activated during plasticity, variation of elastic moduli, and in the case of non cubic lattices, variations in thermal expansion coefficient are all sorts of local variations that can lead to the formation of RS. Indeed, if the material is mechanically or thermally loaded, these displacement mismatches will be compensated with residual stresses of type II, σ^{II}. Similarly, RS of type II develop easily in multiphase materials.

The last type of residual stresses, σ^{III}, develops at the intragranular scale (i.e. the elementary defect size). Various crystallographic defects, such as vacancies, atoms in solid solution and dislocations always cause nanoscopic local variations in the RS profile.

These three contributions can be summed up to obtain the global residual stress (σ^{RS}) as follow:

$$\sigma^{RS} = \sigma^{RS,I} + \sigma^{RS,II} + \sigma^{RS,III} \tag{2.12}$$

As σ^{II} and σ^{III} are stress variations at a really local scale, they are usually neglected for structural scale analyses. It is important to recall that on a global scale, these stresses self-balance as well as the resulting moments due to basic equilibrium conditions.

2.3.2 Elevating material performance: The role of shot-peening

Shot-peening is a fundamental processing technique in the realm of materials engineering, specifically in the treatment and modification of metallic alloy surfaces. It is the most commonly used process to introduce compressive stresses and to harden a surface. During shot-peening, as illustrated in Figure 2.14, small hard spheres are projected at high speed onto the metal surface. When a sphere impacts the material, it induces plastic deformation below the impact point. As the material is deformed, the metal hardens locally, increasing the surface hardness of the piece. Moreover, as the material tries to expand laterally, the sub-surfacic layer constrain the extension, creating a compressive stress state in the first 0.15-0.3 mm depth [39].

Figure 2.14 Illustration of shot-peening process - adapted from [40].

These stresses are mainly from **type I** (macroscopic stresses) and should satisfy force and moment equilibrium through the structure. Classical residual stress profiles produced by shot-peening involve a tensile stress state below the compressive layer as shown in Figure 2.15. Such tensile stresses

added to the loading stress state can overcome the fatigue limit and generate a subsurface crack. But, the net result is that shot-peening increases the surface resistance to crack initiation.

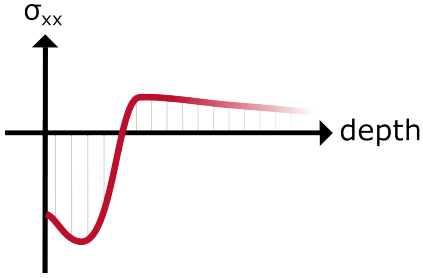

Figure 2.15 Usual stress diagram of a shot-peened part - adapted from [40].

This process is widely employed for various applications, ranging from improving fatigue resistance to enhancing wear and even corrosion resistance. The effectiveness of the shot-peening process is influenced by parameters such as particle velocity, size, and material, but also exposition time and surface coverage. Shot-peening provides important benefits to materials, making it a valuable process in engineering. Firstly, the accumulated plastic deformation improves surface hardness and wear resistance, making it an effective method for extending the lifespan of components subjected to harsh operating conditions. Additionally, it induces compressive residual stresses in the treated material, thereby enhancing its fatigue life and resistance to stress corrosion cracking. Despite these advantages, the process also presents certain issues. The potential for surface roughening and material removal poses challenges in applications where precise dimensional control or surface finish is crucial [41, 42].

Durability of residual stresses introduced by shot-peening

Once purposely introduced in the structure, it is crucial to ensure stability of residual stresses. Thermal treatments can relax unintended RS. However, the loading conditions can also be at the origin of RS vanishing. First, static loading can be responsible for RS relaxation. In the handbook of *Fundamentals of machine component design*, it is reported [43]:

> *An overload causing yielding produces residual stresses that are favorable to future loads in the same direction and unfavorable to future loads in the opposite direction.*

Therefore, compressive residual stresses introduced by shot-peening (corresponding to an expansion loading) tend to be easily relaxed when loaded in compression [44]. Residual stresses are also prone to relaxation through cyclic loading. This relaxation has been described by various models which indicate that RS relax linearly with respect to the logarithmic number of cycles [45–47]. Even if the current state of the literature does not provide a generalized prediction model which takes into account residual stresses and all the side effects for fatigue prediction, it is already clear that situations dealing with cyclic loading causing plasticity should not rely on residual stresses to improve their fatigue resistance [39].

The multifactorial phenomenon of fatigue makes the processing step more challenging [39]. Indeed, as shot-peening is the result of multiple impacts, the roughness of the targeted zone is usually increased. In some cases, this side effect can counteract the positive impact of compressive stresses, and lead to a general decrease in fatigue performance [48].

2.3.3 From residual stress to kinematic hardening

The hardening mechanisms in materials originate from diverse interactions between dislocations and precipitates within the crystal lattice. Dislocations interact with precipitates during plastic deformation. This interaction varies, involving processes like dislocation bypass or cutting through precipitates [49].

As illustrated by Figure 2.16 (step 1 to 3), bypass occurs when a dislocation bows around the precipitate rather than penetrating it. This phenomenon happens when the precipitates are too hard to cut due to their size, atomic arrangement or incoherency. In order to continue moving on the other side of the precipitates, the dislocation will bend until it meets itself and creates a dislocation loop around the precipitate. The rest of the dislocation is then free to continue moving through the crystal until it reaches the next obstacle. As loading continues, other dislocations moving through the crystal will interact with the precipitate creating an accumulation of dislocation loops around the precipitates (step 4 in Figure 2.16). Each loop introduces residual stresses in the surrounding material exerting a repulsive force on the subsequent dislocations of the same sign moving in the same direction [50].

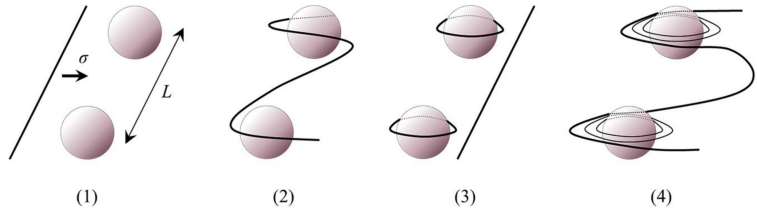

Figure 2.16 Bypass interaction between dislocations and precipitates - from [50].

In Figure 2.17a, two loops have been created by a forward movement of dislocations *1* and *2* around the precipitate. When the external load is reversed, as illustrated by Figure 2.17b and c, the dislocations move backwards, towards the particle. As the loops exert an attractive force on these dislocations, the load required to initiate motion in the opposite direction is lower compared to the load needed to sustain the initial dislocation motion. When the dislocation meets the precipitate on the way back, it annihilates the loop formed during the forward straining. The residual stresses between dislocations and precipitates (i.e. **Type III** intragranular stresses) originating from the initial loading, create an asymmetry in the material's mechanical response, known as *kinematic hardening* [49].

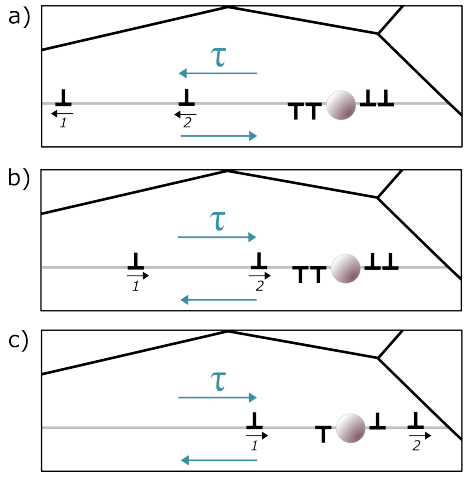

Figure 2.17 Dislocation motion and loops on non-shearable precipitates (a) during forward straining, (b) and (c) during reverse straining - adapted from [51].

Another potential origin of kinematic hardening lies in stress heterogeneity between neighboring grains or phases presenting different flow stress in polycrystals due to dislocation pile-ups [52]. Such stress heterogeneity presents a larger length scale than the stress originating from dislocation loops around the precipitates but are more local than the residual stress profile resulting from shot-peening. These are categorized as **Type II** residual stresses (i.e. intergranular stresses). As illustrated by Figure 2.18, after a primary tensile loading, the hard region present positive stress, while the soft region is in compression. Consequently, during reversed loading, the pre-existing local residual stresses can influence the material's response. They promote an early yielding process in the soft regions of the materiel, reducing the load required to initiate dislocation motion and the apparent yield strength σ_y^-.

2.4 Conclusions and open questions

In the work presented in this manuscript, two implants have been the central focus of research: *growing rods* and *stents*. After a more complete presentation of the specifications and issues related to these two categories of implants in *Chapters 3* and *7*, their lifespan will be analyzed in the light of surface conditions such as internal stresses in the first case, and geometric defects in the second.

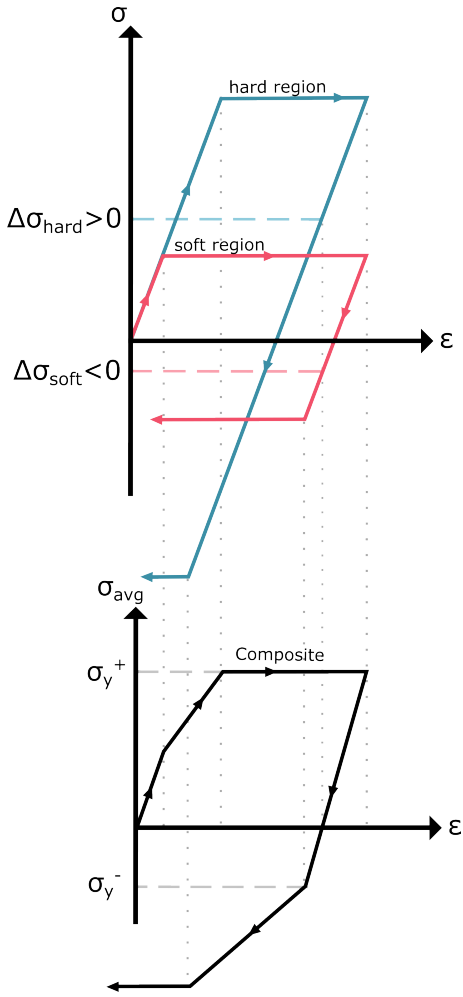

Figure 2.18 Asymmetry in yield strength explained by composite model - adapted from [52].

PART II
Failure analysis of growing rods

3

Context of growing rods: surgical practices and failure problems

THE aim of this chapter is to present the context of severe scoliosis affecting children. In some cases, this pathology is treated using biomedical implants called growing rods. The chapter is introduced by the terminology necessary for a good understanding of the problem. The context of early-onset scoliosis is then introduced in terms of the causes and treatments. As this work concerns biomedical implants, the solution of implementing growing rods in the body is presented in detail, with a particular focus on the state of the art dedicated to the failure of these implants. Finally, in light of the current knowledge, the technological and medical problems will be transposed into research questions presented together with the structure of this section.

3.1 Planes, directions and deformities

Every human is characterized by its spine morphology. Severe deformations are sometimes occurring in different directions. These distortions can be classified into 3 categories: lordosis, kyphosis, and scoliosis as presented in Figure 3.1.

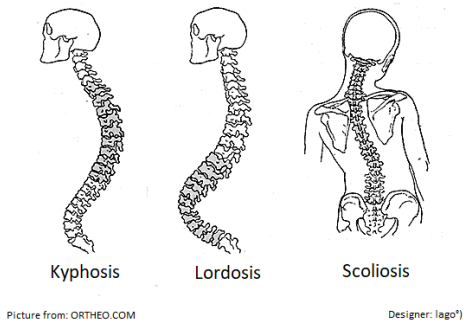

Figure 3.1 Kyphosis, lordosis et scoliosis - [53].

In the anatomical context, a specific vocabulary is used to describe planes and directions. Figure 3.2 shows the three main planes passing through a human body and defines the proximal and distal directions. As an example, the proximal vertebrae are those closer to the head and the distal vertebrae are closer to the pelvis.

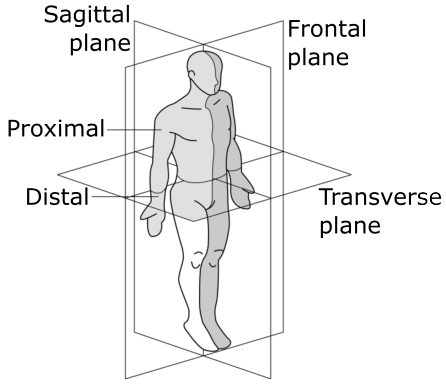

Figure 3.2 Anatomical vocabulary - Adapted from [10].

3.2 Scoliosis

Scoliosis is defined as an abnormal spine curvature (larger than 10°) in the frontal plane [54]. It can be associated with vertebrae rotations as well as sagittal deformations [55].

Scoliosis severity is measured by the mean of Cobb angle as illustrated in Figure 3.3. To determine this angle, two lines are drawn at the locations of the two most shifted vertebrae. These two lines should be parallel to each vertebra. Then, two perpendicular lines are drawn, and the Cobb angle is measured between them. A healthy spine has a Cobb angle close to 0° [54].

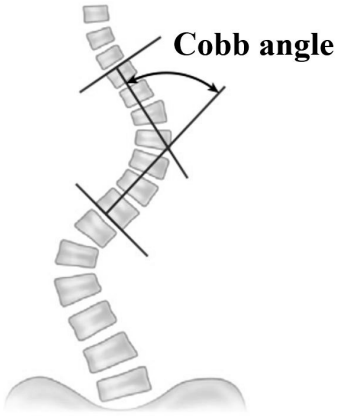

Figure 3.3 Cobb angle measurement - [55].

Dobbs et Weinstein have defined Early Onset Scoliosis (EOS) as scoliosis detected between birth and 5 years of age [56]. These scoliosis must be monitored carefully because the child is still growing. One of the major risk is abnormal lung development, as lung growth is closely linked to spine growth. Both phenomena are complex and continuous until puberty [57]. As illustrated in Figure 3.4, the number of alveoli as well as the lung volume increase strongly in the early growth period. Any abnormal spine distortion may lead to development and functional respiratory problems [58]. It is therefore essential to deal with this issue as soon as possible [59].

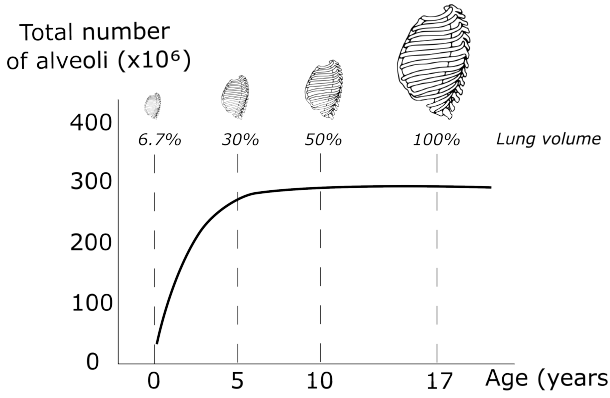

Figure 3.4 Lung volume and alveolar development as a function of child age - Adapted from [58].

3.2.1 Causes

Scoliosis can have different origins, which are classified into 3 main categories [60]:

- **Congenital scoliosis:** This type of scoliosis is due to a deformity present since birth. Scoliosis can develop later on (during growth) but its origin is a spine malformation existing since birth. This origin can be detected by the mean of radiography.

- **Neuromuscular/syndromic scoliosis:** This type of pathology is due to a disease or a muscle disorder. While muscles are weakened, they fail at keeping the spine in an upright position. Such kind of scoliosis usually goes along the weakening of other muscles in the body and is detected during childhood.

- **Idiopathic scoliosis:** This last family gathers all scoliosis with undetermined reasons, and can be diagnosed when vertebrae present rotations. People presenting idiopathic scoliosis are in general in good health. Between 4 and 17 years of age, idiopathic scoliosis is more common in women than in men.

Holy cow!
Human beings are not the only creatures suffering from scoliosis. These deformations have also been observed in cats, dogs, horses... and even fishes ! Surprisingly, chimpanzees and gorillas are exempt from such spine deformities [61]. Some researchers elaborate protocols to induce spinal deformities in animals. Even if primates are close to humans in the evolutionary history, the procedure to create scoliosis fails for them [62].
The scientific literature identified zebrafish as a good model for studying the biological origins and the mechanisms of scoliosis, due to their high susceptibility to develop scoliosis as well as the high genetic similarities with humans [63].

3.2.2 Treatments

The most efficient way to avoid an amplification of the scoliosis over time is vertebrae arthrodesis, which consists in merging vertebrae together to prevent any movement of these articulations. This technique is useful for adult or adolescent patients that almost reach the end of their growth phase. For children with a large growth potential, the consequences of such a treatment are considerable as it can be associated to poor alveolar development. To delay the arthrodesis surgery, different EOS treatments exist [54] but the choice will be patient-dependent. The two main options are the following:

- Wearing a **brace** that surrounds the child's chest, as illustrated in Figure 3.5, is considered as the reference solution as it can already give good corrections without the need for surgery.

- **Growing rods**, used in more complex cases, are inserted during a surgical operation and aim at correcting spine deformations. They can apply corrections gradually all along the child growth, or maintain an applied correction of the spine, induced by the surgeon during the surgery itself.

Figure 3.5 Example of a brace placed on scoliotic child - adapted from [55].

3.3 Growing rod implants

The introduction of growing rods delays merging surgery until the spine reaches its maturity. One or two rods can be attached to the spine with multiple anchor points. The construct used by the surgical team we have been working with is composed of a single-rod and is called the "3-hook & 2-screw" (H3S2) construct, as illustrated in Figure 3.6. The surgical protocol, which is fully described in the article of Miladi & Mousny [64], is summarized hereafter.

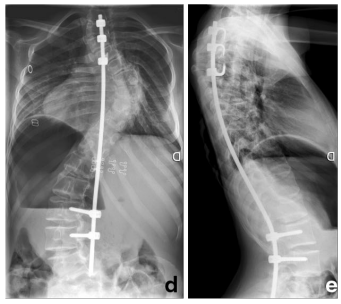

Figure 3.6 Attachment of the 3 hooks and 2 screws in the 3H2S configuration - [64].

Preoperative. Prior to surgery, the objective is to already obtain a reduction of the Cobb angle using a gradual corrective technique such as with a cast or with an external tension device.

Patient positioning. When surgery begins, the patient is placed in an intraoperative traction device, which aims at applying an average force of 100N. This force helps to correct spine deformity, while the patient is anesthetized. By doing so, the stresses at the anchoring sites are reduced temporarily, which helps for the rod implantation stage. Once in position, radiographies are performed to decide on which vertebrae the anchors will be placed. In most cases the surgery is a posterior-only procedure.

Anchors placement. The H3S2 construct is composed of 3 hooks, placed in 3 adjacent proximal vertebraes, and 2 monoaxial pedical screws, placed distally as illustrated in Figure 3.6. All these anchors need to be located in the same frontal plane and as vertically as possible, to maximize the efficiency of the construct.

Contouring. The single rod, which is still not introduced, needs to be bent to accommodate the patient's physiological lordosis and kyphosis, as shown in the sagittal view of Figure 3.6. By using specific bending tools, the surgeon gives the rod a curvature which fits the natural sagittal curvature of the spine.

Rod fixation. The rod is then slided through paravertebral muscles from distal to proximal position to limit the contact with bones, and thereby preventing any bone fusion. The rod is rotated and placed in the sagittal plane. The proximal screw is then locked, followed by the pedicle hook to maintain its position. The two other hooks and the second screw are finally locked as well. The rod is systematically too long and the extra-length is kept distally to allow later lengthening procedures.

Lengthening procedure. From the day following the surgery, patients are allowed to stand up, without any brace. As children continue to grow, a lengthening procedure is needed to maintain a good correction over time. On average, the child comes back every 10 months to get a lengthening surgery, that will allow the spine to keep growing. Henceforth, only a small cut at screws location is needed to loosen both of them, allowing the rod to slide, followed by a tightening procedure.

3.3.1 Lifetime of growing rods

To better understand the issues associated with growing rods, this section presents a step-by-step overview of the lifespan of growing rods, covering material selection, shaping, installation and use as shown in Figure 3.7.

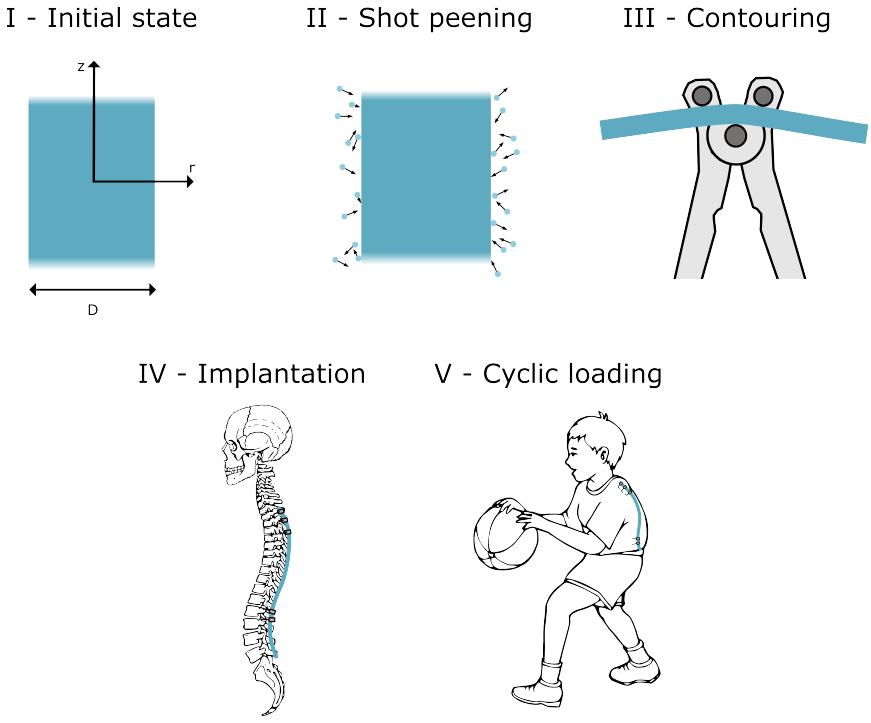

Figure 3.7 Illustration of the five main steps of growing rods lifetime, from production to in vivo solicitations.

I - Material choice

The choice of materials is very important in the medical field. Their performance depends first on their biocompatibility, but also on their biofunctionality. The most important properties for growing rods involve a high yield strength, a high stiffness and a good fatigue resistance [65]. The yield strength and stiffness influence the ability to maintain the correction, while the fatigue resistance determines its endurance. Beyond the intrinsic properties of the rod material, the performance of the structure also depends on its length, shape and cross-sectional area and morphology. Moreover, biocompatibility is very important because the implant can cause irritation

once it is in place, or corrode in the case of metals [65]. Therefore, biocompatibility takes precedence over functionality when selecting the material. Different materials having these specifications can be used; the most common include: austenitic stainless steel, pure titanium or its alloys and finally cobalt-chromium alloys.

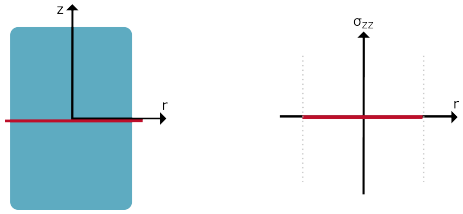

Figure 3.8 Stress state in the rod in the initial configuration.

In this work, it is essentially Ti-6Al-4V rods which are under study. Their typical mechanical properties are summarized in Table 3.1.

Table 3.1 Mechanical properties of Ti-6Al-4V - from [66].

Parameters	Values
Young's modulus	110 - 117 GPa
Yield strength	760 - 900 MPa
Tensile strength	828 - 970 MPa
Fatigue strength at 10^7 cycles	300 - 350 MPa

II - Shot peening

As compressive residual stresses are known to enhance the resistance to crack nucleation, a shot-peening process is commonly used in the context of biomedical implants as illustrated in Figure 3.9. Consequently, the surface of Ti-6Al-4V growing rods (presented in Figure 3.10) is covered by craters. Up to now, no study on fatigue enhancement by shot-peening has been published for the specific case of growing rods. However, a shot-peening step on titanium alloys spinal implant fixtures has demonstrated an increase of the fatigue resistance in the study of Takakuwa et al. [67]. Indeed, by introducing 600 MPa of compressive residual stress via cavitation peening, the fatigue strength was enhanced by a factor 2.2.

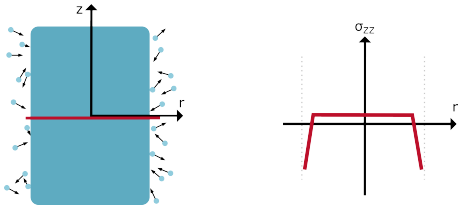

Figure 3.9 Stress state in the rod after the shot-peening process.

Figure 3.10 Surface of a growing rod where the craters indicate that the rod has probably been shot-peened.

III - Contouring

During the surgery, it is necessary to adapt the curvature of the rod to the curvature of the column as explained above. Various instruments are used by the surgeon to bend the rod. The most common one is the "French bender" shown in Figure 3.12 and represented schematically in Figure 3.11 [68]. When the two handles come into contact, angles up to $\sim 15°$ can be obtained. As the insert in Figure 3.12 shows, the tool leaves indentations on the surface of the rod which can be a source of weakness later on.

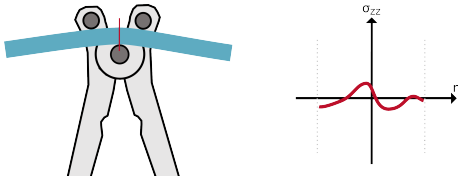

Figure 3.11 Stress state in the rod after shot-peening and bending.

In a recent study, Berti et al. investigated via numerical modeling the radial distribution of the mean residual stress induced through contouring with a French bender [70]. They considered a straight rod with no internal stress before bending. The results indicated the generation of tensile stresses of approximately 400 MPa on the concave side of the rod.

Figure 3.12 The French bender is a tool for locally bending the growing rod. This tool leaves marks on the surface of the rod - [69].

IV - Implantation

As the rod is attached to the spine when the patient is stretched, it will undergo static loading once the load is removed, which is designed to correct the spinal deformity. This static loading will be added to the stress profile resulting from the two previous stages (shot-peening and contouring) as illustrated by Figure 3.13.

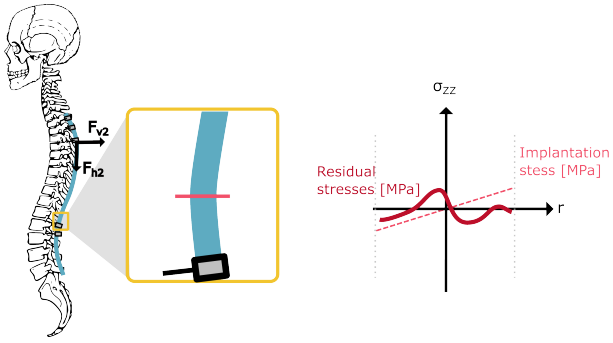

Figure 3.13 Addition of a static loading to the prior implantation stress profile.

In the current literature, very few researches tackled the challenge of predicting the residual stress state resulting from the implantation stage. In 2017, Agarwal et al. compared the maximum von Mises stress in a dual

rod construct for various values of *distraction forces*[1] [71]. The stress levels after implantation were found to vary between 100 and 600 MPa for the lowest and the largest distraction forces, respectively. Moreover, they predicted the stress level in the rod for different distraction intervals and found that the maximum stress level was equal to 810 MPa if the distraction procedures were spaced by 12 months.

V - Cyclic loading

Once placed, the rod will be solicited by a combination of low and high stresses due to patient movements, as illustrated in Figure 3.14. Small loadings are often associated with higher frequencies (as walking or breathing). Larger stress events as coughing or vomiting are scarcer. In a study of 1966, Waugh et al. found that the stress level increases by respectively 206% and 490% during these occasional events. Due to these cyclic loadings, a common complication is rod fracture as presented in Figure 3.15. In a previous study, the average lifetime of rods before failure was evaluated at 25 $\pm$ 21 months [72]. Given that implant failure is a major issue, many studies attempted to understand, and subsequently minimize, the occurrence of such events. This is also one of the motivations for this thesis.

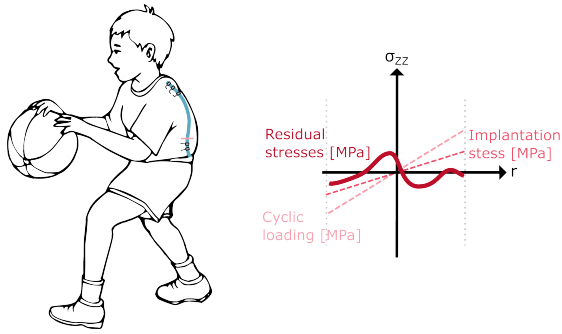

Figure 3.14 Superposition of the 2 loadings (static and cyclic) to the prior implantation stress profile.

[1] *Distraction* depicts the tendency to separate, pull away. In the context of growing rods it is the force exerted by the rod on the spine to make the correction. *Distraction* is also used to define the intermediate surgeries to allow lengthening of the rod.

Figure 3.15 Illustration of a single rod having broken in the patient's back.

3.4 State of the art on growing rod failure

This section aims to gives a general overview of the literature that led us to the research question. More detailed reviews will be presented at the beginning of each chapter in relation to the subject covered in it.

Since the beginning of the use of growing rods, fracture has been a recurrent complication, occurring in 15 % of patients [72]. Yang et al. tried to determine the factors favoring fracture by relying on statistical analyses. They investigated the case of 327 patients aged 6.1 ± 2.5 years at the time of their first surgery and presenting various types of scoliosis (neuromuscular, idiopathic, congenital). In the case of single rods, as compared to double rods, there is a larger risk of fracture (36% versus 11%, $P<0.001$) and repeated fractures are more present (13% versus 2%, P=0.0002). Stainless steel rods break more often than titanium rods (29% versus 18%, P=0.02). In addition, for the group of children who did not have a broken rod, these rods have a larger diameter on average compared to the broken cases (4.8mm versus 4.1mm, P=0.01).

Several studies have already been carried out to try to understand the origin of the failure of growing rods. First of all, it was necessary to determine the failure mechanism in order to subsequently study the parameters that could lead to this fracture. The mechanism was identified as being fatigue, and various aggravating factors such as bending and indentations, were pointed out.

3.4.1 Identification of failure mechanism

In their study, Yamanaka et al. [73] analyzed 2 rods that had failed in vivo. The mechanism of fracture was clearly identified as fatigue. Figure 3.16 shows that the crack propagates from the top of the image in the direction of the dotted arrows, until the rod is weakened enough for an external force to break part C in a ductile manner. These two failure mechanisms can be confirmed by looking at the fracture surface via scanning electron microscopy (SEM).

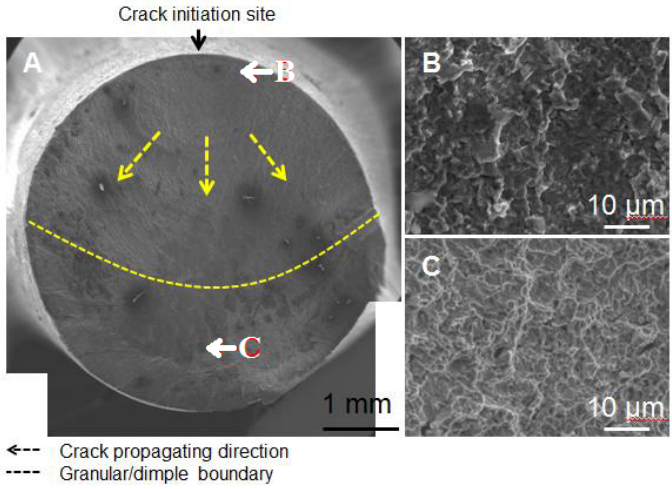

Figure 3.16 Fatigue failure in zone B and ductile fracture in zone C - [73].

In the same study, they found that the microstructure in the region near the fracture was similar to what it was before the rod was implanted. This observation was related to a poor selection of the material (Ti-6Al-4V) or to the treatment that the rod underwent [73].

3.4.2 Fatigue resistance and plasticity

Lindsey et al. investigated the effect of bending with the French bender tool on the fatigue strength of different materials. They compared the fatigue of the straight rods with that of the bent rods at a frequency of 4 Hz with different loading ratios ranging from 250N/25N to 700N/70N. Figure 3.17 shows the results obtained for the Ti-6Al-4V rods: a straight rod is more resistant to fatigue than a bent rod. The same conclusion was reached for TiCP rods.

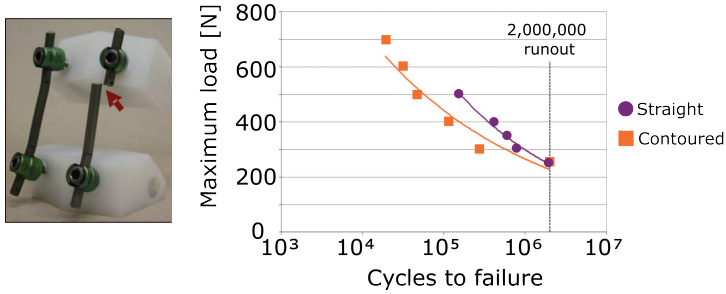

Figure 3.17 Comparison of 2 Ti-6Al-4V rods subjected to fatigue, one bent, the other straight - adapted from [69].

A study by Slivka et al. on the effect of bending on fatigue endurance demonstrated that it is safe to first over-bend and then re-bend the rod in the opposite direction. In their protocol, Ti-6Al-4V growing rods were bent using a different bending tool than the French bender. Straight rods were compared to two bent configurations achieved by either direct of indirect contouring techniques. The direct method gives directly to the rod its final radius of curvature (100 $\pm$ 10 mm), while in the indirect technique, the rod is over-bent (50 $\pm$ 10 mm) and then reverse-bent to generate a similar radius of curvature as that obtained from direct contouring. The fatigue performance of all bent rods is reduced compared to that of straight rods. However, the indirect technique limits this performance drop.

A recent study of Piovesan et al. combined experimental results with computational analyses to assess the fatigue resistance of rods having experienced contouring using a French bender tool [75]. The novelty of their research lies in the distinction between a lordotic and a kyphotic configuration during fatigue solicitation, as illustrated in Figure 3.19. From the residual stress estimated by finite element models, they predicted that the

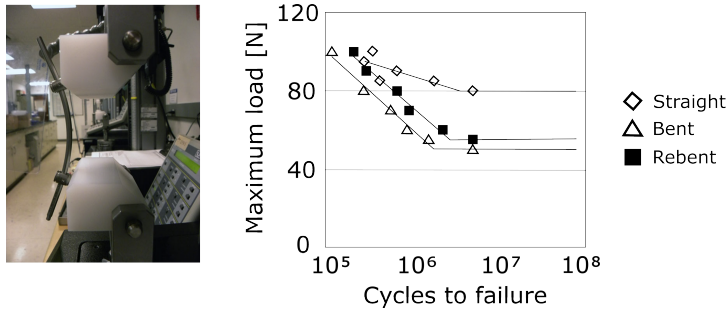

Figure 3.18 Comparison of three Ti-6Al-4V rods subjected to fatigue, one bent, one rebent, and the other straight - adapted from [74].

kyphotic configuration should withstand a larger number of cycles compared to the lordotic configuration (see Figure 3.20). This explanation turns out to be consistent with the experimental results, as the rods tested in lordotic configuration performed 24,495 cycles on average as compared to the one tested in kyphotic configuration which did not fail after 1,000,000 cycles.

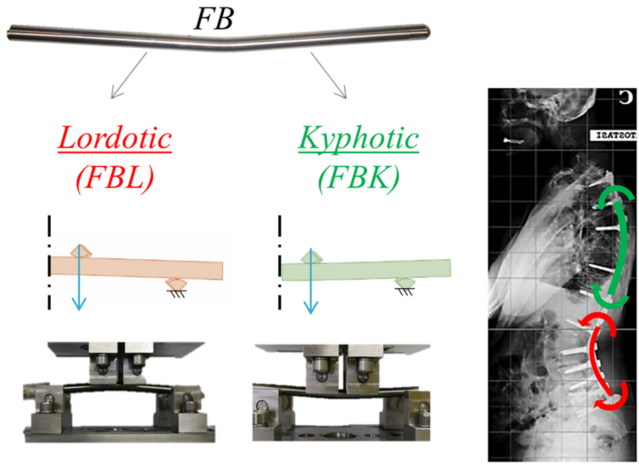

Figure 3.19 Configurations analyzed by computational and experimental analyses - [75].

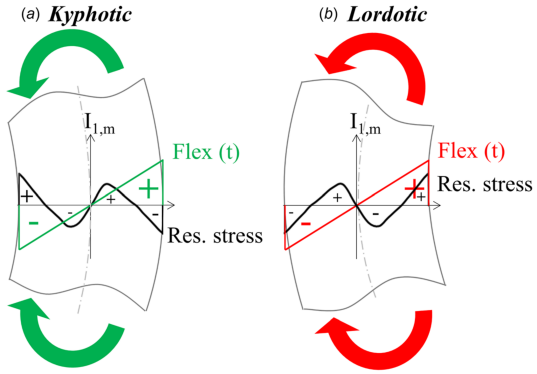

Figure 3.20 Schematic representation of the superposition of stress profiles from bending (*Res. stress*) and cyclic loading (*Flex(t)*) - [75].

3.4.3 Fatigue resistance and indents

Dick et al. studied the impact of indents on the fatigue resistance of three different materials (SS, Ti-6Al-4V and TiCP) [76]. The indents were of three types. The first samples were slightly bent with a French bender in order to introduce indents on the surface but to minimize the plastic deformation of the rod (samples called "French"). The second solution was to mark the rods with the used connectors either by leaving them in place ("Bolt") or by removing them afterwards ("Mark"). Finally, some samples were kept without indentation in order to provide a control group ("Normal"). All samples were tested in 4-point fatigue with an applied moment of 11.86 Nm, this value having been chosen arbitrarily.

As shown by Figure 3.21, the indentations left by the bending tool (as well as by other tools such as connectors) have a significant impact on both titanium alloys. Indeed, titanium is a material that is sensitive to notching as it has a low hardening capacity [74].

In addition to the indentations left by the bending tool, Yamanaka et al. considered that the rough surface, left by the shot-peening process after shaping, created preferential sites from which cracks could potentially propagate [73]. However, it should be kept in mind that the shot-peening process improves fatigue properties.

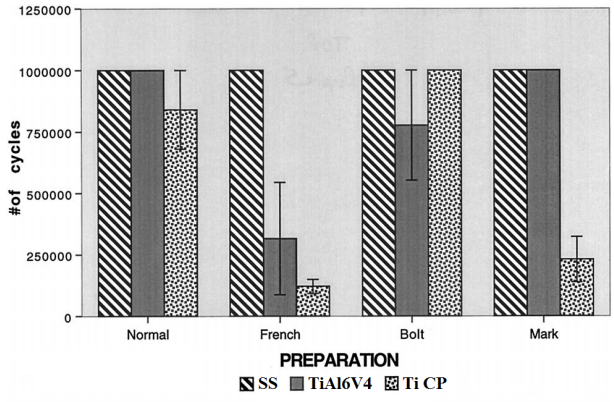

Figure 3.21 Comparison of the number of fatigue cycles before failure for three different materials with four different initial states - [76].

3.5 Research questions

The current state of the art suggests that straight rods are more resistant to fatigue than bent ones. However, it would not be appropriate to insert perfectly straight bars into children's backs. Surgeons should therefore only bend the rod if found absolutely necessary. In such cases, the literature gives no recommendation regarding the "intensity" of bending. Furthermore, models predicting residual stress profiles do not currently rely on any experimental measurements to confirm their predictions. Finally, these models never take into account the shot-peening stage, which is a major gap in the understanding of the parameters primarily setting the durability of growing rods.

In this context, the following chapters are part of an in-depth analysis aimed at addressing the following question:

How do the near-surface residual stresses, resulting from inhomogeneous plastic deformation, influence the fatigue resistance?

Figure 3.22 summarizes the contributions of each chapter with respect to the different life stages of these rods.

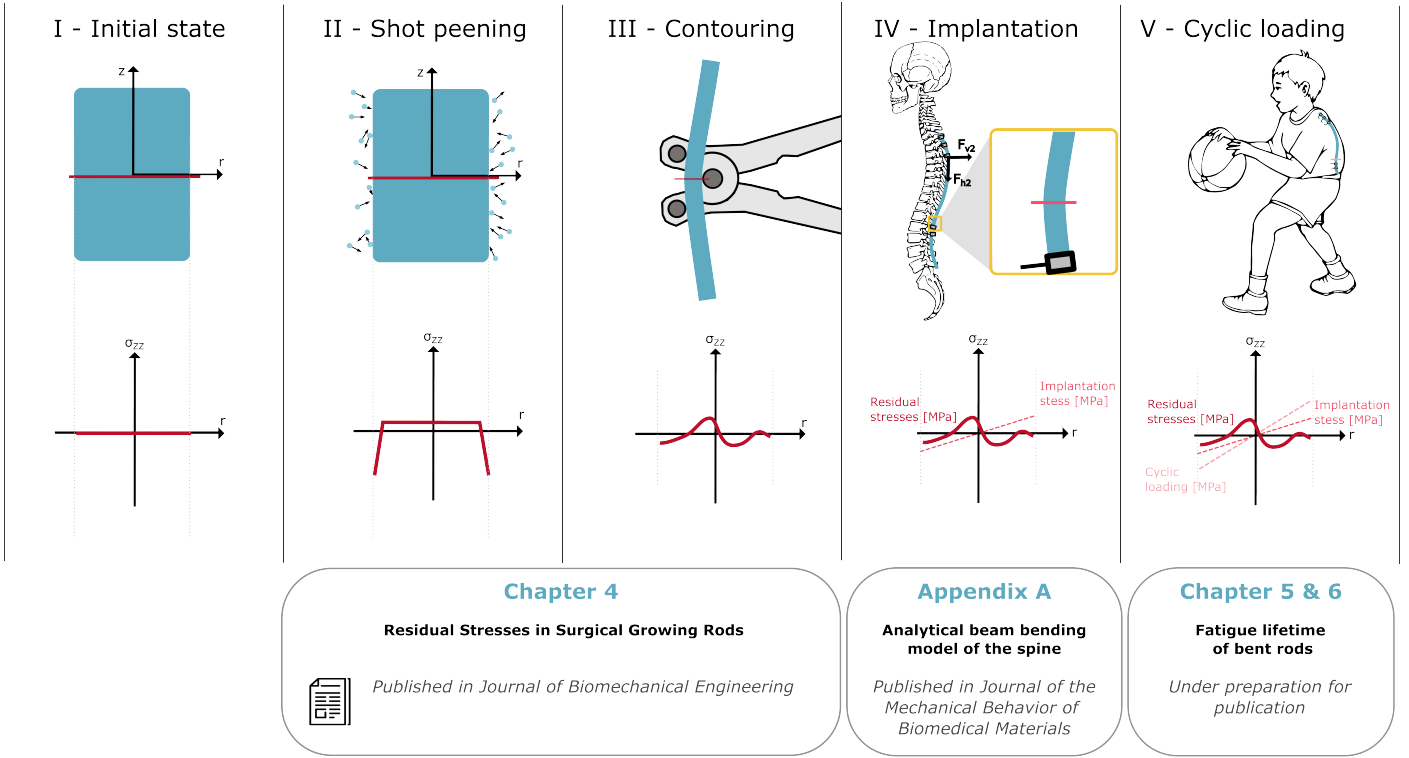

Figure 3.22 Illustration of the residual stress states at each stage in growing rods and the respective Chapters dealing with each problematic.

Chapter 4 discusses the residual stress variations at stages II and III (i.e. shot-peening and bending) as shown in Figure 3.22. A finite element model, validated by experimental measurements, is used to explore the stress fields with respect to the surgeon's practice and to the properties of the chosen material. It is also used to analyze the combined effects of both stages of plastic deformation, which has not yet been reported in the literature.

Appendix A discusses the residual stresses once the rod has been placed along the spine (stage IV in Figure 3.22). Based on X-ray images of the rods before and after failure, a beam bending model allows the extraction of stress intensities at the failure site for different patients. This chapter is the result of a collaboration between several researchers and the contribution of the author of this thesis was relatively modest. Therefore, these results are presented in an Appendix and not in the core of the thesis.

Chapter 5 is a preamble to Chapter 6, as it required to develop a novel 3-pt bending test setup which maintains curved rods in the unstable upward position. This chapter presents the design process and experimental validation of this setup. It concludes with a presentation of the test protocols. This setup allows maintaining rods during cyclic loading, in order to test growing rods up to failure (see stage V in Figure 3.22).

Chapter 6 concludes this part by looking at the fatigue failure of growing rods resulting from cyclic loading (see stage V in Figure 3.22). The setup presented in Chapter 5 is used to test bent growing rods in order to reproduce the fracture surface observed in in-vivo broken rods. The aim of this chapter is to better assess the effects of shot-peening and bending on the fatigue resistance of growing rods.

3.5 Material presentation

The same growing rods, made from titanium alloy, are studied through the four chapters. Therefore a general presentation of its properties and characteristics is gathered hereafter. The growing rods investigated are Ti-6Al-4V rods with 5.5 mm diameter. They were purchased from Medtronic Sofamor Danek under the tradename CD Horizon® Legacy™ System.

At the initiation of this study, contact was made with the supplier of the rods to inquire about their production processes. In all industries, but particularly in the biomedical field, innovation often coexists with a culture of confidentiality. Even it the manufacturer has maintained a veil of secrecy around the specifics of the material, they disclose that Ti-6Al-4V rods are wire-drawned and shot-peened with stainless beads. However, detailed information regarding the process parameters, heat treatments or mechanical properties remained undisclosed. Nevertheless, we initiated the research with preliminary characterizations aimed at acquiring a better understanding of the material.

The microstructure of the rod material was characterized based on metallographic cross-sections taken parallel to the rod axis (i.e. horizontal direction in the micrographs). The preparation involved grinding and polishing with diamond suspensions followed by a 20-min silica suspension step. The microstructure was revealed after etching, which consisted in 30-s immersion in a 3 mL HF, 6 mL HNO_3, and 91 mL water solution. Micrograph was taken using scanning electron microscopy (SEM) (Ultra-55 FEG SEM, Carl Zeiss, Oberkochen, Germany). The material was characterized using backscattered electron detector (AsB) with an acceleration voltage of 20 kV.

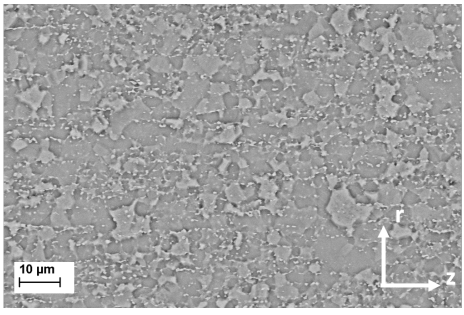

Figure 3.23 SEM micrograph of axial microstructure from a rod made of Ti–6Al–4V alloy.

Fig. 3.23 shows that the Ti–6Al–4V alloy is made of two phases: an α matrix composed of isotropic grains with a mean grain size of 3 µm to-

gether with smaller elongated β grains with a mean grain size of 0.5 µm. The crystal structure of both phases are illustrated in Figure 3.24a and 3.24b, respectively. The volume fraction of the β phase is equal to 5%. The equiaxed microstructure is obtained by thermal treatment after wire-drawing/extrusion process.

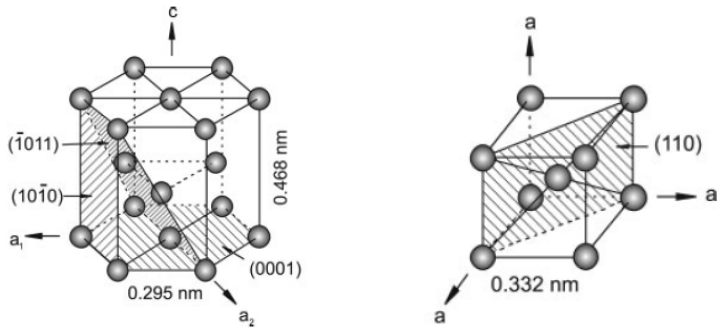

Figure 3.24 Crystal structures of the 2 phases present in Ti–6Al–4V (a) alpha phase, hexagonal close packing (HCP) structure (b) beta phase, body centered cubic (BCC) structure - from [77].

During wire-drawing process, some plastic deformation occurs in the material leading to a reorientation of the crystalline structure. As α-titanium is deformed, the primary dislocation slip activated is the prismatic <a> $\{1\,0\,\bar{1}\,0\}$ as it has a lower energy barrier for glide motion followed by the basal <a> $\{0\,0\,0\,1\}$ and the pyramidal <a> $\{1\,0\,\bar{1}\,0\}$ planes families [78]. Crystals rotation results in a texture with major component $\langle 1\,0\,\bar{1}\,0\rangle$ [79] as illustrated in Figure 3.25.

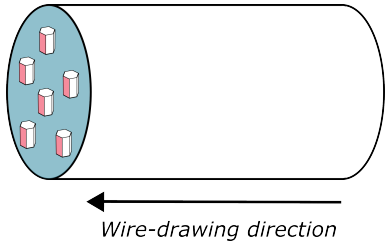

Figure 3.25 Preferential orientation of the HCP crystal units in a Ti-6Al-4V rod subjected to wire-drawing.

X-ray diffraction (XRD) was used to study the texture of the Ti-6Al-4V rod. The rod was cut along its longitudinal cross-section and the surface was mirror-polished. Figure 3.26 shows the experimental XRD pattern with the theoretical peaks positions and relative intensities of α and β phases. The obtained diffraction pattern reveals low or non-existent relative intensities for the associated 1,0,0, and 1,0,1 Miller indices of the α matrix. This result is consistent with the expected texture as the observation was made in the longitudinal cross-section.

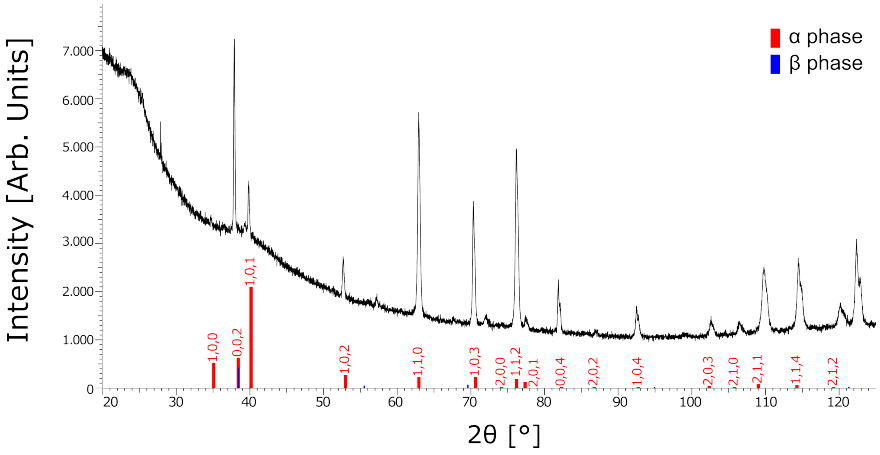

Figure 3.26 XRD curve for Ti-6Al-4V rod in the longitudinal cross-section.

The tensile test samples were machined into cylindrical dog-bone shape with a diameter of 4 mm representative of the core of the rod (see Fig. 3.27a). The tests were carried out until fracture on a Zwick Roell stress rig. The applied displacement rate was set to 1 mm/min.

Fig. 3.27b shows the uniaxial tension response in terms of the variation of the true stress:

$$\sigma = \frac{F}{A_0}\left(1 + \frac{u}{L_0}\right), \tag{3.1}$$

as a function of the true strain:

$$\epsilon = ln\left(\frac{L}{L_0}\right). \tag{3.2}$$

where F is the tensile force, A_0 is the initial cross-section area, u is the elongation and L_0 and L are, respectively, the initial and the deformed gage length. Three tests were performed to control reproducibility.

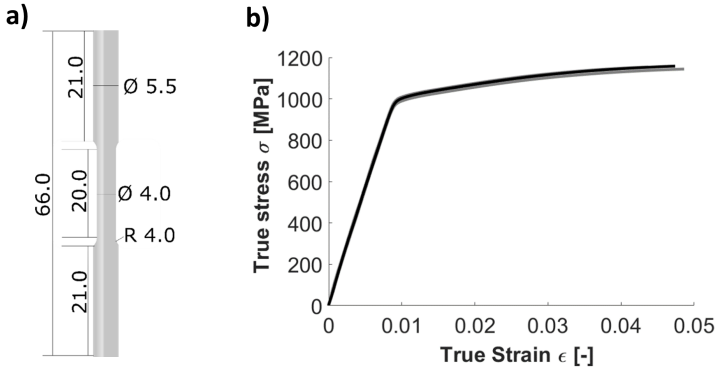

Figure 3.27 Uniaxial tensile tests: (a) samples geometry; (b) true stress – true strain uniaxial tension response from three Ti-6Al-4V specimens.

The following properties were determined from the uniaxial tension response, shown in black in Fig. 3.27b: Young's modulus E = 113 $\pm$ 1 GPa; yield stress $\sigma_{0.2\%}$ = 1000 $\pm$ 5 MPa.

Nanoindentation tests were performed with an Agilent Technologies Nano-Indenter G200 using a Berkovich tip of known stiffness. Sixteen indents were performed both on the transverse cross section of the rod at the center as well as close to the surface. The hardness is equal to 4.1 $\pm$ 0.2 GPa at the surface and 3.8 $\pm$ 0.1 GPa in the core along the axis of the rod. The surface hardness is thus larger by about 10% compared to the center, which is attributed to the accumulation of plastic deformation due to shot-peening.

4

Residual Stresses in Surgical Growing Rods

INTERNAL stresses before rod implantation are investigated in this chapter. Experimental stress profiles in shot-peened rods after bending demonstrated that compressive residual stresses are maintained at both concave and convex rod sides. Using a finite element model developed to predict residual stresses in the rod, a parametric analysis identified the first-order impact of initial yield strength, kinematic hardening parameters and intensity of the shot-peening operation, while the bending angle and the depth of shot-peening stresses were found to be of minor importance.

This chapter is based on the published article *Residual Stresses in Surgical Growing Rods,* Croonenborghs, M., Ismail, K., Mousny, M., Delannay, L., Everaerts, J., Korsunsky, A. M., Jacques, P. J. & Pardoen, T., Journal of Biomechanical Engineering (2023), 1-45 [80] with minor corrections and addings made after publication.

4.1 Context

When children suffer from severe scoliosis pathology, fusion-type surgery is not acceptable due to the severe impact on the growth of the spine. Among others, proper lung development is closely related to adequate spine growth [58]. As spinal fusion method is not suited for immature skeletons, other corrective techniques have to be used [57, 59]. The decision about the alternative option is made based on the patient profile. Among these alternative techniques, the implantation of growing rods is widely used throughout the world.

The growing rod strategy consists in one or multiple long cylindrical rods inserted in the back to correct for spurious spine curvature. Fig. 4.1 shows a timeline illustrating the different steps. Both metallic and polymeric spinal rods exist, with diameters ranging from 3.5 to 6.5 mm (Fig. 4.1a). During surgical intervention, rods are bent by the surgeon to reproduce the patient's sagittal curvature (Fig. 4.1b). Bending is performed using specific tools such as the French Benders (FB), which often leaves permanent markings at the rod surface. Then, implants are attached directly to the spine with distal and proximal anchor points. The anchoring illustrated in Fig. 4.1c consists of three hooks placed proximally and two monoaxial pedicle screws placed distally (H3S2 construct) [64]. Some extra length is left available below the screws to anticipate patient growth. The rods are distracted at regular time intervals in order to avoid hindering the spine lengthening. Between each surgery, patient movements induce complex and varying stress states in the rods (Fig. 4.1d). A common very detrimental complication is the fracture of the rod (Fig. 4.1e). Such fracture events have been the subject of many studies, trying to elucidate the underlying mechanisms and to find ways to avoid the very invasive replacement surgery.

Several origins of rod failure have been suggested in the context of studies performed during the last decade. In 2011, Yang et al. analyzed records from 327 patients, with single and dual rod constructs, to identify failure risk factors [72]. It was found that (i) 15% of the patients experienced at least one fracture event; (ii) the thoracolumbar junction was identified as a frequent fracture site; (iii) looking at material impact, stainless steel rods exhibited higher fracture rates compared to titanium alloy. Yamanaka et al. identified from the fracture surface of Ti-6Al-4V alloy rods a fatigue

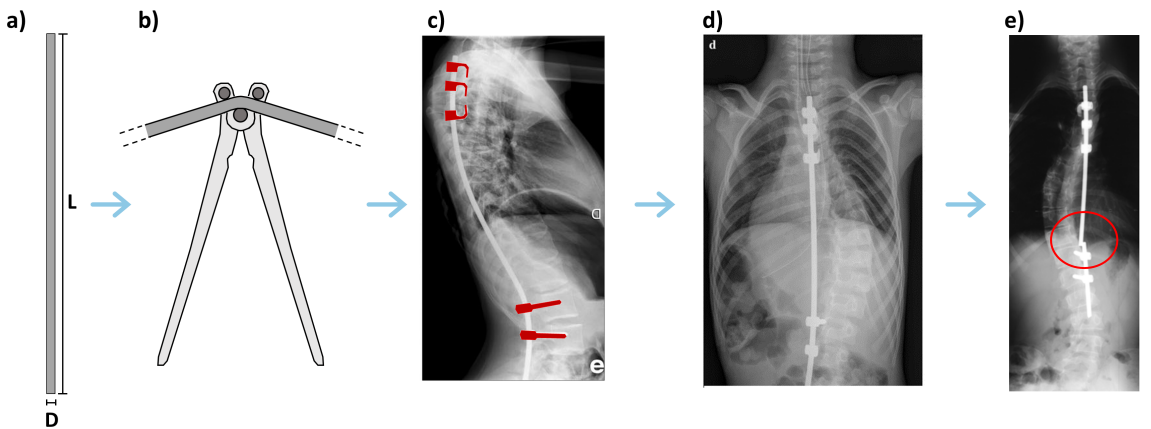

Figure 4.1 Spine correction by growing rod surgery: (a) initial straight rods with specific diameter; (b) contouring by the surgeon using a French Bender tool ; (c) anchoring to the spine (here H3S2 construct); (d) dynamic loads during daily life; (e) rod failure event.

failure mechanism [73]. In another study of broken rods of Hill et al., it was concluded that failure often occurs at locations where the rods had been highly bent [81]. In a more recent study, Ribesse et al. reached the same conclusion for pure titanium and cobalt chromium alloys [82]. Based on a beam bending model, thoracolumbar regions were also found to be the high risk fracture sites.

Four key factors can potentially affect the material lifetime:

(i) The magnitude of the residual stresses resulting from manufacturing and shot-peening. Shot-peening is usually performed in order to induce a compressive stress state at the surface, a well-known way to delay fatigue crack initiation [33].

(ii) The evolution of the residual stresses resulting from shaping. During rod contouring, the surgeon bends the rod plastically. This changes the stress state locally, reorganizing the residual stress distribution and changing the accumulated plastic strain field.

(iii) The generation of surface defects such as indentations. During the shaping process, the bending tools often leave residual imprints at the surface of the rods. These imprints create stress concentrations, plastic strains and also change the local residual stress state.

(iv) The accumulation of load cycles. During operation in the body, rods are bent repeatedly due to patient movements. These fluctuating loads may induce the nucleation and propagation of fatigue cracks.

Taking into account all these factors within a predictive model is a scientific challenge. This study focuses primarily on the evolution of the residual stresses related to steps (i) and (ii).

Berti et al. investigated point (ii) using numerical methods [70]. The authors analyzed the radial distribution of the mean residual stress due to static contouring of the spine rod for two bending methods. Both techniques, FB and uniform contouring, resulted in the same stress profile. This profile, being the result of static contouring only, indicated the generation of tensile stresses on the concave side of the rod. The aim of our study is to further investigate the following questions about point (ii):

- Is it possible to develop a predictive model that captures the experimental trends about the residual stress profile and its evolution?

- How do hardening properties change the stress profile after bending?
- Does the bending angle imposed during contouring affect residual stresses?
- What is learned from such analysis in terms of guidelines for surgeons towards extending the lifetime of growing rods?

The objective is to provide answers to these questions using the following methodology. Residual stress measurements are first performed on unused rods and bent rods relying on the advanced focused ion beam milling technique combined with digital image correlation (FIB-DIC). The second step is to develop a numerical model that predicts the stress profile while accounting for shot-peening and bending, and relying on mechanical tests to extract the hardening law. This requires a relatively advanced plasticity model, including kinematic hardening. After identification and validation, the model is used to perform a parameter study in order to elucidate the primary factors affecting the stress state.

4.2 Materials and methods

4.2.1 Materials

Ti-6Al-4V rods with 5.5 mm diameter were purchased from Medtronic Sofamor Danek under the tradename CD Horizon® Legacy™ System. The tensile properties as well as local hardness variations along a radius of the rod were determined by mechanical testing. In addition, 10 cm length specimens were extracted to perform residual stress measurements in straight and bent rods.

The tensile test samples were machined into cylindrical dog-bone shape with a diameter of 4 mm representative of the core of the rod (see Fig. 4.2a). The tests were carried out until fracture on a Zwick Roell stress rig. The applied displacement rate was set to 1 mm/min.

Fig. 4.2b shows the uniaxial tension response in terms of the variation of the true stress

$$\sigma = \frac{F}{A_0}\left(1 + \frac{u}{L_0}\right), \tag{4.1}$$

as a function of the true strain

$$\epsilon = ln\left(\frac{L}{L_0}\right). \tag{4.2}$$

where F is the tensile force, A_0 is the initial cross-section area, u is the elongation and L_0 and L are respectively the initial and the deformed gage length. Three tests were performed to control reproducibility.

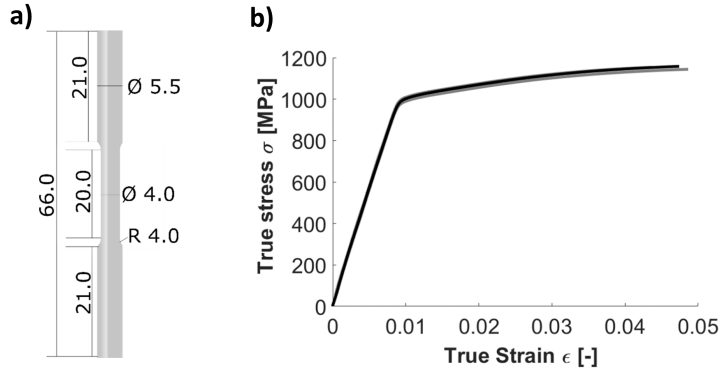

Figure 4.2 Uniaxial tensile tests: (a) samples geometry; (b) true stress – true strain uniaxial tension response from three Ti-6Al-4V specimens.

The following properties were determined from the uniaxial tension response, shown in black in Fig. 4.2b: Young's modulus E = 113 $\pm$ 1 GPa; yield stress $\sigma_{0.2\%}$ = 1000 $\pm$ 5 MPa.

Finally, nanoindentation tests were performed with an Agilent Technologies NanoIndenter G200 using a Berkovich tip of known stiffness. Sixteen indents were performed both on the transverse cross section of the rod at the center as well as close to the surface. The hardness is equal to 4.1 $\pm$ 0.2 GPa at the surface and 3.8 $\pm$ 0.1 GPa in the core along the axis of the rod. The surface hardness is thus larger by about 10% compared to the center, which is attributed to the accumulation of plastic deformation due to shot-peening.

4.2.2 Methods

Rod bending

Two 10-cm-long samples were cut out of the as-received Ti-6Al-4V rod, and subsequently bent using the French Bender device by a trained surgeon. The goal was to apply the surgical practice as closely as possible. Two bending amplitudes were considered and the corresponding contouring angles were measured after elastic springback, using a profile projector (Mitutoyo PJ 300, Illinois, USA). The latter angle was measured between the two tangents aligning with the two ends of the rod. The two specimens had residual bending angle equal to 4° and 13°, respectively.

FIB-DIC ring-core milling

Among all techniques devoted to residual stress measurement, the FIB-DIC method provides a high spatial resolution and the possibility of measuring very close to the surface of the material.

Both samples were cut longitudinally (see Fig. 4.3a) and the cross-sections were electrochemically polished during 10 min using a current density of 2 kA/m² in an electrolyte containing 700 ml/L ethanol, 300 ml/L isopropanol, 60 g/L $AlCl_3$ and 250 g/L $ZnCl_2$. This ensured removal of the layer exposed to cutting and grinding residual stresses [83]. The residual stress along the longitudinal (x) and radial (y) directions was evaluated at ten evenly spaced locations over the cross-section of each sample by means of focused ion beam (FIB) ring-core milling and digital image correlation (DIC) [84]. This technique consisted of several steps. First, a pattern suitable for DIC was created by depositing a thin Pt layer via sputtering and then performing two FIB scanning passes on the area of interest. Next, a micropillar (diameter 5 µm) was machined incrementally by FIB milling in 40 steps of 125 nm (see Fig. 4.3b). After each milling step, ten images of the top surface of the pillar were taken by scanning electron microscopy (SEM) with a pixel size of 8 nm and an electron beam energy of 5 keV. The micropillar undergoes a gradual strain relief upon progressive milling, which was measured via DIC on the SEM images. For the DIC analysis, a grid with a marker spacing of 12 pixels was used and the marker displacements were averaged over ten images for each milling step. The DIC analyses were carried out using an open source software Digital Image Correlation and Tracking available on MathWorks [85]. This produced a relief strain curve, in the x and y directions, as a function of milling depth. These curves were fitted to the master curve function as de-

scribed by Korsunsky et al. [86] to obtain the total relief strain in the x ($\Delta\epsilon_x$) and y ($\Delta\epsilon_y$) directions. Complete stress relief was achieved when the total milling depth was equal to the pillar diameter [86]. Most pillars include more than one grain which justifies the approximation of using isotropic elasticity [87]. Combined with the assumption of non-equi-biaxial stress state, the residual stress in the x direction (σ_{xx}) and in the y direction (σ_{yy}) were determined using Hooke's law as:

$$\sigma_{xx} = -\frac{E}{(1-\nu^2)}\left[\Delta\epsilon_x + \nu\Delta\epsilon_y\right], \tag{4.3}$$

$$\sigma_{yy} = -\frac{E}{(1-\nu^2)}\left[\nu\Delta\epsilon_x + \Delta\epsilon_y\right], \tag{4.4}$$

with E and Poisson ratio ν equal to 113 GPa and 0.3, respectively. The error bars, which represent a 95% confidence interval, were calculated as described by Lunt et al. [88]. This includes the error due to DIC tracking, the error caused by fitting the data to the master relief curve, and the error caused by the assumption of isotropy.

The Ti–6Al–4V alloy is made of two phases: an α matrix composed of isotropic grains with a mean grain size of 3 µm together with smaller elongated β grains with a mean grain size of 0.5 µm. In the current study, the FIB-DIC measurements (micropillars of 5µm diameter) were not located purposefully inside individual grains. This means that multiple grains were present in each gauge volume and supports the simplification of assuming elastic isotropy.

4.3 Experimental results

Fig. 4.3c shows the variation of stress in direction x along the rod axis as a function of position as deduced from the FIB-DIC method. The surface layers of the as-received (straight) rod are under 800 MPa compression[1] over a thickness of 0.3 mm from the surface. Such stress state may be expected after shot-peening.

[1] In-vivo broken rods show crack propagation along the y direction. In this study, even if there is no crack in the model, we will focus on the stress component σ_{xx}, which will be the driving force for fatigue crack propagation.

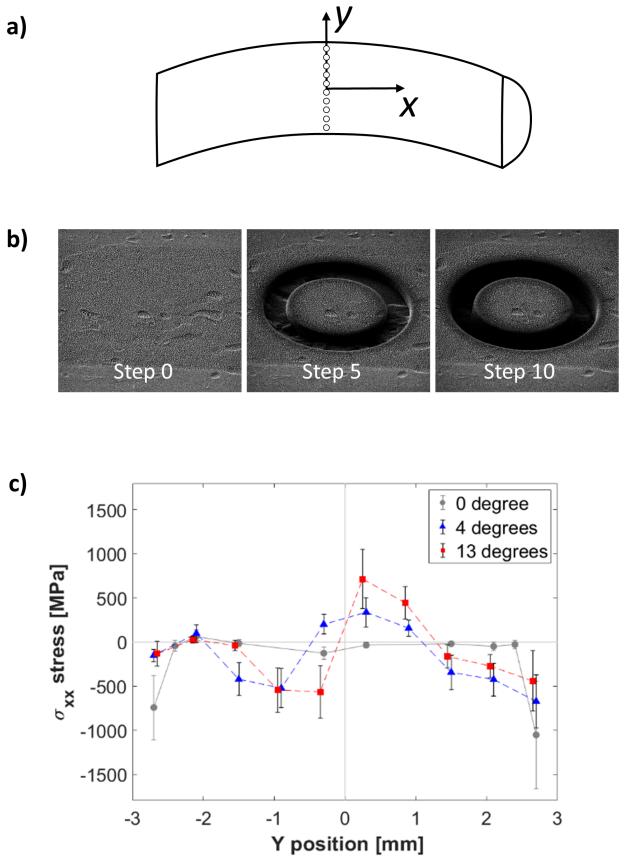

Figure 4.3 (a) Coordinate system for the bent rod indicating the location of the FIB-DIC measurements (b) SEM images of the milled area with DIC pattern, before and during milling steps (c) Radial profile of the residual stress along the rod axis in a Ti-6Al-4V (gray circle) unbent (unloaded) rod, (blue triangle) 4° bent rod, (red square) 13° bent rod measured by FIB-DIC.

After 4° and 13° bending, Fig. 4.3c shows that the residual stress profile inside the Ti-6Al-4V bent rods becomes more complex. At the surface of the concave part of the rod (i.e. y = -2.75 mm), the stress is slightly compressive reaching -150 MPa. Within the next two millimeters, the stress first increases slightly to reach a few hundreds of MPa in tension, before returning to a compressive stress of about -500 MPa. Close to the core, a

steep inversion of the stress state is observed, resulting in a tensile state on the other side of the core, decreasing gradually to reach a compressive state again towards the convex surface (i.e. y = 2.75 mm) of about -500 MPa. Both surfaces remain thus in compression but the magnitude of the residual stress is reduced especially on the concave part. Note that the residual stress profile does not vary very much between 4° and 13° bending, especially near the concave surface(i.e. y = -2.75 mm).

4.4 Modelling and simulation

The model must account for the impact of both shot-peening and bending to predict the residual stress profile. The mechanical history of the material at the periphery of a growing rod is complex. Initially, the rod surface is uniformly compressed during the shot-peening stage. Then, when the surgeon bends the rod with a FB, the axial segments along the convex side are stretched, while the axial segments on the concave side experience further compression. During the elastic unloading after bending, the axial segments extend on the concave side, while contraction occurs on the opposite side.

Description of the models

To select the most representative constitutive plasticity model, both isotropic hardening and kinematic hardening models have been compared.

Isotropic hardening model. As illustrated in Fig. 4.4a, during a uniaxial solicitation, the center of the elastic domain of a plastically loaded isotropic material does not move but the size of the domain increases resulting in the same yield stress in tension and in compression. The isotropic hardening model of his study assumed a constant hardening slope $\mathrm{d}\sigma_Y / \mathrm{d}p$ where σ_Y is the current yield stress and p the accumulated plastic strain.

Kinematic hardening model. The mechanical response during a uniaxial solicitation for purely kinematic hardening is illustrated in Fig 4.4b. During the loading, the elastic domain maintains a constant size equal to $2\sigma_0$ with σ_0 the yield stress, but its center progressively shifts due to heterogeneous residual stress developing at microscale (also called "backstress") and which have a different origin related to the microstructure compared to macroscopic residual stress profile on which this study focuses.

Under multiaxial loading condition, the backstress is a tensor $\mathbf{X}$ and one possible law describing its evolution has been proposed by Chaboche and Marquis [89] in the form:

$$\dot{\mathbf{X}} = A\dot{\boldsymbol{\epsilon}}^p - B\mathbf{X}\dot{p}, \tag{4.5}$$

where A and B are two scalar parameters. Their ratio A/B defines the maximum amplitude of the backstress, whereas $\dot{\boldsymbol{\epsilon}}^p$ is the plastic strain rate and $\dot{p}$ is the rate of increase of the accumulated plastic strain. In the following, the amplitude of deformation will be essentially quantified by the bending angle, which is the operating parameter [2]. In the practice, the surgeon does indeed not control the amplitude of $\boldsymbol{\epsilon}^p$.

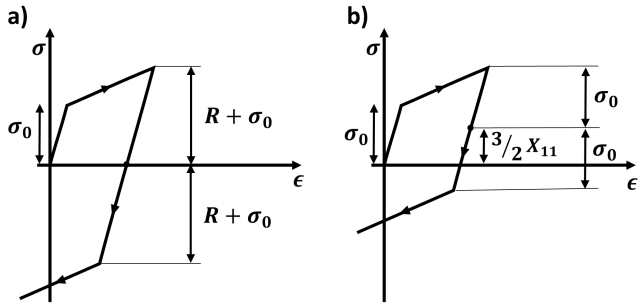

Figure 4.4 Graphical representation of a load cycle under uniaxial stress condition based on either (a) isotropic hardening, or (b) kinematic hardening – inspired from [89].

4.4.1 Finite element model

The elastoplastic linear isotropic hardening model is directly available in the commercial Finite Element (FE) solver Abaqus while the elastoplastic non-linear kinematic hardening model from Chaboche and Marquis was implemented through a user-defined material law UMAT of Abaqus based on implicit Newton–Raphson method [90]. For all simulations the Nlgeom

[2] If the magnitude of deformation is more closely linked to the ratio of bending radius to rod diameter instead of the bending angle, the choice remains justified. Representing an angle is more intuitive than a radius of curvature. Additionally, the dimensions of the bending tool remain constant throughout the entire study, therefore a larger bending angle will always be associated to smaller bending radius.

algorithm was used to account for large deformations. The bending is symmetrical with respect to two planes. Firstly, the two outer rollers move in an mirror-image motion, creating an initial symmetry perpendicular to the central tool. Then, once the bar has been bent, a plane parallel to the bending plane and located at mid-thickness in the bar constitutes the second plane of symmetry. Taking advantage of those symmetries, only 1/4 of the rod was modelled in 3D (see Fig. 4.5a). In order to avoid numerical locking due to the nearly-incompressible response, C3D8R three-dimensional linear solid elements were adopted to simulate the bending process. The diameter of the rod was discretized into 22 elements while 33 elements were used along the length.

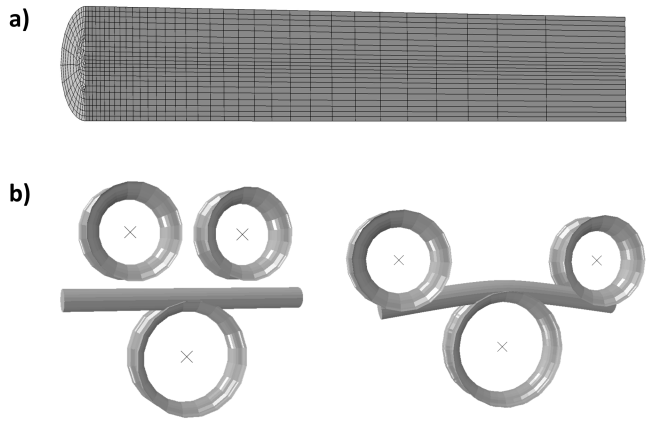

Figure 4.5 (a) Illustration of FE mesh in the 1/4 rod using taking advantage of symmetries, (b) illustration of the complete structure (rod + tool) reconstructed using symmetries showing the configuration before and during contouring.

At first, the model aimed at replicating the state of the rod prior to bending. Shot-peening introduces a compressive stress field in the near surface region. Effectively simulating the shot impacts in a realistic direct way requires advanced numerical models out of the scope of the present study [91]. Another advanced technique, relying on residual stress and work hardening measured and evaluated by X-ray diffraction, was developed by Zhou et al. [92]. This method accurately reconstructs the mechanical behavior of shot-peened materials and the hardening gradient through the

thickness without simulating each shot impact. To implement this technique effectively, a reliable characterization method of the accumulated residual plastic strain is necessary.

Our research did not aim to predict the realistic mechanical behavior of the shot-peened rod precisely but rather to understand the underlying mechanisms explaining the drop in residual stress captured via FIB-DIC. Therefore, no X-ray evaluation of the residual accumulated plastic strain was performed. Instead, the eigenstrain method was used to introduce residual stresses considering a fictitious thermal step forcing a dilation inside a layer of thickness h of one element at the surface (0.22mm). This induces compressive hoop and axial stress equal to -820 MPa. Although this technique does not correctly predict the hardening gradient through the material, a different material law was assigned to the outer layer to accommodate the local variation of yield strength (see section 4.4.2a). As the equivalent von Mises stress reaches the yield point during the thermal loading, plastic deformation is induced and the external elements develop a backstress change during this step.

Subsequently, the bending was simulated by describing the kinematics imposed by the French Bender. Fig. 4.5b shows the geometry of the rod and of the tool assembly after applying the two mirror symmetries to represent the complete structure. The tool is composed of two pins, a fixed one, located at the central symmetry plane, and a mobile one. The position of the center of the mobile pin was set and maintained 35 mm away from the center of the fixed pin. The motion of the mobile pin is a circumferential rotation applied around an axis passing through the center of the fixed pin. All dimensions were extracted from a real FB. After checking that the deformability of the tool (slight flattening of the contact surface) did not affect the results significantly, the tools were modeled as rigid bodies. The friction coefficient was set to 0.2. The angular motion of the mobile pin led to the right configuration after unloading (i.e. after elastic springback).

4.4.2 Results

a. Identification and validation of the models

The rod was partitioned into two parts, the core and the skin, to capture the local effect of shot-peening, each one obeying a different hardening law. Both kinematic and isotropic hardening models were identified. The core response was imposed in order to match the uniaxial stress strain re-

sponse obtained experimentally on a dog bone specimen as illustrated in Fig. 4.6a. In the shot-peened region, the material experienced successive indentations that introduced plastic strains resulting in a residual stress field. Due to the anisotropic nature of the crystal, different crystal orientations create stress fields with variable intensities and patterns below the indents [40, 93]. Tensile residual stress zones can be locally present below the surface even after multiple impacts, creating stress heterogeneity. The combination of tensile and compressive stresses in this area leads to the selection of a lower elastic limit for the macroscopic mechanical response. Indeed, a composite model with soft regions (i.e., regions with tensile stresses) and hard regions (i.e., regions with compressive stresses) will lose its macroscopic linear elastic behavior sooner. The A and B parameters were adjusted to retrieve a similar tensile strength after 8% deformation as illustrated in Fig. 4.6b. The identified values are gathered in Table 4.1 with parameters selected for the isotropic model.

Table 4.1 Core and skin parameters for the kinematic hardening and isotropic hardening models for Ti-6Al-4V alloy.

Kinematic model				
Parameter	E[MPa]	σ_0[MPa]	A[MPa]	$B[-]$
Core model	113000	1000	4000	20
Skin model	113000	600	7000	5

Isotropic model			
Parameter	E[MPa]	σ_0[MPa]	$\mathrm{d}\sigma/\mathrm{d}p$[MPa]
Core model	113000	1000	3057
Skin model	113000	600	8865

The residual stresses predicted with both isotropic or kinematic hardening have been compared to the stress distributions determined by FIB-DIC. As illustrated in Fig. 4.7, for identical $\sigma_{xx}^{initial}$ profiles (Fig. 4.7a), isotropic and kinematic hardening result in two distinct σ_{xx}^{final} profiles (Fig. 4.7b). The FEA stress contours for the kinematic hardening model are represented below each plot. At the concave side of the bent rod (y = -2.75 cm), the compressive stresses measured experimentally are not captured by isotropic hardening, validating the choice of kinematic hardening. Note that we played with a large range of isotropic hardening and could never capture the experimental trends with reasonable parameters.

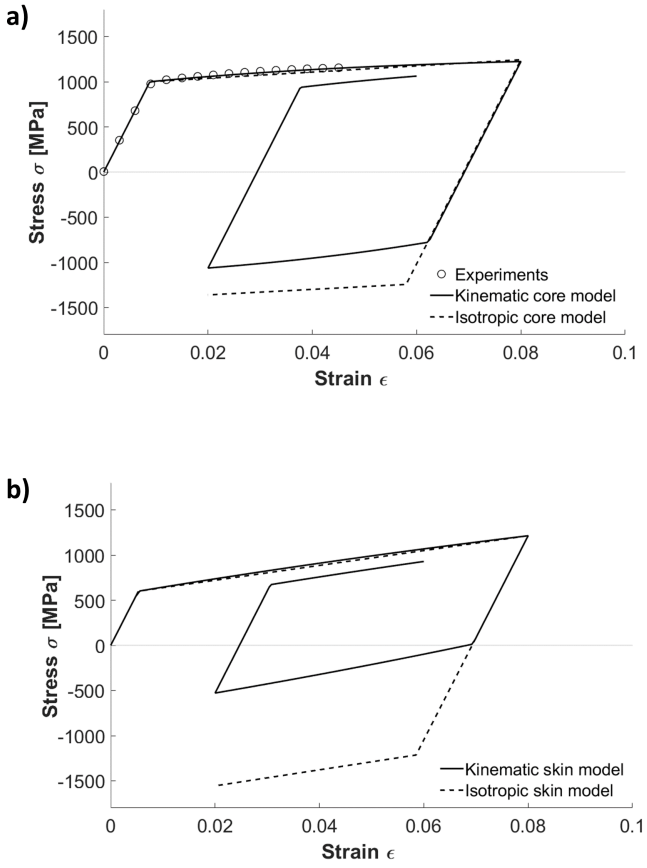

Figure 4.6 Cyclic stress - strain curves for the identification of the isotropic hardening and kinematic hardening models: (a) for the core of the rod compared to the tensile stress strain curve from experiment; (b) for the skin of the rod.

Figure 4.8 provides a deeper understanding on the difference of stress distribution after bending for the two models. Each graph illustrates the stress evolution at the concave side and the convex side of the rod with the equivalent plastic strain during shot-peening, bending and elastic recovery for a hardening model. The shot-peening step introduces a stress of -800 MPa in all the peripheric elements. Then, as bending begins, the concave side

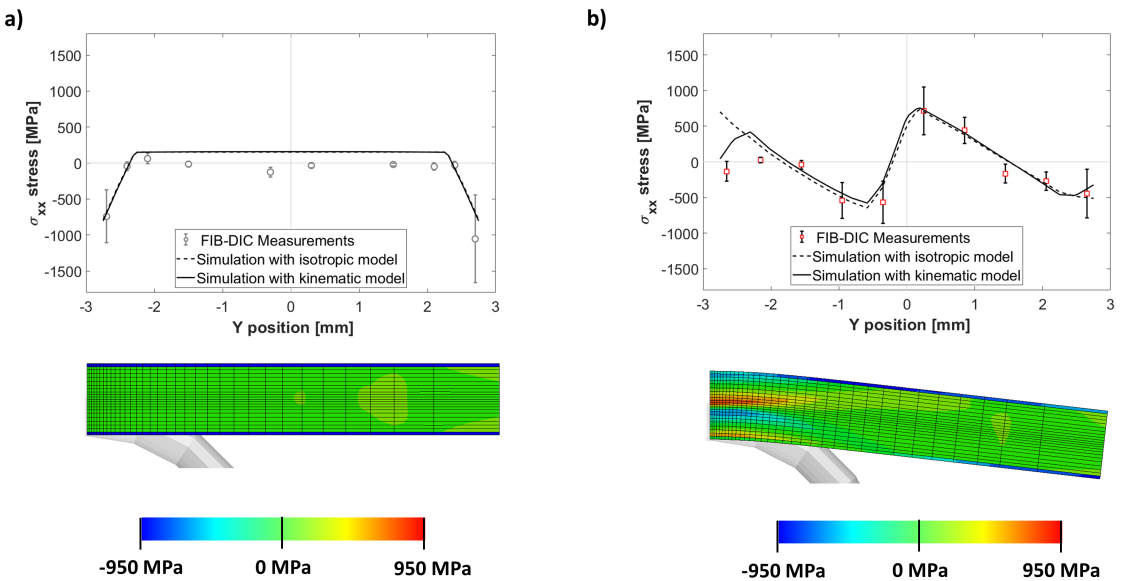

Figure 4.7 Superposition of FIB-DIC measurements and simulations results obtained with either kinematic or isotropic models of radial profile of the longitudinal residual stress for: (a) a straight rod; (b) a rod bent at 13 degrees, made of Ti-6Al-4V supported by the respective FEA stress contour predicted with the kinematic hardening model.

of the rod is subject to further compression while the convex side experiences tension. Finally, during elastic recovery both elements in the kinematic model are found to re-enter plasticity whereas the elements in the isotropic model stay in the elastic domain. The lower stress level for kinematic hardening in previous Figures at y=-2.75 mm (i.e. concave side) is better understand by looking at the elastic recovery stage. As the element unloads, it enters plasticity preventing the development of excessive tensile stresses.

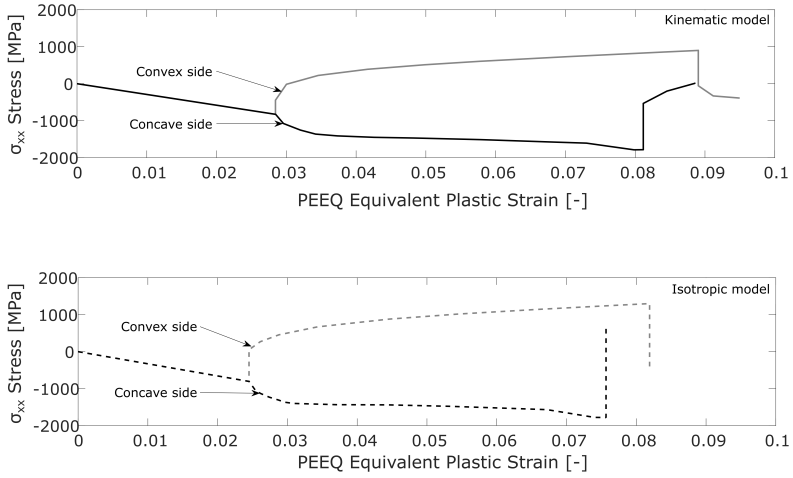

Figure 4.8 Simulations results with either kinematic (top) or isotropic (bottom) models showing the variation of the longitudinal stress with equivalent plastic strain in the peripheric elements for two rod bent at 13 degrees.

b. Parametric study

After identification and validation of the model, a parametric study was performed to determine the evolution of the residual stresses at the likely site of cracking initiation. The thoracolumbar junction was identified as the most at-risk location [72, 73, 82, 94]. Moreover, fractography analysis indicates that cracks systematically initiate on the dorsal side of the rod and propagate towards the ventral side [81, 82]. In the lumbar region, the rod is usually bent in a lordotic configuration [75], inducing the most likely site of fatigue crack initiation at the concave side of the rod (i.e. at y = -2.75mm in our model).

The residual stress state at the rod surface is essentially controlled by seven parameters :

$$\sigma_{xx}^{final} = F(E, \sigma_0^{skin}, A^{skin}, B^{skin}, \sigma_{xx}^{initial}, h, R), \tag{4.6}$$

where E is the Young's modulus ; σ_0^{skin}, A^{skin} and B^{skin} are hardening parameters; $\sigma_{xx}^{initial}$ is the initial stress state imposed to the surface elements after the shot-peening step through the fictitious thermal loading, h is the thickness of the surface shell which undergoes compressive stresses and R is the radius of the rod. Equation 4.6 is non-dimensionalized as follows

$$\sigma_{xx}^{final} = F\left(\frac{\sigma_0^{skin}}{E}, \frac{A^{skin}}{E}, B^{skin}, \frac{\sigma_{xx}^{initial}}{E}, \frac{h}{R}\right). \tag{4.7}$$

The master set of parameters, presented in Table 4.2, was defined as the one providing the best match with experiments as a result of the identification. The parameters associated to the core elements were fixed and all the other parameters can be varied to assess their impact. For the sake of simplicity, the parameters σ_0^{skin}, A^{skin},B^{skin}, are noted as σ_0, A, B in the sequel.

Table 4.2 Master set of parameters for Ti-6Al-4V alloy.

σ_0/E		A/E		B		$\sigma_{xx}^{\text{initial}}/E$	h/R
core	*skin*	*core*	*skin*	*core*	*skin*		
0.009	0.005	0.0035	0.06	20	5	-0.007	0.08

In order to analyze the impact of the surgeon's practice, Figure 4.9 depicts the effect of the bending angle on the final stress level by plotting the variation of the final near surface residual stress state as a function of the bending angle for three initial stress levels produced by shot-peening. For this set of simulations, the angular motion of the mobile pin was tuned to produce pre-selected contouring angles after springback. The σ_{xx}^{final}/E ratio increases steeply at very low angles, levels off, reaches a maximum and then decreases slightly at larger angles. The angular motion of the mobile pin was fixed to 0.62 rad for all the following simulations. All imposed bending angles after springback lie between 9°5′ and 12°3′. As the bending angle was found to have a limited effect, we did not attempt to reach exactly the same final angle for each set of material parameters.

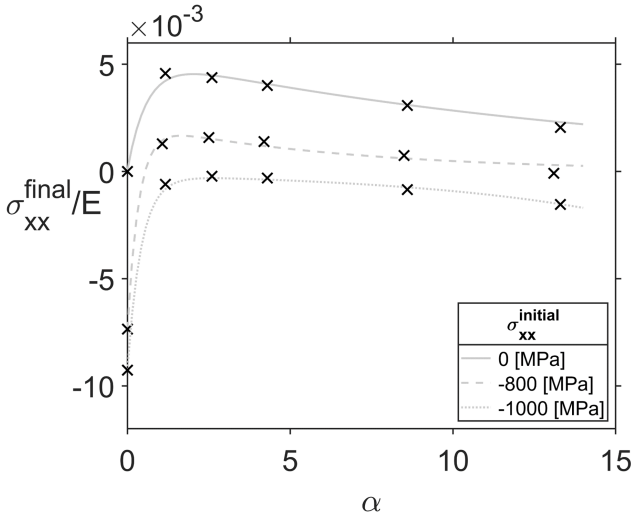

Figure 4.9 Variation of the stress along the rod axis at the concave rod surface after bending as a function of bending angle α.

Figure 4.10 shows the variation of σ_{xx}^{final}/E with (a) A/E, (b) B, (c) σ_0/E and (d) h/R for three different initial stress levels. Increasing A/E reduces the magnitude of σ_{xx}^{final}/E see Fig. 4.10a. For high ratio of A/E, a compressive residual stress is produced at the concave rod surface. When the parameter B increases, σ_{xx}^{final}/E gradually rises as shown in Fig. 4.10b. This effect is less important than the impact of the A/E value.

Increasing σ_0/E leads to a general increase of σ_{xx}^{final}/E as shown in Fig. 4.10c. Again, a compressive residual stress state is generated at the concave rod surface for low σ_0/E ratio. The effect of the thickness of the compressive layer on the variation of σ_{xx}^{final}/E with respect to the rod diameter in Fig. 4.10d shows that the final stress state is independent of h/R for the three shot-peening intensities. Regarding the effect of $\sigma_{xx}^{initial}/E$ addressed in both Fig. 4.9 and Fig. 4.10, the generation of a compressive initial stress state leads to a decrease σ_{xx}^{final}/E. If the initial stress state is sufficiently low, bending leads to a compressive residual stress state at the surface. The relationship between $\sigma_{xx}^{initial}/E$ and σ_{xx}^{final}/E is not perfectly linear.

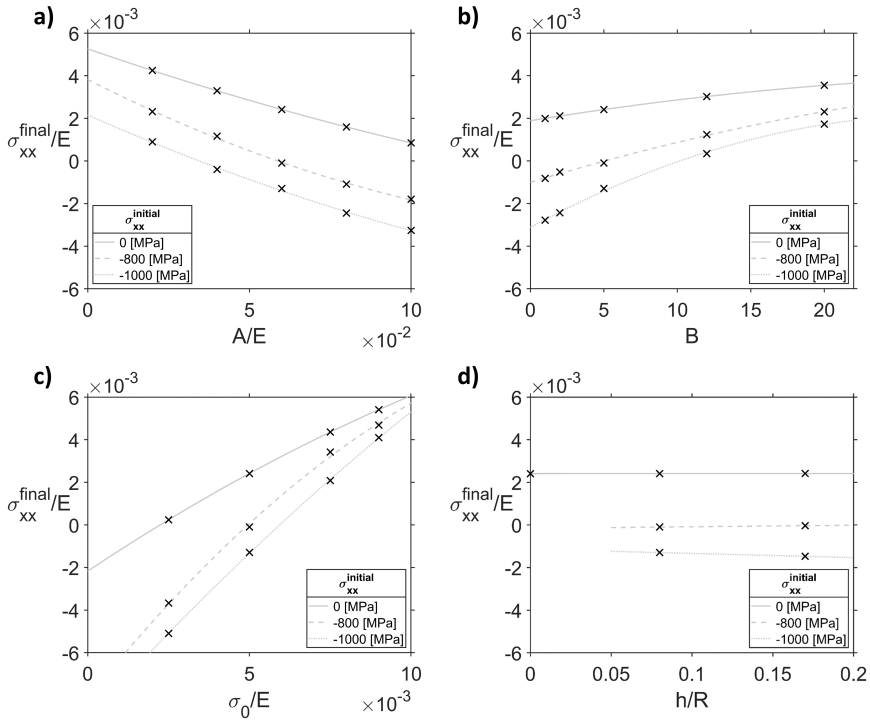

Figure 4.10 Variation of near surface residual longitudinal stress at the concave rod surface normalized by Young's modulus after bending as a function of A/E, B, σ_0/E and h/R. The reference set of parameters are A/E= 0.05, B=5, σ_0/E=0.005 and h/R= 0.08 with a bending angle ranging from 9°5′ to 12°3′.

4.5 Discussion

Residual stresses play a major role in mitigating fatigue crack initiation and growth, which is the mechanism identified as leading to the failure of the growing rods [73, 81, 82]. Currently few studies investigated the residual stresses in growing rods, prior and during their implantation. Analyzing and understanding the residual stress distribution and their dependence on the materials, geometrical and loading parameters is key to guide towards enhancing rod durability through surgeon techniques and/or better material selection. Comparing numerical simulations results with mea-

sured stress fields improves the accuracy of the analyses and provides a better starting point to observe the impact of various parameters.

4.5.1 Prediction of the residual stress profile

The first aim of this study was to create a numerical model capturing the residual stress field measured by FIB-DIC after FB bending, while accounting for the initial stress field induced by shot-peening. Fig. 4.7b illustrated that an isotropic model, such as the one used in the study of Berti et al. [70], is not able to correctly predict the compressive stresses found experimentally at the concave rod surface. A core element of novelty of our approach was thus to combine the initial stress field with a kinematic hardening-based model. As illustrated in the study of Zhang, the material model selection is key when performing residual stress distribution analyses [95]. Compared to isotropic hardening, for which the yield surface expands with plastic deformation, the surface undergoes a shift if the hardening is a kinematic nature. If the source of kinematic hardening lies in the residual stresses of type II and type III, its effect can be observed on the macroscopic stress profile as it is the case for shot-peening. Fig. 4.11 illustrates three scenarios: (i) a growth rod made of a material with isotropic hardening undergoing the following loading sequence: shot-peening, forward bending and bending unloading; (ii) a growing rod made of a material with kinematic hardening (loading sequence without shot-peening); (iii) a growing rod made of a material with kinematic hardening and full loading sequence. The model shows that a springback may involve reverse plastic deformation with kinematic hardening while it is not the case for isotropic hardening. By combining a kinematic model with the shot-peening process, the flow surface shifts twice towards the compression zone during the first two plasticity events, shot-peening and forward bending. This shift mitigates the tendency of ending up with a tensile state near the surface after springback. The model eventually captures the compressive residual stress at the concave surface of the rod compared to the literature.

4.5.2 Towards favoring compressive residual stresses

The second aim of this study was to identify the main parameters that could enhance the fatigue life from the perspective of the residual stress state. As explained in Section 4.4.2.b, shifting the residual stresses towards the compressive regime at the concave surface of the rod could help increasing the fatigue lifetime of the rod. Various ways to reduce the ampli-

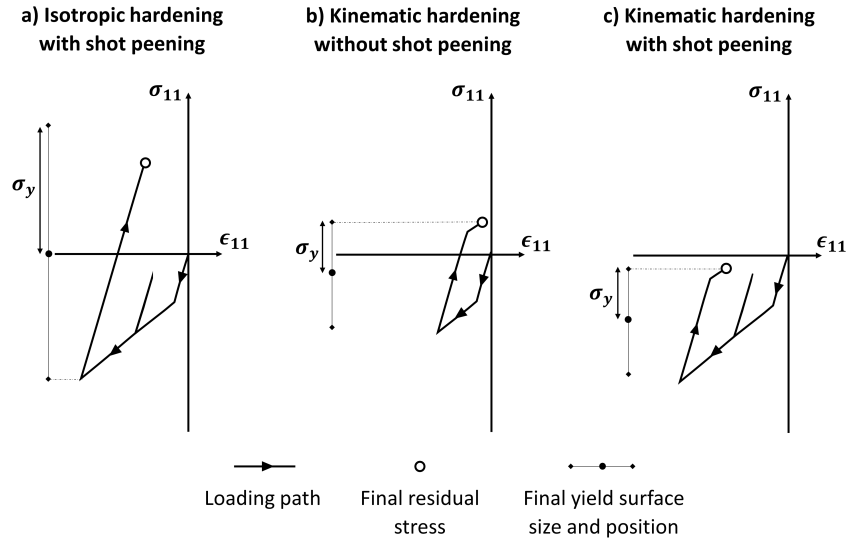

Figure 4.11 Schematic representation of yield process during the bending process at concave surface of the rod for: (a) isotropic hardening with shot-peening; (b) kinematic hardening without shot-peening; (c) kinematic hardening with shot-peening.

tude of residual stresses have been suggested in the literature relative to the distraction frequency, contouring technique and loading configuration. In multiple studies, Agarwal et al. analyzed the optimal distraction frequency [71, 96]. When the time period between two distractions is reduced, the stresses in the rods decrease. In the study of Berti et al. [70], the authors compared the mean residual stress radial evolution due to static contouring for two bending methods by the mean of numerical simulations. Both techniques, FB and uniform contouring, resulted in an identical stress profile, introducing tensile stresses at the concave side of the rod. Based on these results, Piovesan et al. assessed the fatigue behavior for bent rods loaded in lordotic and kyphotic configurations. By moving, patients add a dynamic stress state in the rod. If the rod is placed in a lordotic configuration, the sum of the two contributions to the stress amplitude will increase the risk of fatigue failure compared to a kyphotic configuration [75]. Finally, using their numerical method to describe the local residual stress distribution induced by contouring, Berti et al. introduced a sensitivity

analysis by changing hardening modulus in the material law. Controlling the final radius of curvature, ideal elastoplastic material showed the highest levels of residual stresses [70].

Here, we performed a parametric analysis after proper non-dimensional reduction. The intent was to provide trends about the most relevant parameters that could be potentially manipulated to reduce the local residual stress level, but not necessarily to quantify the very precise stress level in the rod. First, the bending angle applied by the surgeon with a FB is examined to question their practices in Section 4.5.2a. After that, processing parameters are addressed such as the shot peening depth and intensity to determine the impact of shot peening on the residual stress evolution in growing rods in Section 4.5.2b. Finally, we analyze material properties, such as yield strength and hardening coefficients to give guidelines about material selection, in Section 4.5.2c.

a. Guiding better surgeon practice

The plastic deformation associated to the rod bending imposed to conform to the spine morphology fully removes the initial compressive stresses at the rod surface and this even for low bending angle. The model (and the experiments) show that applying a small or a large angle does not result in large variations of σ_{xx}^{final}/E. A slight decrease of σ_{xx}^{final}/E is even found for the largest angles suggesting that the bending angle is not responsible for a decrease of the fatigue properties from a residual stress viewpoint. This trend may not be true for all sets of parameters and we cannot thus conclude that surgeons can apply any bending angle without any impact on fatigue lifetime of the rod. The main reason for the limited effect is the small amount of plastic deformation induced by bending, negligible compared to the total plastic deformation accumulated during shot peening and later during life due to patient movements.

In a previous study on the effect of bending on fatigue endurance, Slivka et al. demonstrated that it is safe to first over-bend and then re-bend the rod in the opposite direction in order to lower the bending angle (called *indirect bending* technique). The fatigue performance of the indirectly-bent rods were lower than that of the straight rods, but higher than that of the rods bent directly to the same angle. This was only supported by experimental results. With the developed numerical model, a simplified[3] numerical

[3]The de-bending process was not carried out with the FB's geometry. Instead, it was executed using a set of three supports with a 4 cm span, creating a three-point bending loading.

analysis on the stress states in both configurations was performed. Figure 4.12 shows the evolution of the stress on the concave side of the rod, for a direct bending to an angle of 4 degrees and for an over-bent rod (i.e. 12 degrees) re-bent to 4 degrees. The residual stress state in the re-bent rod is significantly lower than in the directly-bent rod (i.e. respectively -730 MPa and 100 MPa). However, the stresses during a subsequent fatigue loading (with the concave side under tension) could be in the same order of magnitude. Indeed, the *directly-bent* rod would directly go through plastic deformation while the *indirectly-bent* rod would first deform in the elastic domain, causing the stress value to increase sharply, before increasing more gradually after entering plasticity. This would mean that surgeons' practices need to evolve; more precisely, they should overbend the rod during each correction in the lumbar region, and then straighten it to the desired angle. However, before advising a change in surgical practices (which would be far from insignificant), an extensive analysis should be performed in order to validate this hypothesis.

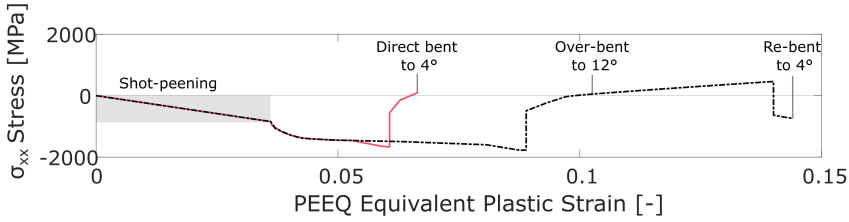

Figure 4.12 Simulations results with kinematic models showing the variation of the longitudinal stress with plastic strain in the element at the concave side of the rod for a direct bending (red curve) and an indirect bending (black dashed curve).

b. Processing parameters

Considering the processing parameters, the initial compressive stress upon shot-peening has a positive impact on the final surface stress level. The analysis of the effect of $\sigma_{xx}^{initial}/E$ demonstrates the efficiency of shot-peening even at locations that undergo subsequent plastic deformation. In addition to an initial compressive stress state, this process goes along with an initial yield surface shift due to local plastic deformation. It should be noticed that the initial magnitude of the compressive stress does not reveal the final compressive stress level after bending and springback. Depending on the parameter set, a certain amount of compressive stress should be intro-

duced during shot-peening in order to produce surface compressive stress after bending. The depth of the outer compression ring plays a negligible role on the intensity of the final stress level at the surface. The main advantage of increasing h/R is to reduce the stress level in the inner part of the rod. This could reduce the propagation rate of a potential fatigue crack.

c. Material selection

The stress level σ_{xx}^{final}/E significantly depends on σ_0/E, A/E and B. Material selection for biomedical implant aims at selecting materials with stiffness close to the one of bone. The flexibility is thus higher on parameters σ_0 and A than on E. Lowering the yield strength and keeping the same Young's modulus will decrease the stress level in the rod. The main reason for this effect is explained by the unloading of the rod after bending. By reducing σ_0, reverse plasticity is more easily produced. Considering hardening properties, Fig. 4.7b demonstrates that material exhibiting kinematic hardening develop a specific residual stress profile, with reduced residual stresses at the concave side of the rod. In their study, Berti et al. concluded that the (isotropic) hardening of elastoplastic materials reduces the amplitude of tensile residual stresses [70]. Our results indicate that kinematic hardening can improve residual stresses even more. According to Fig. 4.10a and Fig. 4.10b, the saturating value of the backstress (A/B ratio) should be large, and it should not be reached too quickly during bending process (thanks to a small B value). Such kinematic hardening induces a stress gradient in the bent rod and this promotes compressive residual stresses after unloading. This tends to be consistent with the conclusions of Berti et al [70]. From this sensitivity analysis, some recommendations for microstructural improvements can be formulated. Indeed, the yield stress and back stress are related to the grain size following respectively:

$$\sigma_0 = \sigma_p + \frac{k}{\sqrt{d}}, \tag{4.8}$$

$$\sigma_b = \frac{M\mu bn}{d}, \tag{4.9}$$

with σ_p the frictional stress resisting the motion of the gliding dislocation (so called Peierls stress), k the Hall-Petch constant, d the grain size, σ_b the backstress, M the Taylor factor, μ the shear modulus, b the magnitude of the Burger's vector and n the mean number of the dislocations in a pile-

up. These equations, combined with the results of the parametric analyses, suggest that the grain size has an antagonistic effect on the magnitude of the final residual stress. Indeed, Equation 4.8 indicates that an increase in grain size reduces the yield strength, which in turn reduces the residual stress in the growing rods. Conversely, Equation 4.9 shows that by increasing the grain size, the material will exhibit less backstress and therefore less kinematic hardening, which will increase the value of residual stress in growing rods. Based on these relationships, one could potentially determine an ideal grain size for each shot-peening intensity, an idea left for further investigations.

4.5.3 Limitations of the model and perspectives

As an additional possible contribution to the mechanical behavior, texture and mechanical anisotropy were not taken into account in our analysis. In their study, Everaerts et al. estimated the variation of the residual stress, for a Ti-6Al-4V bent bar, to be equal to 150 MPa depending on the orientations of the grains due to Young's modulus and Schmid factor fluctuations [87]. Another source of known anisotropy in titanium alloys is the α phase which presents for instance an asymmetry for $< c + a >$ slip between tension and compression [97]. These aspects were disregarded. Moreover, the possible development of a deformation texture during shaping process was not addressed but could be taken into account in the numerical model to produce more realistic results. The analysis considered only kinematic hardening, but some degree of isotropic hardening should also be ideally introduced which would modify at least quantitatively the prediction. We, however, think that the main shortcoming of our work is more the absence of anisotropy than of some minor isotropic strain hardening effect also in view of the low strain hardening capacity of Ti-6Al-4V. Understanding these effects may help further refining the material selection for growing rods. Regarding the model geometry, the tool used to simulate the bending process is based on the geometry of FB. Surgeons could potentially use other bending techniques, such as so called "in situ benders". In the literature, the analysis of the residual stresses resulting from various bending technique has already been performed assuming isotropic hardening [70, 98]. Nevertheless, the result of the parameter study in Section 4.4 tend to show that no first order effect is expected. But, maybe, the marking due to the contact with the bend tool could vary from one device to another and lead to specific local deleterious residual stress concentration not in-

vestigated here. Finally, residual stresses are not the only points of concern regarding the fatigue life of a system. In the literature, the impact of prestraining on the fatigue behavior has already been studied. Chiou & Yang 2012 found that prestraining is detrimental to fatigue lifetime for similar stress amplitude tests [99]. However, in the studies of Kang & al 2007 and Froustey & Lataillade 2008, the residual fatigue lifetime was not impacted in the same way based on the alloy considered [100, 101]. Therefore, the coupling of these numerical analyses with experimental fatigue tests on bent rods seems very promising to determine the impact of bending on fatigue life while having a deeper understanding of the residual stresses present in the rods before fatigue loading. The later contribution for growing rod is currently under investigation by running complex fatigue tests on bent rods.

4.6 Conclusions

This chapter proposed a new model for predicting the residual stresses in growing rods, identified and validated based on original experimental results generated with the FIB-DIC micro-ring method. On the basis of this model, parametric analyses have been carried out to identify the parameters that could play a major role in the objective of mitigating the residual stress level and, ideally, create compressive stresses. The main findings of the study are the following:

- Proper account of the kinematic hardening nature of the plastic behavior is essential to predict the local evolution of the residual stress profile in particular to capture the correct magnitude of the compressive stresses on both concave and convex sides of the rod after bending.
- The surgeon practice in terms of bending manipulation does not play a significant role on setting the final magnitude of the near surface residual stresses where fatigue initiates, but shot-peening does.
- In the context of the present findings, the best material choice is with low initial yield stress and higher kinematic hardening. Guidelines on microstructural modifications involve contradictory requirements. Materials with smaller grain size, higher mobile dislocation density and larger second phase particle, will exhibit more kinematic hardening but with a higher yield strength.

An attractive option for future research is to investigate multiphase alloys with large strength mismatch among the phase with one relatively soft phase, which will potentially combine low to moderate initial yield strength and significant kinematic hardening.

5

Fatigue testing of curved rods

The investigation of fatigue behavior of curved metallic elements should ideally be performed in the shaped configuration to avoid modification of the residual stress field. In this chapter, a novel setup which allows testing of curved profiles as loading tends to straighten the rod is designed, simulated, fabricated and validated

This chapter is being prepared for publication under the following title *Fatigue testing of curved rods*, Croonenborghs, M., Delannay, L., Bollen, X. Jacques, P. J. & Pardoen, T., (2024).

5.1 Introduction

Curved metallic elements can be produced by direct machining, molding, or 3D printing, with the net shape or frequently, by plastic deformation. In the latter case, complex residual stress profiles may be generated depending on prior manufacturing steps, e.g. shot-peening. The fatigue behavior of such curved rods should ideally be investigated in the shaped configuration to avoid modifying the residual stresses and microstructure if produced straight or if stretched to straight shape. Testing the component with the curved profile is essential, in particular to determine the fatigue response under conditions in which the loading either further bends or straightens the rod. Testing the second configuration is complex as the curved rod is in an unstable state and will tend to flip over under three point bending. Here, we propose, for the first time, a fatigue setup to test curved rods in the unstable straightening configuration.

The fatigue resistance of growing rods constitutes a challenging illustration of the importance of investigating the mechanical response in an unstable curved configuration. Growing rods consist in biomedical implants, used to correct spinal deformities in scoliotic children [57–59]. When the patient suffers from high deformities and still has a large growth potential, surgical intervention is considered. This solution consists in one or two rods, placed along the deformed spine to progressively straighten it back. During the initial surgery, the rods are bent by the surgeon, in order to adapt their shape to patient's spine morphology. The bent rods are then placed and fixed to the spine without any subsequent annealing process, giving the rods a complex and variable residual stress state. Unfortunately, these implants suffer from a high failure rate [72]. Post-mortem analyses of broken rods revealed that the failure process involved fatigue cracking. More precisely, a fatigue crack initiates at the concave side of a bent area and propagates towards its convex side [73, 81, 82, 102]. Hence, these bent rods typically fail due to a crack initiating at the concave side [80].

In order to increase the fatigue lifetime of growing rods, the surgeon's practices are investigated, and more precisely, the bending amplitude. To do so, an experimental scenario, consisting in fatigue tests performed on rods bent to different amplitudes was conceived. However, to reproduce the failure pattern as closely as possible, the crack must be forced to initiate at the concave side of the rod. By using a classical 3-pt bending test, the rod

would immediately flip into its stable configuration, causing the crack to initiate on the convex side. This constituted the motivation to work out a specific bending setup which could potentially be used for other applications.

The objective of this study is thus to design, simulate, fabricate and validate a novel 3-pt bending test setup that can maintain curved rods in the unstable position. The onset of plasticity was analyzed using finite element analyses. The force range at the yield point is significantly impacted by a pre-bending. An evaluation of the behavior of the setup under monotonic and cyclic loading was performed and supplemented by experimental tests comparing fatigue performances of straight and curved Ti-6Al-4V rods. Finally, the protocol for an experimental study dealing with fatigue life evaluation of a curved profile is discussed.

5.2 Design process

a. Statement of the general concept and working principles

To start the design process [103], the design requirement is stated as follows: *Create a setup to perform a fatigue bending test on a curved rod, applying tensile stresses at the concave side to promote unfolding* (see Fig. 5.1a). Subsequently, one needs to select a bending configuration among different options:

- The type of the support can be changed on each side of the rod (Fig. 5.1b), chosen among free end, roller support, hinged support, or fixed support (as clamping) (in the order of increasing number of degrees of freedom);
- For the loading conditions, one or several pointwise loads; a distributed load or a torque can be applied to the beam (Fig. 5.1b). These loads have two goals: to prevent rod from changing position (rotation) and to impose the fatigue loading.

b. Screening and embodiments

Various combinations of the above-mentioned options (illustrated in Fig. 5.1b) can be used to design a bending setup. The extra constraint in the selection was to be implementable in any mechanical testing lab, equipped with tension/compression uniaxial machines. Therefore, direct torque based designs were not kept. In the same way, distributed loads are com-

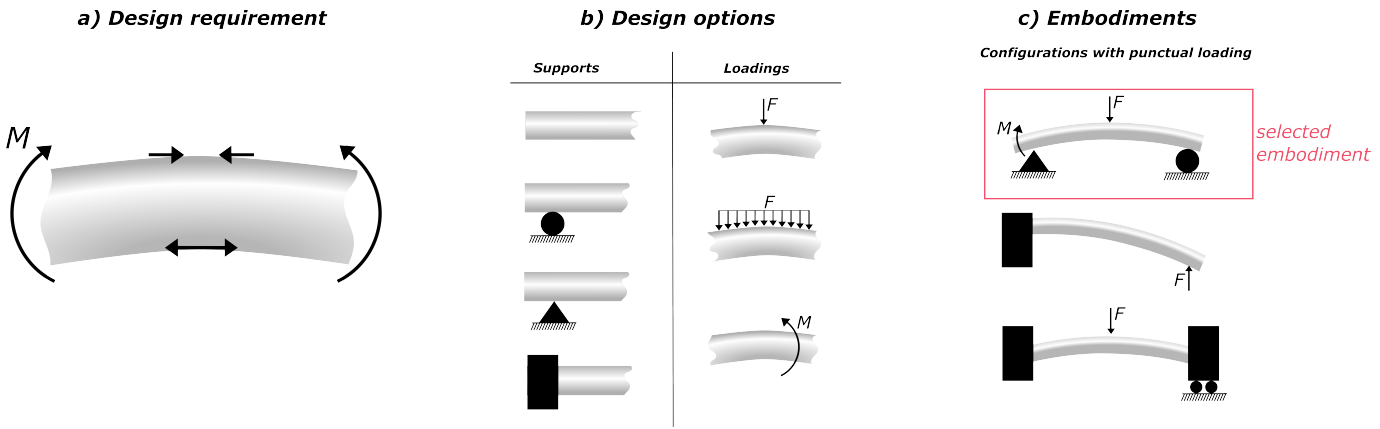

Figure 5.1 Design process illustration: (a) Illustration of the design requirement; (b) Illustration of several design options (supports + loading configuration); (c) Subselection of three embodiments which use pointwise loading as fatigue solicitation.

plex to set up due to the various possible geometries and curvatures. The choice was thus oriented towards a pointwise loading and, more precisely, towards a single load testing method.

Among all configuration designs, Figure 5.1c represents the subset which uses pointwise loading as fatigue load. Among the three configurations, two contain clamped boundary conditions. To keep the focus on the fatigue resistance at the maximum curvature location and not at the built-in terminations, it is desirable to avoid stress concentration away from the region of interest. The disadvantage of clamped boundary conditions is that they have a very high bending moment near the anchors. The final configuration is thus a three point bending test with a roller support on one side and a pinned support on the other side, assisted by a mobile torque that prevents the rod to rotate.

c. Details of the selected design

The final design needs to meet the following constraints:

1. Support the bent rod to prevent any rotation under loading;
2. Allow the vertical and angular motion of rod extremity during the test;
3. Prevent the horizontal translation of the rod.

In the final design shown in Fig. 5.2, the rod is held by a mandrel at one extremity (Fig. 5.2a), which prevents the rotation by keeping the rod position in the vertical plan with the convex side up. This mandrel is extended by a metallic pin, which is attached to a rotating axis (Fig 5.2b). Thanks to rotational degree of freedom, this axe is designed to be able to adapt to different angles. This assembly is attached to a plate (Fig. 5.2a) that slides along four metallic poles (Fig 5.2c). In order to adapt the height of the plate to each specimen, different sized adjustment studs can be placed around each pole (Fig. 5.2a). Springs are placed above and below the plate to allow its vertical motion during the fatigue test (Fig. 5.2d). Finally, the whole set-up can be moved horizontally on the bending bench before locking its position with two additional screws to keep the specimen in central position during the test with respect to the bench (Fig. 5.2d).

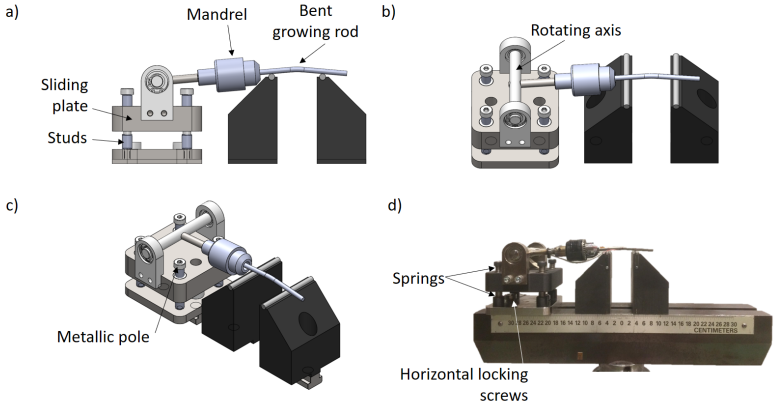

Figure 5.2 Detailed design of the fatigue set-up that maintains the rod in upward position during fatigue test. (a) lateral view of the virtual mode; (b) lateral diving-view; (c) isometric view and (d) lateral view of the set-up placed on the bottom flexion bench.

5.3 FE Model of a curved rod under loading

Finite element (FE) simulations are performed in order to anticipate the range of forces that must be applied on the curved rod to work below or at the yield stress level. In our advanced 3-point bending set-up, two factors are modified compared to a test on a straight bar: (i) the geometry of the sample and (ii) the mechanical history of the material. This model does not include the design of the presented setup (mandrel fixed to a moving platform). Instead, the rotation of the curved rod is prevented using boundary conditions. Stress and strain during fatigue loading for various bending angle are examined for our specific application. Although this application on growing rods addresses the case of bent rods of Ti-6Al-4V and a specific range of geometries and load levels, a more general approach will be proposed in the discussion to address the multiple configurations that this new setup makes possible.

5.3.1 Numerical model

J2 flow theory is selected to represent the plastic behavior using a Swift type hardening law extracted from a uniaxial tensile test (presented in Section 5.4.1):

$$\sigma_y = \sigma_0 \left(1 + \frac{\epsilon^p}{p_0}\right)^n, \tag{5.1}$$

where σ_0 is the initial yield stress, ϵ^p is the accumulated plastic strain, p_0 is a hardening parameter and n is the strain hardening exponent. The following values, corresponding to Ti-6Al-4V, were used: σ_0= 915 MPa, p_0= 0.3, and n = 0.07. Figure 5.3a is the stress-strain curve representation of the Swift model compared to the experimental uniaxial test. A fourth of a rod was represented, taking advantage of symmetries, accompanied by two sets of pins pairs, whose surfaces were assigned to rigid bodies. The first pair of pins, separated by 35 mm, were used to reproduce a bending procedure (Fig. 5.3b), while the second set of pins, separated by 20 mm, were chosen to replicate the fatigue bending configuration (Fig. 5.3c). The loading was controlled by pin angular motion in step 1, and vertical motion in step 2. The rod was discretized into 22 elements along its diameter and 33 elements along its axis (see Fig. 5.3d). C3D8R elements were used.

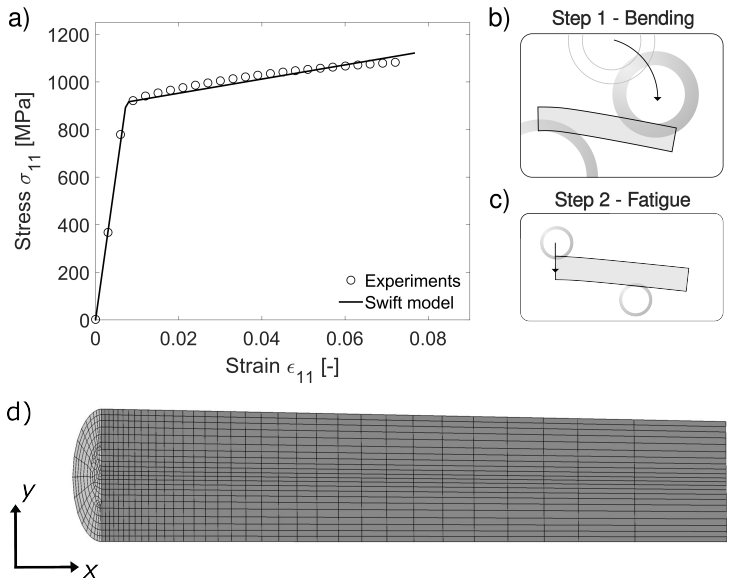

Figure 5.3 Numerical model: (a) isotropic hardening law compared to experimental uniaxial test; (b) first step - the bending process; (c) second step - 3-pt fatigue loading; (d) FE mesh in the 1/4 rod taking advantage of symmetries.

Different specimens were generated going from straight rod (0°) to the most bent rod (12°) by changing the rotational amplitude of the moving tool in first step. All the configurations were subsequently loaded with a 3-pt fatigue setup during the second step. The force during this step was recorded on the mobile pin while plastic strains ϵ^p, logarithmic strains ϵ, and internal stresses σ were extracted from the element opposite the moving tool in the fatigue step, i.e. the crack initiation site.

5.3.2 Strain life or stress life approach

Stress life methods are usually selected when structures are loaded in the elastic regime, meaning no plastic deformation occurs in the structure except for the area ahead from the crack tip. In that case, if all samples have the same dimensions, an identical force level is used for all tests of similar stress level. In the case where the loading generates a combination of elastic and plastic strains, the strain-life method is more appropriate and strain gauges or an extensometer are then needed [33].

Figure 5.4a illustrates the accumulated plastic strain ϵ^p with respect to the force applied during step 2 normalized by the force applied to the straight rod at yield ($F/F_0^{straight}$). The force after yielding continues to increase in the straight rod due to strain hardening. Compared to a straight rod, all the bent rods exhibit a force at yielding (F_0) between 0% and 25% of $F_0^{straight}$. The decrease by $F_0/F_0^{straight}$ with increasing angle is illustrated in Figure 5.4b, along with the difference between the von Mises stress σ_{Mises} after bending step and the current yield stress σ_y normalized by the same difference for the straight rod:

$$\frac{\Delta\sigma}{\Delta\sigma^{straight}} = \frac{\sigma_y - \sigma_{Mises}}{\sigma_y^{straight} - \sigma_{Mises}^{straight}}. \tag{5.2}$$

As the straight rod has not been strain hardened during a bending procedure, its yield stress is still equal to the initial yield stress ($\sigma_y^{straight} = \sigma_0$), and the rod has no residual stress ($\sigma_{Mises}^{straight} = 0$). Equation 5.2 becomes

$$\frac{\Delta\sigma}{\Delta\sigma^{straight}} = \frac{\sigma_y - \sigma_{Mises}}{\sigma_0}. \tag{5.3}$$

This stress ratio is in the same order of magnitude as the force ratio, and

exhibits a similar trend with the bending angle. Indeed, comparing stress difference to each other is a good indicator of what force increment will be needed to enter plasticity.

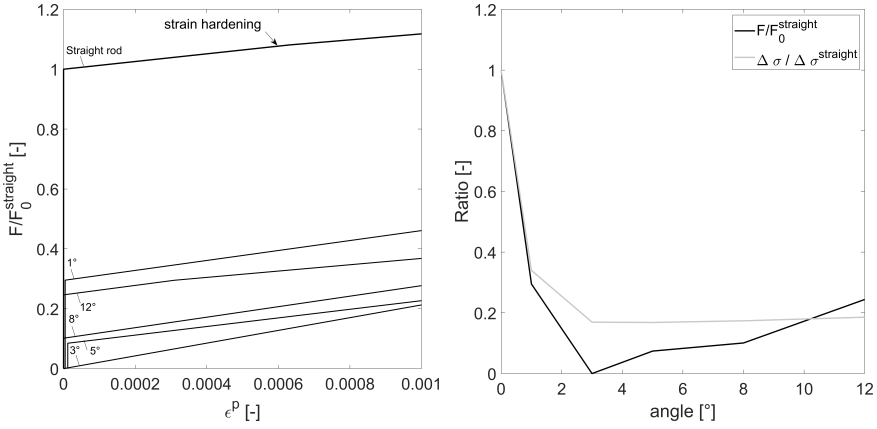

(a) (b)

Figure 5.4 (a) Variation of force during second step (fatigue loading) with respect to the plastic strain for various bent rods, normalized by the force at yield of the straight rod; (b) superposition of the ratios of the force at yield with respect to the one of the straight rods and stress difference between residual stress and elastic limit for each angle, with respect to the straight one.

Figure 5.4 shows that when the samples are bent, they cannot be tested at the same force level than a straight rod, while being in the elastic domain. Therefore, the most suitable approach here would be a strain-life approach fatigue test. However, for the sake of demonstration, a few tests with the stress-life approach were also performed (as explained in Section 5.4.2).

5.4 Validation and experimental results

5.4.1 Materials

Rods of Ti-6Al-4V alloy (same grade as the rods used in growing rod surgeries) with 6.0 mm diameter were purchased from Salomon's Metalen B.V. in the Netherlands. Cylindrical tensile specimens were extracted with a diameter of 4 mm. Tensile tests were carried out with a displacement rate set to 1 mm/min until fracture on a Zwick Roell stress rig. From the uni-

axial tension response, the following properties were determined: Young's modulus E=124 $\pm$ 8 GPa; yield stress $\sigma_{0.2\%}$= 914 $\pm$ 3 MPa; and ultimate tensile strength (eng) σ_{UTS}= 1006 $\pm$ 2 MPa.

Fifteen samples of 10 cm length were cut, machined to 5.5mm diameter using turning technique, and nine of them were bent to obtain various angles between 2° and 12°. Contouring angles were measured after elastic springback, using a profile projector (Mitutoyo PJ 300, Illinois, USA).

5.4.2 Methods

The 3-pt flexural bench was installed with the new setup in a tensile device (MTS servohydraulic Bionix 25 kN) with the two external points of the bench spaced by 40 mm. In addition to the existing instrumentation, two sensors have been added. Figure 5.5a illustrates the positioning of these sensors with respect to the setup to determine the local behavior in monotonic and cyclic loadings. The former is a laser attached to the rigid frame, as illustrated in Figure 5.5b, to track the vertical motion of the black deck during cyclic solicitations. The goal of this measurement is to control the possible appearance of resonance, which may originate from the presence of the spring in the setup. The second sensor is directly placed on the tested sample, at the concave side of the rod, i.e. the crack initiation site, as shown in Figure 5.5c. It consists in a deformation gauge, aligned with the rod axis, used to measure the longitudinal extension upon loading. The gauges are bound using MBond 200 cyanoacrylate glue.

For validation during monotonic loadings, the force was ramped to 1470 N in 60 seconds, which corresponds to a maximum stress equal to 90% of the yield stress of a straight rod. The loading was imposed 3 times successively, going down to -50 N in between. For cyclic loading conditions, an instruction force of 1470 N was set, and frequencies of 1, 2, 5 and 10 Hz have been tested with an R ratio of 0.1.

After the setup validation, the fatigue resistance of straight and bent titanium rods was investigated. As explained in Section 5.3.2, rods tested in this study exhibit some variability in the yield stress, and so a constant strain based fatigue condition is more relevant. In this experimental campaign, four straight rods are compared to four bent rods at an imposed strain level of 0.011. All tests were conducted until sample failure or up to a total 3,000,000 cycles. The temperature of the test room was controlled to 23°C. Moreover, as the goal of this study is to demonstrate the working ca-

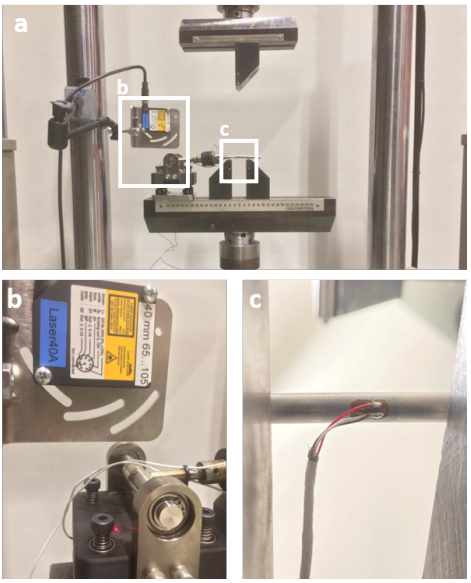

Figure 5.5 (a) Setup with two sensors: (b) Laser sensor to measure deck vertical motion and (c) Strain gauge placed at the concave position on the rod.

pacity of the setup, seven additional samples (two straight and five bent) have been tested under iso-force configuration with a force level of 1470 N. Table 5.1 lists the samples tested. The goal of these two experimental campaigns is not to perform a definitive analysis on the influence of the bending angle in the context of growing rods but to extract first order key effects. Fractography analyses of broken rods were taken with Keyence VHX-7000 3D microscope using 3D mapping.

Table 5.1 Summary of the geometries tested in fatigue.

Strain-controlled	
Straight	*Bent*
0°	2°
0°	6°
0°	11°
0°	13°

Force-controlled	
Straight	*Bent*
0°	3°
0°	6°
	8°
	10°
	13°

5.4.3 Validation for monotonic loading

Apparent yielding

Figure 5.6 shows the force as a function of the strain upon first loading. As predicted by the numerical model in Figure 5.4a, the strain gauge measurements show significant variation of the force corresponding to the onset of plastic yielding between straight and bent rods. As expected, for the 0° rod, the behavior is linear throughout the loading process between the applied force and the recorded strain by the strain gauge. Meanwhile, for the same loading path, the inner strains in the pre-bent rods deviate from linearity relatively early in the course of loading. This indicates that the pre-bent rods enter plasticity earlier and, therefore, the fatigue properties will be significantly different under force-controlled loading if there is no systematic load adjustment so that similar stress levels are imposed for comparison.

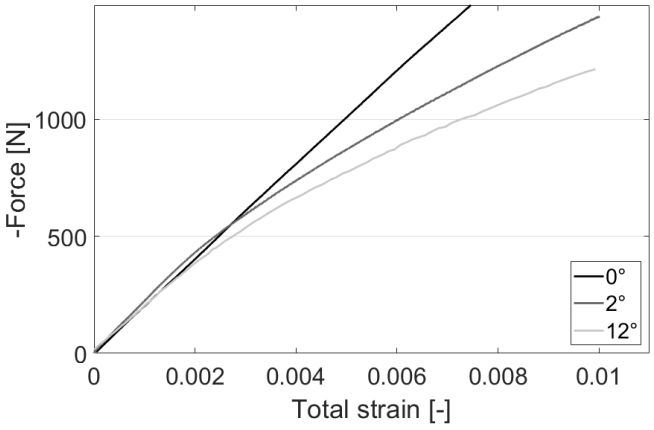

Figure 5.6 Experimental strain measurements at the inner side of the rod for the first loading for a straight rod and two rods bent at 2° and 12°.

Asymmetry assessment

As explained in Section 5.2c, the height of the platform is adjusted by means of studs of varying thicknesses to adapt to the different geometries of bent rods (see Fig. 5.2d). The aim is to place the rod in a neutral position, i.e. the rod touches both supports of the flexion bench at the same time. However, the combination of the available stud thicknesses does not allow to always exactly find this position, resulting in a slightly left or

right-side elevated position as shown in Figure 5.7. Before starting the fatigue test, a quick optical verification is performed to determine if the rod touches both supports or if it is elevated on either side. To evaluate if a small initial asymmetric configuration can potentially lead to major variations during the test, a deliberate gap was left before one of the monotonic loading tests. The angle difference ($|\alpha_{right} - \alpha_{left}|$) was bounded for each rod as presented in Table 5.2.

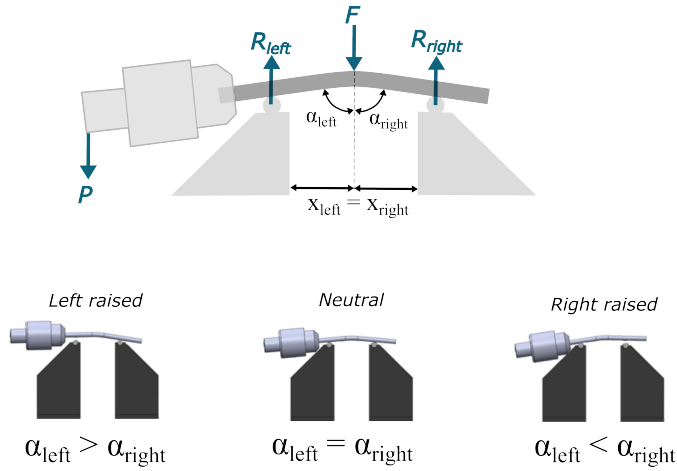

Figure 5.7 Definition of the asymmetries in rod position before fatigue loading.

Table 5.2 Angle asymmetry for a straight rod and two rods bent at 7° and 12°.

Rod bending angle	Angle misalignment boundaries $\lvert\alpha_{right} - \alpha_{left}\rvert$
0°	~0.1°
7°	[0.8° - 1.3°]
12°	[0.8° - 1.2°]

We evaluated the relative error on the deformation of the inner fiber (ϵ_i), at a constant force of 1470 N, for a straight rod and two rods bent at 7° and 12°, for the elevated configuration as compared to the neutral one. For each asymmetric position, the relative error on the attained deformation relative to the neutral configuration, of the same bending angle, is computed as follows:

$$RE = \frac{\epsilon_{\theta,neutral} - \epsilon_{\theta,elevated}}{\epsilon_{\theta,neutral}} \tag{5.4}$$

The relative absolute errors for each bending angle and for the two elevated configurations are given in Table 5.3. The maximum relative error on the strain variation associated with an asymmetric initial configuration is equal to 6% when a force equal to 1470 N is applied. Therefore, if the samples are placed with sufficient attention, the effect of an initial misalignment will be limited to values well below this level of 6%, say typically 2-3%.

Table 5.3 Relative error on the strain amplitude for an initial asymmetric position and three different bending angles.

Rod bending angle	Left-raised relative error	Right-raised relative error
0°	1%	3%
7°	6%	1%
12°	4%	2%

5.4.4 Validation for cyclic loading

A first cyclic test was run at 10 Hz with a thermocouple located on the concave side of the rod to control the absence of significant increase in temperature ($\Delta T < 5°C$).

The effect of the dead weight entering the fixture system on the dynamic of the system was determined to find the window in which the device can operate in a reliable manner. An evaluation of the vertical displacement of the deck during cyclic loading for four frequencies has been performed to find the optimum loading frequency. To compare the four tests, the force and displacement signals at 1 Hz have been normalized to - 1 for the lowest force (-1450 N) and position, and +1 for the highest force (-180 N) and position. The same normalizing factors are then used for all signals. Figure 5.8 illustrates the normalized signals for each frequency. The curves for 2 Hz show that the signals stay in the same boundaries as those recorded in the reference test. At 5 Hz, the displacement is overshooting at the lowest position by 13% compared to the 1 Hz reference. At 10 Hz, the displacement overshoots by 23% at the highest position and by 25% at the lowest position. This last result suggests that a resonance phenomenon is taking

place as the overshoot is observed at both low and high positions. The test cannot be carried out properly under controlled conditions at such higher frequencies.

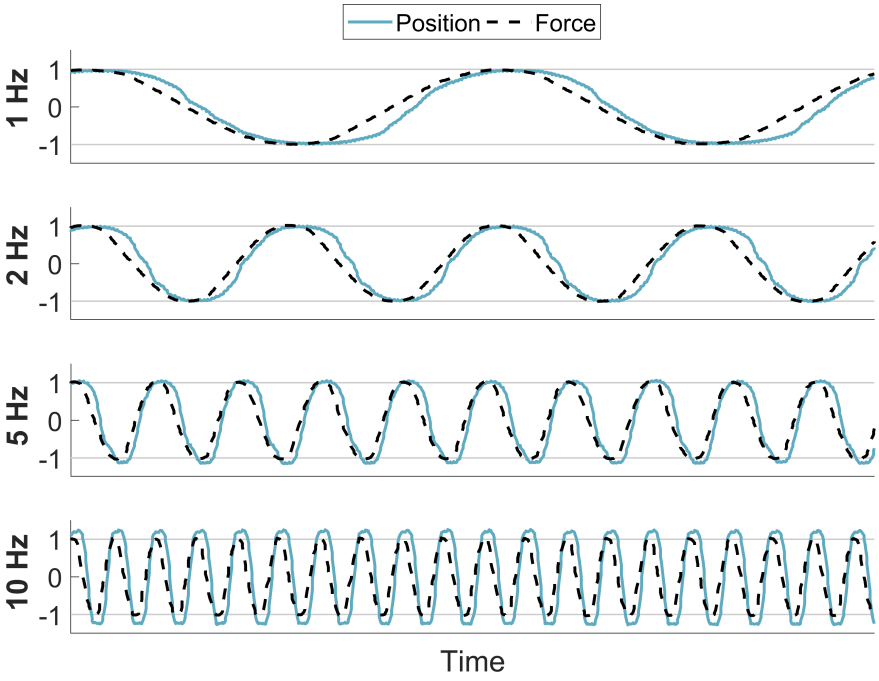

Figure 5.8 Variation of the force and of the vertical displacement of the deck as a function of time for fatigue tests performed at 1, 2, 5 and 10 Hz. The signals are normalized based on the measurements made for 1 Hz condition.

A test in three phases was performed to assess the strain gauge measurements as depicted in Figure 5.9a. The first phase was composed of three monotonic loadings up to 0.009 strain level. As rods can enter plasticity during the first cycle, the maximum force of the second cycle was recorded (F_1). The second phase of the test involved 1000 cycles at 5 Hz, up to a force level F_1. Finally, a third phase was performed during which three more monotonic loading cycles were imposed still at the same stress level.

As soon as the test enters a cyclic loading regime (Phase 2 in Figure 5.9b), the measurement made by the strain gauge deviates from the measurements made during the monotonic loading phases (Phases 1 and 3). There-

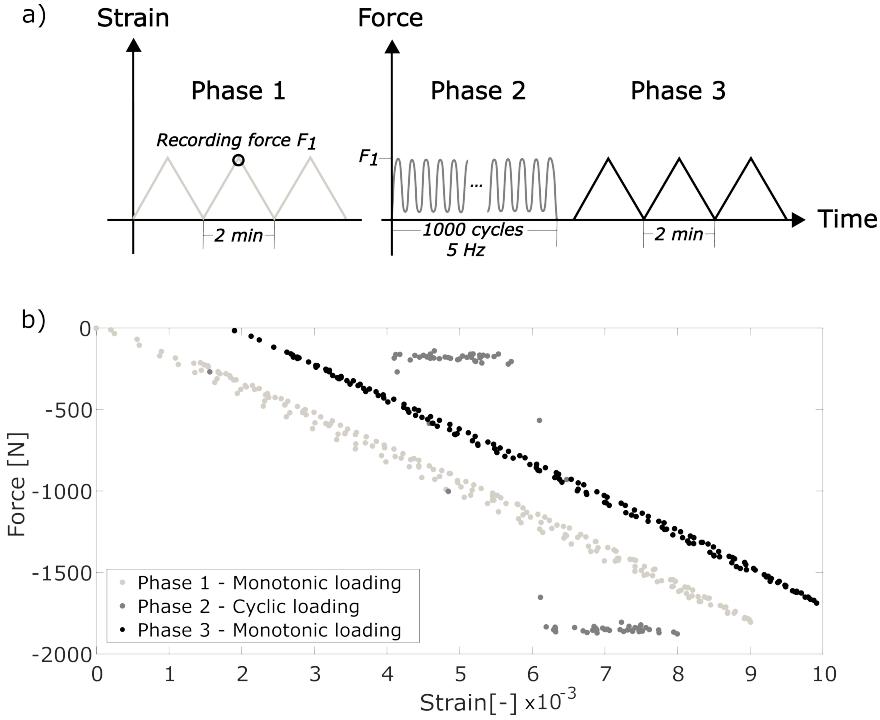

Figure 5.9 Strain measurements during monotonic loading phases separated by a cyclic loading phase.

fore, the values measured during a cyclic loading are not valid and a force control is preferred based on the force measured during the second monotonic loading (Phase 1). However, the progressive strain shift recorded during this fatigue phase is representative of a real ratcheting effect, which is detected when comparing strain measurement of the two monotonic loading phases.

5.4.5 Fatigue test campaign on bent Ti rods

The number of cycles at failure obtained with both the strain and force-controlled protocols are shown in Figure 5.10 for the 15 samples comparing the two categories of geometries: straight and bent rods. The specimens which did not fail after 3,000,000 cycles are indicated with a full symbol, while empty symbols represent tests which lead to fracture.

The experimental results for the iso-strain protocol show an increase in fatigue life when rods are bent. Indeed, three straight rods over four failed at around 80,000 cycles, while all the four bent rods went through the 3,000,000 cycles without fracture. In the force-controlled experiments, the opposite trend is found: four bent rods over five tend to fail at around 50,000 cycles, while two straight rods underwent 3,000,000 cycles without failure.

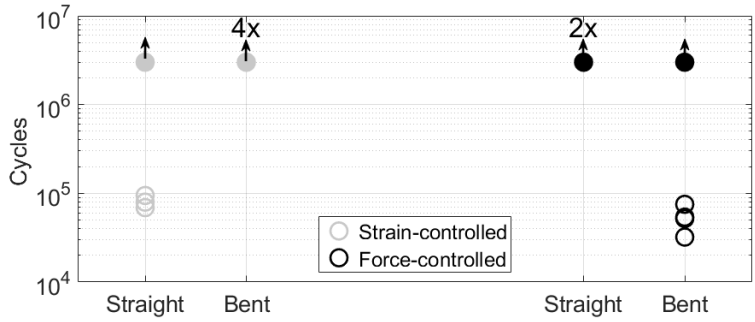

Figure 5.10 Number of cycles at failure for various bending angles of Ti-6Al-4V bent rods at (grey) 0.011 imposed strain tests (black) or a 1470 N imposed force. The empty symbols depict failure by fatigue while the full ones represent a run-out.

The fractographies of all broken bent and straight specimens, shown in Figure 5.11, revealed the same features on the fracture surfaces. Cracking initiates by surface crack nucleation at the concave side (i.e. lower part in Figure 5.11). Then multiple striations can be observed in the bottom half of the sample, which are progressively getting more dimpled in the next half disk. Finally, shear lips appear at the last stage and a slant mode can be observed at the periphery.

It should be mentioned that the only problem noticed during the experimental tests is the gauge detachment after a few thousand cycles.

5.5 Discussion

In the following, the terminology *bent* will be used for a rod which developed a residual stress field prior to fatigue testing, while the term *curved* will refer to profiles with no residual stresses.

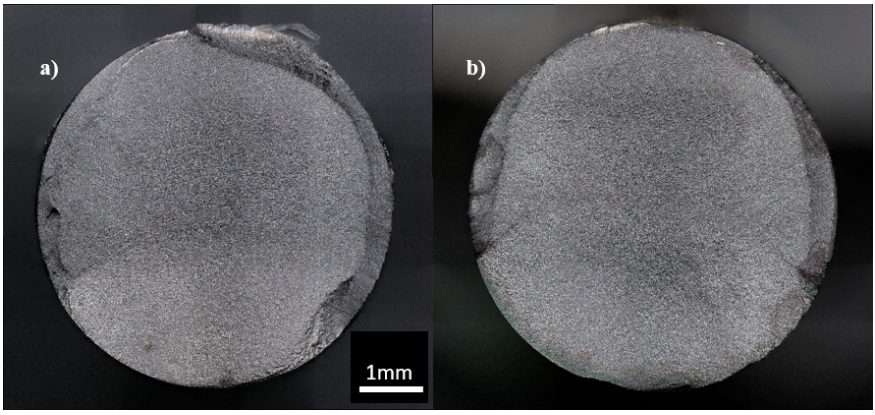

Figure 5.11 Fractographies for (a) 0° straight rod and (b) 12° bent rod having being tested with setup. Initiation sites are located on the lower part of both pictures.

The first key point is that the set-up proposed in this study is working properly, as it maintains the rod in its unstable position under both monotonic or cyclic loading. From asymmetry assessment, it was concluded that if the sample is introduced in the loading set-up with sufficient attention, the strain variation due to an initial misalignment is certainly smaller than 6%. The numerical model along with gauge measurements indicate that bent rods enter plasticity at lower forces compared to a straight rod. The measurements at 10 Hz indicate that the displacement of the platform is larger than at lower frequencies. This difference, typical of a resonance effect, is likely due to the presence of springs at the top and bottom of the platform. To keep a test duration time reasonable, a frequency of 5 Hz is suggested. The strain gauge, located at the crack initiation site, gives an indication on strain ratcheting during cyclic loading as long as it is correctly bonded to the surface. For a precise strain measurement, the loading rate should be low enough.

Bent rods, on top of the geometrical variation compared to a straight rod, show significantly different residual stress fields related to plastic deformation as a result of the contouring. In a previous study on growing Ti rods, the residual stress evolution with bending angle have been extensively studied, with various hardening types and pre-processing steps such as shot-peening [80]. It was shown that the prediction of the residual stress is complex and that the amplitude of the stress field generated by the bend-

ing is not negligible. The FE model presented in this study predicts that bent rods enter plasticity at a lower force level compared to straight rods. When Ti rods are tested at a similar force level, straight rods show higher fatigue resistance than the bent rods, which is coherent with the higher yield strength. On the other hand, the strain-controlled protocol show an opposite trend, where straight rods have a lower fatigue resistance than bent rods. Therefore, depending on the way rods are solicited during their application, the bending procedure can enhance or decrease their fatigue lifetime. While the context of growing rods justifies the need for such set-up, these experimental results demonstrate the importance of the selected test protocol.

The choice of testing protocol depends on the specimen type and its application field. By running an additional FE simulation to look at curved rods, i.e a rod having identical geometry to the bent rod but with its material properties and stress field reset to zero after the bending operation, the stress strain curve of straight rod is almost recovered as illustrated in Figure 5.12. It is therefore the bending procedure, and the associated residual stresses, that have the largest influence on the mechanical response of a bent bar and this will influence the choice of the test protocol.

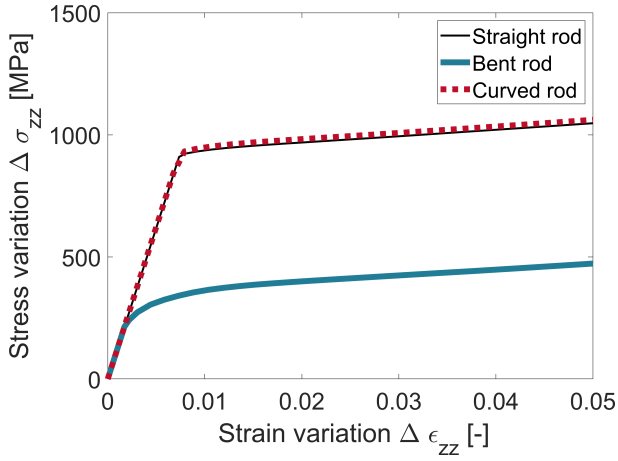

Figure 5.12 Representation of the variation of the stress change as a function of the strain change for three rods (reference step set at the beginning of fatigue loading): (black) a straight rod (gray full line) a bent rod with residual stresses due to bending (gray dashed line) and a curved rod with the same geometrical profile than the bent rod, but residual stress are reset.

Depending on the context under study, various protocols may be suggested:

(i) **Force-controlled:** For curved rods with the same cross-section area and shape (e.g. same moment of inertia), applying an identical force level for all samples correspond to a stress-life approach. The stress can be easily determined using beam theory for a straight rod. This protocol can be used to create angle-dependent S-N curves.

(ii) **Internal stress-controlled:** This method is meaningful only for curved rods. It suggests a complete and accurate characterization of the material hardening law, as well as the bending and fatigue tool geometries. By performing finite element simulations, an inverse approach can be achieved, in which each angle is correlated to a force level that will give the desired final stress level. Although this method is not representative of what happens in a real applications, it can be used in experimental protocols, in which each parameter must be decorrelated from the other. The result is also an angle-dependent S-N curve.

(iii) **Strain-controlled:** A strain-life approach can be applied but it requires using a strain gauge. It is particularly useful to test bent rods without the necessity to systematically run numerical simulations. In this way, angle dependent ϵ-N curves can be obtained. The use of strain gauges comes with several recommendations. At first, the placement of gauge on double curved profiles is a challenging process. We recommend to cut the four corners to limit its detachment. Moreover, as illustrated in Fig. 5.9, the strain measurement is not relevant during cyclic loading tests. This can be due to a phase offset between the force signal and the strain gauge signal, added with the possible presence of a damping filter. Finally, gauge overloading or detachment can make the measurement impossible after a few thousand of cycles. Here we suggested to overcome these problems by using the force measured during a monotonic strain controlled loading. However, one could think about other solutions to control the complete test with strain gauges.

5.6 Conclusion

A new setup has been proposed to evaluate fatigue properties of curved and bent rods under an unstable loading configuration that tend to reduce the curvature. Thanks to this setup, it is possible to initiate a crack at the concave part of the rod. The setup has been evaluated with monotonic and cyclic loading conditions and a numerical study has given additional information to decide on the selected protocol. The main conclusion are the following:

- The setup allows maintaining the rods in the unstable position during the test and a frequency of 5 Hz can be reached without resonance effect.
- Due to prior bending process, the bent rods cannot be subjected to an identical internal stress if a constant load is used for different bending angles.
- The testing protocol should be defined based on the residual stress state in the specimens.
- A numerical model should be developed for any protocol based on internal stress control. This requires having a good knowledge of the material's hardening behavior.

The developed fatigue device also makes it possible to study more fundamental questions, for example, by comparing materials with different hardening modes, since their respective strain-hardening mechanisms could lead to variations in fatigue strength. It could also be used to assess whether the choice of a material with high mechanical strength or high ductility would be more suited for the fatigue life of bent rods.

6

On the mitigation of fatigue failure in growing rods through plastic deformation

THIS chapter concludes the investigation on growing rods by performing fatigue tests on bent rods. The goal is to distinguish the major and minor parameters influencing the fatigue life of the rods among bending angle, shot-peening process, and the loading configuration.

This chapter is being prepared for publication under the following title *On the mitigation of fatigue failure in growing rods with plastic deformation*, Croonenborghs, M., Delannay, L., Ismail, K., Mousny, M., Jacques, P. J. & Pardoen, T., (2024).

6.1 Context

Scoliosis is an abnormal three-dimensional deformation of the vertebral column with an angle larger than 10° in the frontal plane. When scoliosis develops during childhood, it leads to severe growth troubles such as improper lung development. Therefore, a surgical intervention is needed to correct the scoliosis while allowing the growth of the child. Among other techniques, growing rods consist into inserting one or two cylindrical rods along the spine and fixing it with hooks and screws, during a very invasive surgery.

These rods come in several sizes and materials that the surgeon will have to select according to the patient's profile (see Figure 6.1a). During the manufacturing process, metallic rods are usually shot-peened in order to increase the residual compressive stresses at the rod periphery (see Figure 6.1b). This stress profile is modified subsequently as the surgeons bend the rods during implantation surgery to fit natural lordosis of the patient (see Figure 6.1c). The rods are then fixed to the patient and, as they try to correct the spinal deformation, some forces are present at the anchorages (see Figure 6.1d). After the operation, the young patient can continue with an active lifestyle, which will introduce cyclical stresses into the rod (see Figure 6.1e). Unfortunately, a common issue in the use of growing rods is fatigue failure. If such event occurs, a full new invasive surgery is needed to perform rod replacement.

The factors that dictate fatigue performance can be classified in four categories (Fig. 6.2). They comprise (i) material properties, (ii) surface conditions, (iii) environmental conditions, and (iv) loading conditions. In each of these categories, multiple aspects can have beneficial or detrimental impact on the durability [104]. In the following we will discuss each of these possible effects in the context of growing rods and more precisely of rods made of the alloy Ti-6Al-4V, widely used for this application. The two first categories can be related to the choice of the material made by the surgeon and to the surgical practices, as bending is an inevitable step during implantation surgery. The two last categories are related to the lifetime of the rod once placed in the child's back.

Material selection, from the choice of the composition to the processing parameters, will have an impact on the fatigue performance of the structure (Fig. 6.2a). In biomedical implants, the stiffness is a first key design factor.

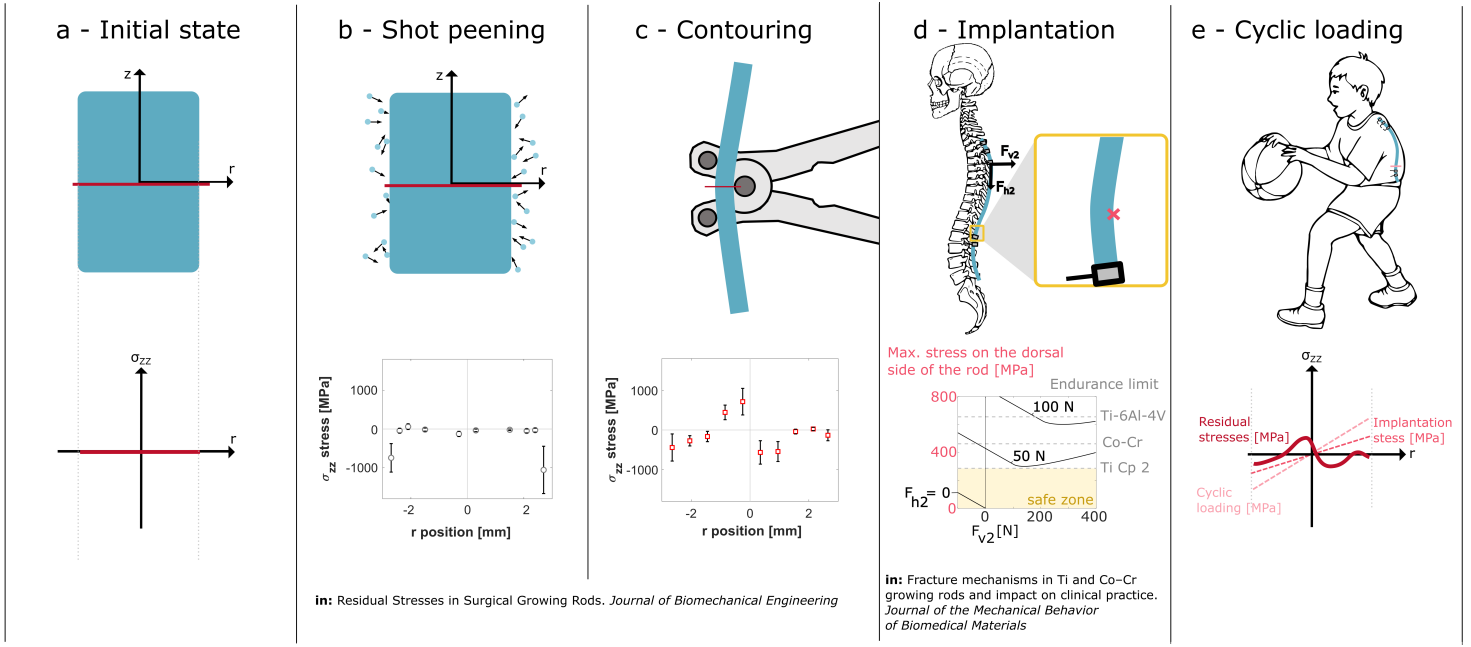

Figure 6.1 Illustration of the residual stress states at each stage in growing rods: (a) the initial state is a material without residual stresses; (b) the metallic rods are usually shot-peened, introducing compressive stresses at rod periphery as measured by the study from Croonenborghs et al. [80]; (c) during contouring process, the stress field changes and become more complex as measured by the study from Croonenborghs et al. [80]; (d) implantation results in forces acting on anchorages and a static stress added to the rod. The study of Ribesse et al. [82] evaluates the maximum stress in the rod after implantation; (e) patient everyday movements introduce cyclic loading which add to residual stress from steps b, c and d.

A too large stiffness mismatch between the implant and the bone favors implant failures [13]. Titanium alloys are the metals with the closest match to bone stiffness. In search of the optimum fatigue resistance, it is preferred to select materials with a high ultimate tensile strength and large ductility [104]. In the context of growing rods, it is important to mention that by bending the rod, the surgeon potentially decreases its remaining ductility before the fatigue solicitations starts. In structural applications and materials in which the crack growth stage constitutes an important part of the fatigue process (with respect to the initiation stage), the fracture toughness plays also an important role on the durability. The cleanness of the material in terms of second phase inclusions is a necessity, to reduce strain concentrators (more important for high cycle fatigue). Finally, if creep is not an issue, a finer grain size is associated to more grain boundaries, acting as crack arrestors, which is beneficial for fatigue performances.

Surface conditions are usually very much dictated by the processing steps (Fig. 6.2b). As fatigue cracks usually initiate from the surface, the roughness of the product is of significant importance. A smoother surface provides larger fatigue resistance, especially for titanium alloys which are particularly notch sensitive [105]. Residual stresses just below the surface are beneficial when being compressive to delay crack initiation. In the case of growing rods, a previous study from Croonenborghs et al. indicated that rods are shot-peened to introduce a compressive residual stress at its periphery [80]. The plastic deformation induced by the bending applied by the surgeon modifies the residual stress profile while the tool leaves marks on the surface. These marks can decrease the fatigue performances as they can act as stress concentrators.

Environmental conditions, like humidity, temperature, corrosive media, are known to have an important influence on fatigue (Fig. 6.2c). The growing rods are surrounded by body fluids, with corrosive impact. This is why titanium based materials are usually used for biomedical applications. By creating a passivation oxide layer, titanium based rods are initially protected from corrosion [106]. However, if cracks propagate through this layer, the corrosive environment can lead to an acceleration of fatigue crack propagation [107]. Elevated temperatures change fatigue performances, but growing rods are maintained at constant temperature inside the human body. It is therefore not a key parameter in this research domain.

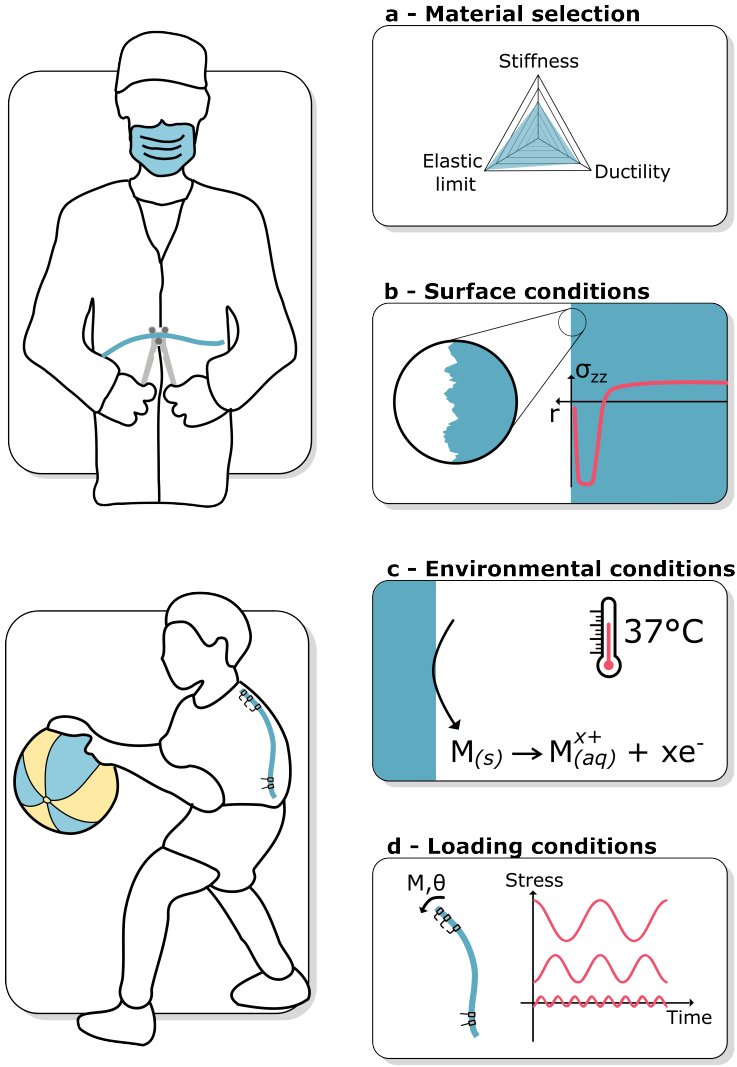

Figure 6.2 Determining factors on fatigue performance of growing rods: (a) selection of material and its microstructure influence structural properties; (b) surface conditions as roughness and residual stress profile ; (c) environmental conditions as corrosion and temperature; (d) loading conditions as frequency or mean stress.

Loading conditions can be characterized by multiple parameters such as the stress or strain-controlled frequency, R ratio, mean stress or overloads oc-

currence (Fig. 6.2d) [108]. The mean stress and the amplitude of these solicitations in growing rods are not well characterized in the current literature. Chronologically, implantation surgery modifies the residual stress state inside the rods due to anchoring, and then the rod is loaded during everyday life activities of the child. Growing rods are probably controlled by a mixed loading, moment-imposed (in N.m) or bending-imposed (in cm) depending on the task, as suggested by of Ribesse et al. [82]. In this work, the forces acting in the rod after implantation were estimated owing an analytical beam-bending model. Waugh investigated the force variations by intravital measurements and observed large variations during involuntary movements as coughing and vomiting with respectively 206% and 490% of increase [109]. From average lifetime of in vivo broken rods and number of cycles reached during 3-point bending test, Ribesse et al. derived a theoretical frequency of 1 solicitation every 3 minutes to explain the experimental data [82].

The in-depth study, by X-ray and fractography, of growing rods fractured after spinal instrumentation surgery by Ribesse et al. identified the common characteristics of the failure events. Based on seven post mortem analyses, their study revealed that the crack propagates from the dorsal side to the ventral side and is usually located in the thoracolumbar junction [82]. In this area, rods are commonly bent to fit the natural lordosis of the patient (see Fig. 6.3), leading to the conclusion that, in the majority of failures, the crack propagates from the concave side of the bar to the convex side. It is therefore important to know how the bending process, influences the fatigue resistance.

The impact of the bending process has already been much scrutinized in the literature. At first, as shown in the research of Demura et al. the bending process modify the apparent rigidity and the apparent elastic limit of the structure [68]. These apparent properties decrease with increasing angle, in unfolding configuration. This indicates that two rods with different profiles subjected to the same loading conditions will not give the same answer and therefore, their stress solicitations can be variable due to geometry. The fatigue performance of growing rods after bending have been discussed in studies since 2001 [69, 74, 76, 110], and remains a concern [70, 75, 82]. Lindsey et al. and Slivka et al., compared the fatigue resistance of straight rods with a unique bent geometry, respectively 13°-15 bending and 50 ± 10 mm radius of curvature. In the two studies they concluded that contouring reduced the fatigue life of rods made of Ti-6Al-4V, CP Ti and

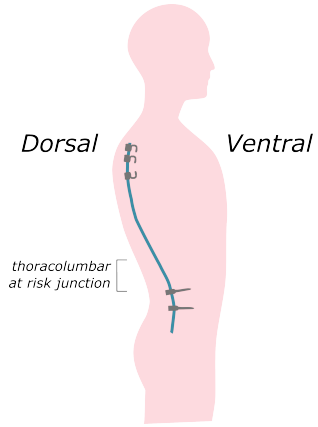

Figure 6.3 Schematic representation of the area with the largest risk of failure. The crack propagates from the dorsal to the ventral zone, i.e. the crack initiates on the concave side of the bend and propagates towards the convex side.

316L by testing their resistance using a lumbar vertebrectomy construct [69, 74]. In another study, Dick et al analyzed in more details the use of a French bender tool. This tool, in addition to the angle modification, introduces also marks on the surface of the rods. To evaluate the effect of these marks decoupled from the angle modification, they introduced rods into a French bender and applied a minimal force to mark the rod without noticeably bending it. They observed a reduced life on these samples compared to straight rods [76].

During EOS surgeries, bending process is limited by the tool amplitude. As a reference, the French bender achieves approximately 15° maximum amplitude in one-step. Nevertheless, larger corrections can be achieved with multiple bends. In a study by Tang et al., about pedicle subtraction osteotomy, fatigue tests on 20-, 40- and 60-degree bent rods were performed with two force levels. Compared to the 20-degree bent rods, the fatigue performances of the 40 and 60-degree bent rods were found to be significantly lower [111]. In a more recent study, Piovesan et al. compared the fatigue life of contoured rods subsequently solicited in lordosis or in kyphosis. The rods solicited in lordosis have a lower fatigue resistance and this was confirmed by numerical simulations [75]. Finally, a recent study established the evolution of residual stresses after shot-peening and bending.

The *largest shift* in residual stress occurs in the early-first degree imposed during bending. The stress level then tends to level of for all angles up to 15 degrees [80].

All these studies have two common elements: (i) the comparison is made between two configurations (straight and bent) without a continuous spectrum of bending angle and (ii) the comparisons are made at a similar loading level.

In this study, we are broadly interested by the impact of plastic deformation, associated to shot-peening and bending, on the implant lifetime as a result of a cyclic fatigue-type solicitation. These two steps modify the local state of hardening, residual stress and surface conditions. The impact on fatigue lifetime is the result of multiple effects that are addressed here. We first developed a new fatigue set-up that matches as closely as possible the realistic loading conditions and that leads to failure mechanisms closely reproducing the fractographic observations made on in-vivo broken growing rods. The experimental parameters were varied in order to choose a protocol that distinguishes between the primary and secondary parameters influencing the fatigue life of the rods. This set-up is then used to evaluate how the bending performed by the surgeon has a detrimental effect on the fatigue performances. As bending induces plastic deformation, a comparison between shot-peened rods with not shot-peened rods was found relevant as well. The final objective is to provide guidelines to surgeons on their bending practices as well as recommendations on material processing. The importance of the choice of experimental protocol on fatigue life will also be addressed.

6.2 Materials and methods

6.2.1 Materials

In vivo rods

The rod used for fractography analysis is a 5.5 mm diameter rod made from Ti-6Al-4V alloy placed in a 8 years old male patient. The rod lasted 253 days before in-vivo failure. The X-ray after rod failure is presented in Figure 6.4. The same rod has already been analyzed in the study of Ribesse et al. under the denomination of Patient 3 – Rod 2 [82].

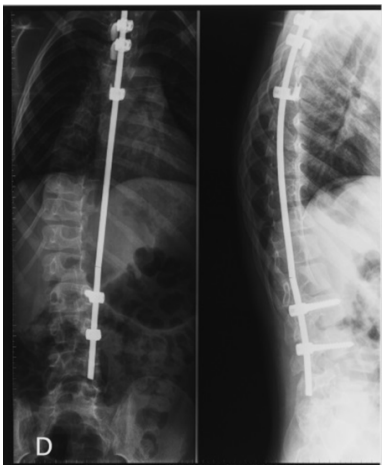

Figure 6.4 X-Ray of the broken rod which failed in vivo used for fractography analysis.

In lab rods

Multiple rods were purchased from two suppliers. The first set of rods, of 5.5 mm diameter, were purchased from Medtronic Sofamor Danek under the tradename CD Horizon® Legacy™ System. These rods, used as biomedical implant and commonly known as being shot-peened to increase their fatigue resistance. Therefore, they are denoted as *shot-peened rods* in the following. The second set are Ti-6Al-4V Grade 5 alloy rods, of 6 mm diameter, purchased from Salomon's Metalen B.V.. These rods which did not underwent shot-peening process, were subsequently machined down to a diameter of 5.5 mm to have an identical geometry as Medtronic rods. This set is denoted as *untreated rods* in the rest of the Chapter.

The elastoplastic mechanical properties (Fig. 6.5a) of the two materials are close to one another. Young's modulus, E, for shot-peened and untreated rods are respectively equal to 113 ± 1 GPa and 124 ± 8 GPa, while their respective yield stress, $\sigma_{0.2\%}$, are equal to 1000 ± 5 MPa and 914 ± 3 MPa.

In the Medtronic's rod, the hardness increases close to the surface confirming the shot-peening, while hardness is constant in the Salomon's rod (Fig. 6.5b), clearly indicating that there has been no shot-peening applied on these rods.

Figure 6.5c indicates that roughness profiles along the z-axis of the bar show two different amplitudes. Shot-peened rods show large amplitude roughness, due to impacts of shot balls. Untreated rods present a regular pattern of smaller valleys, resulting from the turning process.

A multiphasic microstructure is observed on the SEM micrographs of Figure 6.5d (top) for both materials formed by an α matrix with small β precipitates. Figure 6.5d (bottom) shows that the surface relief of shot-peened rods is characterized by an irregular cratered pattern, whereas untreated rods are marked by regular grooved pattern.

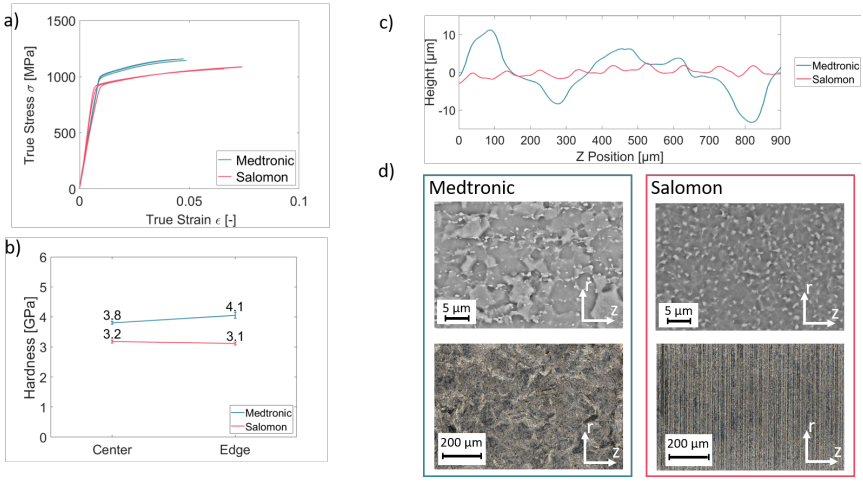

Figure 6.5 Comparison of Ti-6Al-4V rods used as growing rods (Medtronic) with a regular Ti-6Al-4V Grade 5 rod (Salomon): (a) true stress – true strain uniaxial tension response; (b) hardness variation between the core and the periphery; (c) surface profile roughness along longitudinal direction; (d) micrographs and surface relief.

6.2.2 Characterization Methods

Tensile properties

Cylindrical tensile specimens were extracted from the two batches with a diameter of 4 mm. Tensile tests were carried out with a displacement rate set to 1 mm/min until fracture on a Zwick Roell stress rig. Figure 6.5a shows the uniaxial tensile response of the two batches, in terms of true stress (σ)

$$\sigma = \frac{F}{A_0}\left(1 + \frac{u}{L_0}\right), \tag{6.1}$$

as a function of the true strain (ϵ)

$$\epsilon = ln\left(\frac{L}{L_0}\right), \tag{6.2}$$

where F is the tensile force, A_0 is the initial cross-section area, u is the elongation, and L_0 and L are, respectively, the initial and the deformed gauge length.

Hardness

Hardness measurements were performed with an Agilent Technologies NanoIndenter G200 using a Berkovich tip of known stiffness. For each batch, sixteen indents were realized at the center of the transverse cross section and close to the surface.

Surface characterization

Roughness profiles along the z-axis of the bar and surface pictures were obtained using Keyence VHX-7000 3D microscope. Even if the software can be used to compute arithmetical mean roughness values, R_a and mean roughness depths, R_z, we have decided to use profiles representation rather than roughness values. Indeed, The minimum length needed to measure roughness profiles ($2<R_a<10$ µm) is 12.5 mm (ISO4288:96'). However, some of our samples do not have a continuous roughness over such distance in the zone of interest. Moreover, multiple parallel roughness measurements is not ideal due to the double-curved profiles. Finally, for the smoothest sample, the noise in the measurements gived inaccurate values.

Microstructure

Both microstructures were characterized on cross sections parallel to the z-axis. The surface were first ground and then polished with diamond suspensions followed by a 20-min silica suspension step. Finally, the microstructure was revealed with a chemical etching of 30 seconds in a solution composed of 3mL HF, 6mL HNO3 and 91 mL water. Micrographs were taken using scanning electron microscope (SEM) (Ultra-55 FEG SEM, Carl Zeiss, Oberlochen, Germany). A backscattered electon detector (AsB) with 20kV acceleration voltage was used.

Fractography

Fractographies were taken with Keyence VHX-7000 3D microscope using 3D stitching.

6.2.3 Experimental and numerical methods

Fatigue testing

Short specimens of 10 cm length were cut in the rods. Untreated samples have been machined to get a diameter equal to the diameter of the shot-peened rods. Two thirds of the samples have been bent by a surgeon, using a French bender, matching the practices performed during surgeries. The bending angles, measured with profile projector (Mitutoyo PJ 300, Illinois, USA), spread over a range from 2°3′ to 13°3′, determined by the maximum amplitude achieved with a one step bending process.

The samples were then tested using an original in house 3-point fatigue bending device. To mimic the in-vivo crack propagation path, the rod needs to be placed in an unstable configuration. Therefore, a specific setup, described and validated in Chapter 5, has been used to maintain the rods with the concave side head on (which is an unstable position) all along the test duration. The full setup has been adapted to a Bionix (25kN) machine, and the distance between the external points was fixed at 4 cm. The diameter of the support rods were of 6.35 mm. The frequency of dynamic loadings was fixed at 5Hz to avoid self-heating and resonance effects.

The real solicitations in growing rods once implanted are complex and variable. Based on the data presented in Ribesse et al. study [82], we computed an approximated maximal moment, for each of the seven patients, at fracture site by means of Equation 6.3. The mean moment was 27.3 N.m with a standard error of 2.1 N.m. This value is slightly overestimated because the term $\delta(x)$ is unknown and was considered as zero for the sake of simplicity:

$$M(x) = F_{v2}\left(\delta(L_{rod}) - \delta(x)\right) + F_{h2}(L_{rod} - x). \tag{6.3}$$

Our experimental protocol has been subdivided into two categories of tests to represent two different situations. The first category represents force-controlled loading. When a child carry a load, the stress in the rod will be proportional to the weight of the object carried. A force of 1470 N has been

set arbitrarily to reach 90% of the yield stress for straight shot-peened rod. The same force represents a loading at 99% of the yield stress for straight and untreated rod. The maximal torque associated to this force is 14.7 N.m, which is in the same order of magnitude as the one found above. The second category of fatigue tests carried out in this study are strain-controlled tests. When the patient movement is driven by reaching a position (i.e. grab the chocolate pot at the center of the table during breakfast), the amplitude of the deformation is the main parameter controlled by the patient. To be able to control strain amplitude, deformation gauge were glued on the concave surface of the rod at its central position, allowing longitudinal extension measurement. The gauges were placed using MBond 200 cyanocrylate glue.

The protocol for the strain-controlled configuration is composed of two steps:

(i) At first, a static loading is performed to reach the expected strain level. In our case, this strain level was fixed to 0.011. This strain level induces a low-cycle fatigue failure for both batches. As the rod may enter plasticity during the first cycle, the loading is repeated three times to reach a reproducible curve. The force needed to reach the strain level is then recorded and is used in the second step.

(ii) The cyclic test is started, using the force level recorded at stage 1. The gauge measurements cannot be used as instruction during fatigue loading because the acquisition frequency is too low, and that the gauge progressively detaches during the test. The test plays out until sample failure or 3,000,000 cycles run out.

The force levels reached in this second category, leads to moments values between 11 and 22 N.m. These moments again match relatively well with the one determined by the analytical model of Ribesse et al. [82].

Table 6.1 provides a comprehensive overview of the tested samples for both protocols, detailing the angles corresponding to each supplier. In the result's figures, configurations subjected to multiple tests are marked only once and labeled by the notation $N\times$, with N representing the number of tests conducted on each configuration.

Numerical model

To supplement the experimental results, the bending model developed in Chapter 5, has been used. It is composed of three steps: (a) an optional

Table 6.1 Summary of the geometries tested in force-controlled mode and in strain-controlled mode.

Force-controlled	
Shot-peened	*Untreated*
0°	0°
0°	0°
3°	3°
6°	6°
7°	8°
9°	10°
	13°

Strain-controlled	
Shot-peened	*Untreated*
0°	0°
0°	0°
3°	0°
4°	0°
8°	2°
10°	6°
13°	11°
13°	13°

thermal step to introduce periphery compressive stress, (b) a bending deflection which reproduces surgeon handling and (c) a 3-pt bend aiming to replicate a single cycle test as represented in Figure 6.6. The same parameter set was used as in Chapter 4 (presented in Section 4.4.2a) for the kinematic model. The material parameters and stress-strain curves can be found in Appendix B. A complete description of the geometry of the mesh as well as the steps (a) and (b) can be found in Croonenborghs et. Al [80].

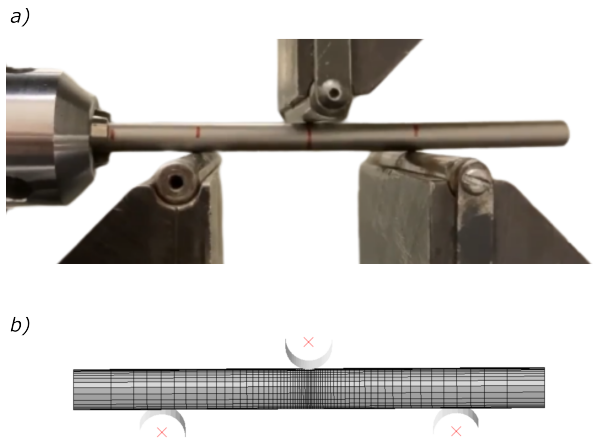

Figure 6.6 Fatigue 3-pt bending test: (a) experimental setup; (b) numerical model.

6.3 Results

6.3.1 Fatigue lifetime

Strain-controlled fatigue tests

Figure 6.7 represents the number of cycles to failure (or run out) during fatigue test as a function of the bending angle of the two materials. If the sample does not break after 3,000,000 cycles, the test is stopped. The run out events are depicted by full symbols with an arrow while empty symbols depict samples that fail during the test. For *straight rods*, rods from both suppliers fail between 69,000 and 185,000 cycles apart from one sample owing to the untreated batch. When *bent rods* are tested, all untreated rods reach 3,000,000 cycles without failure while shot-peened rods fail after reaching between 38,000 and 181,200 cycles.

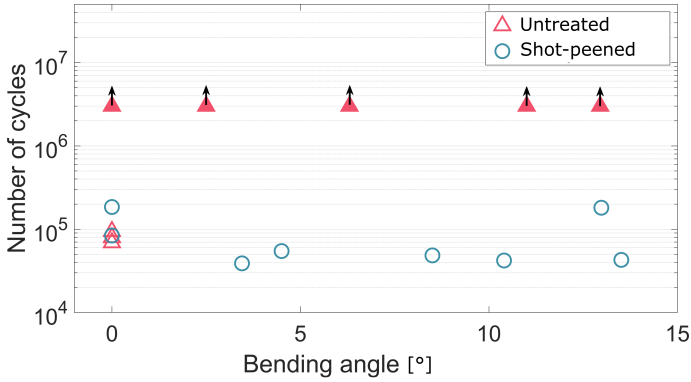

Figure 6.7 Fatigue resistance of the rods in strain-controlled configuration (ϵ=0.011). Triangles and circles are for untreated and shot-peened rods, respectively. Empty symbols depict failure by fatigue, while full symbols represents a run out after 3,000,000 cycles.

In Figure 6.7, a significant scattering of the fatigue performances can be observed for the untreated straight rods and for the ∼13° shot-peened rods. The dispersion in fatigue results can have multiple origins [112]. At first, the material itself can present variation in fatigue resistance along the rod or among different batches. These fluctuations can originate from the presence or the absence of initial defects, or from local variation of microstructure. If the 3-pt bending setup is aligned with a weak or strong region, the resistance will invariably vary. It is important to mention that in the field of

biomaterials, it is necessary to ensure high stability in the material's quality. A second source of scattering originates from the experimental protocol itself. A misalignment of the sample in the setup or of the strain gauge on the sample can result in differences in stress levels. To check if such misalignment could have occurred, Figure 6.8, illustrating the forces applied for each bending angle in the strain-controlled protocol and highlighting the linear trend among the bent rods using linear regression, is presented below. A 100 N difference was applied between the two shot-peened rods, both bent approximately to 13°. Notably, the rod subjected to the lower loading level lasted 4 times longer during the fatigue test. Although misalignment have been kept to a minimum, they might still have occurred resulting in results scattering.

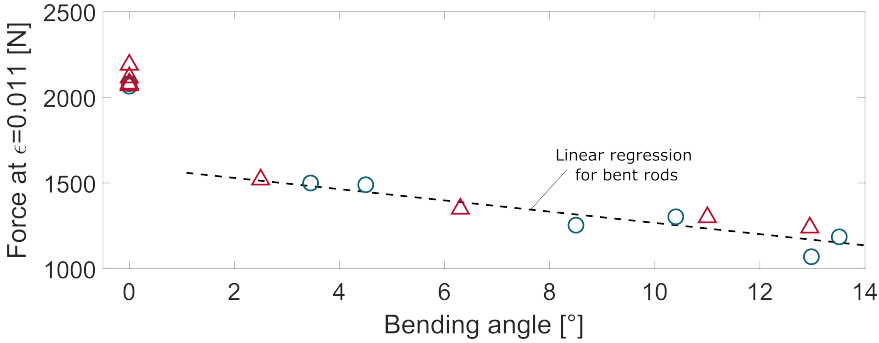

Figure 6.8 Forces applied for each bending angle during fatigue solicitation in the strain-controlled protocol. Triangles and circles are for untreated and shot-peened rods, respectively. A linear regression among the bent rod is highlighted.

To statistically analyze the effect of bending on fatigue resistance of shot-peened rods, an ANOVA test is carried out on a linear regression method. The null hypothesis is that the linear regression on the angle parameter does not explain the variance of the number of cycles to failure. Using SPSS software, a p-value of 0.73 is found. We can thus accept the null hypothesis.

Figure 6.9 shows the residual stress in longitudinal direction at crack initiation site during fatigue solicitation as a function of the bending angle as predicted by the FE simulations for both types of rods with their respective FEA stress contours nearby. The stress level in shot-peened rods at a strain level of 0.011 is close to 100 MPa, for any bending angle while it is

around 1,000 MPa for the untreated ones. The tensile stresses decrease by approximately 100 MPa for pre-bent untreated rods, representing a drop of 8% compared to straight rod.

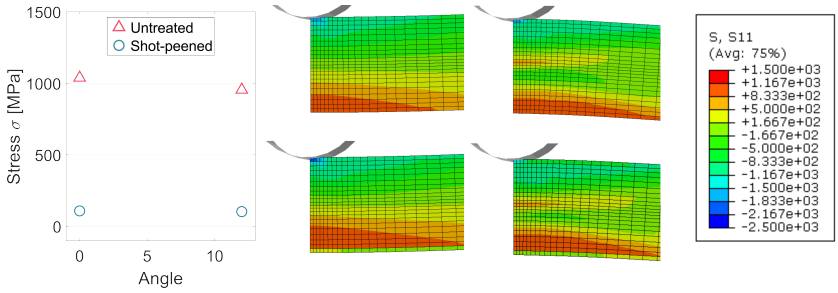

Figure 6.9 Residual stress in longitudinal direction at crack initiation site during fatigue solicitation (ϵ=0.011) for four mechanical histories. Triangles and circles are for untreated and shot-peened rods, respectively. The respective FEA stress contours are presented nearby.

Figure 6.10 presents the variation in stress and strain during the two first cycles of the fatigue loading at the crack initiation site. The strain variation $\Delta\epsilon_{zz}$ takes as reference the strain at the beginning of fatigue loading. On the first cycle, all configurations undergo plastic deformation. The stress levels, reached at a strain level of 0.011, are identical in each batch for any angle as already illustrated in Figure 6.9. During the second loading, the only rod accumulating plastic strain is the initially straight shot-peened rod while the three other configurations stay in the elastic domain. The gradual accumulation of plastic deformation over repeated cyclic loading is called *ratcheting effect*. It accelerates the damage process which can lead to premature failure [113]. The R ratios, defined as $\sigma_{min}/\sigma_{max}$, of the second loading are indicated in the same figure.

Force-controlled fatigue tests

Figure 6.11 represents the fatigue performance of the rods for fatigue tests performed with a constant force of 1470N. As in Fig. 6.7, the run-out events are depicted by full symbols with an arrow while empty symbols depict samples that fail during the test. For both rods, small or unbent rods show high fatigue resistance (>3,000,000 cycles) while all rods with a bending angle higher than 3°23′ fail. Moreover, the shot-peened rods show lower performances compared to the untreated ones.

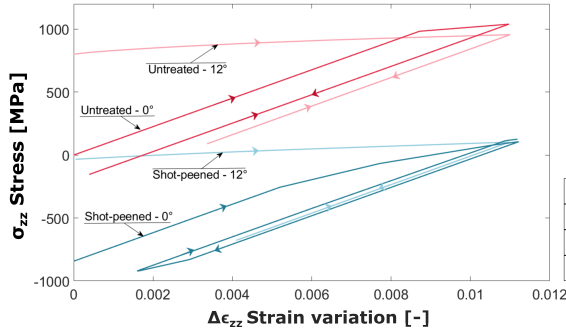

	R ratio
Untreated - 0°	-0.1
Untreated - 12°	0.1
Shot-peened - 0°	-8.9
Shot-peened - 12°	-6.6

Figure 6.10 Stress level as a function of strain variation in longitudinal direction during the two first fatigue loadings to a strain level of 0.011 for four mechanical histories. The R ratios of the second loading are presented nearby.

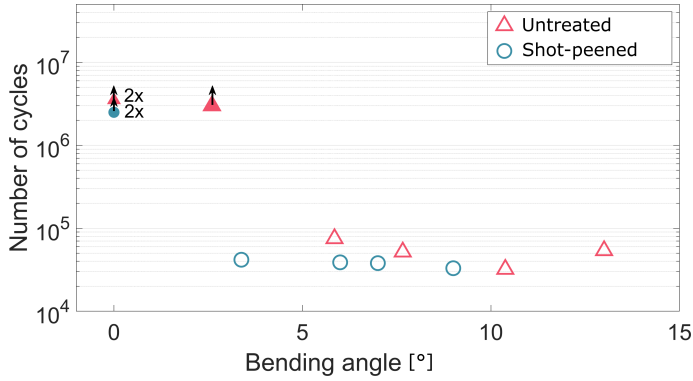

Figure 6.11 Fatigue resistance of the rods in force-controlled configuration (F=1470 N). Triangles and circles are for untreated and shot-peened rods, respectively. Empty symbols depict failure by fatigue, while full symbols represents a run out after 3,000,000 cycles.

Figure 6.12 shows the residual stress in longitudinal direction at crack initiation site during fatigue solicitation as a function of the bending angle predicted by the FE simulations for both types of rods. Their respective FEA stress contours are presented nearby. The predicted stresses in Abaqus show a higher stress level in untreated rods, for any bending angle compared to shot-peened rods. The stress field at the initiation site can even be in compression during fatigue loading as shown by the straight shot-

peened rods. The stress level increases with bending by 140 MPa for untreated rods and by 170 MPa for shot-peened rods.

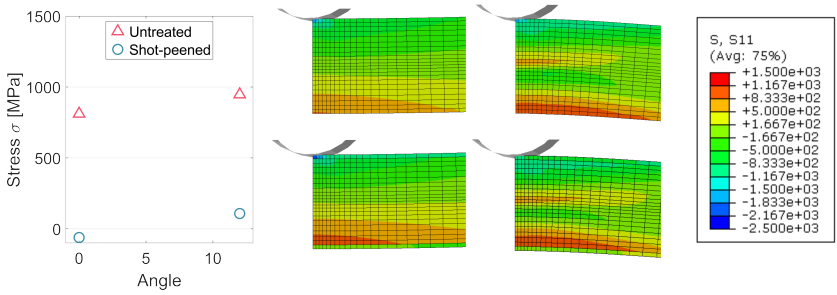

Figure 6.12 Residual stress in longitudinal direction at crack initiation site during fatigue solicitation (F=1470 N) for four mechanical histories. Triangles and circles are for untreated and shot-peened rods, respectively. The respective FEA stress contours are presented nearby.

The stress and strain variations during the two first cycles of force-controlled fatigue loading at the crack initiation site are presented in Figure 6.13. The strain variation $\Delta\epsilon_{zz}$ takes as reference the strain at the beginning of fatigue loading. During initial loading, the straight untreated rod is purely elastically solicited while the three other configurations undergo plastic deformation. In the subsequent loading, all rods are purely elastically loaded. The associated R ratios are indicated in the same figure.

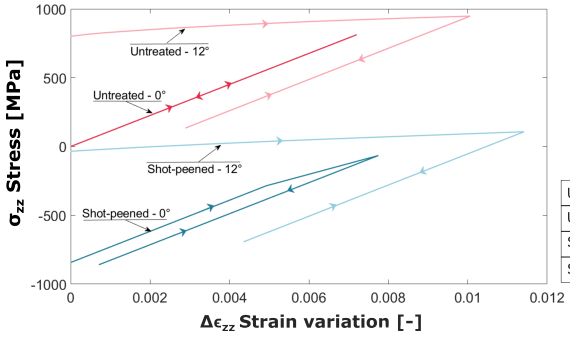

	R ratio
Untreated - 0°	0
Untreated - 12°	0.1
Shot-peened - 0°	13.2
Shot-peened - 12°	-6.5

Figure 6.13 Stress level as a function of strain variation in longitudinal direction during the two first fatigue loadings to a force level of 1470 N for four mechanical histories. The R ratios of the second loading are presented nearby.

Effect of surface roughness on fatigue resistance

To grasp how roughness plays a role on fatigue lifetime for growing rod applications, we have conducted two supplementary fatigue tests. The first one was performed on a untreated specimen, bent to 5°35, slightly depolished with P80 SiC paper to increase its roughness on the concave side. The second one was performed on a shot-peened specimen, bent to 6°00, whose surface roughness was decreased to get a mirror polished aspect using SiC papers and OPS on its concave side. Their initial and final surface states are shown in Figure 6.14.

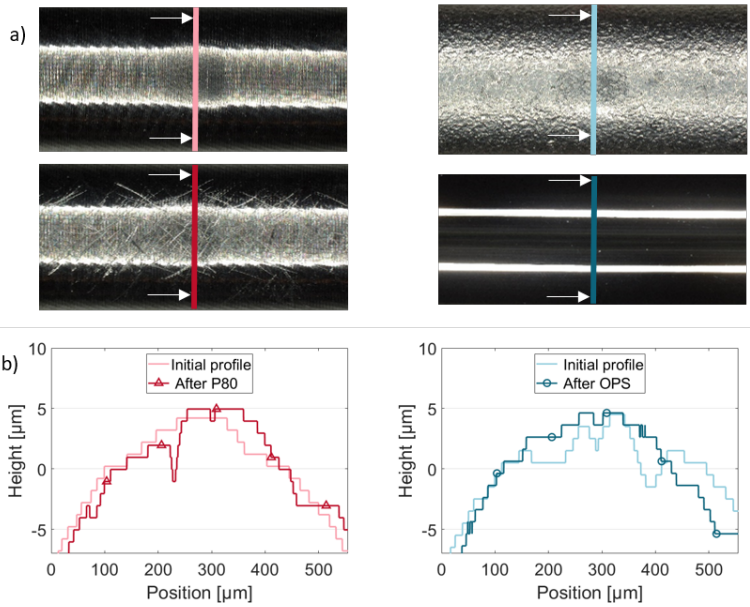

Figure 6.14 Surface states: (a) optical images before (top) and after (bottom) polishing step; (b) superposition cross section profiles (light profile = before, dark profile =after) at x400 magnification.

The bending angle and diameter reduction were controlled before and after polishing using profile projector measurements. The rod angle did not change, and only the shot-peened rod underwent a "significant" diameter change of 40,1 µm. As the difference in fatigue resistance between untreated and shot-peened is well marked in strain-controlled protocol, the two polished rods were tested on this basis without correcting the little change of diameter.

Figure 6.15 compares the fatigue performances of the two polished rods to the unpolished specimen as already presented in Figure 6.7. The major impact is that the fatigue lifetime of the two rods are switched. The depolished (and untreated) rod failed after 67,000 cycles, while the polished (and shot-peened) did not fail after 3,000,000 cycles, indicating a major effect of surface finish.

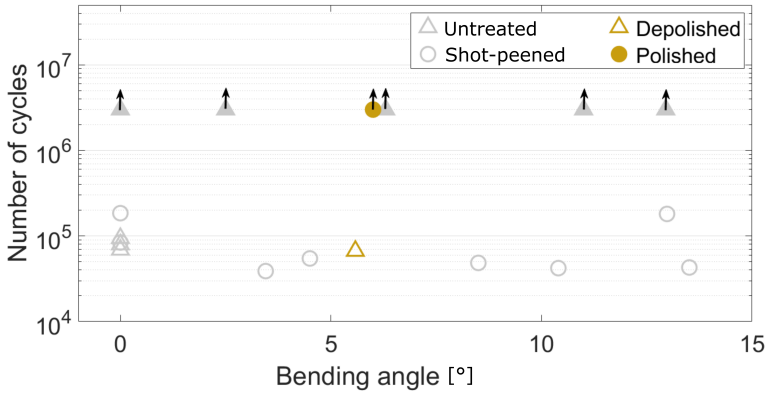

Figure 6.15 Fatigue resistance of the rods in strain-controlled configuration (ϵ=0.011). Grey symbols depict the results presented in Fig. 6.7. The yellow triangle is the untreated rod depolished. The yellow circle is the polished shot-peened rod.

6.3.2 Fractographies

In-vitro testing does never completely reproduce in-vivo conditions. However, it is important to check if the failure patterns are sufficiently similar to the one observed on rods that broke in-vivo, to assess the reproducibility of the protocol.

The failure pattern analysis of in-vivo broken rods was discussed in the Article of Ribesse et al. The cracking process is composed of three main zones shown at the top of Figure 6.16 [82]. The first area is characterized by clamshell marks, indicating the successive arrests in crack propagation. This area is also characterized by ratchet marks which indicate the presence of multiple cracks propagating in different planes. Further, the failure pattern in the central zone shows striations with dimples. This represents the second stage of crack propagation. The transition between clamshell

marks to striations with dimples is highlighted in Figure 6.16a by a dashed red line. The last regions composing the fractured surface are the two symmetric slant edges. These shear lips develop at the end of fracture, due to plastic localization and are highlighted by full red lines in the same Figure. All the others fracture surfaces shown in Figure 6.16 (b to h) are the fractographies of broken rods presented in this study. The same zones, as the broken in-vivo rod, were highlighted in white.

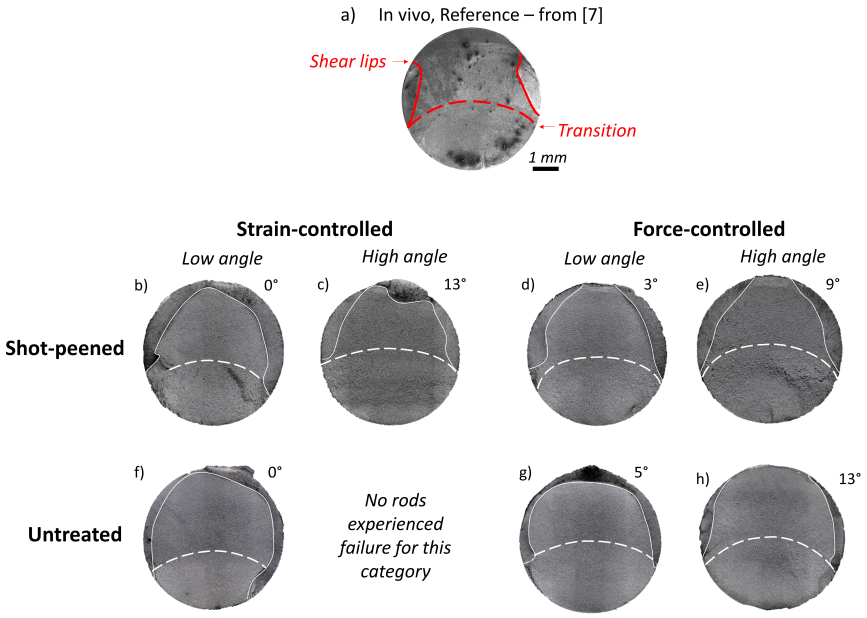

Figure 6.16 Fatigue fractographies from an in-vivo broken rod (a), Shot-peened in-vitro broken rods (b-e) and untreated in-vitro broken rods (f-h). Enlarged pictures are presented in Appendix C.

6.4 Discussion

This study proposes an in depth exploration of the effect of bending on fatigue lifetime of growing rods. The fatigue results are discussed hereafter, with support of the FE simulations, materials characterizations and literature.

a. Representativeness of the test method

The experimental approach followed in this study is, to the best of our knowledge, a first-of-a-kind in terms of reproducing in-vitro as realistically as possible the fatigue failure conditions experienced in a growing rod based on fractographies and crack propagation direction. These tests are obviously not perfectly representative as they have not been performed into a fluid mimicking the body fluid, and the solicitation was not variable and complex as in real life. Flexion bending was selected for this study as fractography analysis from Ribesse et al. indicated that failures were dominated by anteroposterior bending, suggesting that torsion motions were negligible [82]. With the same approach, the fractography analysis of this study showed that the tests properly reproduce the failure pattern observed on in-vivo broken rods. Therefore, the trends observed in this study can be considered as representative to what would happen in the human body, while the absolute values should be discussed with caution.

As predicted in previous studies, a lordotic configuration during fatigue test results in lower lifetime compared to kyphotic configuration [75, 82]. While fracture occurs after around 200,000 cycles in the study of Ribesse et.al, the average in the present study is around 38,000 cycles for the same rods (i.e. shot-peened, Medtronics rods), tested under the same force levels. Still in the same research, Ribesse et al. computed a theoretical frequency of solicitation based on a number of cycles obtained experimentally and average lifetime of rods after implantation. The computed value of 1 mechanical solicitation every 3 minutes was given as a lower bound. The frequency can now be recomputed based on the average number of cycles to failure for all tested lordotic configurations (i.e. 70,000 cycles). The new frequency computed is about 1 mechanical solicitation every 10 minutes. The conclusion on the type of human activities causing fatigue failure, as cited in Ribesse et al. article, is still realistic: walking, squatting, jumping, which are regular movements in a child's life.

b. Effect of bending angle

The evolution of the fatigue resistance with bending angle is crucial to guide surgeons practice. Within a strain-controlled protocol, **shot-peened rods** keep a relatively constant resistance level (Fig. 6.7) while, based on numerical prediction, the stress imposed level is constant with bending angle (Fig. 6.9). These two results are consistent with one another. By looking closer at the stress-strain curves, a ratcheting effect is observed for the

straight rod. In addition, the R ratio evolves from -8.9 to -6.6 going from a straight to a bent configuration. These two observations, known for reducing fatigue resistance, were not associated with a shorter service life of the straight rod. In the second protocol, based on force-control, straight rods resist to 3,000,000 cycles while bent rods fail after approximately 38,000 cycles (Fig. 6.11). A first explanation for this decrease could be the increase in the residual stress level at the crack initiation site. Indeed, simulations show an increase of 170 MPa between the straight rod and the one bent at 12°. This lower fatigue strength could also be explained by the lower yield force needed to plastically deform the bent rods compared to the straight ones. Indeed, stressing a structure below its yield stress leads to higher fatigue life. This seems to be the most likely explanation.

For the second batch, made of **untreated** Ti-6Al-4V, some interesting trends are worth considering. Indeed, in the strain-controlled protocol, the experimental results (see Fig. 6.7) show an enhancement of the fatigue properties when untreated rods are bent. Comparing those performances to the stress levels predicted by numerical simulations, the enhancement can be hardly anticipated. Indeed, even if bent rods are supporting a 8% lower tensile stress level than straight rods, its level is still too high (around 1,000 MPa) to explain a fatigue run-out. Taking a look at full the stress-strain curves (Fig. 6.10), the straight rod experiences cycles of larger amplitude with a lower mean stress. Lower mean stress is usually resulting in better fatigue performance. Unfortunately, even with the information given by the numerical model, the experimental result remains to be understood. In the fatigue protocol with a force-controlled mode, a trend really close to the shot-peened rods is observed: the low bending angles resist to a higher number of cycles (see Fig. 6.11). Simulations show an increase of 140 MPa in residual stress between the straight rod and the one bent at 12°. However, the favored explanation for this reduction in properties is the lowering in the yield stress level with bending.

The former experimental papers comparing straight and bend rods, concluded that bending was detrimental to fatigue resistance [69, 74], and that cyclic loading in lordotic configuration leads a higher failure rate than in kyphotic configuration [75]. An in-depth analysis of residual stress demonstrated that even a slight bending was erasing the initial compressive stresses present on shot-peened rods, but that changing the bending angle does not result in large residual stress variations [80]. This stabilizing trend is also present in the present study which considered a one-step bending

process using FB, limiting all conclusions for angles below 13°. The biggest contrasts in fatigue lifetime are mainly between straight and bent rods. However, bending was not always detrimental. Indeed, the untreated bent rods, showed exceptional fatigue resistance compared to shot-peened rods in the strain-controlled tests. In any case, as a firm conclusion, imposing some bending never leads to major systematic drop in fatigue resistance under strain control conditions but it does under force control when compared to straight rod. In future investigations, it would be interesting to focus on other tools as *in-situ* benders, which allow larger angles to be reached in one pass compared to FB [114]. The rod surface state evolution during bending across a broader range of angles could be characterized using tomography to observe the development of shear bands. Subsequently, it becomes pertinent to discern whether a reduction in fatigue strength occurs beyond 13°.

c. Impact of shot-peening

In both protocols, untreated rods performed better than the shot-peened ones. This difference is particularly noticeable under strain controlled conditions, for which untreated rods survived 3,000,000 cycles while shot-peened rods failed after approximately 100,000 cycles. For both protocols, the FE model predicts a significantly lower stress level in the shot-peened rods compared to the untreated ones, which is not consistent with the fatigue results.

By looking at Fig. 6.5c, a major difference between the two batches are their roughness. Roughness plays an important role in fatigue, and titanium alloys are well known for their notch sensitivity [69, 76, 105]. As shot-peened rods have a rougher surface, their fatigue lifetime are reduced compared to untreated rods, even if the later have larger tensile stresses during loading. To confirm this hypothesis, we changed roughness of two rods. The result demonstrated that by increasing roughness of untreated rod, their fatigue resistance is drastically reduced, while smoothing shot-peened rod increased their performance by at least 3,000%. For few millimeters thick structures, the benefit brought by the reduction in internal stresses close to the surface can quickly be counterbalanced by the increase in roughness coming from shot impacts. Further study on the potential increase in fatigue resistance by smoothing rod surface after shot-peening could be of high interest.

The FE simulations allow isolating a stress effect from others side effects,

as roughness. In both configurations, the residual stresses of shot-peened rods are significantly lower than in the untreated rods. This suggests that shot-peening, through residual stress variations, is promoting higher growing rods lifetime. This is still consistent with the results of a previous study which was focused on residual stress prior to fatigue loading [80]. They have concluded that shot-peening was efficient even at locations that undergo subsequent plastic deformation due to bending process. The numerical results in this paper took this conclusion even further by considering an arbitrary in-vivo solicitation after the bending process.

Finally, the trajectories of the stress-strain curves in growing rods can be quite complex. The first non-monotonic loading applied to the rods is the shot-peening process where impacts induce a series of cyclic plastic deformations (both tension and compression) in the rod periphery. This leads to Bauschinger effects in the material [42]. The subsequent non-monotonic loading occurs during bending, where the rod successively undergoes plasticity in forward bending and elastic recovery [80]. Finally, fatigue loading introduces plastic deformation during the initial loading cycle and even more if the material undergoes ratcheting. This sequence of solicitations can raise questions about the benefits of shot-peening in a material with low hardening capacity, such as Ti-6Al-4V. If the residual stresses are indeed lower with this technique, it may potentially significantly compromise the remaining material's work-hardening capacity, which could be examined in further investigations.

6.5 Conclusion

Fatigue is a multifactorial phenomenon and growing rods constitute a concrete example where events linked to plastic deformation prior to operation, such as shot-peening and bending, modify both the surface roughness and the internal stress field while accumulating large amounts of plastic deformation within the material. In this study, we used a specific setup to evaluate fatigue resistance on a continuous range of bending angles, while reproducing as closely as possible the fracture pattern observed in vivo. These results, for shot-peened and untreated rods, were subsequently compared to the residual stresses predicted by FEA as well as to their surface conditions.

The combination of numerical and experimental analyses has led to con-

siderable progress in our understanding of the early failure of growing rods with the following findings:

- Shot-peening process does not give the expected enhancement in fatigue resistance. The roughness introduced by the process is excessive, overcoming the effect of the reduction of residual stresses.
- Sometimes, a difference in fatigue resistance of straight rods is observed compared with bent rods. However, among the bent rods, there is no marked change in the fatigue lifetime. Therefore, when the surgeon has to bend a rod, the bending angle can be increased as much as necessary without worrying about reducing the life of the implant.
- The choice of the protocol for assessing the fatigue resistance of growing rods is crucial. Nowadays, the type and amplitude of in-vivo stresses are not perfectly characterized. It is therefore important to keep a critical view on the results obtained as rods can reach run-out in one condition while suffering from failure in the other.

Peening techniques associated to lower roughness introduction as laser shock peening or a polishing of the rod prior surgery should be further considered. Exploring operative methods, the investigation of the impact of two closely spaced bends or examining the outcome of a larger bend achieved through tools distinct from the French Bender would offer valuable insights. Additionally, a more in-depth study on post-operative loading and the comparison with the option of wearing a corset are of interest.

PART III
Failure analysis of stents

7

Context of stents: characteristic sizes and expansion process

THIS chapter introduces the disease of arteriosclerosis, which, in some cases, is treated with biomedical implants called stents. These implants are presented with a particular focus on their material specifications. Emphasis will be placed on their topological evolution and on the expansion process taking place during stent placement.

7.1 Arteriosclerosis

Arteriosclerosis consists in accumulation of fatty deposits on blood vessel walls. These deposits leads to a progressive narrowing of the vessels alongwith the decrease of the blood flow. It is the first cause of coronary heart disease which is responsible of 1.8 million deaths each year in Europe [115].

A serious heart attack
All around the world, it has been noticed that the number of coronary events is significantly higher on days the national soccer team is playing [116–118]. These stressful moments are responsible for higher plaque rupture event rates, leading to higher risk of myocardial infarction [119]. Who is being attacked? The goalkeeper or the supporter?

7.1.1 Treatments

If plaque deposition is detected early enough, various treatments exist to restore the blood flow and prevent future heart attack. Each of these treatments uses a specific healing strategy:

- **Change in lifestyle:** Increasing physical activity and improving diet help reducing cholesterol.
- **Medication:** Various drugs can help by lowering the cholesterol level, decreasing the blood pressure, or by preventing clot formation which all help to reduce the risk of heart attack.
- **Coronary artery bypass grafting surgery:** A new alternative path for the rich-oxygen blood is created by taking a piece of vein from elsewhere in the body and place it alongside the blocked artery.
- **Angioplasty without stent:** This technique aims to re-open the vessel. During this surgery, a catheter with a balloon is placed at the position of plaque deposition. The balloon is then inflated, compressing the fatty deposits along the vessel walls. This compression of the plaque is intended to restore a sufficient cross-sectional area for blood flow. The main condition for success is that the deposits must preserve the opening created by the balloon once it has been deflated.

- **Angioplasty with stent:** In cases where stentless angioplasty does not result in sufficient space after the balloon is deflated, a similar but improved technique with a stent can be considered. A small cylindrical mesh, called a stent, is placed around the balloon. During expansion, this mesh is permanently stretched and thus supports the vessel walls after deflation to maintain a sufficient diameter as illustrated in Figure 7.1.

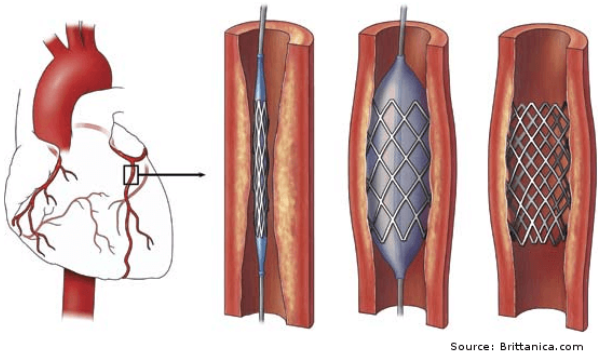

Figure 7.1 Placement of a stent in a vessel with plaque deposits.

7.2 Stent implants

Stent design is a complex project requiring expertise from many fields such as biomedicine, biomedical engineering, materials science, cardiology and small-scale manufacturing. From the point of view of materials science, the specifications of a stent are particularly demanding [115, 120] :

During **implantation**, the stent should be able to travel through curvy vessels to reach its final position. A thinner stent, with higher flexibility, can be achieved using a material with higher mechanical strength. In addition, radiopacity allows surgeons to observe the progression through the arteries and ensure proper positioning before expansion.

While **expanding** the balloon, another set of properties is needed. Again radio-opacity is required to stop inflation when the stent achieves a sufficient size. A material with a low yield strength is preferred to limit the pressure required to deploy the stent while a large ductility is needed to be able to deform until the new diameter.

Finally, once the stent is **in place**, the material should withstand radial strength. Therefore, a high strain hardening allows increasing the yield strength during the expansion process, giving to the final device a higher resistance to recoil. The implant, being subjected to the regular pulse of the artery, should be fatigue resistant. Besides mechanical properties, the stent needs also to be harmless and thus should be biocompatible with blood and vascular tissues while being resistant to corrosion.

But stents present a second challenge to materials science. Because of their size, the physical mechanisms that underlie their mechanical properties may be different from those of larger structures [121]. This is called the size effect. Indeed, as shown in Figure 7.2, a stent is generally 1 to 2 cm long when deployed, and the struts of which it is composed are only 50 to 100 µm thick.

Figure 7.2 Size of a stent before and after implantation on a human scale - [122].

Research about strut thickness have been conducted to evaluate complication rate for 2 struts thicknesses of 50µm and 140 µm [123]. It has been observed that thicker struts showed a higher risk of developing angiographic restenosis compared to thin-struts (26% and 15%, respectively). Moreover, thinner struts give to the structure better deliverability properties. Still, the strut cannot be thinned out indefinitely as their radiopacity decreases with their thickness. As metallic stents have good mechanical properties, their strut diameter are smaller compared to polymer based stents. Figure 7.3 illustrates the span of strut thicknesses available on the market in 2018, but the thinnest stents that are currently used are 50µm thick, and were developed by Meril Life Sciences company [124].

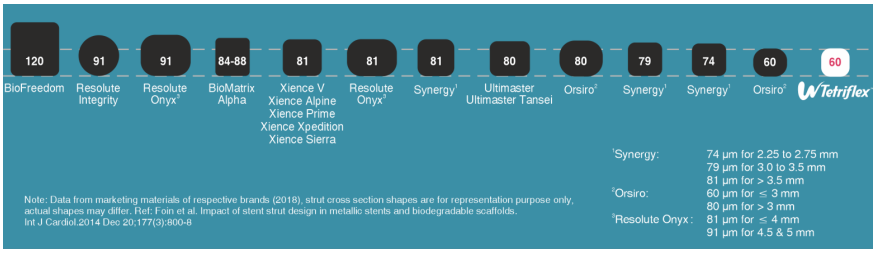

Figure 7.3 Comparison of strut thickness made by SMT company for various commercially available stents in 2018 - [125].

7.2.1 Surface state

The final surface roughness is the result of successive surface modifications:

The selected **manufacturing technique** for mesh creation is associated to a roughness amplitude. Nowadays, commercially available stents are produced from seamless metallic tubes carved by laser cutting as illustrated in Figure 7.4a. The outer surface roughness will depend on initial tube quality while the laser machining surface depends on cutting parameters. Zhao et al. [126] evaluated those roughnesses for a 316 stainless steel coronary stent to 120.52 $\pm$ 25.65 nm and 491.26 $\pm$ 52.46 nm, respectively. The laser machining surface conditions is too high to be implanted right away and will need a further processing step as, according to the PN-EN ISO 14630 standard, the mean roughness coefficient, R_a, for implants made from 316L steel should be smaller than 160 nm. Another technique that is currently being extensively studied in the literature is Selective Laser Melting (SLM) (see Fig. 7.4b). The advantage of SLM is that it not only reduces the number of steps required to manufacture a stent, but also allows the stent profile to be easily customized to suit the patient's profile [127–129]. Langi et al. evaluated the mean roughness of a 316 stainless steel stent made by SLM to 8,450 nm [128].

Both of these manufacturing techniques require a **post-treatment step** to achieve the roughness levels specified by the standards. Laser-cut stents are usually followed by pickling, heat treatment and electropolishing. In the article of Zhao et al. these different steps allow a roughness of 491.26 nm to be reduced to 268.67, 302.90 and 15.01 nm, respectively. The post-processing after SLM varies from one study to another, but electrochemical

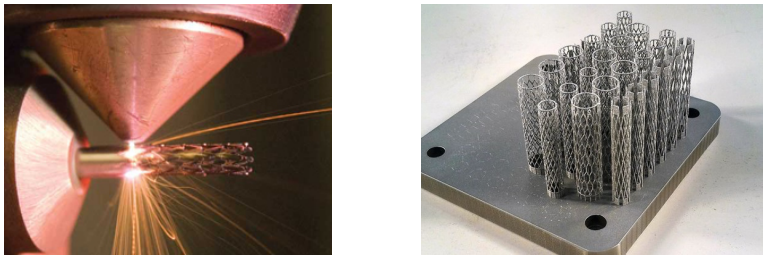

(a) (b)

Figure 7.4 Stent manufacturing techniques (a) Laser cutting [130] (b) SLM process [131].

polishing is a common method. The roughness of Langi stents after electropolishing decreases by 30%, to 5,960 nm.

Finally, during **expansion process**, roughness increases as plastic deformation takes place in the material. Migliavacca et al. observed in scanning electron microscope the zone which underwent the largest equivalent plastic deformation in a 316L stent. As illustrated in Figure 7.5, some surface markings are present in this zone [132].

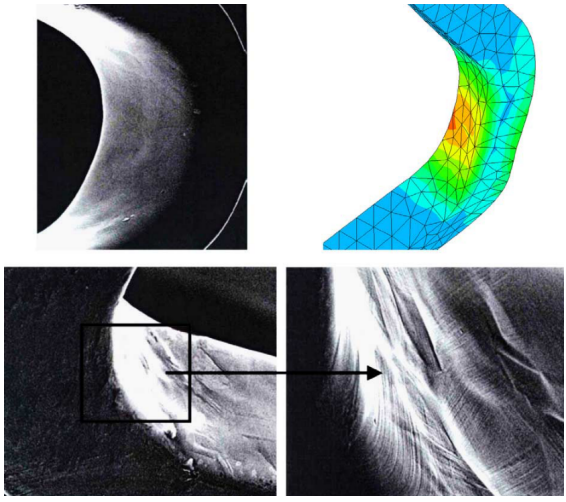

Figure 7.5 SEM images of the stent surface after plastic deformation. The FEM illustration depicts the equivalent plastic deformation field in the strut - [132].

Stent roughness is a key point in manufacturing process as their biocompatibility with blood are directly related. Multiple in vitro studies, performed between 1996 and 2002, showed that a smoother surface result in lower risk of thrombosis [133–137]. These studies have led to the introduction of standards to limit stent roughness. In addition, smoother surfaces reduce the risk of perforating the balloon during angioplasty [138]. Figure 7.6 shows the surface state of two stents which are used commercially nowadays presenting respectively a mean roughness of 61.55 ± 13.45 nm and 22.93 ± 3.62 nm.

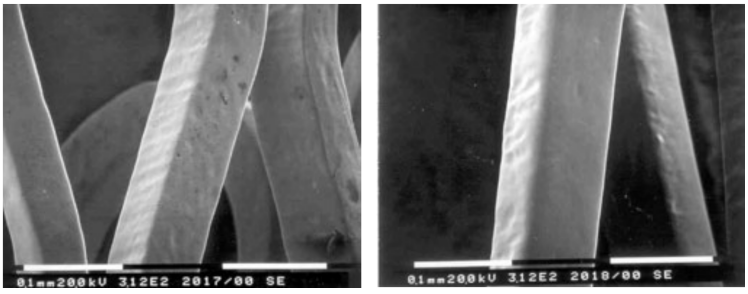

Figure 7.6 SEM images of the stent surfaces of commercially used stents (Cook and ACS respectively) - [126].

While the prevailing trend has been towards making stents smooth in order to reduce the risk of thrombosis, a more recent branch of the literature has shown that rough stents are just as safe as smooth stents [139] and can even accelerate the endothelialisation process [19]. In 2005, Dibra et al. implanted smooth and rough stents to 200 patients and compared the complication rate during the follow-up. No significant difference was found comparing the major adverse cardiac events during the next 12 months in the two groups [139]. Rougher stents are however more promising as they can be associated with antirestenotic drug at their surface using a polymer coating.

Further research on rough stents has shown that by mimicking the surface state of the aortic lumen, the endothelialisation process is accelerated. In the 2013 research by Li et al., a roughness combining a micron-scale structure (from 1,000 to 20,000 nm) and a nanometer-scale structure (from 50 to 500 nm), as illustrated in the Figure 7.7, was able to promote the adhesion and proliferation of endothelial cells. In a recent review on surface engineering by laser-based processes on stents, Dong et al. indicate that the

current state of the art is well developed in this field [140]. The laser based processes offers various 3D topographic possibilities such as grooves, pits, pillars,... These techniques also go along with changes in surface chemistry which also have a huge impact on biological response. Therefore, such kind of surface modification techniques are now incorporated in the latest generation of stents.

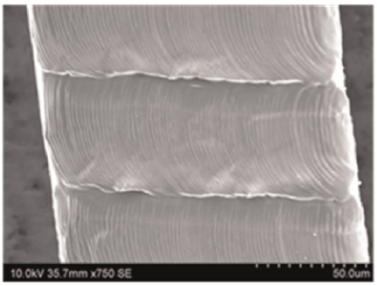

Figure 7.7 SEM image of the laser engineered surface of a 316L stent - [19].

7.2.2 Mechanical answer of a stent

In addition to acute biological responses as restenosis, long-term success of stent implantation is subject to stent fracture itself. Such fracture events are reported in 1 to 2 % of patients within the 10 first months after angioplasty, but the failure rate increases up to 29% with time [141]. This increase of fracture events with time suggests that the origin of fracture is fatigue. Indeed, stents are subject to cyclic pulse loading. The literature does not indicate that stent expansion is a cause of early implant rupture. However, stent overexpansion is indicated as a factor that weakens the struts over the long term [142].

While the expansion process does not currently represent a risk, future advances in the field of stents, and more specifically their topological evolution as presented above, could cause this expansion fracture. The mechanical answer of stent during expansion is described in the following.

Due to their small dimensions and their complex shape, the mechanical answer of stent is commonly investigated in the literature. With an average grain size of 25µm, stainless steel stent struts consists in oligo-crystals, with only 5 to 10 grains along their cross-sections as illustrated by Figure 7.8.

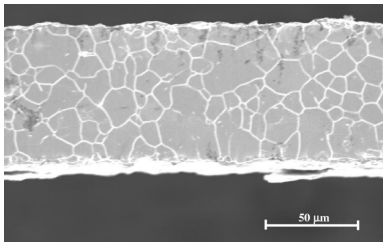

Figure 7.8 316L stent strut with its grain structure highlighted in white - [143].

In the study from Murphy et al., the dependence of strut size on mechanical response was analysed for 316L stainless steels [143]. Figure 7.9 shows that the strain at necking decreases with strut size, in the range size of stent struts. Indeed, when the number of grains across the thickness decreases, the presence of a less well-oriented grain cannot be compensated by better-oriented neighboring grains [144]. It is therefore important to assess the mechanical properties of the material at the adequate scale otherwise the structure could experience an unexpected local failure.

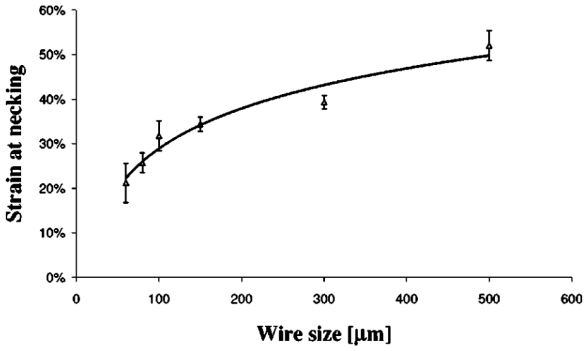

Figure 7.9 Effect of strut size on strain at necking for 316L struts - [143].

Stent expansion includes large deformations in the material. The mesh opening, as illustrated by Figure 7.10, is stent geometry dependent. In general, there are two stages in the expansion process as depicted by Figure 7.11. In the first stage, the curved struts open up through a process of unfolding, allowing large deformation with low loading pressure. Once straightened, the struts offer larger resistance because it is subjected to a

global axial load. Larger pressure must therefore be applied to the balloon in order to continue increasing the diameter of the mesh [132].

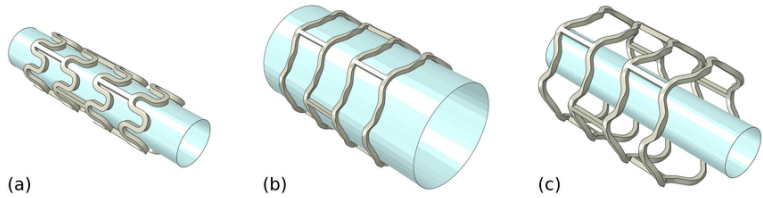

Figure 7.10 Stent crimped on a balloon and then expanded - [145].

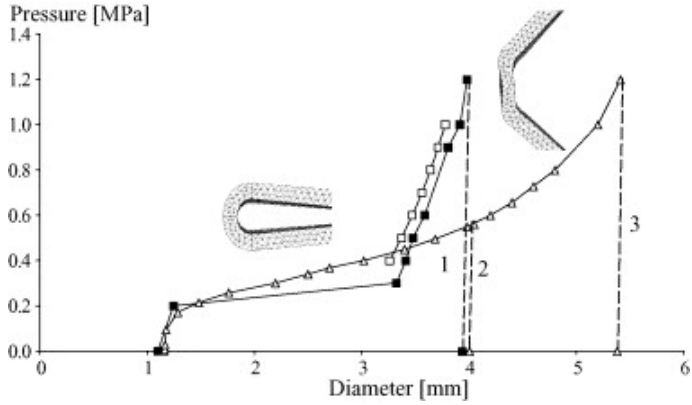

Figure 7.11 Relation between balloon pressure and stent diameter during expansion process (triangles are from FEA, and squares from experiments) - [132].

Finite element analyses are often used in stent design as they provide important informations on structural integrity which are difficult to obtain experimentally [146]. Numerical methods are efficient to test multiple configurations and to converge to the most effective one [147].

In their research, Dumoulin and Cochelin observed stress and strain fields in 316L stent struts upon expansion. For the larger final diameter, their model predicts a maximum local strain of 40% as illustrated in Figure 7.12 [147]. Other values of maximum strain upon expansion can be found in the literature. In 2002, Migliavacca performed multiple FE analyses on diamond-shape stents with variable dimensions. Their parametric analysis included the variation of the slot length l, the stent thickness s and the

metal/artery index α_P/α_V (see Figure 7.13). All the stents were loaded with an uniform radial pressure up to a central radius of 1.5 mm, followed by a load removal. After elastic recoil, the equivalent plastic strains (PEEQ) were evaluated for each structure. From the 10 tested geometries, the PEEQ variation goes from 10% to 40%.

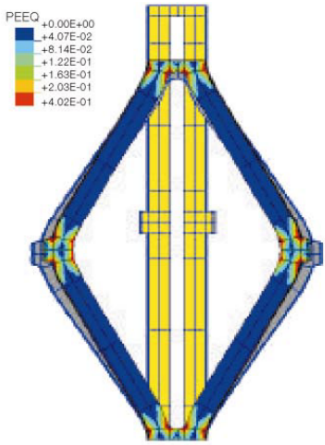

Figure 7.12 Equivalent plastic strain field (PEEQ) in cell during its opening (yellow structure represents the initial configuration) - [147].

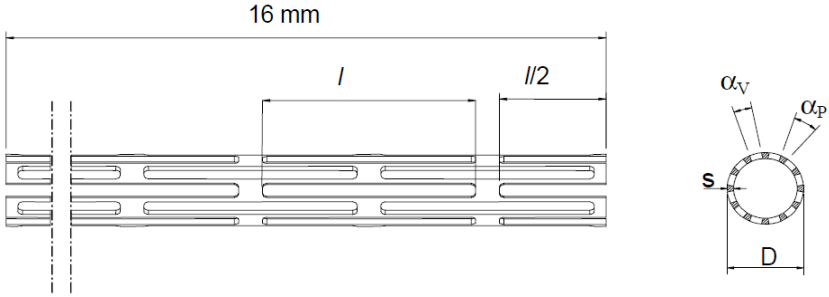

Figure 7.13 Geometry of a diamond-shape stent - [148].

Finally, in another study from Migliavacca et al., they observed the global behavior of the stent during radial expansion and elastic recoil, and compared their results to some laboratory experiments [132]. From Figure 7.11, they concluded that their model was able to predict correctly the rela-

tion between pressure and expansion diameter up to 0.5 MPa. Figure 7.14 shows the strain field in the stent structure at that pressure. The maximum local strain is 27%.

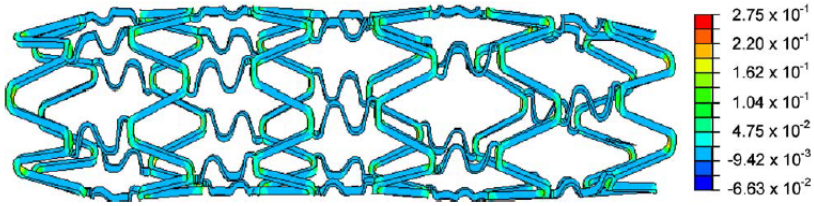

Figure 7.14 Equivalent plastic strains obtained by FEA in 316L stent opened with 0.5 MPa pressure - [132].

As all these numerical analyses show it, the maximum local strain in a stent structure is highly variable but always exceeds 20%. Moreover, the strain field is not uniform as the stent expansion occurs in two steps: the opening of the cell followed by a uniaxial loading.

7.3 Research questions

As presented above, the trend of surface engineering is in expansion in the context of stent implants. It is therefore important to know how these surface pattern could change the expansion capacity of such small structures. In addition, some singular geometrical imperfections coming from manufacturing processes could be detected and a limit on defect tolerance should be set to avoid early implant failure.

Before checking that the surface irregularities will not reduce the fatigue life of the stents too much, these structures must still be able to be plastically deformed to reach the radius of the blood vessel. The expansion process involves large plastic deformations, first through an unfolding process and then under a global axial loading.

In the initial sections of the thesis, two types of implants were introduced: growing rods, prone to surface irregularities due to handling tools and shot-peening, and stents, with deliberately engineered surface textures. It is reasonable to inquire about the potential impact of these irregularities on the implants' functionality, particularly under plastic deformation. However, as these implants are predominantly subjected to non-axial loading, the analysis becomes complex. This complexity led us to shift our research focus, choosing to simplify the forthcoming chapter's analysis by concentrating on a more straightforward scenario: uniaxial tension loading in straight macroscopic specimens. Consequently, readers should not be surprised by the limited connection to the implant context in the subsequent chapter.

The research question for the next chapter is therefore the following:

How does the geometry of surface imperfections influence the localization conditions of a simple structure in tensile loading condition?

Chapter 8 will start by presenting the state of the art of localization in sample with geometrical imperfections. Then, some experimental DIC results will be compared to analytical and FE analyses. On the basis of these results, the elongation capacity of long metallic components will be examined in relation to stent context.

8

Plastic localization in inhomogeneous rods

THIS chapter addresses the question of necking in elongated profiles which present an initial geometrical inhomogeneity. This study combines experimental, numerical and analytical results to completely characterize the evolution of neck shape as the initial imperfection geometry is modified. The final objective is to extrapolate these results to the effect of an inhomogeneity in a stent strut.

8.1 Introduction

When a material sample is loaded in uniaxial tension, a plastic instability occurs once the material is no longer able to compensate the reduction of cross-section area by work hardening as illustrated by Figure 8.1. During that stage, the deformation in a localized zone continues to increase, while the deformation outside experiences elastic recovery. Several studies have already quantified the height of the necking zone as a function of the initial geometry of the sample. The presence of imperfections in the sample is known to reduce its elongation capacity and has been the subject of multiple studies since the 1980s.

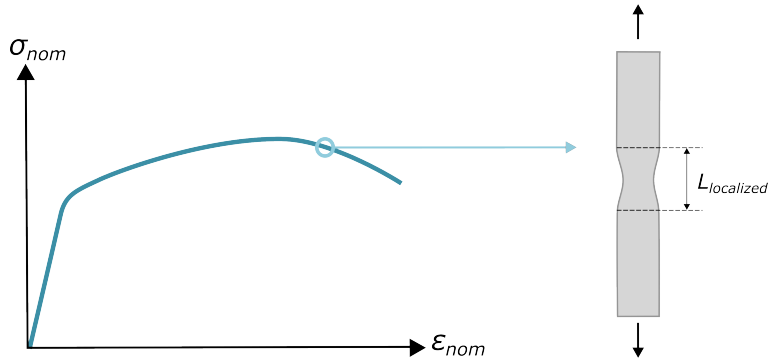

Figure 8.1 Illustration of plastic localization in a cylindrical specimen during a uniaxial tensile test.

8.1.1 Localization length definitions

The analysis of necking under uniaxial tension conditions is an old subject but still involving some open questions. Some theoretical or numerical results were published in the recent years to analyze the post peak behavior [149–151] and it is only in 2020, that few papers analyzed this localization phenomenon with 3D DIC methods [152, 153].

In the literature, different criteria have been defined to evaluate the necking zone length $L_{localized}$:

a. Average strain method

The average strain method is the most common criterion found in the literature. The principle is to compute the average strain along the sample

for each step after necking initiation. The length of the localized zone is deduced from the intersection of the strain profile of this step with the average value as illustrated in Figure 8.2.

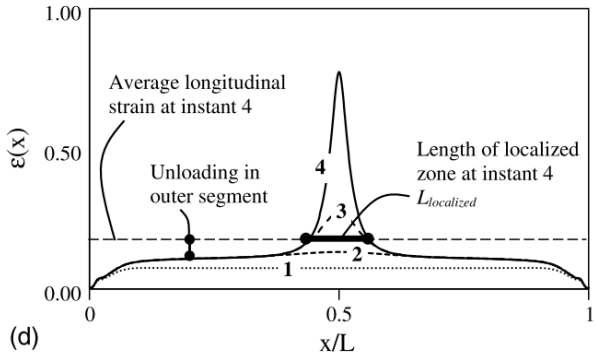

Figure 8.2 Illustration of strain field at 4 loading levels. The length of neck for curve 4, using the average strain method, is depicted - [149].

With this method, Kolwankar et al. [149] observed in their numerical simulations that the localized length is decreasing with strain after peak load (Figure 8.3). Moreover, for different bar diameter, the localized length at onset of necking was approximately 5 times the initial diameter of the bar.

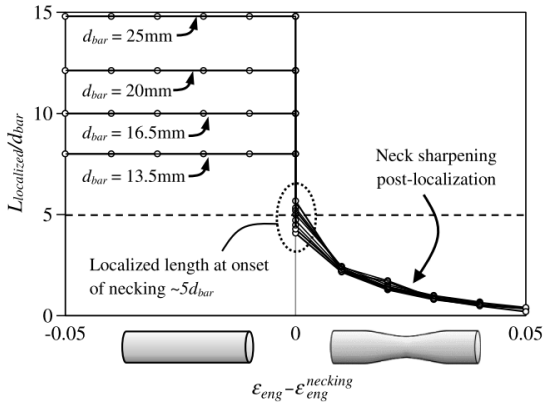

Figure 8.3 Localization length normalized by the diameter of the bar for different strains. The origin is set to the initiation of necking - [149].

The major drawback of this method is that the total length of the sample has an influence on the computed neck length. Moreover, this criterion applied to experimental results showed that localization could start before peak load which is not coherent with the theoretical instability condition of necking [152].

b. Longitudinal strain method

In this second method, each longitudinal strain profile is compared to the last longitudinal engineering strain profile before failure. The distance between the intersections of the two curves gives the localization length for each step. Figure 8.4 illustrates this method.

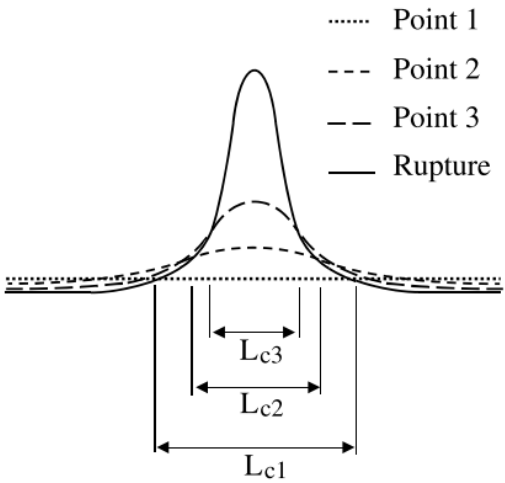

Figure 8.4 Illustration of the localization length for 3 strain curves using the longitudinal strain method - [152].

In the experimental study of Altai et al., this method gave an average localization length at onset of necking of almost 5 times the initial diameter of the sample (for 3 samples with initial total length larger to 5D). The evolution of the localization length between bifurcation event and failure is similar for those 3 samples as illustrated in Figure 8.5.

If this method allows to get rid of the dependence on the sample length, it takes the strain field of the last stage as an arbitrary reference.

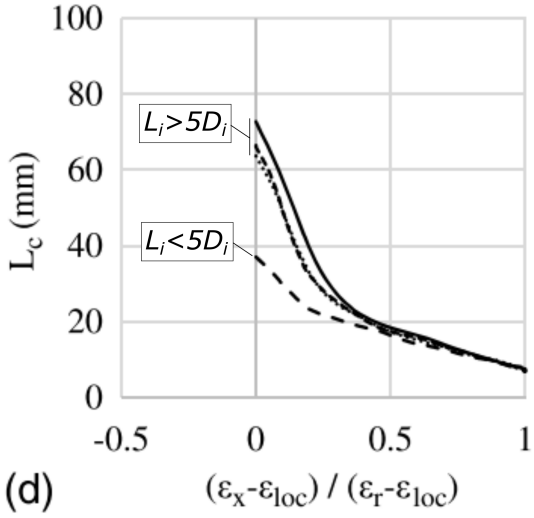

Figure 8.5 Localization length for 4 tensile rods of same initial diameter (12.7mm), but different initial lengths (3D, 6D, 12D and 24D). The x-axis is normalized to have the bifurcation event represented by 0 and the failure represented by 1 - adapted from [152].

c. Active necking zone method

In the study of Pardoen et al. in 2004, a finite element analysis was performed on simple tension of cylindrical bars [154]. Using the effective plastic strain rate as indicator, the shape of the active necking zone was established with h_n being the current height of the active region ($\dot{\epsilon^p} > 0$), and t_n its current thickness as illustrated by Figure 8.6a. A adimensional shape factor, denoted by α is defined as the ratio of the current height of the neck (h_n) over its current thickness (t_n). This factor has the advantage of being independent of the initial length of the sample and of another deformation step. Figure 8.6b shows the evolution of this factor as a function of straining ($\bar{\epsilon}$) for different strain hardening exponents (n). All curves are decreasing with straining, with an asymptotic trend for an alpha value of 1. The hardening coefficient plays an important role on the neck shape. Indeed, smaller hardening capacity gives a smaller localized neck.

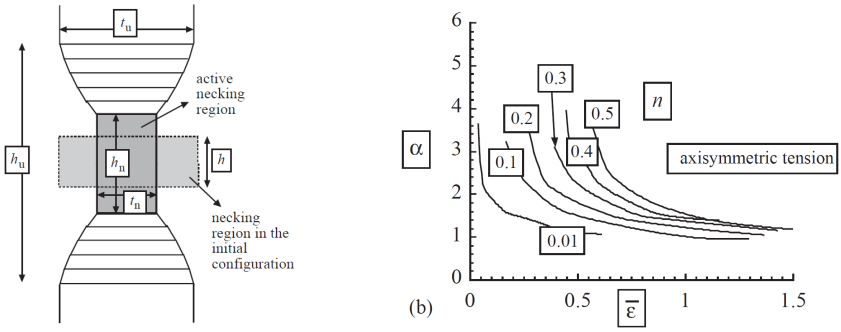

Figure 8.6 (a) Representation of the characteristic dimensions of the neck and the zone being actively strained (b) Evolution of the shape factor of the active necking zone as a function of straining for different strain hardening exponents for a cylindrical rod in tension - [154].

d. Versaillot's method

The experimental method developed in the study of Versaillot et al. is based on longitudinal or transverse strain measurement by 3D-DIC. This method is independent of the length of the sample, and can be computed at each step independently. To evaluate the necking zone length, the authors subtract the constant (longitudinal or transverse) strain outside the necking zone, from the entire strain profile for different loads (see Figure 8.7).

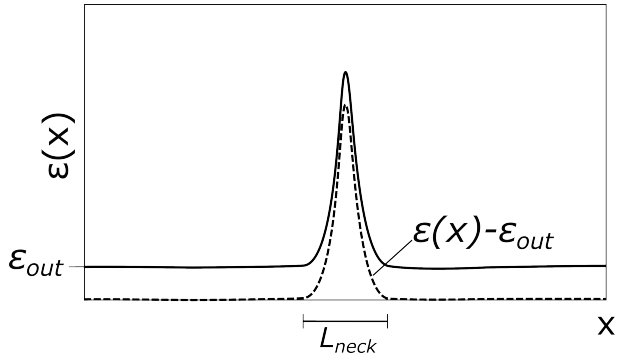

Figure 8.7 The longitudinal or transverse strain profile is modified by subtracting the strain level reached outside from the necking zone.

By using this criterion, the necking length is increasing while the material is strained after maximum loading peak [153]. This trend is opposed to the trends observed in the three other methods. As a matter of fact, the three first methods characterize the portion of material which is still deforming and thus it decreases as it is getting closer to failure. In Versaillot's method, the length includes all portions which underwent larger deformation than the reference section as illustrated in Figure 8.8. Additionally, by comparing the average necking length of 3 materials, Versaillot et al. found that the length at failure was 4 to 6 times the initial diameter of the tested samples. They concluded that their method gives longer necking zone for more materials showing high uniform elongation.

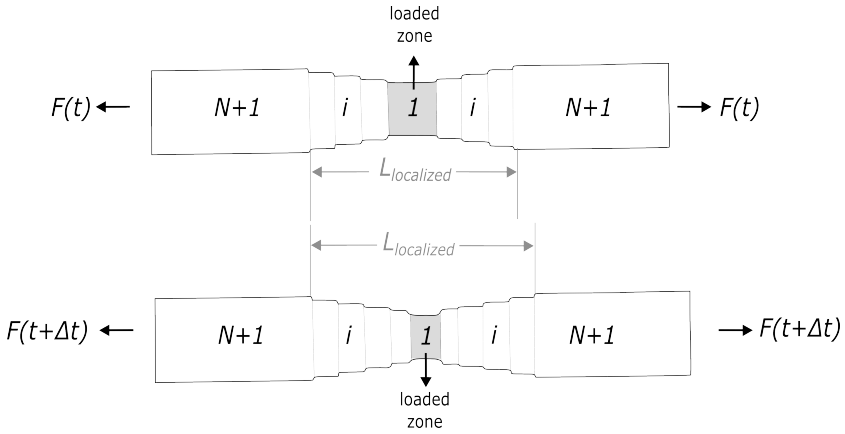

Figure 8.8 Progressive increase of the neck length according to Versaillot's method.

As illustrated by these four methods, the necking length is not a singular value: it evolves during postpeak straining. However, the length range is in some way reproducible whichever method is used, making necking length an attractive parameter to consider.

8.1.2 Effect of geometrical imperfections on necking

A metallic part is never perfectly homogeneous. They may exhibit heterogeneities in grain size, shape, texture, impurities or thickness due to roughness or the presence of a surface imperfection [24]. All these imperfections can lead to local weakening, giving the structure a preferential site for necking. In the second half of the twentieth century, the effect of ge-

ometric imperfections associated with necking was extensively studied in the scientific literature [26, 155–163].

Imperfections in metallic sheets

Many forming processes include stretching of metallic sheets. As those sheets are stretched, their thickness decreases until strain concentrates in a region of the sheet, before its definitive fracture occurs. It was important to be able to predict the Forming Limit Diagram (FLD) to know ahead of time, if the structure will be able to undergo the forming process without necking [164].

In 1967, Marciniak and Kuczynski developed a model which takes into account the presence of a local reduction of section in an infinite sheet [26]. This model, still widely used nowadays, allows to predict the instability generated by the imperfection. In their model, they considered two zones, depicted by A and B in Figure 8.9a, with two different thicknesses: t_A and t_B. The groove was placed normally to the greater principal stress. Based on the force equilibrium, an analytical development allows to find an expression which related the strain in zone A, $\epsilon_{i,A}$, with the strain in the zone B, $\epsilon_{i,B}$. The expression, which depend on many material parameters, can be resolved for various initial imperfection $f = t_B/t_A$ size and the resulting curves are presented in Figure 8.9b. Points C depict the moment where strain localizes in the imperfection and that the limit strain, ϵ^* is reached in zone A. The theoretical analysis was complement by an experimental test, represented by a dashed curve in Figure 8.9b. As the curve reaches a limit strain between the curves of f=0.99 and 0.98, they concluded that the sheet used in the experiment presented an imperfection bounded by these two values [26].

Within a sample, there are microstructural heterogeneities. These heterogeneities can locally create a weaker zone in which plastic localization can develop. When a geometric imperfection is present on the surface, necking can appear either in the intrinsically weaker zone or in the zone with a cross-sectional irregularity, depending on the size of the irregularity [156]. As each material is different, the critical dimension of the imperfection for moving the position of the neck will also be different. As an example, in the study of Hiroi et al. two aluminum with different thermal treatments were compared. The FLD of the softer sheet was unchanged for imperfections below 2% thickness reduction while the hard sheet could withstand only 0.5% imperfections [157].

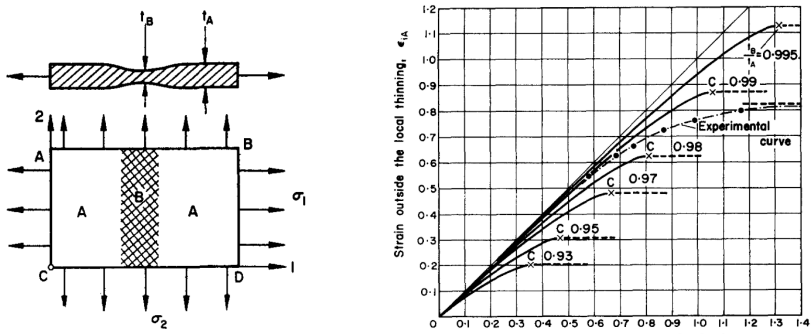

Figure 8.9 (a) MK model imperfection (b) Experimental curve compared to MK model - [26].

Based on M-K model, other studies have been carried out to better understand and characterize the effect of imperfections on metal sheets. In 1984 and 1988, Chan et al. and McCarron et al. furthered the analysis by addressing the effect of the orientation of the imperfection (Figure 8.10a) as well as of its size (Figure 8.10b) [156, 159]. The analytical model predicted that the orientation of the groove influences the location where necking initiates while experimental results demonstrated that increasing the width or length of the imperfection both reduces the limit strain ϵ^*.

A more recent study, from Pilkey et al. introduced grooved imperfection on both sides either symmetrically (as in M-K model) or asymmetrically [165]. Through experiments and numerical models, they found that this new spacial arrangement promotes a through thickness shearing as compared to necking in the symmetrical configuration. Moreover, the configuration with the lowest limit strain depends on the width of the groove.

Imperfections in long metallic components

Imperfections in flat profiles have been widely analyzed in the literature by means of numerical simulations, analytical models and experiments because of its industrial importance [158]. It is less the case for very long profiles such as wire or long rods to which stent strut can be compared.

The majority of the papers dealing with plasticity instabilities in tensile samples with geometric imperfections were published in the 1980s [158,

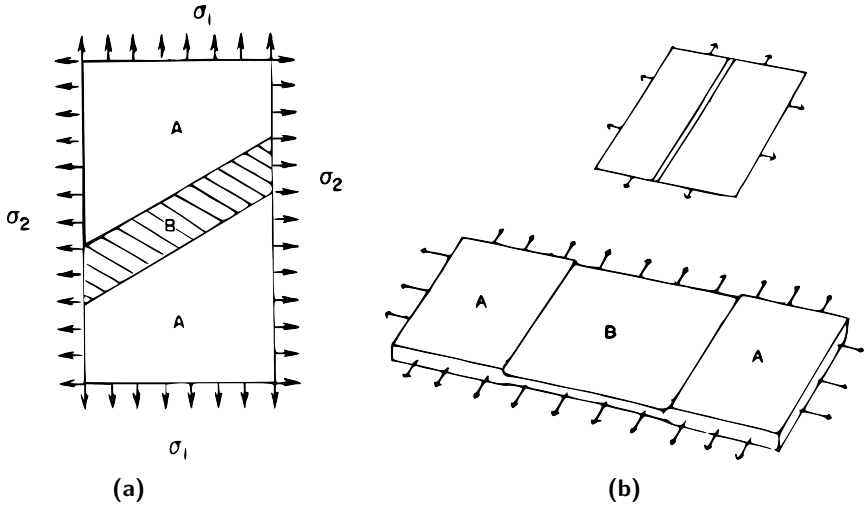

Figure 8.10 (a) Groove orientation from [156] (b) Groove size from [159].

160–162]. These studies are mainly based on analytical models and primarily focus on the effect of material parameters such as m, the rate sensitivity exponent, and n, the strain hardening exponent. In addition, it worth mentioning that some of these works are based on Hart's model, which has since been discussed.

In 1971, Chen emphasizes the necessity of knowing the stress-strain fields at any position of a uniaxial tensile specimen at any loading moment. He performed numerical analyses to evaluate the effect of an imperfection in a cylindrical rod following the expression

$$R(z) = R_0(1 - \epsilon e^{-\alpha z^2}), \tag{8.1}$$

with ϵ being the maximum amplitude of the imperfection.

At this time, Chen performed the first numerical analysis of a inhomogeneous cylindrical profile (see Figure 8.11a) and was able to extract the geometrical evolution as well as the stress and strain fields in the complete structure 8.11b. The author mentioned in the conclusions that this analysis, even if it involved some inaccuracies, helps to further understand the fracture phenomenon inside necking regions.

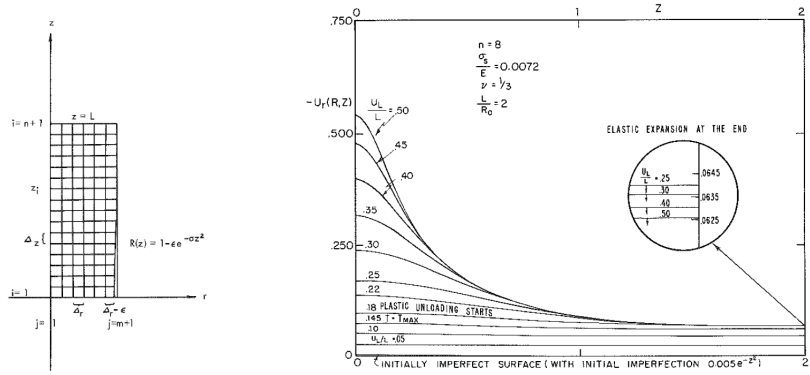

(a) **(b)**

Figure 8.11 (a) Geometric representation of the grid used for numerical analysis by Chen (b) Radial displacement along the sample surface at different elongations - [163].

In a simpler approach, Champier carried out a analytical study based on a 2-slice sample in 1968 (Figure 8.12) [155]. For this sample, force equilibrium and sample elongation can be expressed as the following.

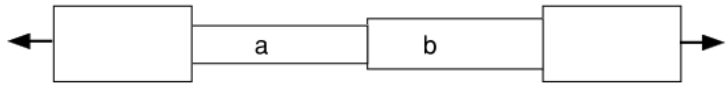

Figure 8.12 2-slice model used by Champier to determine ϵ_b with respect to ϵ_a - [155].

Force equilibrium imposes that

$$F_a = F_b, \tag{8.2}$$

F_i being the force in the part i. Based on material hardening law, each term can be written as:

$$F_i = \sigma_i A_i = f(\epsilon_i) A_i, \tag{8.3}$$

where σ_i is the stress in part i, A_i is its cross-section and $f(\epsilon_i)$ is the hard-

ening law of the material which depends on the strain level ϵ_i. The current cross section A_i can be linked to its initial size $A_{i,0}$ by the mean of deformation

$$F_i = \frac{f(\epsilon_i)}{e^{\epsilon_i}} A_{i,0}. \tag{8.4}$$

Equation 8.2 then becomes

$$\frac{f(\epsilon_A)}{e^{\epsilon_A}} A_{A,0} = \frac{f(\epsilon_B)}{e^{\epsilon_B}} A_{B,0}. \tag{8.5}$$

It it then possible to determine ϵ_B for a known ϵ_A, and based on these two values, to determine to average strain of the sample ϵ_{av}:

$$e^{\epsilon_{av}} = \frac{L_{A,0}}{L_0} e^{\epsilon_A} + \frac{L_{B,0}}{L_0} e^{\epsilon_B}. \tag{8.6}$$

Ten years later, a study by Canova et al. [161] looked at the effect of a geometric or metallurgical imperfection using the same principle as Champier [155] but for a specimen with N+1 slices. This refined method provides a better spatial resolution of the strain distribution along the sample. Based on their calculations, they divided the plastic instability into 3 phases:

- A gradual transition in which the slices progressively transition from elastic to plastic deformation
- A slow localization phase in which all the slices deform plastically, but the deformation is faster in the smallest slice.
- A rapid localization, once the maximum load has been reached, where the deformation concentrates in the thinnest slice.

Finally, using the N+1 slice method, Christodoulou and Jonas addressed the effect of imperfection geometry by comparing sinusoidal and exponential profiles [158]. They showed that the global strain at fracture was slightly lower for the exponential imperfection. In addition, the depth of the geometrical imperfection had a significant effect on the global strain at fracture. They also observed that increasing the neck-to bulk-length, $L_{imperfection}/L_{bulk}$, increased the overall strain before the onset of necking, as well as the overall strain at fracture.

As presented above, only few studies analyzed necking in elongated profiles compared to sheets. Given that (i) few studies combining analytical, numerical and experimental analyses have been carried out on uniaxial tension specimens with geometrical imperfection and (ii) that modern techniques, such as DIC, can provide very detailed information that was not available in the 1980s, it seems interesting to carry out a study combining these different characteristics. More specifically, the combination of these features will enable us to analyze the following questions in details:

- How does the geometry of imperfections influence localization phenomenon in uniaxial tension in terms of strain field, necking development, and total elongation capacity ?
- Are experimental results consistent with analytical and numerical predictions ?

8.2 Experimental and numerical procedures

8.2.1 Material characterization

Stainless steel 316L was purchased at Testas in the form of cylindrical rod of 13mm of diameter. To restore its microstructure, the rod underwent a thermal treatment in a resistive air furnace at 1050°C for 10 minutes, followed by a water quench to obtain a fully austenitic microstructure. The resulting microstructure is represented in Figure 8.13. The microstructure is equiaxed and the average grain size is equal to 30µm.

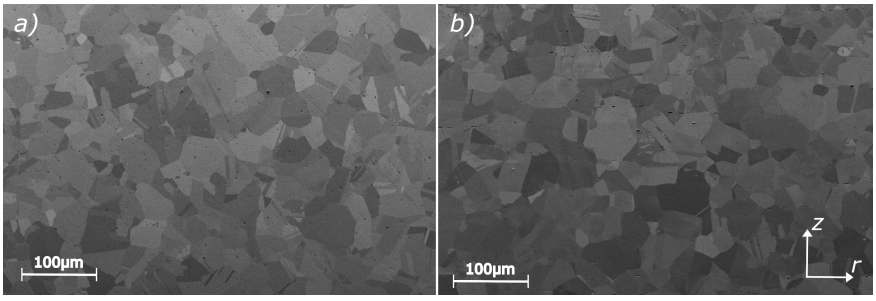

Figure 8.13 Microstructure of 316L rod, after heat treatment. (a) Cross-section view (b) Longitudinal view.

In this rod, a tensile specimen was machined to determine response under

uniaxial tension. The dimensions of the dog-bone specimen are presented in Figure 8.14. The specimen was deformed at a cross-head speed of 1 mm/min up to failure on a Zwick Roell tensile machine. The elongation was measured by the mean of an extensometer and the final diameter was evaluated using a profile projector. Figure 8.15 presents the true stress-strain curve obtained for this specimen in terms of the true stress :

$$\sigma = \frac{F}{A_0}\left(1 + \frac{u}{L_0}\right), \tag{8.7}$$

as a function of true strain:

$$\epsilon = ln\left(\frac{L}{L_0}\right), \tag{8.8}$$

where F is the applied force, A_0 is the initial section, u is the elongation, L_0 and L are respectively the initial and the deformed gauge length. The cross in Figure 8.14 indicates the fracture strain, deduced from the cross section area and defined as :

$$\epsilon_f = ln\left(\frac{A_0}{A_f}\right), \tag{8.9}$$

where A_f is the final section. The corresponding true stress is defined as

$$\sigma_f = \frac{F}{A_f}. \tag{8.10}$$

The Young's modulus is 212 GPa, the yield stress is 246 MPa, and the fracture stress and strain are equal to 1952 MPa and 1.65 respectively.

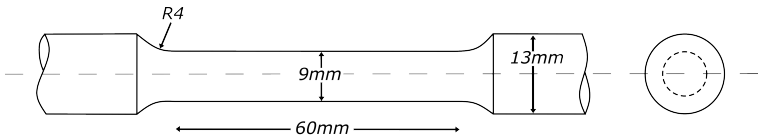

Figure 8.14 Geometry of the tensile specimen.

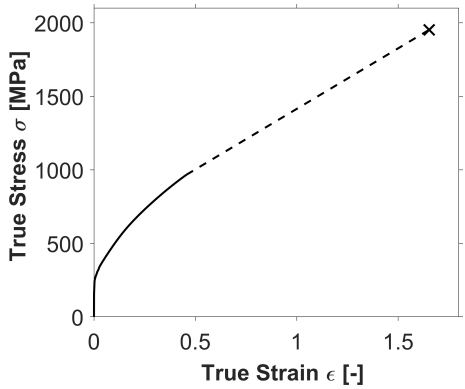

Figure 8.15 True stress- true strain curve and fracture stress and strain, for 316L uniaxial cylindrical tensile specimen.

8.2.2 Imperfection characterization

The imperfections in the cylindrical specimens were all machined at mid-height. These are characterized by a diameter reduction ($D_i < D_o$), and this reduced section has a specific length (L_i), different from the length out of the imperfection (L_o), as illustrated in Figure 8.16. In order not to be influenced by the irregularities present in the area close to the fillets (R4), a gap of 3mm was introduced between the end of the fillet and the start of the outer zone of length L_o. Based on these 4 characteristic dimensions, 3 adimensional parameters have been defined.

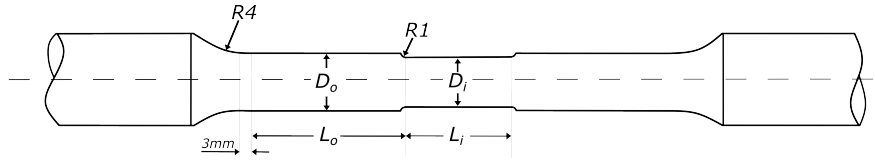

Figure 8.16 Geometry of the tensile specimen with central imperfection.

Section variation χ_A The section variation, χ_A, is defined by the transversal area ratio between the inner zone and the outer zone as illustrated in Equation 8.11.

$$\chi_A = \frac{\pi D_i^2}{4}\frac{4}{\pi D_o^2} = \frac{D_i^2}{D_o^2} \tag{8.11}$$

Length variation χ_L The length variation, χ_L, is defined by the length ratio between the inner zone and the outer zone as illustrated in Equation 8.12.

$$\chi_L = \frac{L_i}{L_{tot}} = \frac{L_i}{L_i + 2L_o} \tag{8.12}$$

Length over diameter ratio variation χ_{LD} The length over diameter ratio variation, χ_{LD}, is defined by the length over diameter ratio of the inner zone as illustrated in Equation 8.13.

$$\chi_{LD} = \frac{L_i}{D_i} \tag{8.13}$$

The parameters selected for sample design are listed in the Table 8.1. The exact sample geometries can be found in Appendix D. In the following of the manuscript, the samples will be denoted by the name of the parameter (X), and the level of the parameter n as χ_X^n.

Table 8.1 Imperfection geometries: Values for χ_A, χ_L and χ_{LD} parameters.

Parameter	Fixed values	Parameter level
χ_A	χ_L=33% and χ_{LD}=200%	100% 98% 90%
χ_L	χ_A=90% and χ_{LD}=100%	25% 20% 16%
χ_{LD}	χ_A=90% and χ_L=20%	300% 100% 75%

8.2.3 Mechanical testing

Prior testing, all samples with geometric imperfections were coated with a black and white speckled pattern, allowing Digital Image Correlation technique (DIC). The samples are subsequently tested under uniaxial tension with cross head speed set to 1mm/min. The deformations were measured using 4 cameras placed on both sides of the specimens and the acquisition

frequency was fixed to 1 Hz. Images were then treated using the software Istra4D with a facet size of 39 pixels and a grid spacing of 17 or 6 pixels.

From DIC analysis, the 3D positions and the principal strain are extracted for each frame (see Fig. 8.17). From these data, the position of the maximum strain is extracted up to fracture.

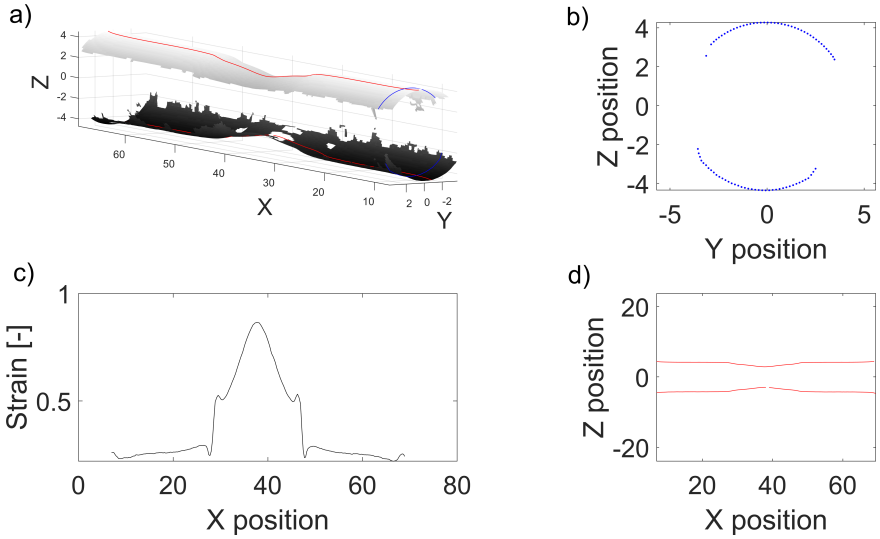

Figure 8.17 χ_L^{25} representation of DIC data at an arbitrary step after necking: (a) 3D view of the sample (b) radial cross-section profile (c) Strain field along the upper red line (d) longitudinal cross-section.

8.2.4 Finite element model

An axisymmetric 2D FE model of a uniaxial tensile test has been developed in Abaqus/ Standard. Isotropic linear elasticity is used to model the elastic behavior and J2 flow theory for the plastic behavior using a Swift type hardening law:

$$\sigma_Y = \sigma_0 \left(1 + \frac{\epsilon^p}{p_0}\right)^n \tag{8.14}$$

where, σ_0 is the initial yield stress, ϵ^p is the accumulated plastic strain, p_0 is a hardening parameter and n is the strain hardening exponent. The following values were selected, σ_0= 915 MPa, p_0= 0.044, and n = 0.57, based

on experimental uniaxial stress curve corresponding to 316L. For all simulations the Nlgeom algorithm was used to account for large deformations.

Taking advantages of symmetries, 1/2 of a slice has been modeled. CAX4R elements were used. The mesh size was kept constant for all sample geometries. The average element size is equal to 0.06×0.06 mm. As an illustration, the mesh of sample χ_L^{25} is presented in Figure 8.18. A convergence analysis was made and is presented in Appendix E. The material properties are extracted from the load displacement data. Strain data were extracted at the central integration points in the surface element set to be comparable with DIC measurements.

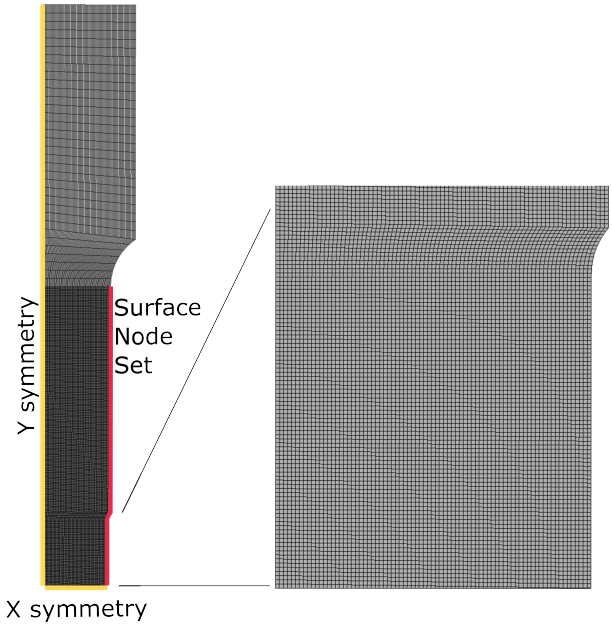

Figure 8.18 Representation of χ_L^{25} mesh.

8.3 Results

In the following section, a red color will be used in the plots to refer to experimental results while a blue color will be used for the FE results.

8.3.1 Deformation along the surface

a. Comparing DIC strain measurements with analytical calculations inside and outside the imperfection

As explained in Section 8.1.2, the strains inside and outside the imperfection regions can be predicted based on analytical calculations for various χ_A values (method used by Marciniak and Kuczynski for sheets [26] and Champier in rods [155]). Figure 8.19a shows the superposition of the analytic resolution of force equilibrium (straight lines), with the strain field measured by DIC (transparent dots). The strain ϵ_{in} is taken at the center of the neck region, while the strain ϵ_{out} is taken at a different distance from the neck dependent of the geometry of the sample. The distance for each geometries are gathered in Table 8.2.

Table 8.2 Distance between ϵ_{in} and ϵ_{out} for each geometry.

Parameters	Values	Distances between ϵ_{in} and ϵ_{out}
χ_A	100%	15 mm
	98%	15 mm
	90%	15 mm
χ_L	25%	10 mm
	20%	10 mm
	16%	10 mm
χ_{LD}	300%	20 mm
	100%	15 mm
	75%	15 mm

Figure 8.19a indicates a good agreement between the analytical prediction and DIC measurements. Figures 8.19b and 8.19c give the same graph for parameters χ_L and χ_{LD}. As presented in Table 8.1, χ_A is kept constant to 90% for all geometries. As predicted by the analytical solution, the evolution of ϵ_{out} with respect to ϵ_{in} is thus identical for each set of 3 samples.

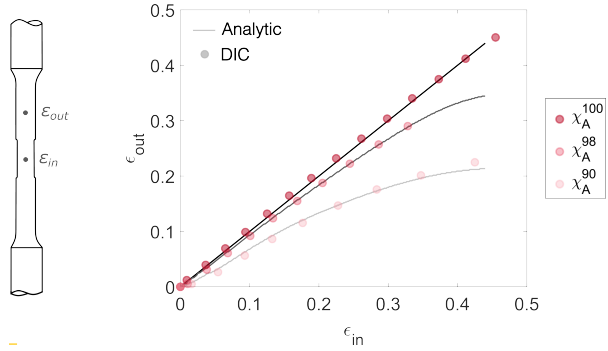

(a) Strain fields from DIC and iso-force constraint for χ_A^{100}, χ_A^{98}, and χ_A^{90}.

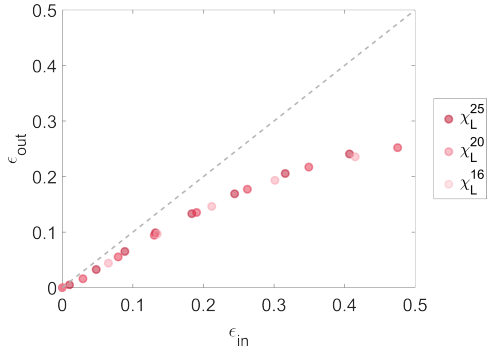

(b) Strain fields from DIC χ_L^{25}, χ_L^{20} and χ_L^{16}.

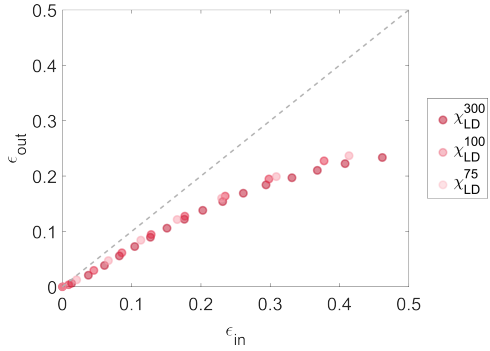

(c) Strain fields from DIC χ_{LD}^{300}, χ_{LD}^{100} and χ_{LD}^{75}.

Figure 8.19 Strain fields in and out from the imperfection for χ_A, χ_L and χ_{LD}.

b. Comparing DIC strain profile with FE results all along the surface

If the analytic model gives the strain level in the outer region, it does not give the evolution close to imperfection boundaries. Therefore, numerical simulations have been used to be able to compare the strain variations all along sample height with the field extracted by DIC. Figure 8.20 superposes the strain profile obtain by DIC and numerical simulations are depicted for each sample geometry. The last curve corresponds to the last step for which the speckled allowed for proper DIC correlation. The plots represent the true strain profiles for multiple steps, with the necking position indicated at the left side of each graph. The profiles are taken on a vertical line, of initial fixed length (see gauge length below each graph). The x axis represents the initial position along this gauge length normalized by the initial length. The strain at necking position was used to associate the numerical profiles to the DIC measurements.

Figure 8.20 presents in pairs the superposition of the strain profile obtained by DIC and numerical simulations for five arbitrary frames with the strain fields obtained by the two methods during necking, for each sample geometry.

On the left-hand side, the plots represent the true strain profiles for multiple steps, with the necking position indicated at the left side of each graph. The profiles are taken on a vertical line, of initial fixed length (see gauge length below each graph). The x axis represents the initial position along this gauge length normalized by the initial length. The strain at necking position was used to associate the numerical profiles to the DIC measurements. The last curve corresponds to the last step for which the speckled pattern allowed for proper DIC correlation.

On the right-hand side, strain fields from numerical simulations and DIC are compared for an arbitrary maximum strain level during necking. The strain field from Abaqus is represented at mid-thickness while the DIC strain field is measured at the surface. Due to light reflection, some areas of the sample could not be analyzed by DIC, leaving gaps in the deformation field.

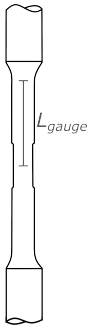

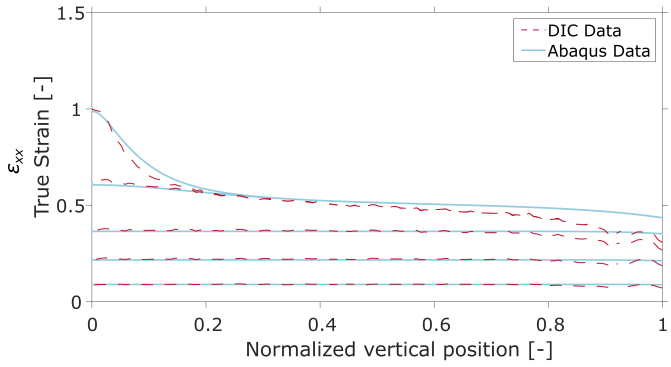

(a) χ_A^{100} - True strain along gauge length (25 mm).

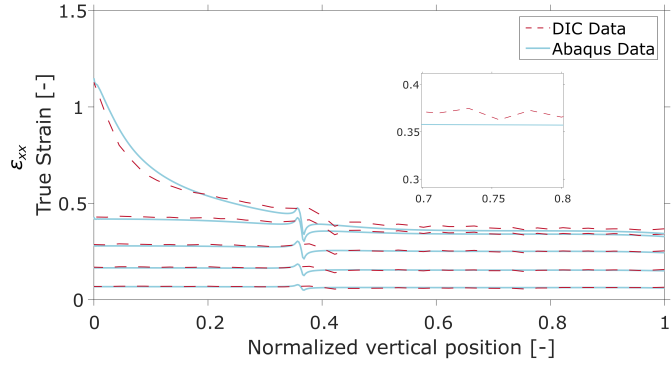

(b) χ_A^{98} - True strain along gauge length (25 mm).

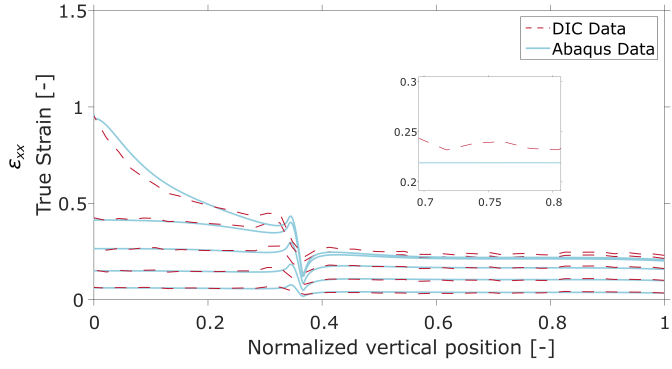

(c) χ_A^{90} - True strain along gauge length (25 mm).

Figure 8.20 Superposition of deformation fields from DIC and Abaqus.

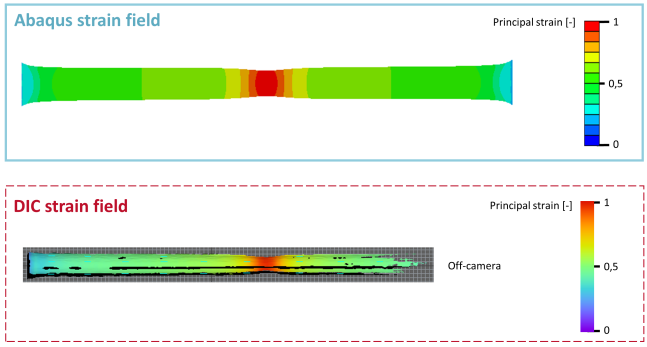

χ_A^{100} - Strain fields at a maximum strain level of 1.

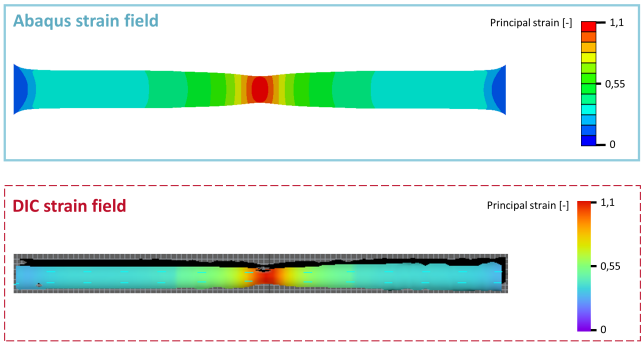

χ_A^{98} - Strain fields at a maximum strain level of 1.1.

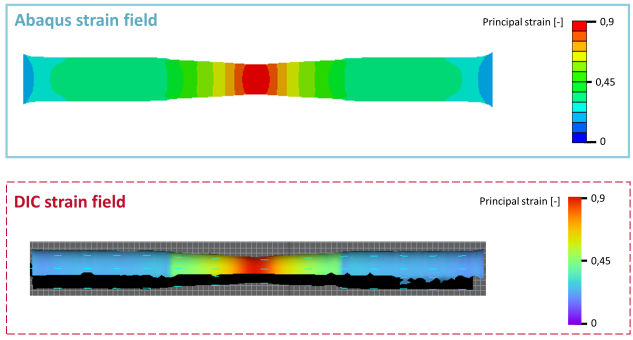

χ_A^{90} - Strain fields at a maximum strain level of 0.9.

Strain fields from DIC and Abaqus during necking.

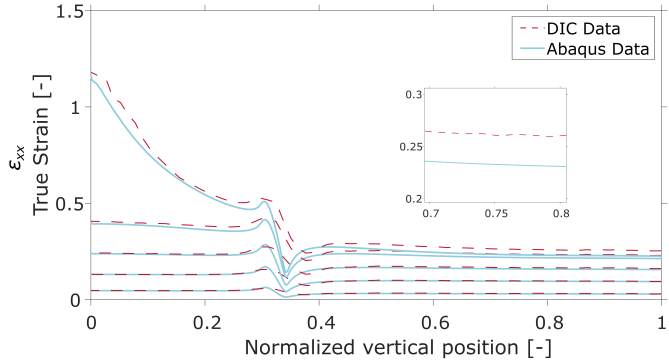

(d) χ_L^{25} - True strain along gauge length (15 mm).

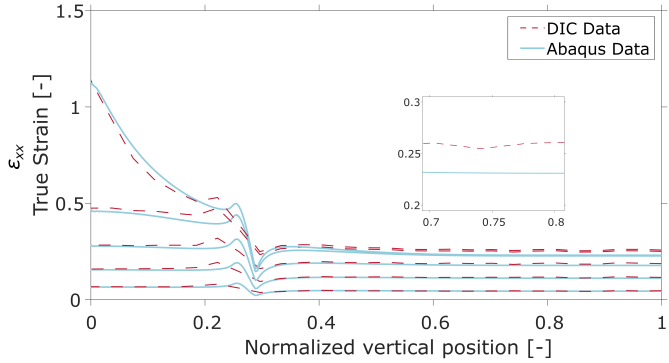

(e) χ_L^{20} - True strain along gauge length (15 mm).

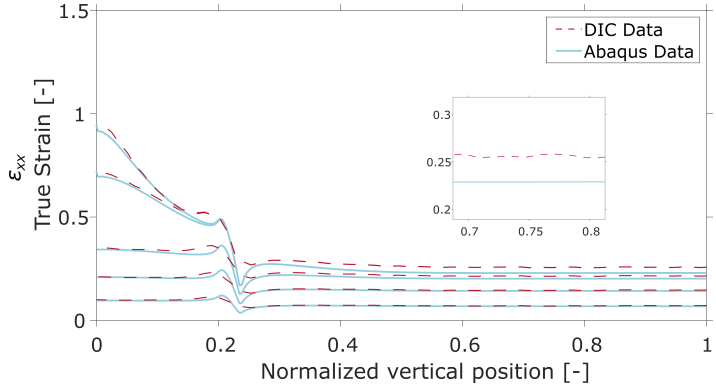

(f) χ_L^{16} - True strain along gauge length (15 mm).

Figure 8.20 Superposition of deformation fields from DIC and Abaqus (cont.).

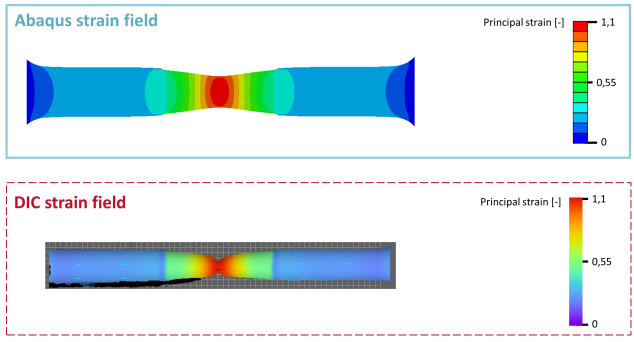

χ_L^{25} - Strain fields at a maximum strain level of 1.1.

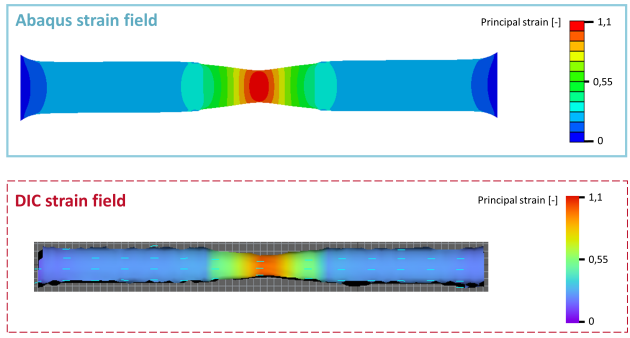

χ_L^{20} - Strain fields at a maximum strain level of 1.1.

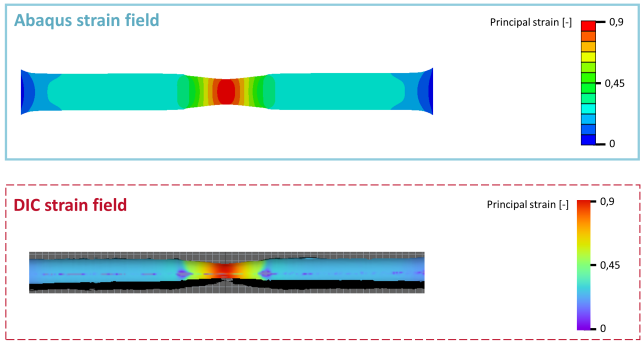

χ_L^{16} - Strain fields at a maximum strain level of 0.9.

Strain fields from DIC and Abaqus during necking (cont.).

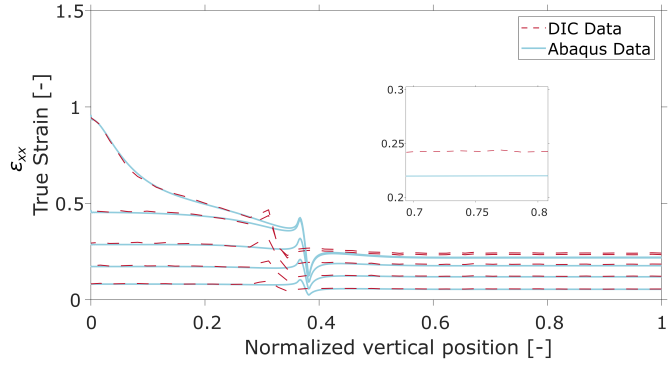

(g) χ_{LD}^{300} - True strain along gauge length (35 mm).

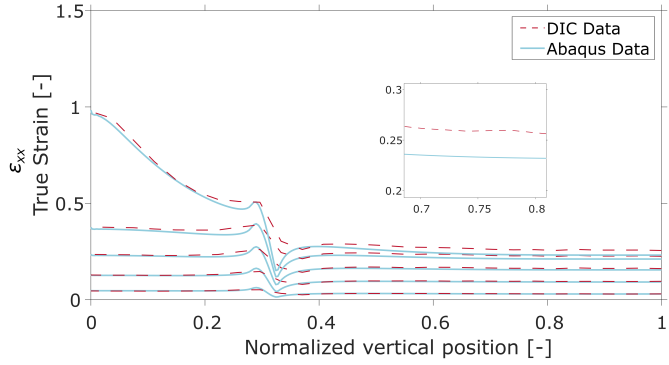

(h) χ_{LD}^{100} - True strain along gauge length (15 mm).

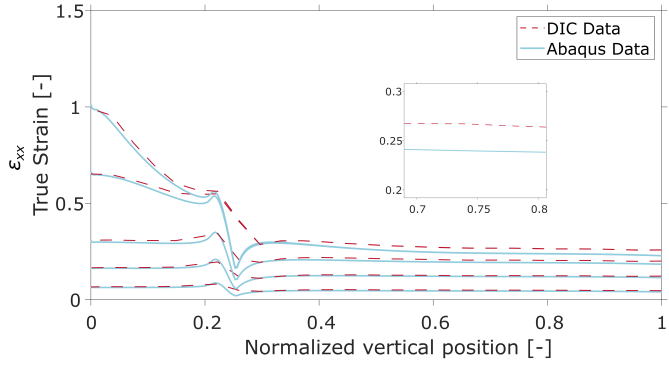

(i) χ_{LD}^{75} - True strain along gauge length (15 mm).

Figure 8.20 Superposition of deformation fields from DIC and Abaqus (cont.).

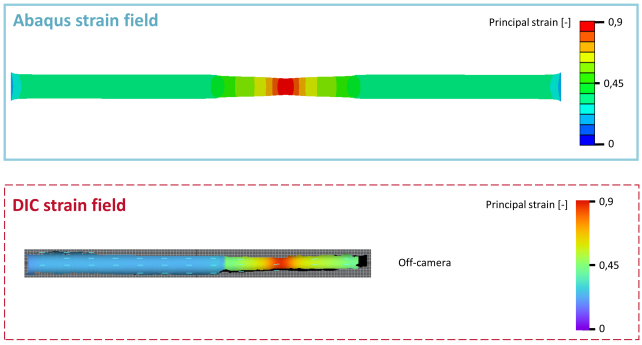

χ_{LD}^{300} - Strain fields at a maximum strain level of 0.9.

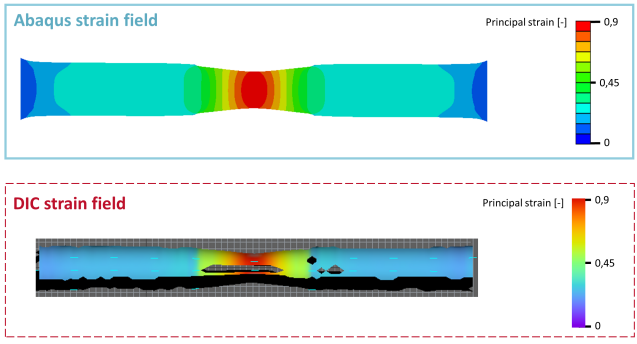

χ_{LD}^{100} - Strain fields at a maximum strain level of 0.9.

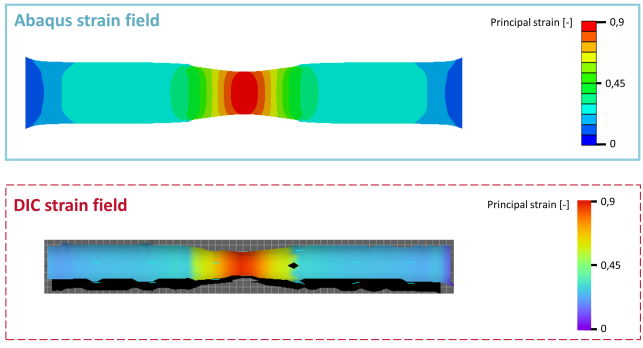

χ_{LD}^{75} - Strain fields at a maximum strain level of 0.9.

Strain fields from DIC and Abaqus during necking (cont.).

From all 9 subfigures, a relatively good agreement between DIC and numerical model is found. The main discrepancies are the followings

- After necking, the strain measured in the outer zone is larger than the one predicted by the simulations for all samples with an imperfection.
- For all samples with varying cross-sections, a wavy deformation profile is observed at the position of the diameter change. However, for some samples, a misalignment of this wave between the two profiles is found. In addition, the wave in the numerical results is accentuated compared to experimental data.
- The experimental strain profile in the neck is not always perfectly matching the numerical results. It is sometimes overestimated (as in χ_{LD}^{100}) and sometime underestimated (as in χ_{A}^{98}).

The origin of the difference in strain in the outer zone could originate from the material properties given to the numerical model. Indeed, the postpeak hardening law was not extracted from the uniaxial tensile test, and thus the approximation can generate variations in strain response.

A wavy pattern is observed in all samples with geometrical imperfections. By looking at the FEA strain contour, peak and drop positions are clearly identified (see Figure 8.21). The strain drop is positioned in a zone which is not mechanically stresses as it is in the external corner. The strain peak is positioned at a place which experience a diagonal component of the stress due to nearby fillet.

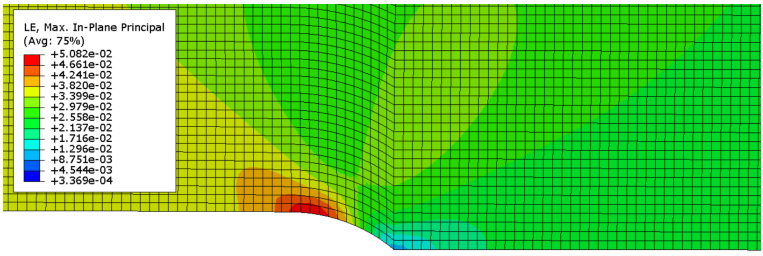

Figure 8.21 χ_{L}^{25} strain contour from FE model at the imperfection surroundings.

The most likely origin for the wave misalignment between DIC and Abaqus data, is because the neck position was always centered in the numerical

model, while it was not always the case in real test condition. Finally, the numerical model show an accentuated wavy pattern compared to values extracted by DIC. As represented by Figure 8.22, the FE results have a larger discretisation than DIC results. Using a smaller facet size in DIC analysis could reconcile the shapes of the wave.

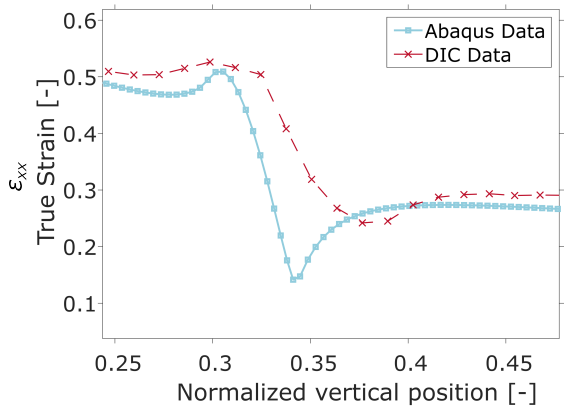

Figure 8.22 Comparison of χ_L^{25} strain field at the imperfection surroundings.

Finally, the strain discrepancies in the neck can come from the combination of theses two origins: poor approximation of postpeak hardening law and misalignment in neck position. However, it is important to point out that the global fitting is good.

The next section will compare profiles among the numerical model to assess the effect of the three adimensional parameters.

8.3.2 Comparison of neck length based on imperfection characteristic dimensions

Figure 8.23 superimposes the numerical strain profile at the central integration points, along the whole surface element set when the maximum strain is equal to 1. The horizontal axis coordinate is defined as :

$$\frac{x - x_{neck}}{D_i}. \tag{8.15}$$

This normalization allows comparing the neck developments for any initial diameter.

Figure 8.23a shows that slightly away from the middle of the neck, the three curves overlap with an identical slope. However, since the strain in the outer zone of χ_A^{90} is lower than the strain of χ_A^{98} (which is respectively lower than the one of χ_A^{100}), the slope continues over a greater distance in the sample. The smaller is χ_A, the wider is the neck.

Figure 8.23b shows strain profile for χ_L parameter. One can observed that the neck develops in a strictly similar way for any values.

Finally, the χ_{LD} variable plays an important role in controlling the neck development. As illustrated by 8.23c, the neck width increases with χ_{LD} evolution. As a matter of fact, while the strain profile decreases progressively in the neck, the strain experience a large drop at the imperfection boundaries. Therefore, the further this boundary is, the larger the neck will be.

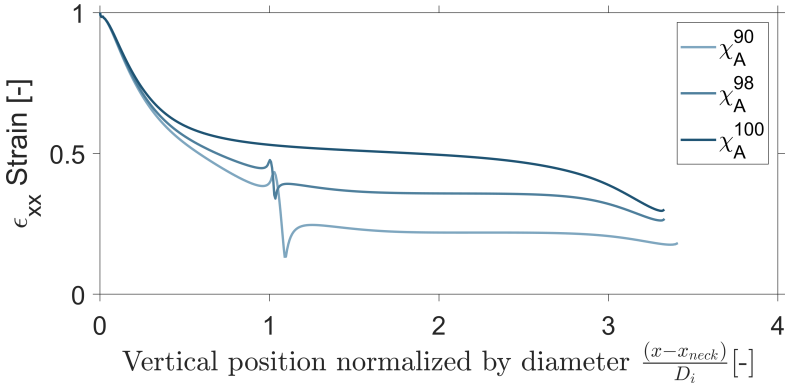

(a) Strain fields from numerical simulation for the parameter χ_A.

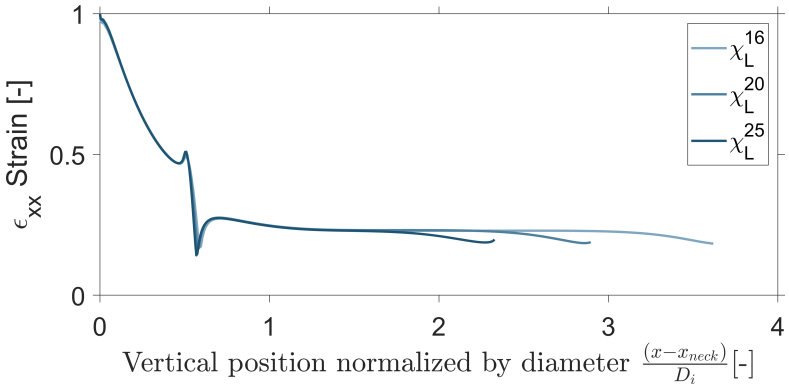

(b) Strain fields from numerical simulation for the parameter χ_L.

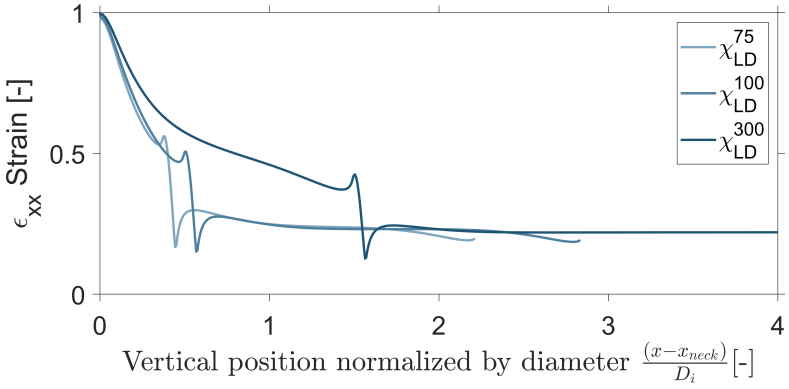

(c) Strain fields from numerical simulation for the parameter χ_{LD}.

Figure 8.23 Strain fields from numerical simulation.

Bridgman expressions are commonly used to evaluate stress triaxiality after onset of necking [166]. It states that when the neck radius decreases, the triaxiality increases. Moreover, higher triaxiality can lead to lower fracture strain [167]. Apart for χ_L, the others adimensional parameters appears to have an impact on neck width as presented in Figure 8.23. However, the change in neck width does not appear to have a big impact on stress triaxiality as the fracture strains, measured on DIC samples, are not varying significantly as illustrated by Figure 8.24

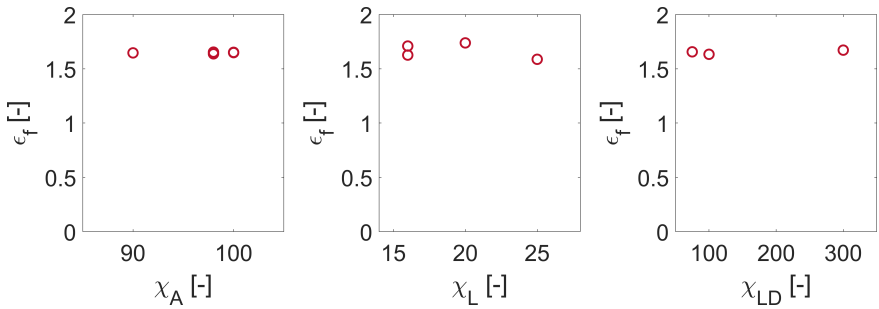

Figure 8.24 Fracture strains obtained by profile projection on DIC sample post-mortem.

8.3.3 Total elongation criteria

This last section will define a *total elongation criteria*. Considering a structural part of initial length L_0, and suppose that the field of application requires that this part extends to a length L_f. The final elongation goal can be expressed as:

$$\epsilon^*_{tot} = \frac{L_f - L_0}{L_0}. \tag{8.16}$$

If the structure present an imperfection, its total elongation capacity will be impact. While ϵ^{max}_{tot} is greater than ϵ^*_{tot}, the imperfection is not problematic. The goal of this Section is to assess the respective importance of the 3 adimensional parameters on the decrease in total elongation capacity of a structure.

In the experiments, the total elongation is defined as the difference in length of the 3 zones ($L = 2L_o + L_i$) compared to the initial length:

$$\epsilon_{tot} = \frac{L - L_0}{L_0}. \tag{8.17}$$

Figure 8.25 shows how the total elongation at the onset of necking and at fracture event evolves for each parameter.

Reducing the inner diameter (changing χ_A), while keeping χ_L and χ_{LD} constant, has a marked effect. Figure 8.25a shows that the achievable total elongation is drastically reduced going from $\chi_A = 100\%$ to $\chi_A = 90\%$. This can be linked to the fact that the strain level reached in the outside zone is limited due to force equilibrium. It is in agreement with the conclusions of Christodoulou and Jonas [158].

Figure 8.25b indicates that a lower χ_L gives smaller elongation capacity. As χ_A is constant for the 3 samples, the strain levels reached in both zones (ϵ_i and ϵ_o) are supposed to be the same for all χ_L values. If the length of the inner zone takes a larger part of the total length (i.e. χ_L increases), the area which undergoes larger strains ($\epsilon_i > \epsilon_o$) will contribute more to the total elongation and therefore, the total elongation is larger for higher χ_L. These results are in agreement with the observations made by Christodoulou and Jonas [158].

The last graph in Figure 8.25, represent the elongation for samples with χ_{LD}=75% and 100%. This parameter has not been studied in the literature yet. The third geometry (χ_{LD}=300%) was not included in this graph because DIC measurements did not allow to capture the whole length of the sample[1]. The two remaining samples are close to one another, which do not allow to have a clear view on the effect of χ_{LD} parameter. However a decreasing trend is expected with larger χ_{LD}. When χ_{LD} is getting larger, the neck has more and more space to develop inside the reduced section. Conversely, if χ_{LD} decreases, the reduced section is too narrowed to contain the whole neck profile. The outer region, close to the imperfection will undergo larger strain which give to the total structure a larger total elongation capacity.

The strain difference between onset of necking and fracture is kept constant

[1]Using numerical simulation, the total elongation at necking can be estimated at 0.32 [-]. This value is reliable as the values for 75% and 100% were validated by the same way.

for all imperfections as illustrated by Figure 8.25. A reduced spacing could be observed in material with higher triaxiality as fracture strain would be lower. However, as shown previously in Figure 8.24, the fracture strain is not significantly modified here and therefore, the strain gap between necking onset and fracture is constant.

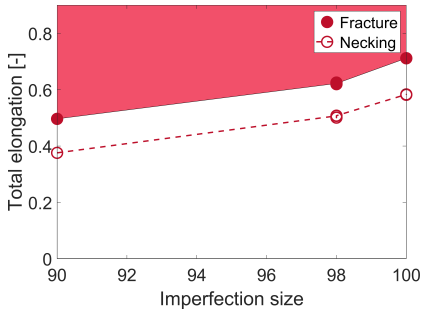

(a) Total elongation as a function of χ_A.

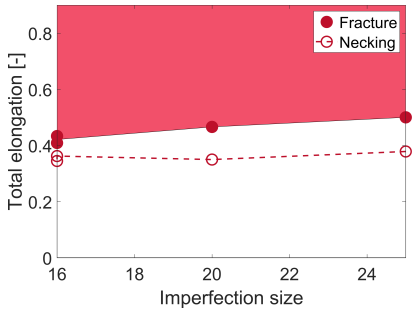

(b) Total elongation as a function of χ_L.

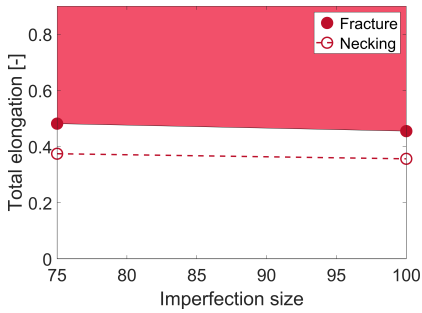

(c) Total elongation as a function of χ_{LD}.

Figure 8.25 Elongation of the whole structure obtained by DIC.

8.3.4 Discussion

Taking a step back from the analyses carried out above, it is logical to ask how these results can be used in a more practical point of view. The presence of imperfections is generally noticed after the machining stage, or during visual inspection once the part is in service. The total length (L_{tot}) of the structure is thus fixed, and it is therefore more natural to focus the discussion on the section variation (χ_A) as well as the imperfection width (L_i).

The imperfection depth is the major key parameter for elongation capacity. By increasing its depth, χ_A decreases while χ_{LD} increases. The first effect is on the total elongation capacity. Indeed, as the deformation reached outside from the imperfection will be significantly reduced, it will greatly reduce the total elongation capacity of the structure. It is worth noticing that this reduction of section will have a second detrimental effect on loading capacity of the structure. It is therefore necessary to determine to what extent this section modification reduces, or exceeds, the safety factor initially put in the specifications.

If a narrow imperfection (small L_i) is found in the structure, the question of re-machining to increase its length, L_i (without modifying χ_A) could arise. As a matter of fact, this re-machining will not have the effect of changing the load capacity of the structure. By lengthening the imperfection, L_i/L_{tot} will increase, as will L_i/D_i. By increasing χ_L, this will have the effect of allowing greater elongation of the whole structure, while χ_{LD} has an opposite but lower effect. In the ranges of values analyzed, in this study, increasing imperfection length could result in a really small enhancement of the elongation potential.

In the context of stents, the typical strut size range between 120 and 50 µm [124, 125]. Thinner strut size are preferred over larger struts for their good deliverability and lower risk of developing angiographic restenosis. The mean roughness coefficient (R_a) of 316L implants are limited by the an ISO standard (PN-EN ISO 14630) to 0.16 µm [168]. The arithmetical mean roughness value (R_a) does not represent the largest imperfection size in a rough profile as illustrated by Figure 8.26. Values as R_z, the mean roughness depth, gives a better approximation of the amplitude of local imperfections. However, this value could be divided by 2 to consider only the groove depth with respect to the mean surface profile.

In the EN ISO 4288 norm, the R_a amplitudes of 0.1 to 2 µm are associated

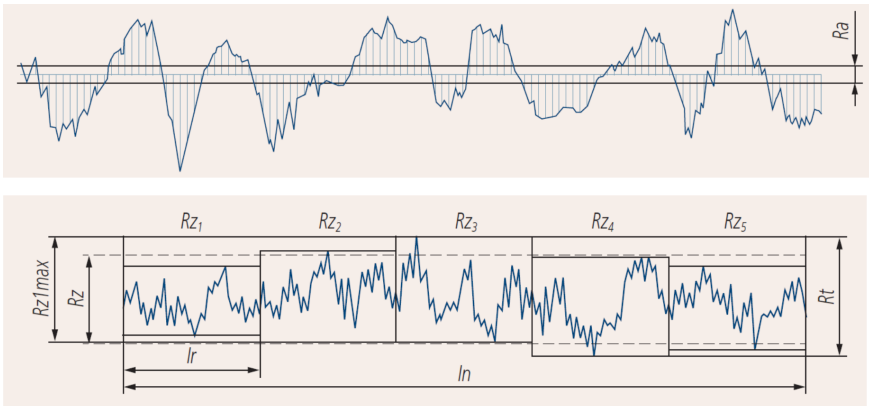

Figure 8.26 Comparison of R_a, R_t and R_z - [169].

to R_z of 0.5 to 10 µm [169]. Considering an annular reduction of section of 0.25 µm over a strut thickness of 50 µm, χ_A parameter is equal to 98%. As it has been presented before, the impact of such area reduction is not negligible on total elongation capacity. Indeed, this amplitude of imperfection resulted in a 15% drop of total elongation capacity. However, in the literature on stent specifications, it is common to find a requirement of 20% elongation [170, 171]. The material tested in this research always reached a minimum 34 % for imperfect conditions.

Cross-section reduction in a stent, originating from its roughness, has in fact a really small length L_i with respect to the strut length. It constitutes a major difference between this study and stent application which is kept for further investigation.

8.4 Conclusions and perspectives

The effect of geometry imperfection on a bar subjected to uniaxial tension was observed by comparing the predictions of an analytical model, numerical simulations and experimental results. Here are the main outcomes of the fundamental approach from this study:

- All the predictions were relatively in good agreement with the measured strain levels inside and outside the imperfection before necking.

- After necking, the experimental measurements were slightly higher than the one predicted which probably results from a poor approximation of the strain hardening law after necking in the numerical model.
- The numerical simulations predict well the strain field in the neck.
- Among the three adimensional parameters, χ_A, χ_L and χ_{LD}, only those including the diameter of the imperfection had a noticeable impact on neck development.

By looking at the applied side of this research, we concluded that the imperfection depth is the key parameter to limit the elongation capacity of a structure, while its length plays a limited role.

To answer the question: *What are the limits in dimension for an imperfection on a stent strut?* further studies are needed. Indeed, when a structure is damaged in shaping process, the imperfection is rarely uniform all around the structure. Therefore an assessment of such asymmetric or irregular imperfections should be done. Moreover, it would be interested to downscale the experimental setup. At such scales, it becomes important to consider statistical scattering of the results. To increase the number of results without becoming time-consuming, structures as the one presented in Figure 8.27, could be further developed. A preliminary trial was done on such structure and gave interesting results which will not be described further in this manuscript.

In addition to scattered results, small-sized metallic specimens exhibit changes in mechanical properties, known as the *size effect*. One of these effects, as discussed in Chapter 7, involves a reduction in ductility (in terms of fracture strain) as the specimen diameter decreases. As the number of grains across the thickness decreases, the presence of a less well-oriented grain cannot be compensated for by better-oriented neighboring grains [143]. In the presence of an initial imperfection, the grain orientation distribution is also responsible for an increase in result scattering. Indeed, an imperfection located at the level of grains with different orientations could alter the mechanical responses. Finally, even in a hypothetical imperfection-free specimen, surface roughness develops upon straining, as plastic strain promotes crystal lattice rotation [172]. At such a small scale, roughness introduced by grain rotation of a few microns can already represent a local reduction of a few percentage points in diameter.

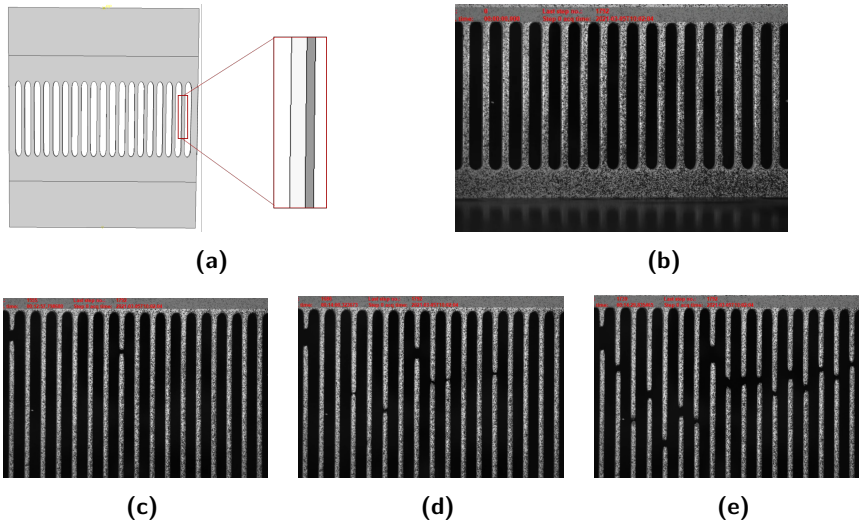

Figure 8.27 Multi-tensile sample (a) Sketch; (b) Sample ready for DIC testing; (c) Picture after 2 failures; (d) Picture after 7 failures; (e) Picture after complete failures of the sample.

Finally, the deployment sequence of a stent strut is composed of two stages: flexion to unfold followed by tensile loading. The effect of loading path on imperfection stability is therefore still an open question.

9

Conclusions and perspectives

The general objective of this thesis is to *contribute to an enhancement of the lifetime of biomedical implants, with an emphasis on growing rods*.

To achieve this objective, it was necessary to develop a new experimental method, which was presented in *Chapter 5* and illustrated by Figure 9.1. This setup was designed to maintain a rod in its unstable position, in 3-pt bending test, during cyclic loading. The yield force was observed to vary with the bending angle in both the numerical simulations and the experiments. After validating the setup for use in monotonic and cyclic operations, two fatigue protocols were compared based on either strain or force control. The main outcome of this assessment is that the type of protocol can significantly modify the conclusions of an experimental campaign: it should be carefully selected based on the context and the purpose of the study.

9.1 Increasing the fatigue resistance of growing rods

Chapters 4 and *6* aimed at unravelling the effect of plastic deformation in growing rods on their fatigue life. As internal stresses were suspected to

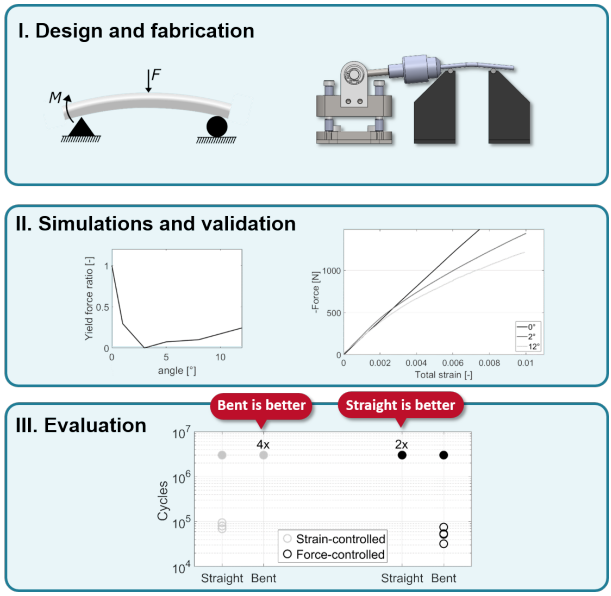

Figure 9.1 Design of a new fatigue setup: Main ideas compiled from *Chapter 5*.

be the main issue, a finite element model based on an advanced hardening law was developed in *Chapter 4*. Using this model, a parametric analyses allows establishing the respective influence of multiple parameters on fatigue resistance. As summarized in Figure 9.2, hardening properties such as the initial **yield stress** and the **hardening coefficients** as well as the **initial residual stress state** have major influence on the final stress in the rods. The shot-peening depth and bending angle, on the other hand, play a minor role.

Given that growing rods undergo several plastic loadings, the model has demonstrated the importance of choosing the appropriate work hardening type to reproduce measured stress fields. For Ti-6Al-4V, selecting a kinematic hardening law is essential. To guide material selection towards further improvement in their fatigue strength, a reduction of the yield point while promoting kinematic hardening seem promising. Shot-peening is a good practice aiming at reducing internal stress but the subsequent bending process significantly modifies the stress level. As rods are slightly bent, the stress level increases suddenly while it tends to level off for larger an-

gles, suggesting that if surgeons need to bend the rod, they can apply any angle with similar outcomes.

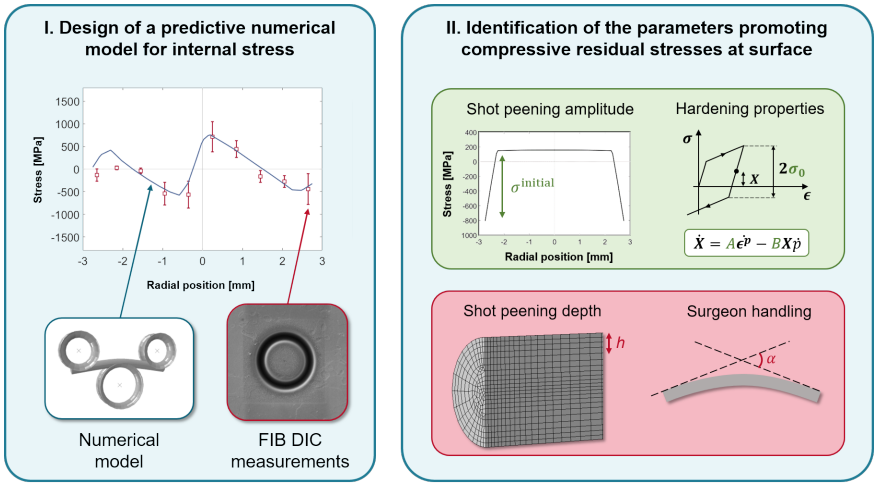

Figure 9.2 Identification of the major and minor parameters to introduce compressive stresses at rod surface based on the numerical model developed in *Chapter 4*.

Using the aforementioned setup, the impact of plastic deformation (associated to shot-peening and bending) on fatigue resistance was experimentally evaluated in *Chapter 6*. After a comparison of failure patterns with the in-vivo broken rods, two fatigue protocols were tested: (i) a series of force-controlled tests supposed to mimic solicitations where the child imposes a specific bending moment to the rod, for example when carrying a load (Figure 9.3a), and (ii) a series of strain-controlled tests which represent actions of the child of a given amplitude, such as dressing up in the morning (Figure 9.3b). As in the literature, a decrease in strength between straight and bent rods was observed in the force-controlled protocol. However, and perhaps most importantly, the main outcome of this study is that contoured rods show identical levels of fatigue resistance whatever the bending angle. As concerns the influence of the shot-peening process on fatigue resistance, it turns out that the shot-peened rods (certified as *growing rods*) fail approximately after 70,000 cycles, as compared to untreated rods (from a non-healthcare supplier) which in some instances hold 3,000,000 cycles without failure. The fatigue resistance of growing rods can thus be related to a frequency of in-vivo solicitation of 1 every 10 minutes. The better fa-

tigue life of untreated rods raises the question of the importance of the various parameters influencing fatigue life.

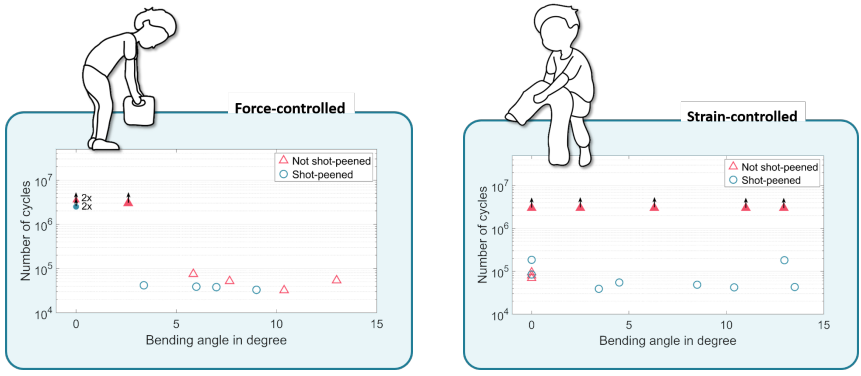

(a) (b)

Figure 9.3 Fatigue results from *Chapter 6*: (a) for a force-controlled protocol (F=1470N) and (b) for a strain-controlled protocol (ϵ=0.011).

All the work suggests that, contrary to our initial expectations, the level of stress in the rods is not enough to predict directly their fatigue life. As illustrated by Figure 9.4 a presumed relative importance degree among the various parameters emerges when compiling results from *Chapters 4*, *6* and from *Appendix A*. First, polishing shot-peened rods has led to a clear improvement in fatigue properties: **Roughness** should therefore be addressed in priority by ensuring the smoothest surface finish. The choice of **rod contouring** during surgery comes second in terms of importance. This choice (i.e. keeping the rod straight or bending it), as already mentioned in the literature and confirmed by controlled force tests, reduces the life expectancy of the rods by significantly increasing the level of internal stresses in the rod as well as by decreasing their yield strength. At a relatively similar level of importance, we find the amplitude of **shot-peening**. Apart from the roughness increase induced by the process, the compressive stresses introduced at rod periphery can significantly increase fatigue resistance in straight rods. However, this improvement is not as marked once the rods have been plastically deformed during bending. **Material selection** is placed at the next level. Among the materials used for growing rods nowadays, Ti-6Al-4V already has a high endurance limit (as compared to Co-Cr or TiCP2). However, one can hope to improve the fatigue

strength of bent rods by adapting the microstructure of the alloy so as to develop a maximum of residual stresses in compression. Finally, considering contoured rods, the **bending angle** does not affect significantly their internal stress state nor their fatigue resistance.

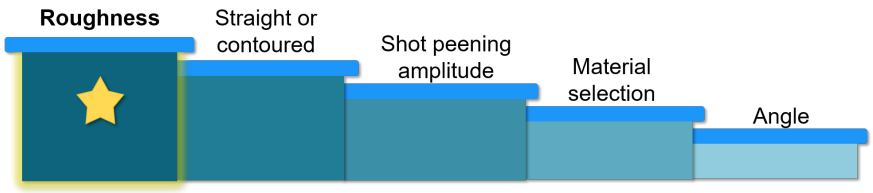

Figure 9.4 Presumed classification of the importance degree of various parameters on growing rod lifetime.

As indicated above, a more in-depth study of the roughness of the growing rods, considering realistic ways of improving their surface condition, seems to be a priority. A study comparing straight and bent samples with different surface conditions (in terms of roughness and internal stresses) would allow assessing the relative importance of these different parameters. Future work could also focus on other techniques used commonly by surgeons, e.g. contouring correction (by *de-bending*) or multiple adjacent bending to achieve larger angles. The advantage of this type of study is that the solutions found can be implemented rapidly, as they depend solely on the surgeons' practices. The development of an optimized microstructure, in biocompatible materials, for improving fatigue resistance, is a technical challenge left for future considerations as it would require more time before being implemented at an industrial scale. Finally, the developed fatigue setup paves the way for a wide range of analyses on different materials with multiple plastic deformation backgrounds. At first, one could study materials with different hardening modes as their respective strain-hardening mechanisms could induce variation in fatigue resistance. Moreover, fatigue resistance increases with tensile strength and ductility. As these properties are usually a trade-off, the question arises whether one of them has a predominant influence on the fatigue resistance of bent components.

9.2 Geometrical imperfections in long metallic components

The analyses of the presence of necking in components displaying geometric inhomogeneities, carried out in *Chapter 8*, showed that the analytical and numerical methods were reliable for predicting the strain levels obtained experimentally by DIC. The origins of the variations in the deformation field have been perfectly identified and explained as illustrated by Figure 9.5. Subsequently, the adimensional geometric parameters that have the main effect on strain development were identified, and include **cross-sectional variation** (i.e. imperfection depth) as well as the **ratio between diameter and width**. The depth of the imperfection was also found to be the most significant effect on the total elongation capacity of a structure loaded in uniaxial tension.

Although these results cannot be directly applied to biomedical applications such as stents, they do contribute to a better understanding of fundamental principles such as the development of a localization phenomenon within an inhomogeneous metallic structure. They could subsequently be adapted to smaller, more complex structures such as stents or structures dominated by elongation. Indeed, going down to smaller scales, the ratio between volume and free surface decreases, which is known to have an effect on the mechanical behavior of structures. One can wonder if surface effects could influence necking dimensions and if the geometric parameters of an inhomogeneity would have similar effects.

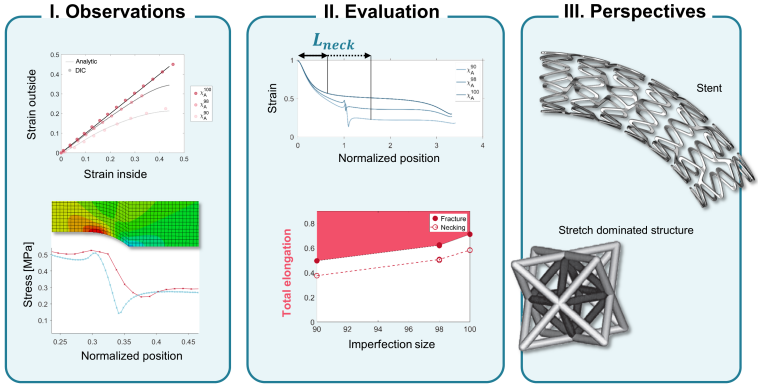

Figure 9.5 Overview of the results obtained in *Chapter 8*.

Bibliography

[1] H. Hermawan and D. Mantovani, "Process of prototyping coronary stents from biodegradable fe–mn alloys", Acta biomaterialia **9**, 8585–8592 (2013).

[2] M. James, "Residual stress influences on structural reliability", Engineering Failure Analysis **18**, 1909–1920 (2011).

[3] L. Doremus, "Etude expérimentale et modélisaton de la micro-propagation à partir d'anomalies de surface dans l'inconel 718da", PhD thesis (ISAE-ENSMA Ecole Nationale Supérieure de Mécanique et d'Aérotechique-Poitiers, 2014).

[4] F. C. Campbell, *Fatigue and fracture: understanding the basics* (ASM International, 2012).

[5] S. B. Block, R. D. da Silva, L. B. Dorini, and R. Minetto, "Inspection of imprint defects in stamped metal surfaces using deep learning and tracking", IEEE Transactions on Industrial Electronics **68**, 4498–4507 (2020).

[6] *Description, reasons and remedies of common sand casting defects*, `https://www.steel-foundry.com/news/description-reasons-and-remedies-of-common-sand-casting-defects/`, [Online; Page available on 28-October-2023], 2021.

[7] J. Park and R. S. Lakes, *Biomaterials: an introduction* (Springer Science and Business Media, 2007).

[8] R. Sobot, *Implantable technology*, `https://technologyandsociety.org/implantable-technology/`, [Online; Page available on 30-June-2023], 2019.

[9] FDA Administration, *Implants and prosthetics*, https://www.fda.gov/medical-devices/products-and-medical-procedures/implants-and-prosthetics, [Online; Page available on 30-June-2023].

[10] L. A. Pruitt and A. M. Chakravartula, *Mechanics of biomaterials: fundamental principles for implant design* (Cambridge University Press, 2011).

[11] R. Magjarevic and B. Ferek-Petric, "Implantable cardiac pacemakers-50 years from the first implantation", Zdravniski Vestnik **79**, 55–67 (2010).

[12] Oticon Medical, *Implant cochléaire: manuel d'utilisation*, https://www.oticonmedical.com/, [Online; Page available on 30-June-2023], 2015.

[13] X. Wang, S. Xu, S. Zhou, W. Xu, M. Leary, P. Choong, M. Qian, M. Brandt, and Y. M. Xie, "Topological design and additive manufacturing of porous metals for bone scaffolds and orthopaedic implants: a review", Biomaterials **83**, 127–141 (2016).

[14] Rocdacier, *Essai de traction!*, https://www.rocdacier.com/essai-de-traction-2/, [Online; Page available on 28-June-2023], 2017.

[15] T. Hanawa, "Overview of metals and applications", in *Metals for biomedical devices* (Elsevier, 2019), pp. 3–29.

[16] C. Yurij, *History of implantology: part i*, https://uniqa.dental/articles/history-of-implantology/, [Online; Page available on 27-June-2023], 2023.

[17] R. Thull, "Surface treatment", in *Metals for biomedical devices* (Elsevier, 2010), pp. 251–259.

[18] C. Moseke and U. Gbureck, "Surface treatment", in *Metals for biomedical devices* (Elsevier, 2019), pp. 355–367.

[19] L. Li, N. Mirhosseini, A. Michael, Z. Liu, and T. Wang, "Enhancement of endothelialisation of coronary stents by laser surface engineering", Lasers in Surgery and Medicine **45**, 608–616 (2013).

[20] J. E. Davies, V. C. Mendes, J. C. Ko, and E. Ajami, "Topographic scale-range synergy at the functional bone/implant interface", Biomaterials **35**, 25–35 (2014).

[21] M. Niinomi, "Fatigue failure of metallic biomaterials", in *Metals for biomedical devices* (Elsevier, 2019), pp. 153–188.

[22] P. Dearnley, "A brief review of test methodologies for surface-engineered biomedical implant alloys", Surface and Coatings Technology **198**, 483–490 (2005).

[23] ANSYS, *Mechanical structural nonlinearities - rate independent plasticity*, Customer Training Material (2010).

[24] W. F. Hosford and R. M. Caddell, *Metal forming: mechanics and metallurgy* (Cambridge University Press, 2011).

[25] Y. Ling et al., "Uniaxial true stress-strain after necking", AMP Journal of technology **5**, 37–48 (1996).

[26] Z. Marciniak and K. Kuczyński, "Limit strains in the processes of stretch-forming sheet metal", International journal of mechanical sciences **9**, 609–620 (1967).

[27] W. F. Hosford, *Mechanical behavior of materials* (Cambridge university press, 2010).

[28] C. Clinic, *Stress fractures*, `https://my.clevelandclinic.org/health/diseases/15841-stress-fractures`, [Online; Page available on 18-october-2023], 2023.

[29] J. Li and H. Gong, "Fatigue behavior of cortical bone: a review", Acta Mechanica Sinica **37**, 516–526 (2021).

[30] J. R. Kardouni, C. J. McKinnon, K. M. Taylor, and J. M. Hughes, "Timing of stress fractures in soldiers during the first 6 career months: a retrospective cohort study", Journal of Athletic Training **56**, 1278–1284 (2021).

[31] Hand and wrist center, *Common hand injuries musicians should be wary about*, `https://northfloridahandandwrist.com/hand-injuries-musicians/`, [Online; Page available on 18-october-2023], 2022.

[32] M. M. Pedersen, "Introduction to metal fatigue", Technical report ME-TR-11, 91 (2018).

[33] S. Suresh, *Fatigue of materials* (Cambridge university press, 1998).

[34] E. Macherauch, "Introduction to residual stress", Advances in surface treatments **4**, 1–36 (2014).

[35] G. E. Totten, *Handbook of residual stress and deformation of steel* (ASM international, 2002).

[36] T. Pardoen, "LMAPR2483 durability of materials, chapter III residual stresses", unpublished.

[37] A. Korsunsky, *A teaching essay on residual stresses and eigenstrains* (Butterworth-Heinemann, 2017).

[38] P. J. Withers and H. Bhadeshia, "Residual stress. part 1 - measurement techniques", Materials science and Technology **17**, 355–365 (2001).

[39] J. Vaara, A. Kunnari, and T. Frondelius, "Literature review of fatigue assessment methods in residual stressed state", Engineering Failure Analysis **110**, 104379 (2020).

[40] S. Breumier, "Methodology for shot-peening induced intragranular residual stress prediction", PhD thesis (Ecole Polytechnique, Montreal (Canada), 2021).

[41] J. Almen, "Shot blasting to increase fatigue resistance", SAE Transactions, 248–268 (1943).

[42] J. S. Chen, D. A. Desai, S. P. Heyns, and F. Pietra, "Literature review of numerical simulation and optimisation of the shot peening process", Advances in Mechanical Engineering **11**, 1687814018818277 (2019).

[43] R. C. Juvinall and K. M. Marshek, *Fundamentals of machine component design* (John Wiley and Sons, 2020), pp. 172–173.

[44] R. McClung, "A literature survey on the stability and significance of residual stresses during fatigue", Fatigue and Fracture of Engineering Materials and Structures **30**, 173–205 (2007).

[45] J. Morrow and G. Sinclair, *Cycle-dependent stress relaxation* (ASTM International, 1959).

[46] S. Kodama, "The behavior of residual stress during fatigue stress cycles", in Proceedings of the international conference on mechanical behavior of metals ii, Vol. 2 (Society of Material Science Kyoto, 1972), pp. 111–118.

[47] J.-C. Kim, S.-K. Cheong, and H. Noguchi, "Residual stress relaxation and low-and high-cycle fatigue behavior of shot-peened medium-carbon steel", International Journal of Fatigue **56**, 114–122 (2013).

[48] T. Klotz, D. Delbergue, P. Bocher, M. Lévesque, and M. Brochu, "Surface characteristics and fatigue behavior of shot peened inconel 718", International Journal of Fatigue **110**, 10–21 (2018).

[49] D. François, A. Pineau, and A. Zaoui, *Mechanical behaviour of materials: volume 1: micro-and macroscopic constitutive behaviour*, Vol. 180 (Springer Science and Business Media, 2012).

[50] O. Bouaziz, H. S. Kim, J. Lee, and Y. Estrin, "Bauschinger effect or kinematic hardening: bridging microstructure and continuum mechanics", Metals and Materials International **29**, 280–292 (2023).

[51] G. Fribourg, Y. Bréchet, A. Deschamps, and A. Simar, "Microstructure-based modelling of isotropic and kinematic strain hardening in a precipitation-hardened aluminium alloy", Acta Materialia **59**, 3621–3635 (2011).

[52] L. E. Levine, M. R. Stoudt, A. Creuziger, T. Q. Phan, R. Xu, and M. E. Kassner, "Basis for the bauschinger effect in copper single crystals: changes in the long-range internal stress with reverse deformation", Journal of Materials Science **54**, 6579–6585 (2019).

[53] Ortheo, *Colonne vertébrale : cyphose, lordose, scoliose*, `http://blog.ortheo.com/general/colonne-vertebrale-cyphose-lordose-scoliose`, [Online; Page available on 05-January-2017], 2015.

[54] A. A. Baaj and P. V. Mummaneni, *Handbook of spine surgery* (Thieme, 2011).

[55] D. K. K. Dutta, *Scoliosis seminar*, `http://fr.slideshare.net/kaushikdutta1884/scoliosis-seminar`, [Online; Page available on 28-December-2016], 2015.

[56] M. B. Dobbs and S. L. Weinstein, "Infantile and juvenile scoliosis", Orthopedic Clinics of North America **30**, 331–341 (1999).

[57] M. Yazici and Z. D. Olgun, "Growing rod concepts: state of the art", European Spine Journal **22**, 118–130 (2013).

[58] V. Cunin, "Early-onset scoliosis–current treatment", Orthopaedics and Traumatology: Surgery and Research **101**, S109–S118 (2015).

[59] N. D. Fletcher and R. W. Bruce, "Early onset scoliosis: current concepts and controversies", Current reviews in musculoskeletal medicine **5**, 102–110 (2012).

[60] S. Donaldson, *Au sujet de la scoliose, qu est ce que la scoliose*, `http://www.aboutkidshealth.ca/Fr/ResourceCentres/Scoliosis-Parents/AboutScoliosis/Pages/default.aspx`, [Online; Page available on 04-January-2017], 2008.

[61] Erika, *10 interesting facts about scoliosis*, `https://www.scoliosissos.com/blog/10-interesting-facts-about-scoliosis`, [Online; Page available on 18-July-2023], 2016.

[62] M. M. Janssen, R. F. de Wilde, J.-W. M. Kouwenhoven, and R. M. Castelein, "Experimental animal models in scoliosis research: a review of the literature", The spine journal **11**, 347–358 (2011).

[63] H. Xie, M. Li, Y. Kang, J. Zhang, and C. Zhao, "Zebrafish: an important model for understanding scoliosis", Cellular and Molecular Life Sciences **79**, 506 (2022).

[64] L. Miladi and M. Mousny, "A novel technique for treatment of progressive scoliosis in young children using a 3-hook and 2-screw construct (h3s2) on a single sub-muscular growing rod: surgical technique", European Spine Journal **23**, 432–437 (2014).

[65] H. Yoshihara, "Rods in spinal surgery: a review of the literature", The Spine Journal **13**, 1350–1358 (2013).

[66] ANSYS, Inc., *Ansys granta edupack software*, Cambridge, UK, 2023.

[67] O. Takakuwa, M. Nakai, K. Narita, M. Niinomi, K. Hasegawa, and H. Soyama, "Enhancing the durability of spinal implant fixture applications made of Ti-6Al-4V eli by means of cavitation peening", International Journal of Fatigue **92**, 360–367 (2016).

[68] S. Demura, H. Murakami, H. Hayashi, S. Kato, K. Yoshioka, N. Yokogawa, T. Ishii, T. Igarashi, X. Fang, and H. Tsuchiya, "Influence of rod contouring on rod strength and stiffness in spine surgery", Orthopedics **38**, e520–e523 (2015).

[69] C. Lindsey, V. Deviren, Z. Xu, R.-F. Yeh, and C. M. Puttlitz, "The effects of rod contouring on spinal construct fatigue strength", Spine **31**, 1680–1687 (2006).

[70] F. Berti, L. La Barbera, A. Piovesan, D. Allegretti, C. Ottardi, T. Villa, and G. Pennati, "Residual stresses in titanium spinal rods: effects of two contouring methods and material plastic properties", Journal of Biomechanical Engineering **140**, 111001 (2018).

[71] A. Agarwal, A. K. Agarwal, A. Jayaswal, and V. K. Goel, "Outcomes of optimal distraction forces and frequencies in growth rod surgery for different types of scoliotic curves: an in silico and in vitro study", Spine deformity **5**, 18–26 (2017).

[72] J. S. Yang, P. D. Sponseller, G. H. Thompson, B. A. Akbarnia, J. B. Emans, M. Yazici, D. L. Skaggs, S. A. Shah, P. Salari, C. Poe-Kochert, et al., "Growing rod fractures: risk factors and opportunities for prevention", Spine **36**, 1639–1644 (2011).

[73] K. Yamanaka, M. Mori, K. Yamazaki, R. Kumagai, M. Doita, and A. Chiba, "Analysis of the fracture mechanism of Ti-6Al-4V alloy rods that failed clinically after spinal instrumentation surgery", Spine **40**, E767–E773 (2015).

[74] M. A. Slivka, Y. K. Fan, and J. C. Eck, "The effect of contouring on fatigue strength of spinal rods: is it okay to re-bend and which materials are best?", Spine Deformity **1**, 395–400 (2013).

[75] A. Piovesan, F. Berti, T. Villa, G. Pennati, and L. La Barbera, "Computational and experimental fatigue analysis of contoured spinal rods", Journal of biomechanical engineering **141**, 044505 (2019).

[76] J. C. Dick and C. A. Bourgeault, "Notch sensitivity of titanium alloy, commercially pure titanium, and stainless steel spinal implants", Spine **26**, 1668–1672 (2001).

[77] M. Peters, J. Hemptenmacher, J. Kumpfert, and C. Leyens, "Structure and properties of titanium and titanium alloys", Titanium and titanium alloys: fundamentals and applications, 1–36 (2003).

[78] L. Dai and W. Song, "A strain rate and temperature-dependent crystal plasticity model for hexagonal close-packed (hcp) materials: application to α-titanium", International Journal of Plasticity **154**, 103281 (2022).

[79] Y. Wang and J. Huang, "Texture analysis in hexagonal materials", Materials Chemistry and Physics **81**, 11–26 (2003).

[80] M. Croonenborghs, K. Ismail, M. Mousny, L. Delannay, J. Everaerts, A. M. Korsunsky, P. Jacques, and T. Pardoen, "Residual Stresses in Surgical Growing Rods", Journal of Biomechanical Engineering, 1–45 (2023).

[81] G. Hill, S. Nagaraja, B. A. Akbarnia, J. Pawelek, P. Sponseller, P. Sturm, J. Emans, P. Bonangelino, J. Cockrum, W. Kane, et al., "Retrieval and clinical analysis of distraction-based dual growing rod constructs for early-onset scoliosis", The Spine Journal **17**, 1506–1518 (2017).

[82] A. Ribesse, K. Ismail, M. Croonenborghs, N. Irda, L. Miladi, P. J. Jacques, M. Mousny, and T. Pardoen, "Fracture mechanisms in Ti and Co-Cr growing rods and impact on clinical practice", Journal of the Mechanical Behavior of Biomedical Materials **121**, 104620 (2021).

[83] J. Everaerts, E. Salvati, and A. M. Korsunsky, "Nanoscale depth profiling of residual stresses due to fine surface finishing", Advanced Materials Interfaces **6**, 1900947 (2019).

[84] A. M. Korsunsky, M. Sebastiani, and E. Bemporad, "Focused ion beam ring drilling for residual stress evaluation", Materials Letters **63**, 1961–1963 (2009).

[85] M. Senn, *Digital image correlation and tracking*, `https://www.mathworks.com/matlabcentral/fileexchange/50994-digital-image-correlation-and-tracking.`, MATLAB Cent. File Exch., p. 1 [Online]. Available: Jan. 22, 2018.

[86] A. M. Korsunsky, M. Sebastiani, and E. Bemporad, "Residual stress evaluation at the micrometer scale: analysis of thin coatings by fib milling and digital image correlation", Surface and Coatings Technology **205**, 2393–2403 (2010).

[87] J. Everaerts, E. Salvati, F. Uzun, L. R. Brandt, H. Zhang, and A. M. Korsunsky, "Separating macro-(type i) and micro-(type ii+ iii) residual stresses by ring-core fib-dic milling and eigenstrain modelling of a plastically bent titanium alloy bar", Acta Materialia **156**, 43–51 (2018).

[88] A. J. Lunt and A. M. Korsunsky, "A review of micro-scale focused ion beam milling and digital image correlation analysis for residual stress evaluation and error estimation", Surface and coatings technology **283**, 373–388 (2015).

[89] I. Doghri, *Mechanics of deformable solids: linear, nonlinear, analytical and computational aspects* (Springer Science and Business Media, 2000).

[90] A. Zinovev, L. Delannay, and D. Terentyev, "Modeling strain hardening during cyclic thermal shock tests of tungsten", Journal of Nuclear Materials **546**, 152776 (2021).

[91] T. Rousseau, C. Nouguier-Lehon, P. Gilles, and T. Hoc, "Finite element multi-impact simulations using a crystal plasticity law based on dislocation dynamics", International Journal of Plasticity **101**, 42–57 (2018).

[92] J. Zhou, Z. Sun, P. Kanouté, and D. Retraint, "Reconstruction of residual stress and work hardening and their effects on the mechanical behaviour of a shot peened structure", Mechanics of Materials **127**, 100–111 (2018).

[93] Q. Xie, R. Li, Y. Wang, R. Su, J. Lian, Y. Ren, W. Zheng, X. Zhou, and Y. Wang, "The in-depth residual strain heterogeneities due to an indentation and a laser shock peening for Ti-6Al-4V titanium alloy", Materials Science and Engineering: A **714**, 140–145 (2018).

[94] J. S. Smith, C. I. Shaffrey, C. P. Ames, J. Demakakos, K.-M. G. Fu, S. Keshavarzi, C. M. Li, V. Deviren, F. J. Schwab, V. Lafage, et al., "Assessment of symptomatic rod fracture after posterior instrumented fusion for adult spinal deformity", Neurosurgery **71**, 862–868 (2012).

[95] Z. Zhang and S. Hu, "Stress and residual stress distributions in plane strain bending", International Journal of Mechanical Sciences **40**, 533–543 (1998).

[96] A. Agarwal, A. Goswami, G. P. Vijayaraghavan, A. Srivastava, P. Kandwal, U. B. Nagaraja, V. K. Goel, A. K. Agarwal, and A. Jayaswal, "Quantitative characteristics of consecutive lengthening episodes in early-onset scoliosis (eos) patients with dual growth rods", Spine **44**, 397–403 (2019).

[97] W. Roberts, J. Gong, A. J. Wilkinson, and E. Tarleton, "Tension–compression asymmetry of< c+ a> slip in ti–6al", Scripta Materialia **178**, 119–123 (2020).

[98] K. D. Kim, R. Panchal, M. Moldavsky, W. Wang, and B. S. Bucklen, "Effects of pre-contoured and in situ contoured rods on the mechanical strength and durability of posterior cervical instrumentation: a finite-element analysis and scanning electron microscopy investigation", Spine Deformity **8**, 569–576 (2020).

[99] Y.-C. Chiou and J.-K. Yang, "The effects of pre-deformation on the subsequent fatigue behaviors of sus 430 stainless steel in load-control", International Journal of Solids and Structures **49**, 3263–3268 (2012).

[100] M. Kang, Y. Aono, and H. Noguchi, "Effect of prestrain on and prediction of fatigue limit in carbon steel", International journal of fatigue **29**, 1855–1862 (2007).

[101] C. Froustey and J. L. Lataillade, "Influence of large pre-straining of aluminium alloys on their residual fatigue resistance", International journal of fatigue **30**, 908–916 (2008).

[102] Z. Zhang, J. Ødegård, O. Søvik, and C. Thaulow, "A study on determining true stress–strain curve for anisotropic materials with rectangular tensile bars", International Journal of Solids and Structures **38**, 4489–4505 (2001).

[103] M. F. Ashby, *Materials selection in mechanical design. burlington, ma*, 2011.

[104] G. R. Halford, *Fatigue and durability of structural materials* (Asm International, 2006).

[105] Q. Chen and G. A. Thouas, "Metallic implant biomaterials", Materials Science and Engineering: R: Reports **87**, 1–57 (2015).

[106] C. Leyens and M. Peters, *Titanium and titanium alloys: fundamentals and applications* (Wiley Online Library, 2006).

[107] M. Niinomi, "Mechanical properties of biomedical titanium alloys", Materials Science and Engineering: A **243**, 231–236 (1998).

[108] H. Fuchs, R. Stephens, and H. Saunders, "Metal fatigue in engineering (1980)", (1981).

[109] T. R. Waugh, "Intravital measurements during instrumental correction of idiopathic scoliosis", Acta Orthopaedica Scandinavica **37**, 1–87 (1966).

[110] T. Nguyen, J. Buckley, C. Ames, and V. Deviren, "The fatigue life of contoured cobalt chrome posterior spinal fusion rods", Proceedings of the Institution of Mechanical Engineers, Part H: Journal of Engineering in Medicine **225**, 194–198 (2011).

[111] J. A. Tang, J. M. Leasure, J. S. Smith, J. M. Buckley, D. Kondrashov, and C. P. Ames, "Effect of severity of rod contour on posterior rod failure in the setting of lumbar pedicle subtraction osteotomy (pso): a biomechanical study", Neurosurgery **72**, 276–283 (2013).

[112] Y. Murakami, T. Takagi, K. Wada, and H. Matsunaga, "Essential structure of sn curve: prediction of fatigue life and fatigue limit of defective materials and nature of scatter", International Journal of Fatigue **146**, 106138 (2021).

[113] S. K. Paul, "A critical review of experimental aspects in ratcheting fatigue: microstructure to specimen to component", Journal of Materials Research and Technology **8**, 4894–4914 (2019).

[114] A. Noshchenko, Y. Xianfeng, G. A. Armour, T. Baldini, V. V. Patel, R. Ayers, and E. Burger, "Evaluation of spinal instrumentation rod bending characteristics for in-situ contouring", Journal of Biomedical Materials Research Part B: Applied Biomaterials **98**, 192–200 (2011).

[115] G. Wall, H. Podbielska, and M. Wawrzynska, *Functionalised cardiovascular stents* (Woodhead Publishing, 2018).

[116] U. Wilbert-Lampen, D. Leistner, S. Greven, T. Pohl, S. Sper, C. Völker, D. Güthlin, A. Plasse, A. Knez, H. Küchenhoff, et al., "Cardiovascular events during world cup soccer", New England Journal of Medicine **358**, 475–483 (2008).

[117] D. G. S. Borges, R. A. Monteiro, A. Schmidt, and A. Pazin-Filho, "World soccer cup as a trigger of cardiovascular events", Arquivos brasileiros de cardiologia **100**, 546–552 (2013).

[118] D. Carroll, S. Ebrahim, K. Tilling, J. Macleod, and G. D. Smith, "Admissions for myocardial infarction and world cup football: database survey", Bmj **325**, 1439–1442 (2002).

[119] M. C. Fishbein and G. A. Fishbein, "Arteriosclerosis: facts and fancy", Cardiovascular Pathology **24**, 335–342 (2015).

[120] S. Shrivastava et al., *Medical device materials: proceedings from the materials and processes for medical devices conference 2003, 8-10 september 2003, anaheim, california* (Asm International, 2004).

[121] T. Zhu, A. Bushby, and D. Dunstan, "Materials mechanical size effects: a review", Materials Technology **23**, 193–209 (2008).

[122] Denis Bertholio, *Stents, des ressorts au secours des artères*, https://www.uncourantpourlavie.org/actualites.php?id_actu=339, [Online; Page available on 23-february-2023], 2018.

[123] A. Kastrati, J. Mehilli, J. Dirschinger, F. Dotzer, H. Schuhlen, F.-J. Neumann, M. Fleckenstein, C. Pfafferott, M. Seyfarth, and A. Schomig, "Intracoronary stenting and angiographic results: strut thickness effect on restenosis outcome (isar-stereo) trial", Circulation **103**, 2816–2821 (2001).

[124] S. K. Sinha, M. J. Jha, V. Mishra, U. Pandey, M. Razi, A. K. Sharma, P. Aggarwal, R. Thakur, and V. Krishna, "Clinical safety and efficacy of world's thinnest (50 μm), very long (> 40 mm) everolimus eluting stent (ses) among real world patients", American Journal of Cardiovascular Disease **10**, 317 (2020).

[125] Smtpl website, *Tetriflex - lowest strut thickness across all the diameters*, https://smtpl.com/products/tetriflex, [Online; Page available on 24-February-2023].

[126] H. Zhao, J. Van Humbeeck, J. Sohier, and I. De Scheerder, "Electrochemical polishing of 316l stainless steel slotted tube coronary stents: an investigation of material removal and surface roughness", Progress in Biomedical Research **8**, 70–81 (2003).

[127] A. G. Demir and B. Previtali, "Additive manufacturing of cardiovascular cocr stents by selective laser melting", Materials and Design **119**, 338–350 (2017).

[128] E. Langi, L. Zhao, P. Jamshidi, M. Attallah, V. Silberschmidt, H. Willcock, and F. Vogt, "A comparative study of microstructures and nanomechanical properties of additively manufactured and commercial metallic stents", Materials Today Communications **31**, 103372 (2022).

[129] M. A. Omar, B. Baharudin, S. Sulaiman, M. Ismail, and M. A. Omar, "Characterisation of powder and microstructure, density and surface roughness for additively manufactured stent using medical grade astm f75 cobalt chromium (cocrmo) by selective laser melting (slm) technology", Advances in Materials and Processing Technologies **8**, 1655–1666 (2022).

[130] Y. Vasconcelos, *Agora feito no brasil*, https://revistapesquisa.fapesp.br/agora-feito-no-brasil/, [Online; Page available on 24-February-2023].

[131] S. Hendrixson, *3d printed nitinol opens new possibilities for arterial stents*, `https://www.additivemanufacturing.media/articles/3d-printed-nitinol-opens-new-possibilities-for-arterial-stents`, [Online; Page available on 24-February-2023], 2020.

[132] F. Migliavacca, L. Petrini, V. Montanari, I. Quagliana, F. Auricchio, and G. Dubini, "A predictive study of the mechanical behaviour of coronary stents by computer modelling", Medical engineering and physics **27**, 13–18 (2005).

[133] I. De Scheerder, E. Verbeken, and J. Van Humbeeck, "Metallic surface modification.", in Seminars in interventional cardiology: siic, Vol. 3 (1998), pp. 139–144.

[134] G. Tepe, H. P. Wendel, S. Khorchidi, J. Schmehl, J. Wiskirchen, B. Pusich, C. D. Claussen, and S. H. Duda, "Thrombogenicity of various endovascular stent types: an in vitro evaluation", Journal of Vascular and Interventional Radiology **13**, 1029–1035 (2002).

[135] S. Sheth, F. Litvack, M. C. Fishbein, J. S. Forrester, and N. L. Eigler, "Reduced thrombogenicity of polished and unpolished nitinol vs. stainless steel slotted-tube stents in a pig coronary artery model", Journal of the American College of Cardiology **2**, 197A (1996).

[136] J. M. Anderson, "Biological responses to materials", Annual review of materials research **31**, 81–110 (2001).

[137] H. Zhao, J. V. Humbeeck, J. Sohier, and I. D. Scheerder, "Electrochemical polishing of 316l stainless steel slotted tube coronary stents", Journal of Materials science: materials in medicine **13**, 911–916 (2002).

[138] B. O'Brien and W. Carroll, "The evolution of cardiovascular stent materials and surfaces in response to clinical drivers: a review", Acta biomaterialia **5**, 945–958 (2009).

[139] Dibra, Alban and Kastrati, Adnan and Mehilli, Julinda and Pache, Jürgen and von Oepen, Randolf and Dirschinger, Josef and Schömig, Albert, "Influence of stent surface topography on the outcomes of patients undergoing coronary stenting: a randomized double-blind controlled trial", Catheterization and cardiovascular interventions **65**, 374–380 (2005).

[140] J. Dong, M. Pacella, Y. Liu, and L. Zhao, "Surface engineering and the application of laser-based processes to stents-a review of the latest development", Bioactive Materials **10**, 159–184 (2022).

[141] A.-M. Bandar, M. Rosaire, and Y. Stephen, "Coronary stents fracture: an engineering approach", Materials Sciences and Applications **2013** (2013).

[142] M. K. Mohsen, A. Alqahtani, et al., "Stent fracture: how frequently is it recognized?", Heart views: the official journal of the Gulf Heart Association **14**, 72 (2013).

[143] B. Murphy, P. Savage, P. McHugh, and D. Quinn, "The stress–strain behavior of coronary stent struts is size dependent", Annals of Biomedical Engineering **31**, 686–691 (2003).

[144] T. Connolley, P. Mchugh, and M. Bruzzi, "A review of deformation and fatigue of metals at small size scales", Fatigue and Fracture of Engineering Materials and Structures **28**, 1119–1152 (2005).

[145] R. W. Blair, N. J. Dunne, A. B. Lennon, and G. H. Menary, "Multi-objective optimisation of material properties and strut geometry for poly (l-lactic acid) coronary stents using response surface methodology", PLoS One **14**, e0218768 (2019).

[146] M. Azaouzi, A. Makradi, and S. Belouettar, "Numerical investigations of the structural behavior of a balloon expandable stent design using finite element method", Computational Materials Science **72**, 54–61 (2013).

[147] C. Dumoulin and B. Cochelin, "Mechanical behaviour modelling of balloon-expandable stents", Journal of biomechanics **33**, 1461–1470 (2000).

[148] F. Migliavacca, L. Petrini, M. Colombo, F. Auricchio, and R. Pietrabissa, "Mechanical behavior of coronary stents investigated through the finite element method", Journal of biomechanics **35**, 803–811 (2002).

[149] S. Kolwankar, A. Kanvinde, M. Kenawy, and S. Kunnath, "Uniaxial nonlocal formulation for geometric nonlinearity–induced necking and buckling localization in a steel bar", Journal of Structural Engineering **143**, 04017091 (2017).

[150] B. Audoly and J. W. Hutchinson, "Analysis of necking based on a one-dimensional model", Journal of the Mechanics and Physics of Solids **97**, 68–91 (2016).

[151] S. Okazawa, "Structural bifurcation for ductile necking localization", International Journal of Non-Linear Mechanics **45**, 35–41 (2010).

[152] S. Altai, S. Orton, and Z. Chen, "Evolution of localization length during postpeak response of steel in tension: experimental study", Journal of Engineering Mechanics **146**, 04020069 (2020).

[153] P. D. Versaillot, Y.-F. Wu, and Z.-L. Zhao, "Experimental study on the evolution of necking zones of metallic materials", International Journal of Mechanical Sciences **189**, 106002 (2021).

[154] T. Pardoen, F. Hachez, B. Marchioni, P. Blyth, and A. Atkins, "Mode i fracture of sheet metal", Journal of the Mechanics and Physics of Solids **52**, 423–452 (2004).

[155] G. Champier, c.r. hebd. Seanc. Acad. Sci., **266A**, 1170 (1968).

[156] T. McCarron, K. Kain, G. Hahn, and W. Flanagan, "Effect of geometrical defects in forming sheet steel by biaxial stretching", Metallurgical Transactions A **19**, 2067–2074 (1988).

[157] T. Hiroi and H. Nishimura, "The influence of surface defects on the forming-limit diagram of sheet metal", Journal of materials processing technology **72**, 102–109 (1997).

[158] N. Christodoulou and J. Jonas, "Effect of work hardening flow law and sample geometry on the forming limit in uniaxial tension", Canadian Metallurgical Quarterly **22**, 379–384 (1983).

[159] K. Chan, D. Koss, and A. Ghosh, "Localized necking of sheet at negative minor strains", Metallurgical Transactions A **15**, 323–329 (1984).

[160] F. A. Nichols, "Plastic instabilities and uniaxial tensile ductilities", Acta Metallurgica **28**, 663–673 (1980).

[161] G. Canova, C. G'Sell, and J. Jonas, "Localisation de l'ecoulement plastique en traction dans un materiau insensible a la vitesse de deformation", Canadian Metallurgical Quarterly **19**, 259–263 (1980).

[162] A. K. Ghosh and R. A. Ayres, "On Reported Anomalies in Relating Strain-Rate Sensitivity (m) to Ductility", Metallurgical Transactions A **7**, 1589–1591 (1976).

[163] W. H. Chen, "Necking of a bar", International Journal of Solids and Structures **7**, 685–717 (1971).

[164] J. W. Signorelli, M. A. Bertinetti, and A. Roatta, "A review of recent investigations using the marciniak-kuczynski technique in conjunction with crystal plasticity models", Journal of Materials Processing Technology **287**, 116517 (2021).

[165] A. Pilkey, C. Bayley, and M. Györffy, "Influence of surface defect geometry on the localization and failure of aa6111 sheet: necking versus shear", in Materials science forum, Vol. 519 (Trans Tech Publ, 2006), pp. 131–138.

[166] P. W. Bridgman, *Studies in large plastic flow and fracture: with special emphasis on the effects of hydrostatic pressure* (Harvard University Press, 1964).

[167] Y. Bai and T. Wierzbicki, "A new model of metal plasticity and fracture with pressure and lode dependence", International journal of plasticity **24**, 1071–1096 (2008).

[168] E. Lyczkowska-Widlak, P. Lochynski, G. Nawrat, and E. Chlebus, "Comparison of electropolished 316l steel samples manufactured by slm and traditional technology", Rapid Prototyping Journal **25**, 566–580 (2019).

[169] Mitutoyo America Corporation, *Quick guide to surface roughness measurement*, `https://www.mitutoyo.com/`, [Online; Page available on 25-October-2023], 2016.

[170] R. Yue, H. Huang, G. Ke, H. Zhang, J. Pei, G. Xue, and G. Yuan, "Microstructure, mechanical properties and in vitro degradation behavior of novel zn-cu-fe alloys", Materials Characterization **134**, 114–122 (2017).

[171] P. K. Bowen, E. R. Shearier, S. Zhao, R. J. Guillory, F. Zhao, J. Goldman, and J. W. Drelich, "Biodegradable metals for cardiovascular stents: from clinical concerns to recent zn-alloys", Advanced healthcare materials **5**, 1121–1140 (2016).

[172] V. Romanova, R. Balokhonov, E. Emelianova, E. Sinyakova, and M. Kazachenok, "Early prediction of macroscale plastic strain localization in titanium from observation of mesoscale surface roughening", International Journal of Mechanical Sciences **161**, 105047 (2019).

[173] B. A. Akbarnia and J. B. Emans, "Complications of growth-sparing surgery in early onset scoliosis", Spine **35**, 2193–2204 (2010).

[174] J. Patterson, J. Webb, and R. Burwell, "The operative treatment of progressive early onset scoliosis: a preliminary report", Spine **15**, 809–815 (1990).

[175] G. H. Thompson, B. A. Akbarnia, and R. M. Campbell Jr, "Growing rod techniques in early-onset scoliosis", Journal of Pediatric Orthopaedics **27**, 354–361 (2007).

[176] B. A. Akbarnia, D. S. Marks, O. Boachie-Adjei, A. G. Thompson, and M. A. Asher, "Dual growing rod technique for the treatment of progressive early-onset scoliosis: a multicenter study", Spine **30**, S46–S57 (2005).

[177] S. Bess, B. A. Akbarnia, G. H. Thompson, P. D. Sponseller, S. A. Shah, H. El Sebaie, O. Boachie-Adjei, L. I. Karlin, S. Canale, C. Poe-Kochert, et al., "Complications of growing-rod treatment for early-onset scoliosis: analysis of one hundred and forty patients", JBJS **92**, 2533–2543 (2010).

[178] W. N. Sankar, D. C. Acevedo, and D. L. Skaggs, "Comparison of complications among growing spinal implants", Spine **35**, 2091–2096 (2010).

[179] K. Watanabe, K. Uno, T. Suzuki, N. Kawakami, T. Tsuji, H. Yanagida, M. Ito, T. Hirano, K. Yamazaki, S. Minami, et al., "Risk factors for complications associated with growing-rod surgery for early-onset scoliosis", Spine **38**, E464–E468 (2013).

[180] T. Akgül, F. Dikici, C. Şar, U. TAlu, and Ü. DomAniç, "Growing rod instrumentation in the treatment of early onset scoliosis", Acta Orthop Belg **80**, 457–63 (2014).

[181] A. Agarwal, M. Kodigudla, A. Kelkar, D. Jayaswal, V. Goel, and V. Palepu, "Towards a validated patient-specific computational modeling framework to identify failure regions in traditional growing rods in patients with early onset scoliosis", North American Spine Society Journal (NASSJ) **5**, 100043 (2021).

[182] L. Miladi, A. Journe, and M. Mousny, "H3s2 (3 hooks, 2 screws) construct: a simple growing rod technique for early onset scoliosis", European Spine Journal **22**, 96–105 (2013).

[183] L. G. Lenke, R. R. Betz, J. Harms, K. H. Bridwell, D. H. Clements, T. G. Lowe, and K. Blanke, "Adolescent idiopathic scoliosis: a new classification to determine extent of spinal arthrodesis", JBJS **83**, 1169–1181 (2001).

[184] J. L. Otegui, "Failure analysis", Fundamentals and Applications in Mechanical Components, Switzerland: Springer International Publishing (2014).

[185] P. P. Milella, *Fatigue and corrosion in metals* (Springer Science and Business Media, 2012).

[186] A. Griebel, "Technical brief: fatigue dimples", Journal of failure analysis and prevention **9**, 193–196 (2009).

[187] T. Akahori and M. Niinomi, "Fracture characteristics of fatigued ti–6al–4v eli as an implant material", Materials Science and Engineering: A **243**, 237–243 (1998).

[188] G. D. Limited., *Ces selector 2016*, V 15.10.8. 2015.

[189] J. Chao and V. Lopez, "Failure analysis of a ti6al4v cementless hip prosthesis", Engineering Failure Analysis **14**, 822–830 (2007).

[190] M. Y. P. Costa, H. J. C. Voorwald, W. L. Pigatin, V. A. Guimarães, and M. O. H. Cioffi, "Evaluation of shot peening on the fatigue strength of anodized ti-6al-4v alloy", Materials Research **9**, 107–109 (2006).

[191] C.-W. Lin, C.-P. Ju, and J.-H. C. Lin, "A comparison of the fatigue behavior of cast Ti-7.5 Mo with cp titanium, Ti-6Al-4V and Ti-13Nb-13Zr alloys", Biomaterials **26**, 2899–2907 (2005).

[192] H. Oguma and T. Nakamura, "Fatigue crack propagation properties of Ti-6Al-4V in vacuum environments", International Journal of Fatigue **50**, 89–93 (2013).

[193] Y. Okazaki, "Comparison of fatigue properties and fatigue crack growth rates of various implantable metals", Materials **5**, 2981–3005 (2012).

[194] H. Rack and J. Qazi, "Titanium alloys for biomedical applications", Materials Science and Engineering: C **26**, 1269–1277 (2006).

[195] M. J. Donachie, *Titanium: a technical guide* (ASM international, 2000).

[196] Ö. Bayrak, A. F. Yetim, A. Alsaran, and A. Çelik, "Fatigue life determination of plasma nitrided medical grade cocrmo alloy", Fatigue and Fracture of Engineering Materials and Structures **33**, 303–309 (2010).

[197] R. V. Marrey, R. Burgermeister, R. B. Grishaber, and R. Ritchie, "Fatigue and life prediction for cobalt-chromium stents: a fracture mechanics analysis", Biomaterials **27**, 1988–2000 (2006).

[198] K. Rivard, A. Craft, T. Smith, and B. Aboud, "Qualification of hot isostatic pressing processes", in Medical device materials vi: proceedings from the materials and processes for medical devices conference:(mpmd 2011) (ASM International, 2013), p. 69.

[199] S. Teoh, "Fatigue of biomaterials: a review", International journal of fatigue **22**, 825–837 (2000).

[200] H. M. Noordeen, S. A. Shah, H. B. Elsebaie, E. Garrido, N. Farooq, and M. Al Mukhtar, "In vivo distraction force and length measurements of growing rods: which factors influence the ability to lengthen?", Spine **36**, 2299–2303 (2011).

[201] H. Serhan, D. Mhatre, P. Newton, P. Giorgio, and P. Sturm, "Would cocr rods provide better correctional forces than stainless steel or titanium for rigid scoliosis curves?", Clinical Spine Surgery **26**, E70–E74 (2013).

[202] M. Teli, G. Grava, V. Solomon, G. Andreoletti, E. Grismondi, and J. Meswania, "Measurement of forces generated during distraction of growing-rods in early onset scoliosis", World Journal of Orthopedics **3**, 15 (2012).

[203] A. White, "Clinical biomechanics of the spine", Clinical biomechanics of the spine (1990).

[204] H. Stürz, J. Hinterberger, K. Matzen, and W. Plitz, "Damage analysis of the harrington rod fracture after scoliosis operation", Archives of orthopaedic and traumatic surgery **95**, 113–122 (1979).

[205] W. Reitz, "Cervical stent failure analysis", Journal of failure analysis and prevention **13**, 678–683 (2013).

[206] K. Shinohara, T. Takigawa, M. Tanaka, Y. Sugimoto, S. Arataki, K. Yamane, N. Watanabe, T. Ozaki, and T. Sarai, "Implant failure of titanium versus cobalt-chromium growing rods in early-onset scoliosis", Spine **41**, 502–507 (2016).

[207] Granta Design Limited., *Ces edupack 2019*, V 19.2.0. 2019.

[208] J. Pan, Y. Wang, Q. Guo, D. Zhang, A. Greer, and Y. Li, "Extreme rejuvenation and softening in a bulk metallic glass", Nature communications **9**, 560 (2018).

[209] Y. Cui, G. Lewis, and G. Qi, "Numerical analysis of models of the standard tsrh spinal instrumentation: effect of rod cross-sectional shape", Computer Methods in Biomechanics and Biomedical Engineering **5**, 75–80 (2002).

A

Fracture mechanisms in Ti and Co–Cr growing rods and impact on clinical practice

This chapter is based on the published article *Fracture mechanisms in Ti and Co–Cr growing rods and impact on clinical practice,* Ribesse, A., Ismail, K., Croonenborghs, M., Irda, N., Miladi, L., Jacques, P. J., Mousny, M. & Pardoen, T., Journal of the Mechanical Behavior of Biomedical Materials (2021), vol. 121, p. 104620 [82].

⋆ Introduction

The management of progressive early onset scoliosis (EOS) is a challenging medical issue. The treatment should produce and maintain a correction without interfering with the spinal growth and lung development [173]. A surgical treatment is considered in case of brace/cast treatment failure or of contraindication [174, 175]. Growth-friendly techniques were progressively developed and non-fusion procedures (growing rod based techniques) are now commonly used for the management of evolutive EOS, unresponsive to conservative treatment [57, 175, 176].

Fusionless surgeries exhibit high complication rates, whatever treatment modality, as reported by [173, 177–179]. Fig. A.1 shows an example of a growing rod fracture through a comparison of X-rays at the time of insertion and after fracture. The consequences of a growth-rod failure are quite dramatic. They lead to severe pain, to a loss of the scoliosis correction and to the need for a new invasive surgery. Such failure events have been described by different authors (e.g. [72, 177]), but the underlying failure mechanisms are still poorly understood. Yang et al. studied 86 stainless steel or titanium alloy broken rods from both single-rod and dual-rod constructs in 49 patients and determined the fracture location based on X-ray images [72]. The most common fracture locations were above or below the tandem connectors (34 out of 86) and near the thoracolumbar junction (35 out of 86). Standard dual growing rods, hybrid growing rods with rib anchors proximally and spine anchors distally, and vertical expandable prosthetic titanium rib are the most commonly used techniques. Single growing rod techniques exhibit a higher complication rate compared to dual-rod constructs [180]. Regarding the failure of dual-rod constructs, Yamanaka et al. observed fatigue crack patterns and suggested that these fatigue cracks occurred during rod use, whereas the application of a large external stress, during falling or twisting movements, was responsible for final rod fracture [73]. According to Agarwal et al. studies [71, 96], the stress distribution and stress amplitude depend on various factors including the scoliotic curvature and the loading conditions during the distraction events. According to their model, the stress in the rod reaches from 85 up to 810 MPa depending on the frequency and amplitude of the distractions and on the spine curvature. In a very recent study, Agarwal et al. discussed the link between high stress regions and fracture locations in dual-rod constructs [181]. Based on finite element analysis (FEA), it was concluded that these

regions coincide and are located on the posterior surface of the rods, close to the distal anchors and at mid construct level [181].

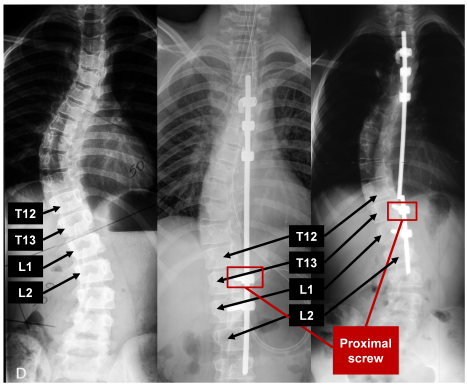

Figure A.1 X-ray of patient "1" with EOS before surgery (left), with H3S2 construct (middle) and rod failure (right).

In the present study, we investigated broken growing rods removed after diagnosis of fracture. These rods are made of three different materials: Ti–6Al–4V alloy, pure Ti grade 2 (Ti Cp 2) and Co–Cr alloy. The specific construct used by our team is composed of a single-rod and is called the "3-hook & 2-screw" (H3S2) construct [64, 182]. This construct is often selected for progressive scoliosis in skeletally immature patients. It involves no connector and a reserve located distally for future lengthening.

The first objective of the research is to unravel the mechanisms of fracture and to investigate the factors that control the failure process. The second objective is, based on the analysis of the failure mechanisms, to deduce strategies to guide towards novel practices that can reduce the risk of fracture. For this purpose, scanning electron microscopy is combined to X-ray analysis and to an analytical beam model to determine the failure mechanisms as well as to estimate the magnitude of the forces at the origin of the fracture process. This analysis finally motivates the formulation of several failure mitigation strategies.

⋆ Materials and methods

Materials

Seven broken rods from three patients were analyzed. Patient "1" fractured one rod, patient "2" broke two rods and patient "3" broke four rods. The rods were rapidly removed after radiographic diagnosis. All patients were males treated for severe EOS, with mean age at first surgery of 8.1 years [6.2–10.9]. All three patients had a right thoracic primary structural curve according to Lenke's classification [183].

No patient had thoracic hyperkyphosis as the antero-posterior curvature of the thoracic spine was always in the range [10° – 34°]. A H3S2 construct on a single sub-muscular growing rod was selected for each surgical procedure, as described by [64, 182]. The CD Horizon ®Legacy^{TM} device (Medtronic, Memphis, TN) was used. The Cobb angle is used to quantify the severity of the spine deformities. The patient is considered scoliotic when the Cobb angle exceeds 10°.

The Cobb angle was corrected from 50° to 26° for patient *1*, from 48° to 43° for patient *2* and from 102° to 35° for patient *3*. The initial correction was maintained owing to rod lengthening (involving a surgical step) performed when a 10° increase of the Cobb angle was observed. The average number of instrumented vertebral segments was equal to 11 [10–13]. The mean duration between insertion and fracture was 13.9 months [4.8–29.6]. The mean body mass index (BMI) at surgery was 16.5 kg/m² [14.8–18]. Table A.1 provides all relevant data about the H3S2 constructs and rod characteristics.

An additional rod made of the alloy Ti–6Al–4V with 5.5 mm diameter, purchased from Medtronic Sofamor Danek under the trade name CD Horizon® Legacy^{TM} System, was used to perform bending fatigue tests.

Methods

X-ray analysis

Posteroanterior (PA) and lateral X-rays, performed using a flat panel sensor (Konica) and a picture archiving and communication system for the archiving of the images (Carestream), were analyzed to identify the location of the crack initiation process. Five geometrical parameters, identified in Fig. A.2, can be extracted from the post fracture X-ray radiography pro-

Table A.1 H3S2 constructs and rods characteristics. The rod materials are made of a titanium alloy Ti–6Al–4V, a pure titanium grade 2 (Ti Cp 2) and of a cobalt-chromium (Co–Cr) alloy. The H3S2 construct extends from thoracic (T) spine to lumbar (L) spine. The time elapsed between rod insertion and rod fracture (rod survival time) is given.

	Patient 1	**Patient 2**		**Patient 3**			
		Rod 1	Rod 2	Rod 1	Rod 2	Rod 3	Rod 4
Rod material	Ti Alloy	Ti Alloy	Ti Alloy	Ti Alloy	Ti Alloy	Ti CP 2	Co-Cr
Rod diameter (mm)	5.5	5.5	5.5	5.5	5.5	6.35	5.5
Instrumented levels	from T5 to L2	from T4 to L1		from T3 to L3			
Rod survival time (months)	17.7	22.4	29.6	4.8	8.4	7.1	7.3

file of the patients to be used in the beam model. The length of the spine (L_{spine}) is defined as the distance between the apexes of the lumbar lordosis and the cervical lordosis. The apexes of the spine are measured along a curved line passing through the center of each of the bodies of vertebrae (Fig. A.2). The sagittal sinuosity of the spine (δ_{spine}) is defined as the distance between two parallel lines, one line being tangent to the two apexes of the lumbar and cervical lordoses and the other line being tangent to the apex of the dorsal kyphosis. X_1 is the distance between the apex of the lumbar lordosis and the proximal screw. X_{fract} is the distance between the proximal screw and the fracture location. L_{rod} is the distance between the proximal screw and the distal pedicular hook.

The post fracture X-ray radiography profiles of the patients were analyzed using the *ImageJ* v1.48 software (ImageJ v1.48, 2014, NIH Image, USA) in order to determine the five parameters defined above. The scaling reference is the diameter of the rod given in Table 1. This reference is used to evaluate the conversion between the pixels and the real length.

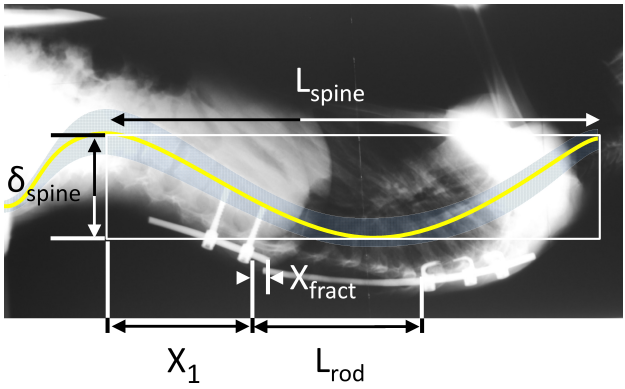

Figure A.2 Post fracture lateral X-ray radiography of patient 1, 3rd rod, with the representation of the five characteristic lengths to be used in the beam model. The yellow line connects the center of vertebrae bodies.

Microstructure analysis

The microstructure of the three rod materials was characterized based on metallographic cross-sections taken parallel to the rod axis. The preparation involved grinding and polishing with diamond suspensions followed by a 20-min silica suspension step for the Ti materials and by a 2-min alumina suspension step for the Co–Cr alloy. The titanium microstructures were revealed after etching, which consisted in 30-s immersion in a 3 mL HF, 6 mL HNO_3, and 91 mL water solution. The Co–Cr specimen was immersed 15 min in 40% HF, followed by a new 10-min alumina suspension polishing.

Micrographs were taken using scanning electron microscopy (SEM) (Ultra-55 FEG SEM, Carl Zeiss, Oberkochen, Germany). The three materials were characterized using backscattered electron detector (AsB) with an acceleration voltage of 20 kV.

Fracture surface analysis

Both pieces of in vivo fractured rod were compared to the corresponding PA and lateral X-rays in order to determine the orientation of the fracture surface with respect to the patient. All samples were cut 1 cm away from the fracture site using a water cooled saw (RGA commodore 300, Meylan, France). The fracture surfaces were analyzed by SEM. The SEM images were compared to PA and lateral X-rays to correlate with the direction of

the forces acting on the rod.

Fatigue tests

Prior to the laboratory fatigue tests, a Ti–6Al–4V rod was cut into three specimens of 10 cm length and subsequently bent by a surgeon using a French rod bender following the surgical practice as closely as possible. Bending angles were measured with a profile projector (Mitutoyo PJ 300, Illinois, USA). The specimens were bent with different angles equal to 4°29′, 10°32′ and 13°02′.

The fatigue tests were performed on a hydraulic testing machine (Dartec, 15 kN) using the three-point bending setup shown in Fig. A.3. The bending setup has three cylindrical supports with a diameter of 6.35 mm. The span between the two lower external supports was fixed at 4 cm.

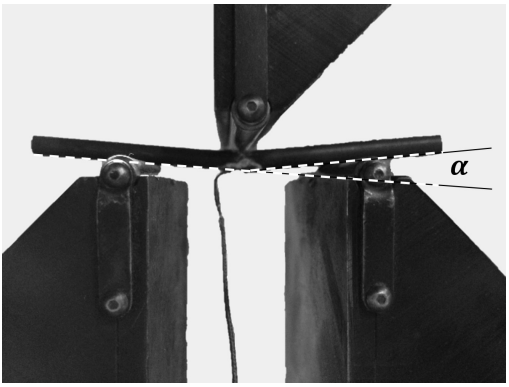

Figure A.3 Three-point fatigue bending setup with a sample bent at an angle α using a French bender prior to fatigue test. The span is equal to 40 mm. Selfheating was monitored to avoid variations of more than 5°C in the central part.

Force-controlled experiments were carried out at a frequency of 10 Hz on all samples. The loading conditions were set to reach a maximum stress inside the rod varying from 10 to 90% of the yield stress of the material, i.e. 100–900 MPa, giving an R ratio equal to 1/9. The number of cycles to failure was determined when detecting a sudden variation in crosshead displacement at fracture event and was rounded to the nearest thousand.

Results

Microstructures of the three rod materials

The microstructures of the three materials presented in Fig. A.4 correspond to cross-sections taken parallel to the rod axis (i.e. horizontal direction in the micrographs).

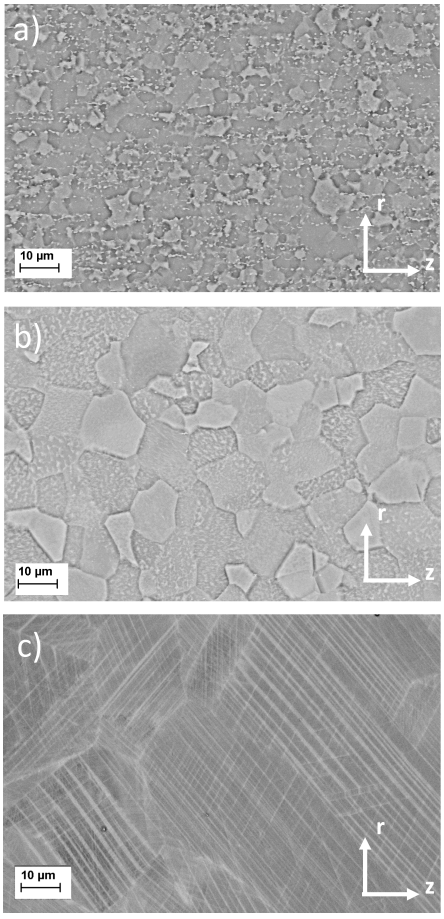

Figure A.4 SEM micrographs of axial microstructures from rods made of (a) Ti–6Al–4V alloy, (b) Ti Cp 2 and (c) Co–Cr alloy.

Fig. A.4a shows that the Ti–6Al–4V alloy is made of two phases: an α matrix composed of isotropic grains with a mean grain size of 3 µm together with smaller elongated β grains with a mean grain size of 0.5 µm.

The volume fraction of the β phase is equal to 5%. In the case of the Ti Cp 2 (Fig. A.4b), the microstructure is equiaxed with a mean grain size of about 10 µm. Most grains at the rod surface present twins, as shown in Fig. A.5, which indicates a plastic accommodation associated to a shot peening process often used to increase fatigue resistance [41]. Finally, the Co–Cr alloy also presents equiaxed grains with an average size close to 40 µm with twins present over the entire diameter (see Fig. A.4c). The equiaxed microstructure is obtained by thermal treatment after wire-drawing/extrusion process.

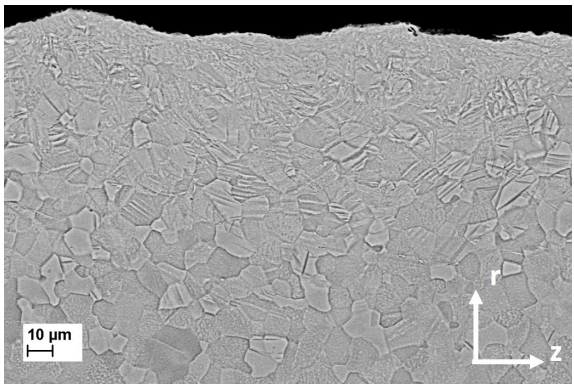

Figure A.5 SEM micrograph of twins at rod surface of Ti Cp 2.

X-ray characterization

Table A.2 reports the location of fracture initiation for each patient extracted from the X-ray images. Table A.3 summarizes the values of the characteristic lengths measured as explained in the Methods section and of the average for all seven patients. Individual patients' data are provided in the Appendix.

Table A.2 Fracture location expressed as spine level, including thoracic (T), lumbar (L) and intervertebral disk (IV disk).

	Patient 1	**Patient 2**		**Patient 3**			
		Rod 1	Rod 2	Rod 1	Rod 2	Rod 3	Rod 4
Fracture Location	T12-T13 IV Disk	T12	T12	L2	L1	T11-T12 IV Disk	T12-L1 IV Disk

Table A.3 Average values with standard deviations of the five characteristic lengths (see Fig. A.2) extracted from X-ray for the 7 patients. All distances are given in centimeters.

δ_{spine} (cm)	L_{spine} (cm)	X_1 (cm)	L_{rod} (cm)	X_{fract} (cm)
5.5 ± 1.1	35.9 ± 2.1	9.0 ± 1.0	14.3 ± 1.7	1.9 ± 1.8

SEM fractography of in vivo broken rods

Ti–6Al–4V

Fig. A.6 shows typical fracture surfaces of Ti–6Al–4V rods. The five Ti–6Al–4V rods involve similar fracture patterns.

Fig. A.7a shows that the surface is covered by curved and striated marks known as "clamshell marks". These constitute the usual imprints of successive arrests of a propagating fatigue crack. Other lines, only found on the dorsal side, originate from the posterior surface and align perpendicular to the clamshell marks. These lines are called "ratchet marks" (see also Fig. A.6), indicating the intersection locus of two cracks propagating in different planes [184] and proving thus the existence of multiple crack initiation sites [185]. Four out of the five rods exhibit a slant region, on both left and right sides. These so-called "shear lips", observed in Fig. A.6, develop when a crack approaches a surface due to plastic localization in 45° inclined bands [185] and lead to a shear-type ductile mechanism.

In the center, the clamshell profile evolves into a set of striations covered with small dimples as observed in Fig. A.7b and known as "fatigue dimples". This pattern indicates a transition of the fatigue propagation mechanism [186], to a low-cycle fatigue mechanism caused by ductile void grow. This last mechanism involves relatively large crack advance at each cycle, quite similar to a static ductile failure .

TiCp2

The fracture surface corresponding to a Ti Cp 2 rod shown in Fig. A.8 exhibits ratchet marks on the dorsal side as well as clamshell marks. Lines perpendicular to clamshell marks were also observed, originating from the crack initiation site. These so-called "river marks", similar to ratchet marks, indicate the confluence of different crack propagation planes [184]. The final fracture zone exhibits a small shear lip between the ventral side and the left side.

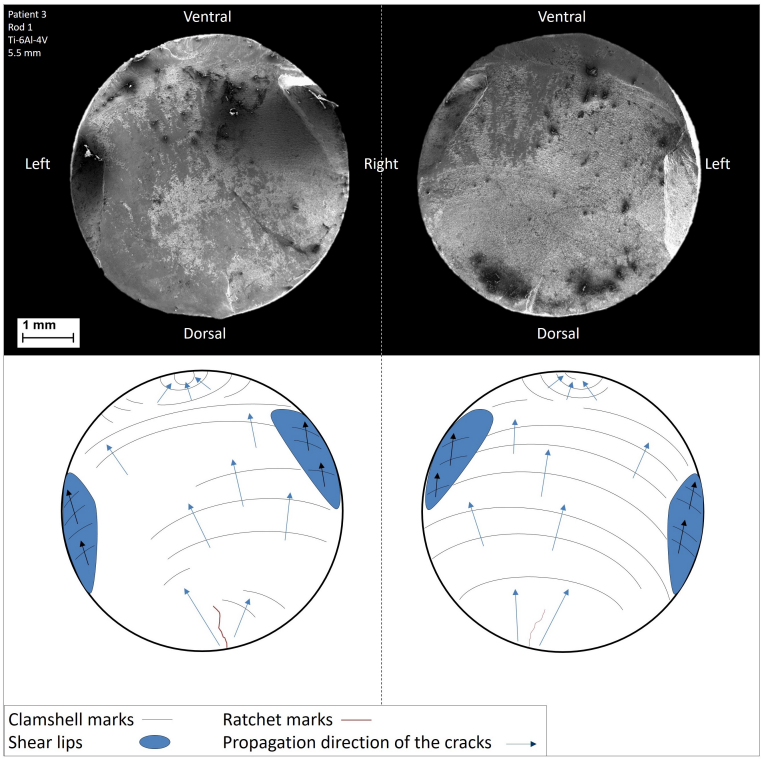

Figure A.6 Top image: SEM micrographs of the fracture surfaces of a broken Ti–6Al–4V rod. The lower part of the broken rods is on the left, the mating counterpart is on the right. Bottom image: schematic representation of the spreading of the fatigue cracks along the two corresponding fracture surfaces.

CoCr

A long ratchet mark can be observed on the fracture surface of the Co–Cr shown in Fig. A.9, starting in the middle of the dorsal region and ending near the rod center. As indicated in Fig. A.10a, river marks can be found on both sides of the ratchet marks with small striations. The rest of the fracture surface exhibits a flat topography suggesting that the propagation direction was repeatedly deviated. The intermediate magnification of Fig. A.10b reveals transverse cracks and the higher magnification (Fig. A.10c) shows striations parallel to each other, with direction varying from one grain to another. This indicates a relatively brittle transgranular fa-

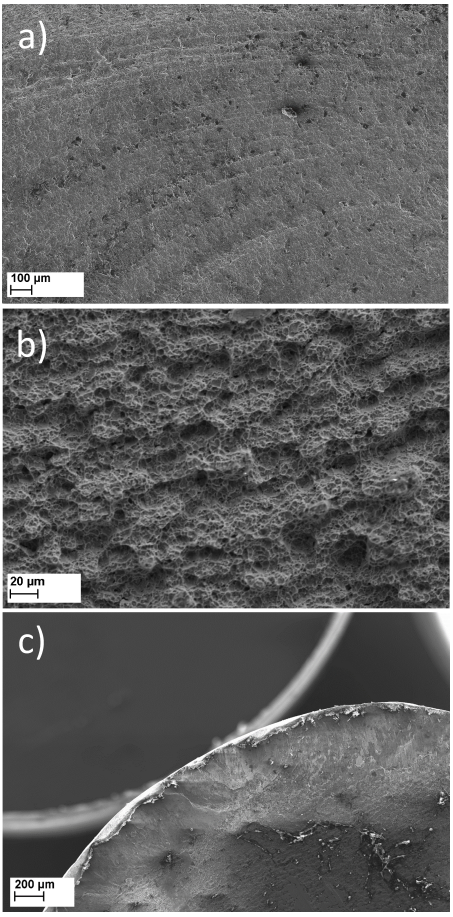

Figure A.7 SEM micrographs of the fracture surface of a broken Ti–6Al–4V alloy rod; (a) clamshell marks in the dorsal side of the surface of the rod; (b) fatigue ductile dimples between the two shear lips; (c) inversion of the clamshell marks curvature surrounding the final fractured zone in the ventral side of the rod.

tigue mechanism. The comparison between the SEM micrographs with the corresponding PA and lateral X-rays shows that, in all investigated rods, cracking initiates on the dorsal side and propagates towards the ventral side, with a tendency to deviate along the left side (bottom images in Figs. A.6, A.8 and A.9).

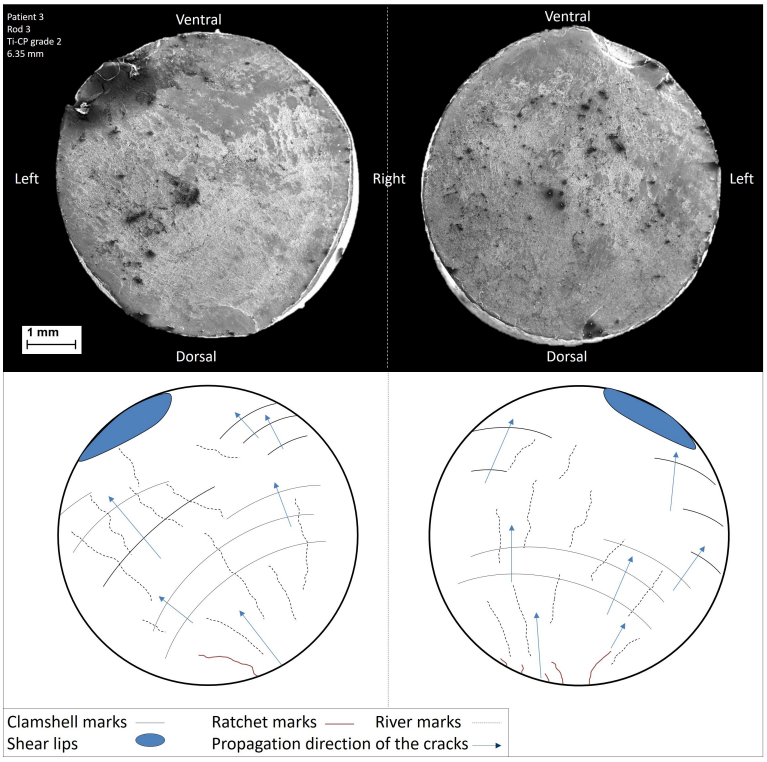

Figure A.8 Top image: SEM micrographs of the fracture surface of a broken pure titanium rod. The lower part of the broken rod is on the left, the mating counterpart is on the right. Bottom image: schematic representation of the spreading of the fatigue cracks along the two corresponding fracture surfaces.

Laboratory fatigue tests

The number of cycles to fracture was extracted from laboratory fatigue bending tests performed on Ti–6Al–4V rod specimens under a maximum stress equal to 90% of the yield stress. Fracture occurs after 369,000 cycles, 162,000 cycles, and 163,000 cycles for bending angles equal to 4°, 10° and 13°, respectively.

Fractographies of the broken 10° bent rod are presented in Fig. A.11. No ratchet marks are observed close to the initiation site. The fracture surface involves an area covered with beachmarks (Fig. A.11c), expressing a rel-

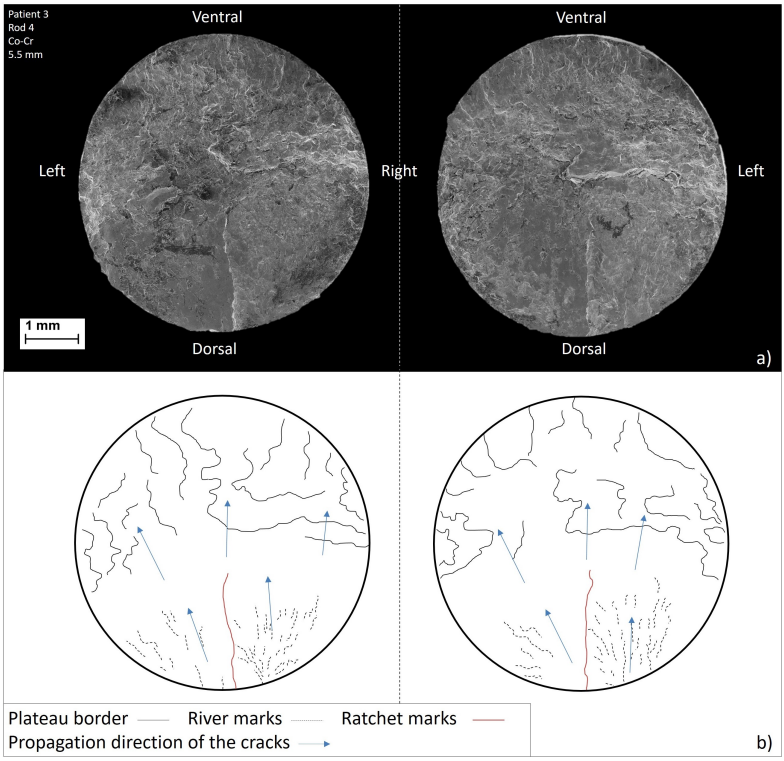

Figure A.9 Top image: SEM micrographs of the fracture surface of a broken Co–Cr alloy rod. The lower part of the broken rod is on the left, the mating counterpart is on the right. Bottom image: schematic representation of the spreading of the fatigue cracks along the two corresponding fracture surfaces.

atively brittle mechanism of initiation during the first stage of the fatigue process, followed by larger striations covered with dimples (Fig. A.11d), indicating a transition to a more ductile low-cycle fatigue failure mechanism. Finally, shear lips are present on both sides. The mechanisms are quite similar to the one observed in the in vivo rods, especially for the low-cycle fatigue part.

Analytical beam bending model of the spine

The model considers a healthy spine with no scoliosis. The shape of the spine between the apex of the lumbar lordosis and the cervical lordosis is

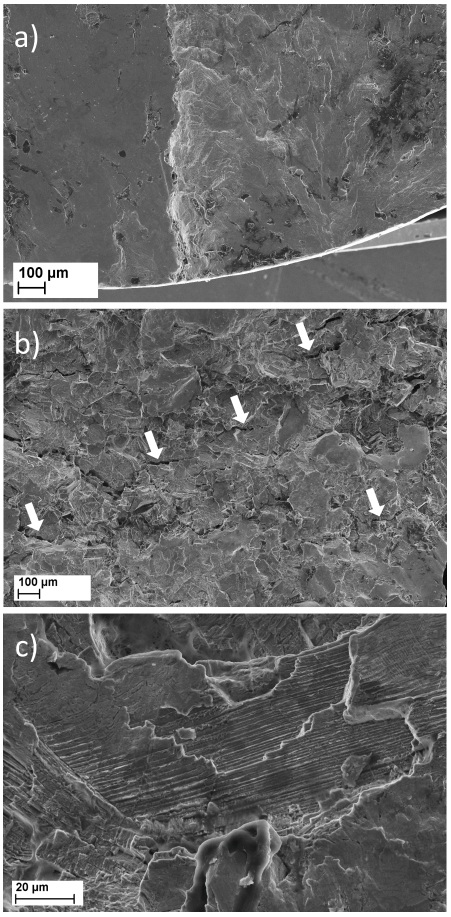

Figure A.10 SEM micrographs of the fracture surface of a broken Co–Cr alloy rod; (a) river marks on the dorsal side of the surface of the rod; (b) transverse cracks from the center of the surface to the ventral side of the rod; (c) fatigue striation at the scale of a single grain exhibiting a stair-step morphology.

approximated, as shown in Fig. A.12, by a perfect sinusoidal function with a periodicity equal to L_{spine} and an amplitude equal to $\delta_{spine}/2$:

$$\delta(x) = \frac{\delta_{spine}}{2} cos\left(\frac{2\pi}{L_{spine}}(x + X_1)\right). \tag{A.1}$$

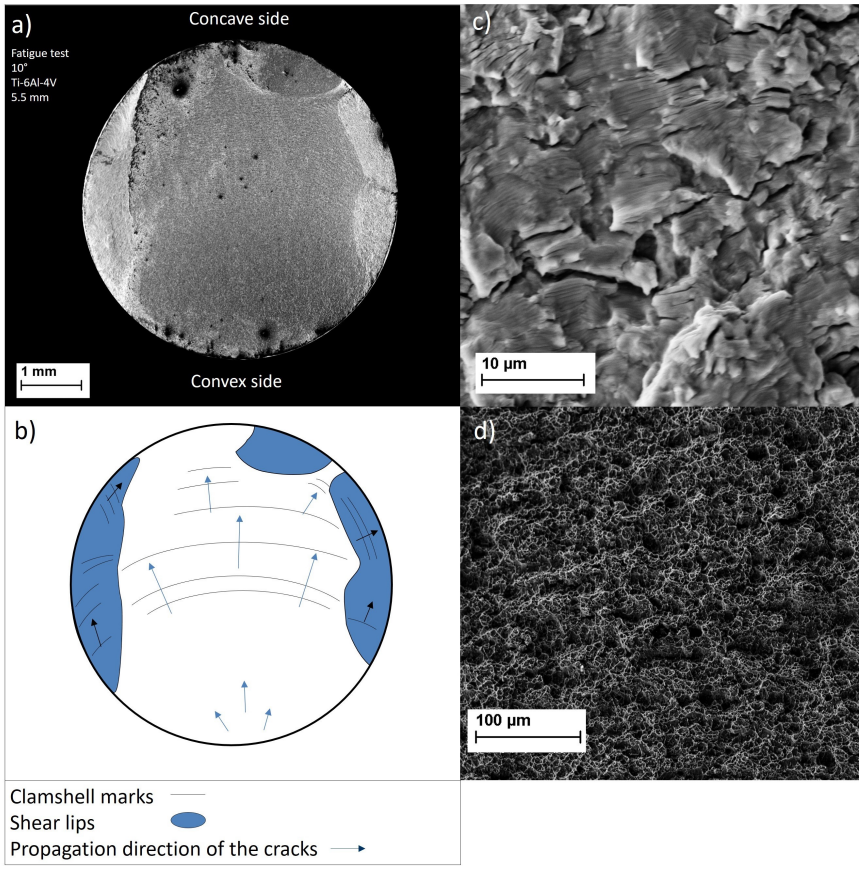

Figure A.11 (a) SEM micrographs of the fracture surface of a 10° bent rod after laboratory fatigue testing (Ti–6Al–4V alloy); (b) schematic representation of the spreading of the fatigue cracks; (c) fatigue striations close to initiation site; (d) fatigue ductile dimples between the two shear lips.

The rod is approximated by a beam with a circular section of radius R_{rod}. The rod follows the sinusoidal shape of the spine between the upper proximal screw and the distal hook. The lower fixation of the rod in the lumbar vertebra is approximated by an embedment acting with a vertical force F_{v1}, a horizontal force F_{h1} and a bending moment M_1. In the same way, the upper fixation imposes a vertical force F_{v2}, a horizontal force F_{h2} and a bending moment M_2. Due to the mobility of the hooks in the upper fixation, M_2 is considered negligible and taken equal to zero. The rod is assumed

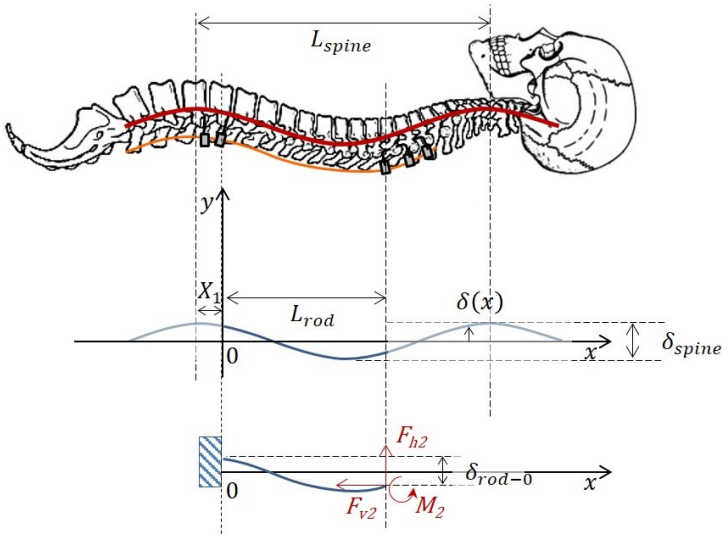

Figure A.12 Schematic representation of the spinal column model.

defect free with no stress concentrator.

Using classical beam bending theory and applying the equilibrium conditions (the complete derivation is given in the Supplementary material [1]), the tensile stress on the dorsal side of the rod is equal to

$$\sigma_{surf} = \frac{F_{v2}R_{rod}}{I_{rod}}\left[\frac{M_2}{F_{v2}} + \delta(L_{rod}) - \delta(x) + \frac{F_{h2}}{F_{v2}}(L_{rod} - x)\right] - \frac{F_{v2}}{A_{rod}}, \quad \text{(A.2)}$$

where I_{rod} is the second moment of inertia of the rod equal to $\pi R_{rod}^4/4$, and the cross-section area of the rod A_{rod} is given by $A_{rod} = \pi R_{rod}^2$. By differentiating Equation A.2 with respect to x, the position of the maximum tensile stress $(x_{\sigma max})$, is found by solving

$$\frac{F_{h2}}{F_{v2}} = \frac{\delta_{spine}}{2}\frac{2\pi}{L_{spine}} sin\left(\frac{2\pi}{L_{spine}}(x_{\sigma max} + X_1)\right). \quad \text{(A.3)}$$

[1] available online at `https://www.sciencedirect.com/science/article/pii/S1751616121003015`

As a first lower bound approximation, we assume that fracture occurs at the position corresponding to the maximum tensile stress ($x_{fract} = x_{\sigma max}$) when the tensile stress along the dorsal part of the rod reaches the fatigue endurance limit σ_{end} of the rod material (i.e. when $\sigma_{max} = \sigma_{end}$). Equation A.3 gives the ratio of the two critical forces (F_{h2} and F_{v2}) that would potentially lead to fracture of the rod. From this ratio, one can estimate their intensities from (with $M_2 = 0$)

$$F_{v2} = \frac{\sigma_{end}}{\frac{R_{rod}}{I_{rod}}} \left(\delta(L_{rod}) - \delta(x_{fract}) + \frac{F_{h2}}{F_{v2}} (L_{rod} - x_{fract}) \right) - \frac{1}{A_{rod}}. \qquad \text{(A.4)}$$

The endurance limit is a material property that depends on a large number of parameters related, among others, to the processing conditions and to the resulting microstructure, surface state, temperature, and/or presence of internal stresses. The endurance limit defined at 10^7 cycles is equal to 655 ± 136 MPa for Ti–6Al–4V [107, 187–194], to 286 ± 39 MPa for Ti Cp grade 2 [188, 191, 194, 195], and to 462 ± 231 MPa for Co–Cr [107, 188, 193, 196–199]. The uncertainty in the measurements and the dispersion on the values of σ_{end} have been taken into account through an error propagation analysis.

Knowing x_{fract} from post-fracture X-ray radiographies, F_{v2} and F_{h2} can be calculated for each patient by solving Eqns A.3 and A.4: F_{v2} varies from 171 to 424 N, and F_{h2} varies from 79 to 152 N. The mean value and the standard deviation of F_{v2} and F_{h2} are presented in Fig. A.13.

An interesting outcome of the model is the possibility to predict the risk of failure of a construct and the position of the maximum stress in a rod directly from the geometrical data extracted from an X-ray radiography (δ_{spine}, L_{spine}, X_1, L_{rod}) and on the forces acting on the rod (F_{v2} and F_{h2}). If F_{v2} and F_{h2} are known, the location of the point of maximum stress in the rod ($x_{\sigma max}$) can be calculated using Eqn A.3. Due to the periodicity of the sinus function, solving Eqn A.3 leads to a multiplicity of solutions for $x_{\sigma max}$ and one should carefully select the appropriate one.

This approach was used to predict the position of the maximum stress in a rod and the amplitude of the maximum stress for a hypothetical patient with geometrical dimensions taken as an average of the 3 patients of this study (δ_{spine} = 5.5 cm, L_{spine} = 36 cm, X_1 = 9 cm and L_{rod} = 14 cm). The

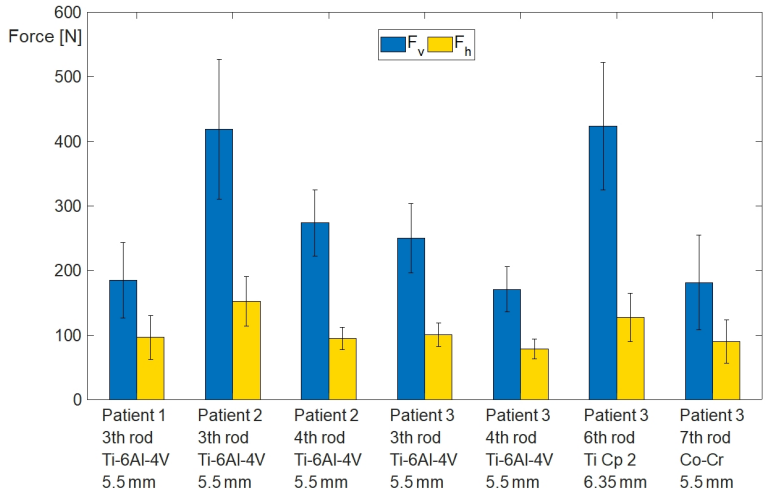

Figure A.13 Vertical and horizontal forces responsible for the fatigue fracture of the rods calculated from the model at the x_{fract} position. The error bars represent the standard deviations.

variation of the maximum stress on the dorsal side of the rod as a function of F_{v2} and F_{h2} is shown in Fig. A.14 along with the endurance limit of the three materials investigated in this study.

The horizontal forces have a larger influence on the attainment of a critical stress state in the rod compared to the vertical forces. This phenomenon is due to a lever effect and is proportional to the lever ratio L_{rod}/δ_{rod-0}, δ_{rod-0} being defined as $\delta(L_{rod}) - \delta(0)$, which is roughly equivalent to the ratio L_{spine}/δ_{spine}.

The model addressed above aimed at representing the mechanical response of a rod in a H3S2 construct in the sagittal plane. The estimates are based on X-ray measurements and fractography analysis. The model has several limitations such as: (i) the residual stress field and the indentation marks coming from the contouring process are not taken into account, neither stress concentrations close to anchorages; (ii) M_2 is neglected because hooks are used at the top fixation systems, while this hypothesis would become incorrect if only screws were used; (iii) torsion motions were not considered but fractographies indicate that failure events were dominated by anteroposterior bending; (iv) the spine curve between the apex of the lum-

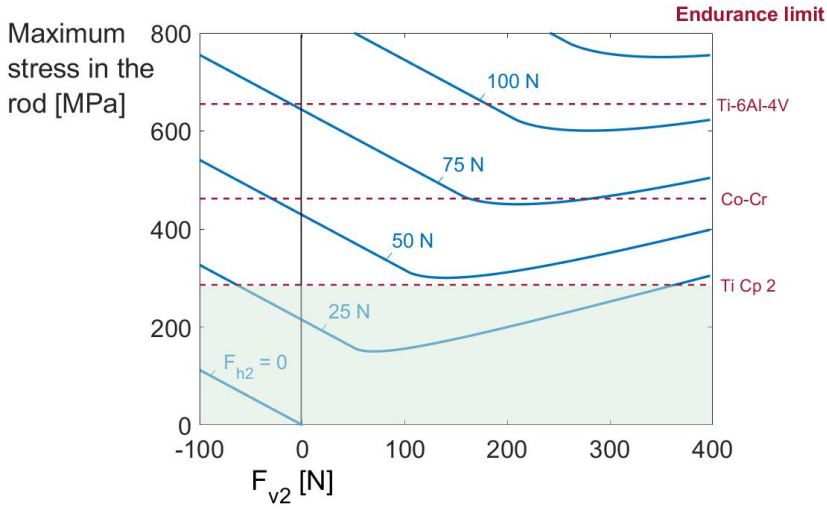

Figure A.14 Variation of the maximum stress in the dorsal side of the rod as a function of the imposed forces F_{h2} and F_{v2} at the upper hook for R_{rod} = 5.5 mm, δ_{spine} = 5.5 cm, L_{spine} = 36 cm, X_1 = 9 cm and L_{rod} = 14 cm. The endurance limit of Ti–6Al–4V alloy, Ti Cp 2 and Co–Cr alloy is indicated in red. A positive value of the stress corresponds to a tensile stress. The green surface represents a safe zone for a rod made of pure Ti.

bar lordosis and the cervical lordosis in the sagittal plane is approximated by a perfect sinusoidal function; (v) the spine deformation in the frontal plane, i.e. Cobb angle, is not considered because the model only represents the rod geometry, and the rods are mainly bent in the sagittal plane, being straight in the frontal plane; (vi) stresses resulting from spine growth are not taken into account. Considering these limitations, the predictions should only be taken as semi-quantitative. Nevertheless, even though the considered constructs were not identical, the predicted critical forces are in agreement with results from previous studies [96, 200–202].

⋆ Discussion

Lifetime of the rods

The present investigation indicates that growth rods fail by fatigue as a result of everyday solicitation related to basic movements such as sitting,

playing, or getting dressed. In order to evaluate the solicitation frequency, the number of cycles up to failure should be divided by the rod lifetime. In our study, the resistance of Ti–6Al–4V rods tested in kyphotic configuration was around 200,000 cycles. Piovesan et al. performed four-point bending fatigue tests on similar rods. In kyphotic configuration, rods run-out 10^6 cycles without failure for a maximum stress level of 577 MPa. In lordotic configuration, rods break after 2.4×10^4 cycles for a maximum stress level of 944 MPa [75]. Stresses acting in vivo are not as regular as in laboratory fatigue tests. We may consider that fatigue solicitation is a combination of low and high stresses. Our fatigue tests invariably induced 900 MPa in Ti–6Al–4V rods, which is a high-stress level not far from the yield stress. 2×10^5cycles is thus probably a lower bound on the number of cycles. The average lifetime of the seven broken rods after implantation is 14 months. Only seven rods have been considered for estimation of the average lifetime. Yang et al. found a larger average time before fracture after initial insertion, of 25 ± 21 months, considering eighty-six broken rods [72]. Assuming that the forces used during fatigue tests are of the same order of magnitude as the one in the back of the child, this is equivalent to a mechanical solicitation every 3 min associated to a bending moment of 14.7 Nm applied to the rod. On this basis, solicitations playing a role on setting the fatigue lifetime should occur over a time scale of the order of a few minutes. A smaller frequency would have been linked to occasional high intensity events, such as coughing or vomiting [109], whereas a higher frequency would depict events occurring every second such as breathing. The obtained frequency fits classical movements such as walking, squatting, jumping, which are regular movements in a child's life.

The four broken rods in patient 3 exhibit a survival time shorter than for the two other patients. This cannot be explained by a higher BMI, nor by severe thoracic kyphosis (i.e. excessive outward curvature of the spine). The high percentage of scoliosis correction could be a predisposing factor but this was not investigated in our study.

Failure location

Thoracolumbar junction is an at-risk location due to stress concentration. Smith et al. evaluated 30 patients with symptomatic rod fracture after posterior instrumented fusion for adult spine deformity, with most fractures occurring in the lumbar spine or thoracolumbar junction [94]. 35 of the 86 rod fractures analyzed by Yang et al. occurred in that region as well [72].

Agarwal et al. concluded, using FEA, that at-risk failure regions are close to distal anchors and at mid construct in dual-rod constructs. From X-ray radiography analyses, it was found that all rods but one (rod 1, patient 3) broke at the thoracolumbar junction. In patient 3, rod 1 failed at the level of L2 vertebra, close to the thoracolumbar junction. Even if the type of growing rod construct can influence the location of the fracture initiation site, thoracolumbar is certainly an at-risk location.

The fatigue cracks always initiate from the dorsal side of the rod and propagate towards the ventral side, with a tendency to slightly deviate towards the left side. This suggests that the rods break mainly because of repeated action of a bending moment in the anteroposterior direction. Piovesan et al. compared residual stresses in kyphotic and lordotic conditions. At the thoracolumbar junction, rods are usually bent in lordotic configuration. In this configuration, the stress state along the dorsal side results from two tensile contributions: residual stresses induced by the contouring process and extra stress induced by anterior flexural loading [75]. Tensile residual stresses favor crack initiation, reducing rod lifetime. The bending process induces residual stresses leading to an effective decrease of the fatigue resistance in the thoracolumbar region. Residual stress after rod bending affects rod fatigue performance [74]. As the spine experiences higher and more frequent loads in flexion [203], rods contoured in lordosis and inserted at the thoracolumbar junction or in the lumbar spine would thus be more susceptible to fatigue cracking due to residual stress contribution [75].

Fatigue mechanisms

Multiple initiation sites are activated due to imperfections at the rod surface. Fatigue cracks usually initiate in areas subjected to the largest cyclic tensile stress. In addition, defects such as surface roughness, indentation, pre-cracks, inclusions, or porosity favor crack initiation by acting as stress concentrators [33]. These defects mostly originate from the manufacturing process [65, 73]. Additional defects can be subsequently introduced during rod contouring and manipulation by the surgeon [65, 68]. Bending instruments such as the French rod bender and the in situ bender are known to introduce shallow notches, affecting the fatigue resistance [65, 69, 76]. The connection between the rod and the screws or hooks also creates permanent marks [65]. The ratchet marks on the dorsal side of each rod denote the presence of multiple initiation sites. No ratchet mark was found on lab-

oratory fatigue rod fractography. In the studied laboratory configuration, the crack initiates along the convex side of the rod. The surface on that side of the laboratory fatigue specimens can be assumed defect-free as no indentation marks were induced in this area during the bending process.

The Ti–6Al–4V rods all show evidences of striations after initiation, typical of a crack tip plasticity induced fatigue mechanism, followed by a low-cycle fatigue ductile stage and a final tearing step, independent of composition and diameter. In all materials, the final ductile tearing process occurs when the crack is sufficiently long for the stress intensity factor to reach the fracture toughness under a particularly severe load excursion. This is consistent with previous studies on different spinal constructs, e.g. Harrington rods [204], Harrington rod cervical stents [205], and posterior rods [73]. Only the Co–Cr rod does not show the same plastic void growth dominated failure stage.

Leaving aside the detrimental effect of the marks and surface defects (that can potentially be mitigated), our calculations show that the observed failure events cannot be attributed to particular internal material defects or to non-expected microstructural problems, but are the consequences of the cyclic stresses generated in daily life which reach, at reasonable force levels, the expected endurance limit.

Loading

The anteroposterior forces have different origins. Distraction is used to maintain the correction of scoliosis, independent of the construct [57, 175]. The force required to straighten the spine is transferred to the rod as a compressive and bending stress. The spine "pushes" on the rod with a force that depends on the correction amplitude. Teli et al. showed a linear relationship between this vertical force and the distraction needed for scoliosis correction [202]. Waugh added the effect of vertical forces during day-to-day movements (20% increase while sitting and standing up), with peaks during involuntary movements like coughing (206% increase) and vomiting (490% increase) [109]. The day-to-day physical activities of a child (walking, running, jumping ...) are expected to increase these vertical forces in a cyclic way. These forces, acting in a direction parallel to the rod axis, are due to the constraint necessary to hold the correction of the scoliotic curve and to resist gravity. Associated, bending moment in the anteroposterior direction may also occur because of anterior flexion movements

of the spine. In our research, all three patients had a right thoracic primary structural curvature without any thoracic hyperkyphosis. The vertical and horizontal forces, responsible for each rod failure, have the same general trend: vertical forces are two to three times larger than horizontal forces. However, the horizontal forces play a dominant role on maximum stress levels due to a greater lever effect in the structure.

Rod diameter

The effect of rod diameter on their lifetime is uncertain. During the contouring phase, Slivka et al. explained in their study that a larger diameter leads to larger strains at the rod periphery for the same bending curvature, which negatively affects fatigue resistance as larger diameter rods are then more prone to fatigue crack initiation [74]. However, the same authors [74] also pointed out that higher rates of fracture were associated to smaller diameters. As a matter of fact, the key question is whether daily activities are force/moment-controlled or deflection/bending angle-controlled. Force-controlled activity is typical of carrying dead loads, but a flexure to reach an object is closer to deflection control. In our study, the effect of the radius of the rods was not investigated experimentally as only one radius was used for each rod material.

Material choice

The clinical objective when using a non-fusion growth-rod technique is to minimize the risks of failure, as already identified in earlier studies [72, 94]. Fracture initiation is influenced by the defects and residual stresses induced by the manufacturing process and preoperative handling. Before being inserted in a patient, a rod is exposed to a succession of contouring operations combined, in some case, with indentation marking. After insertion in the patient, the rod is subjected to fatigue loading. As the bending moment in the anteroposterior direction was identified as the main component responsible for fracture, wearing an anti-kyphosis brace could be seen as an alternative. However, a brace will only decrease the bending forces due to anterior flexion movement of the spine. Therefore, it will, at best, delay fracture, but not prevent it.

Selecting materials with a higher fatigue endurance limit only is not sufficient to prevent rod failure nor does it guarantee a longer lifetime of the rod. Indeed, regarding patient 3, while Ti–6Al–4V exhibits a larger en-

durance limit compared to Co–Cr rods, both were used and showed a similar lifetime. Some studies specifically investigated the fatigue life of contoured rods [65, 74, 94, 110, 206]. Co–Cr rods showed superior fatigue performance compared to Ti alloys, but both lead to failure issues. The optimal material should thus have a high fatigue endurance limit and keep it after the contouring process.

The stiffness of the construct is also important to consider. As already touched upon above, there is still an uncertainty regarding the dominant (cyclic) loading mode of the rod by the patient. Whether it is mainly load-controlled (i.e: the patient applies a given force on the rod) or displacement-controlled (i.e. the patient applies a given deflection on the rod) is not precisely known. If we assume that growth rods are being loaded in a displacement-controlled mode, the stiffness of the Co–Cr alloy (210–220 GPa) being larger than those of the alloys Ti–6Al–4V (110–119 GPa) and Ti Cp 2 (100–105 GPa) [207], the Co–Cr rod will undergo proportionally larger stresses (for similar diameter).

This illustrates the complexity of material selection for a growth rod application. A fail-safe material should have a high fatigue endurance limit, which is related to a high yield stress (the endurance limit is typically equal to 1/3 of the yield stress). A high yield stress makes the contouring process more difficult as the surgeons will need more force for bending and may worsen the indents and thus the defects favoring fracture initiation. Vice versa, a high yield stress guarantees the absence of plastic bending induced by the movements of the patient. A moderately low elastic modulus is preferable to favor an elastic behavior, but it should not be too low, otherwise the correction cannot be maintained (or at the expense of a very thick rod). Future developments should thus focus on selecting new materials with higher strength, strong enough to hold the scoliosis correction, and compliant enough to allow enough spine mobility. This ideal material should resist marking, which means that no or minimum surface defect is induced by the rod contouring or by the connection to the screws and hooks. An option could be offered by new generations of metallic glasses with very high strength and large elastic deformation potential, but only if they can be made less brittle through different types of ductilization mechanisms (e.g. [208]).

In the meantime, alternative solutions exist to improve lifetime based on predictive patient-specific models. One could adapt the rod geometry at

the critical sites. Cui et al. [209] indeed demonstrated better biomechanical performance for square cross-section rods compared to circular cross-section rods. A second solution would be to use pre-contoured rods with internal stress relaxed by adequate thermal treatment or, alternatively, by compressive internal stress pre-induced at the predicted location. The development of advanced predictive models to guide practice optimization is currently under study based on both finite element methods and fatigue tests.

⋆ Conclusions

Growing rod fracture is a major complication of fusionless surgeries used to treat early onset scoliosis. The fracture mechanism in seven growing rods from patients with early onset scoliosis and treated by H3S2 construct was analyzed relying on fractography, fatigue testing and beam theory. The main conclusions of the analysis are the following:

- Fracture occurs through classical fatigue mechanisms caused by a repeated bending in the anteroposterior direction, for all diameters and material types.
- Fracture generally initiates at the thoracolumbar junction, but various fatigue crack initiation sites were found on every rod, stemming from imperfections presumably induced by the manufacturing process and from rod contouring.
- The vertical and horizontal forces predicted based on the beam model, combined to the number of cycles to failure determined from the laboratory fatigue tests on pre-bent specimens, indicate that the fatigue process is controlled by daily life activities taking place at frequency in the minutes to a few tens of minutes range.
- The failure risks can be decreased by wearing an anti-kyphosis brace, changing the intrinsic rod characteristics/materials (strength, compliance, resistance to marking), adapting rod geometry and/or inducing compressive stress at critical sites or using pre-contoured rods with internal stress relaxed.

⋆ Appendix

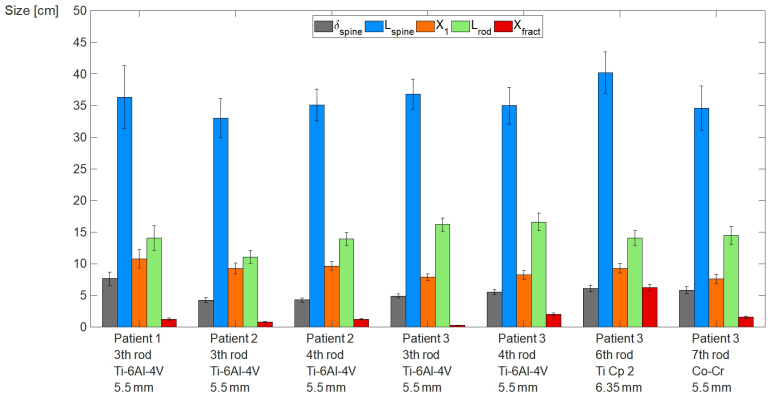

Figure A.15 Geometrical characteristics of each patient.

B

Appendix of Chapter 6 - Hardening laws

Table B.1 Core and skin parameters for the kinematic hardening for Ti-6Al-4V alloy for shot-peened rods (Medtronic) and untreated rods (Salomon).

Parameter	E[MPa]	σ_0[MPa]	A[MPa]	B[−]
Medtronic				
Core model	113000	1017	3955	20
Skin model	113000	565	6780	5
Salomon				
Skin + core model	113000	1017	3955	20

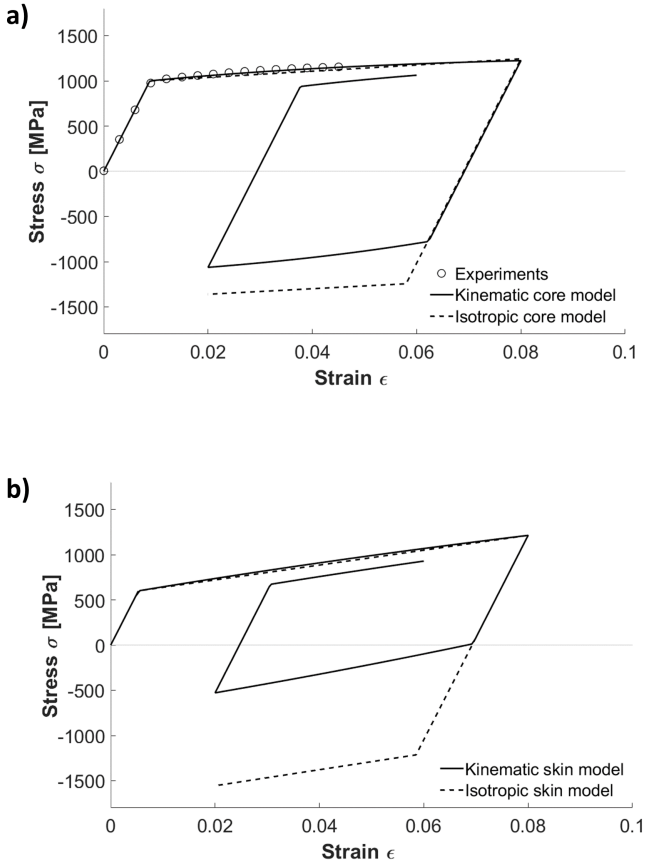

Figure B.1 Cyclic stress - strain curves for the identification of the isotropic hardening and kinematic hardening models: (a) for the core of the rod compared to the tensile stress strain curve from experiment; (b) for the skin of the rod.

C

Supplementary of Chapter 6 - Fractographies

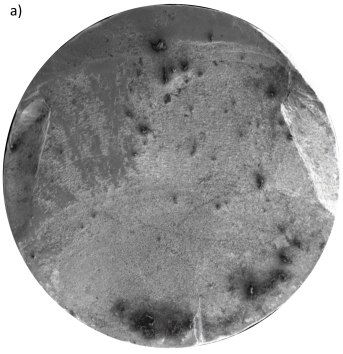

(a) In-vivo broken rod.

Figure C.1 Fractographies of Ti-6Al-4V broken rods in different configurations.

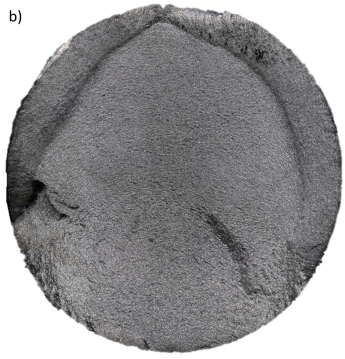

(b) 0°, shot-peened rod, tested experimentally in strain-controlled configuration.

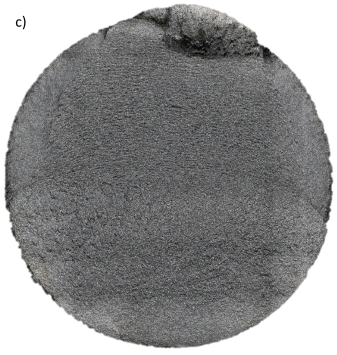

(c) 13°, shot-peened rod, tested experimentally in strain-controlled configuration.

(d) 3°, shot-peened rod, tested experimentally in force-controlled configuration.

Figure C.1 Fractographies of Ti-6Al-4V broken rods (cont.)

(e) 9°, shot-peened rod, tested experimentally in force-controlled configuration.

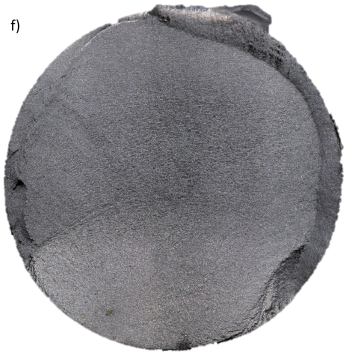

(f) 0°, untreated rod, tested experimentally in strain-controlled configuration.

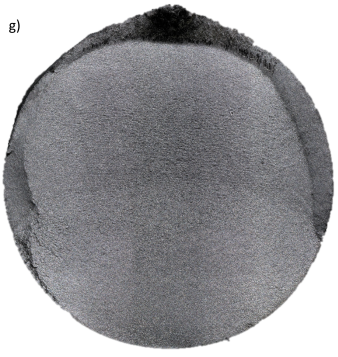

(g) 5°, untreated rod, tested experimentally in force-controlled configuration.

Figure C.1 Fractographies of Ti-6Al-4V broken rods (cont.)

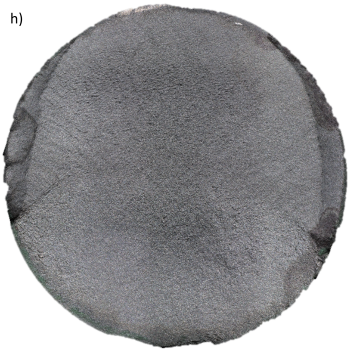

(h) 13°, untreated rod, tested experimentally in force-controlled configuration.

Figure C.1 Fractographies of Ti-6Al-4V broken rods (cont.)

D

Appendix of Chapter 8 - Samples Dimensions

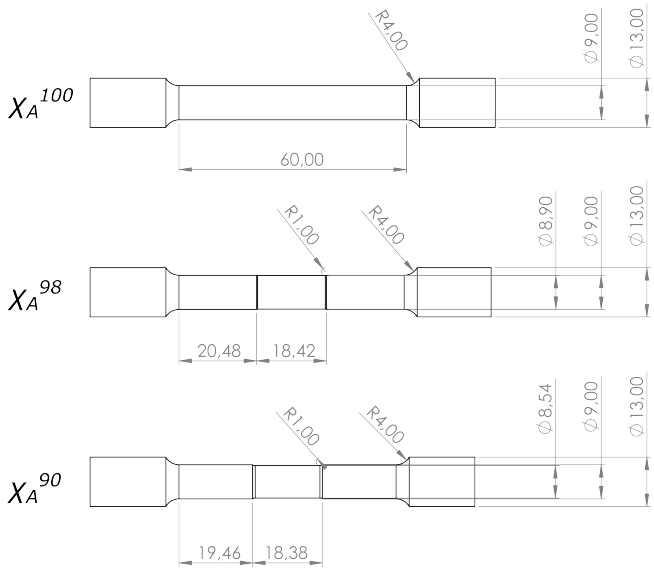

Figure D.1 Geometry of the tensile specimen for χ_A parameter.

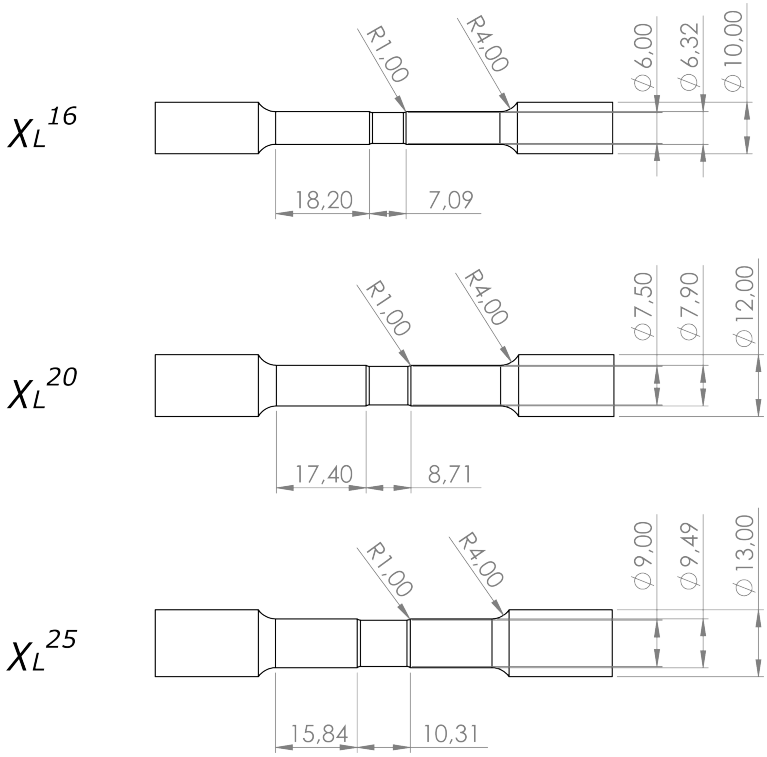

Figure D.2 Geometry of the tensile specimen for χ_L parameter.

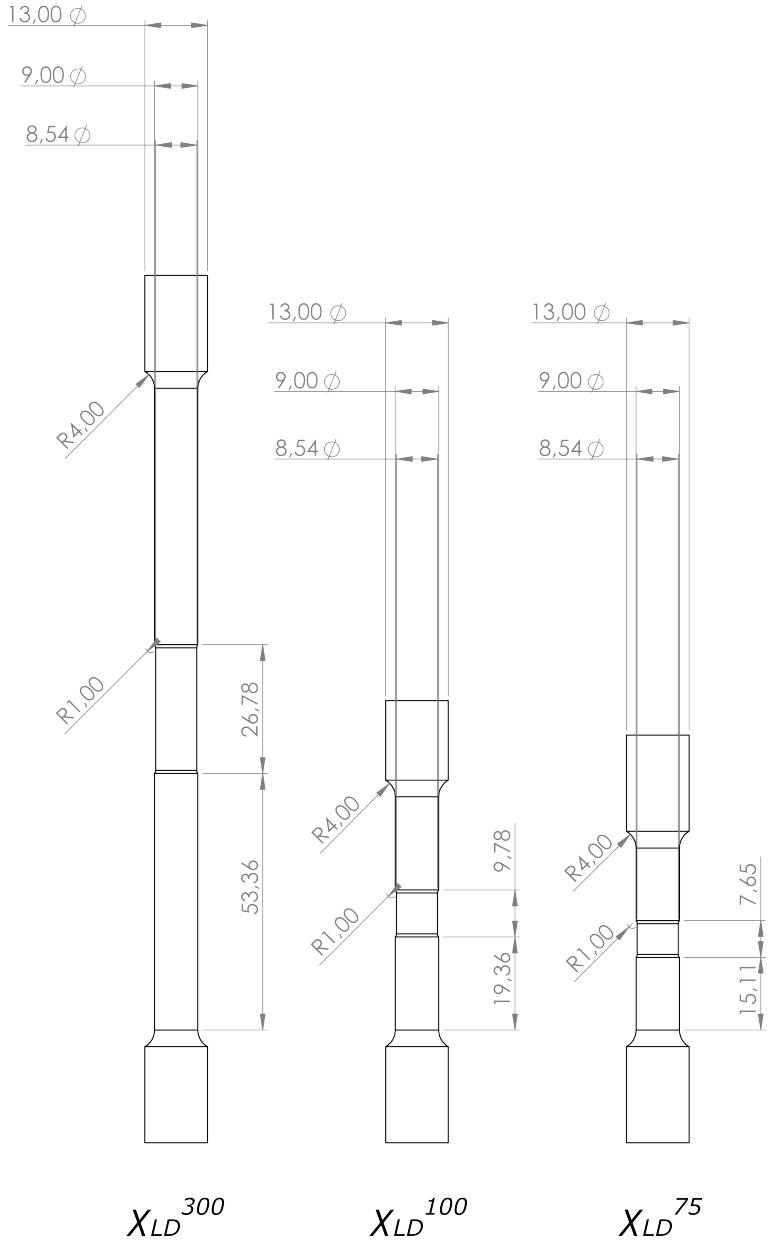

Figure D.3 Geometry of the tensile specimen for χ_{LD} parameter.

E

Appendix of Chapter 8 - Mesh convergence analysis

Two additional simulations were run for the χ_L^{25} geometry with a coarser and a finer mesh. Figure E.1 summarizes the dimensions of the 3 meshes. The average element size used in the manuscript is 0.06×0.06 mm, leading to a distribution of 70 elements through the radius. The coarser mesh is composed of 13 elements through the radius, of approximately 0.35×0.7 mm, while the finer mesh is composed of 130 elements through the radius, of approximately 0.03×0.03 mm.

The resulting strain fields, illustrated in Figure E.2, show a good convergence of the medium mesh as the strain profile is identical to the one of the finer mesh. However, the coarser mesh is not able to capture correctly the wavy pattern at the imperfection boarder. It was concluded that mesh size used in the manuscript was sufficient to ensure good convergence of the results.

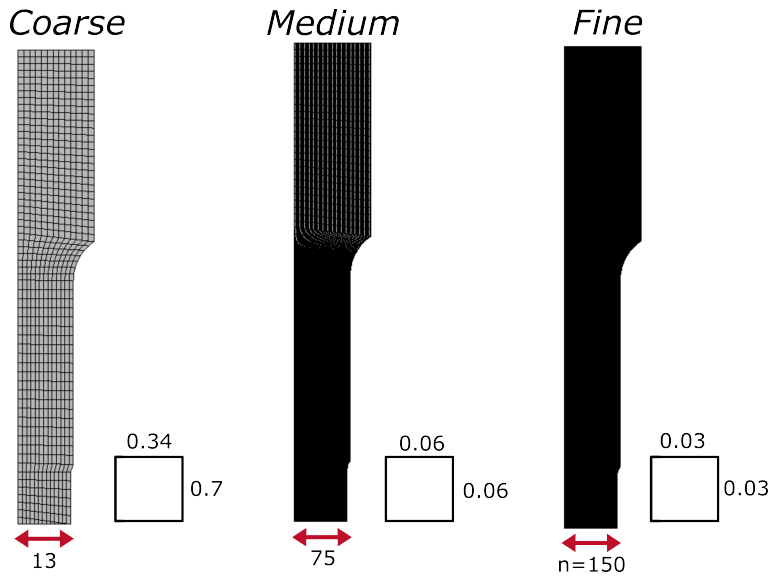

Figure E.1 Representation of 3 meshes in χ_L^{25} geometry highlighting the number of element along the radius and the average element size in mm.

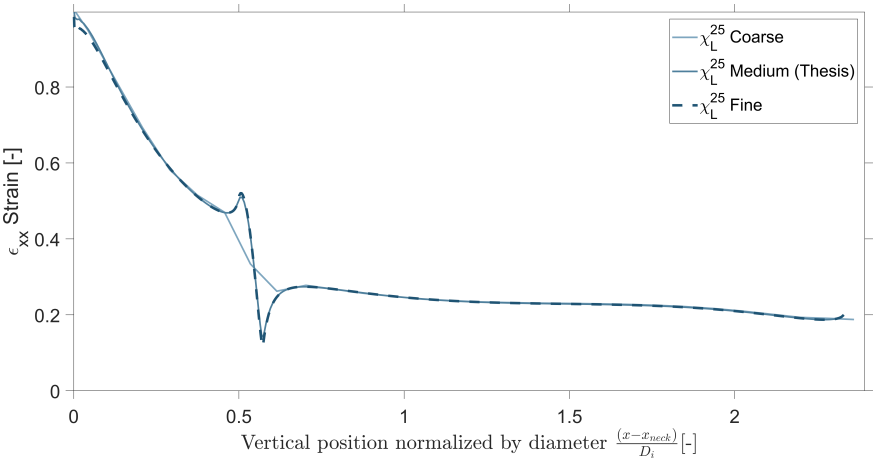

Figure E.2 Representation of the strain fields for 3 meshes in χ_L^{25} geometry.